



UNIVERSIDAD DE SEVILLA

DEPARTAMENTO DE QUÍMICA FÍSICA

TESIS DOCTORAL

---

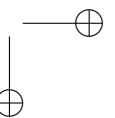
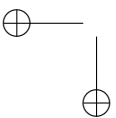
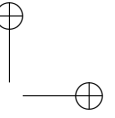
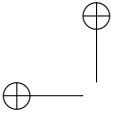
## **Ceria for all seasons**

---

*Doctorando:*  
José Javier Plata Ramos

*Directores:*  
Antonio M. Márquez Cruz  
Javier Fernández Sanz

July 23, 2013





UNIVERSIDAD DE SEVILLA

---

DEPARTAMENTO DE QUÍMICA FÍSICA

Memoria presentada para optar al Grado  
de Doctor por la Universidad de Sevilla

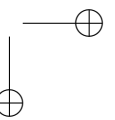
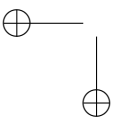
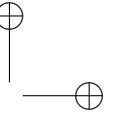
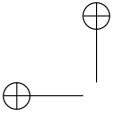
José Javier Plata Ramos

---

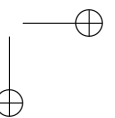
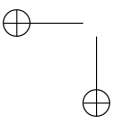
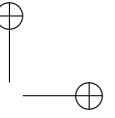
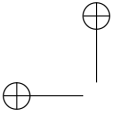
V<sup>o</sup> B<sup>o</sup> Directores de la Tesis

Dr. Javier Fernández Sanz      Dr. Antonio M. Márquez Cruz

---



*A mi familia*



## Agradecimientos

Me resisto a pensar que esta tesis vaya a ser el fin de un periodo en mi vida, me niego en rotundo. He disfrutado tanto durante este tiempo que me es imposible decir que esto se ha acabado. Quiero verlo simplemente como otra señal o punto kilométrico en este maravilloso camino que es el aprendizaje. Aprender y descubrir no sólo nuevos conocimientos, sino nuevas emociones, personas, vivencias. Este camino para mi es algo inherente a la vida, desde que nacemos podemos aprender, explorar, descubrir, sólo es necesario estar atentos a nuestro alrededor y tener ganas. Afortunadamente, este camino no lo hacemos solos, el componente humano es esencial e incuestionable. Desde pequeños, nuestros padres y profesores nos enseñan tanto a comunicarnos o entender nuestro entorno como valores. En las aulas, aprendemos y convivimos con otros compañeros que se encuentran inmersos en el mismo viaje que nosotros. En el día a día compartimos la jornada con familiares, amigos o colegas de trabajo con los que no dejamos de aprender cosas nuevas. Por todo ello, quiero aprovechar este alto para dar las gracias a aquellos con los que he tenido la suerte de compartir camino.

Gracias a mis directores de tesis. A Javier por acogerme en el grupo, durante estos años me he sentido plenamente respaldado por él en todo momento. Siempre me ha llenado de confianza y me ha animado a emprender nuevos proyectos. Ha sabido guiarme y me ha ayudado a seguir aprendiendo y desarrollándome como investigador. Siempre ha compartido su experiencia conmigo y ha tenido palabras de aliento en los momentos de más adversidad. Queda ya muy lejos la primera clase a las 4 de la tarde de Química Física II, sin embargo desde entonces Antonio ha estado ahí para todo. Son incontables las horas que me ha dedicado, los esfuerzos que ha hecho y la paciencia que ha tenido y tiene conmigo. Profesor, director de tesis y mi amigo.

Además de trabajar con mis directores de tesis, he tenido la oportunidad de colaborar con otras personas y grupos de los que he aprendido mucho durante mi doctorado. Gracias al Dr. José Antonio Rodríguez por dejarme colaborar en algunos de sus proyectos que hoy se ven reflejados en esta tesis. Tampoco puedo olvidarme de las personas que me

han acogido en sus centros durante este tiempo, desde la Dra. Nuria López y el Dr. Feliu Maseras, hasta el Dr. Miguel Pruneda o el Dr. Fernand Spiegelman y la Dra. Marie-Cathrine Heitz, gracias por ayudarme y enseñarme tantas cosas.

Gracias a Yanaris, Roger, Rocío y Laura. Ellos han sido muy importantes durante mi doctorado tanto a nivel científico como personal. Atesoro multitud de momentos inolvidables en los que ellos son parte muy activa. También agradecer al resto de personans que componen o han formado parte del grupo, Jesús, Norge, Jaime, Miguel Ángel, Ala', Vero e Igor su ayuda en todo momento.

No puedo olvidarme del resto de becarios con los que he compartido no sólo mil y un menús y cientos de tés. Eva, Noelia, María, Elsa, Elia, ... amigos con los que he convivido muchas horas y me han aguantado los días menos buenos.

Poco puedo decir de mis padres y hermano. Me siento francamente torpe intentando traducir en palabras el sentimiento de agradecimiento que siempre les tendré. Me han cuidado, formado y ayudado en todo momento y lugar, siempre incondicionalmente. Soy la persona que soy gracias a ellos.

A seguir trabajando y aprendiendo...

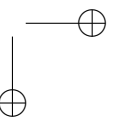
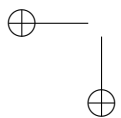
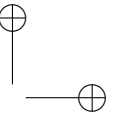
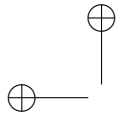


## CONTENTS

<b>Contents</b>	<b>xi</b>
<b>1 Introduction</b>	<b>1</b>
1.1 From cerium to ceria . . . . .	2
1.2 Mining and production . . . . .	3
1.3 Properties . . . . .	4
1.4 Synthesis and structure . . . . .	5
1.4.1 One-dimensional nanostructures . . . . .	6
1.4.2 Two- and three-dimensional nanostructures . . . . .	6
1.5 Applications . . . . .	7
1.5.1 CO oxidation . . . . .	8
1.5.2 Steam reforming of alcohols . . . . .	9
1.5.3 Photocatalysis . . . . .	9
1.5.4 Solid oxide fuel cells . . . . .	10
1.5.5 Sensors and oxygen permeation membranes . . . . .	11
1.5.6 Biomedical applications . . . . .	11
1.6 Theoretical approach . . . . .	12
1.7 Motivations and objectives . . . . .	13
<b>2 Methods</b>	<b>21</b>
2.1 Introduction to <i>ab-initio</i> methods: Hartree-Fock approximation . . . . .	22
2.1.1 Born-Oppenheimer Approximation . . . . .	23
2.1.2 Requirements for the Electronic Wave Function . . . . .	24
2.1.3 Slater Determinants . . . . .	25
2.1.4 Hartree-Fock Theory . . . . .	26
2.1.5 Roothaan SCF . . . . .	27
2.2 DFT methods . . . . .	28

2.2.1	Early Approximations . . . . .	29
2.2.2	From HK theorems to KS approach . . . . .	30
2.2.3	Exchange-correlation functionals . . . . .	32
2.3	Strongly correlated systems . . . . .	36
2.3.1	SIC functionals . . . . .	37
2.3.2	DFT+U . . . . .	37
2.4	Important aspects . . . . .	39
2.4.1	Basis set . . . . .	39
2.4.2	Pseudopotentials . . . . .	40
2.4.3	APW and PAW method . . . . .	43
2.5	Some properties . . . . .	43
2.5.1	Bader Charges . . . . .	43
2.5.2	Transition states search: CI-NEB method . . . . .	45
2.5.3	Electron transfer processes . . . . .	46
<b>3</b>	<b>Ceria as strongly correlated oxide</b>	<b>53</b>
3.1	Introduction . . . . .	54
3.1.1	The Wu-Cohen functional . . . . .	54
3.2	Comparative Study on the Performance of Hybrid DFT Functionals in Highly Correlated Oxides:The Case of CeO <sub>2</sub> and Ce <sub>2</sub> O <sub>3</sub> . . . . .	56
3.3	Improving the Density Functional Theory+U Description of CeO <sub>2</sub> by Including the Contribution of the O 2p Electrons . . . . .	67
3.4	GW approximation . . . . .	72
3.5	Conclusions . . . . .	73
<b>4</b>	<b>Ceria as ionic and electronic conductor</b>	<b>75</b>
4.1	Introduction . . . . .	76
4.2	Electron Mobility via Polaron Hopping in Bulk Ceria: A First-Principles Study . . . . .	77
4.3	Transport properties in CeO <sub>2-x</sub> (111) surface: from charge distribution to ion-electron collaborative migration. . . . .	91
<b>5</b>	<b>Ceria as nanostructure</b>	<b>107</b>
5.1	Introduction . . . . .	108
5.2	Ceria(100) Nanotubes with Negative Strain Energy: A First-Principles Prediction . . . . .	110
5.3	Influence of Dopants on the Conductivity of Ceria/Zirconia Heretoepitaxial Structures . . . . .	116

Contents	xi
<b>6 Ceria as catalyst and photocatalyst</b>	<b>129</b>
6.1 Introduction . . . . .	130
6.2 A Theoretical Insight into the Catalytic Effect of a Mixed-Metal Oxide at the Nanometer Level: The Case of the Highly Active metal/CeO <sub>x</sub> /TiO <sub>2</sub> (110) Catalysts . . . . .	132
6.3 Cu deposited on CeO <sub>x</sub> -modified TiO <sub>2</sub> (110): nature of the metal-support interaction and mechanism of the WGS reaction . . . . .	141
6.4 Nature of the mixed-oxide interface in ceria-titania system for photocatalytic water splitting . . . . .	158
<b>7 Conclusions</b>	<b>169</b>
<b>Appendix A Other publications</b>	<b>173</b>

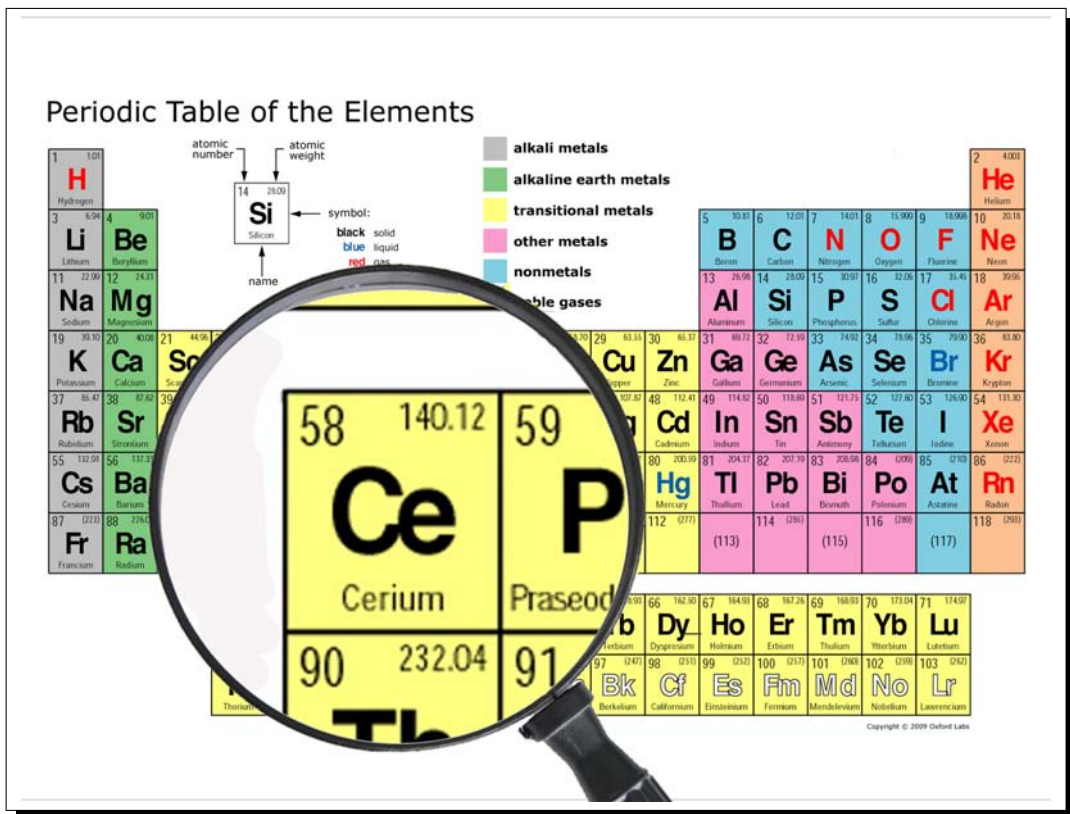


---

CHAPTER  
ONE

---

Introduction



## 1.1 From cerium to ceria

Cerium (Ce) is one of the seventeen elements that IUPAC defined as rare-earth metals in which are included the lanthanides, actinides, scandium and yttrium. Despite the group’s name, cerium is fairly abundant. Ce is not only the more abundant element of this group but also is most abundant in the Earth’s crust (66.5 ppm) than other familiar elements as copper (60 ppm) or tin (2.3 ppm).<sup>1,2</sup> The electron configuration of Ce is  $[\text{Xe}] 4f^2 6s^2$  with two common valence states Ce(III) and Ce(IV). Although we can find Ce in different compounds as cerium ammonium nitrate (CAN), which is used as a potent oxidizing agent, cerium oxide or ceria ( $\text{CeO}_2$ ) is the most common and important because of its technological applications, and actually it is much more present in our lives than we could expect.

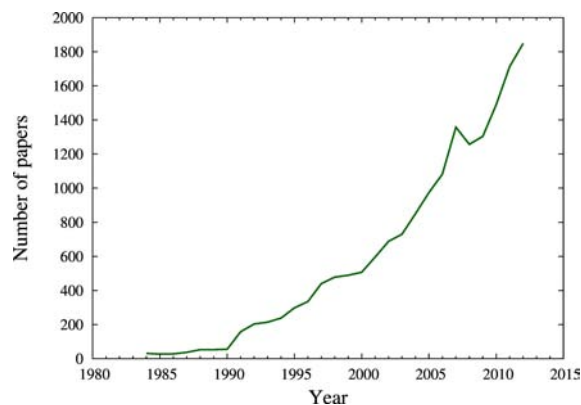


Figure 1.1: Papers related to ceria based materials which has been published in international journals from 1985.

The role of ceria in new technologies and devices can be observed in the impressive increase of the number of publications related to ceria in the last two decades (see Fig. 1.1). The use of ceria in many applications comes from the interconversion between  $4f^1$ -Ce(III) and  $4f^0$ -Ce(IV) oxidation states which is a unique behaviour between rare-earth elements. However, the application in which a higher amount of ceria is used, is not based in this property. Ceria is used for the chemical-mechanical polishing of surfaces, including microelectronic device wafers, electronic displays, eye glass lenses and other optical materials.<sup>3,4</sup> Through chemical attack of basic sites on surfaces, ceria provides better polishing rates than mechanical techniques.

Although a big amount of ceria is used for polishing surfaces, most of the research papers are focused on other applications for this oxide. For instance, ceria is used

as a promoter in three-way catalysts (TWC) for the elimination of toxic auto-exhaust gases,<sup>5,6</sup> low-temperature water gas shift (WGS) reaction,<sup>7,8</sup> oxygen sensors,<sup>9,10</sup> oxygen permeation membrane systems,<sup>11,12</sup> fuel cells,<sup>13–15</sup> electrochromic thin-film applications,<sup>16–18</sup> ultraviolet absorbent,<sup>19</sup> as well as in biotechnology, environmental chemistry, and medicine.<sup>20,21</sup>

Most of the applications mentioned above are related to the redox properties of this material which are associated to defects. Some defects such as oxygen vacancies or the presence of Ce(III) impurities are very common in ceria. With decreasing particle size, the defect formation energy is substantially reduced leading to markedly increased levels of nonstoichiometry and electronic carrier generation.<sup>22</sup> Therefore, nanostructured CeO<sub>2</sub> has attracted much attention due to improvements in the redox properties and transport properties with respect to bulk materials.<sup>23</sup>

## 1.2 Mining and production

Rare-earth minerals, occurring in a variety of geologic environments, are constituents in over 160 minerals, but only a few are recovered for commercial production.<sup>24</sup> Bastnasite, monazite, loparite, xenotime and 'Rare-earth bearing Clay' are the major sources of the world's rare-earth supply. Among them, bastnasite, monazite and loparite are the main cerium ores (Table 1.1).

Table 1.1: Distribution of rare-earth elements in commercial used rare-earth minerals in %

	Bastnasite (China)	Bastnasite (USA)	Monazite (Australia)	Loparite (Russia)
La <sub>2</sub> O <sub>2</sub>	27.2	32.3	23.9	25.0
CeO <sub>2</sub>	48.7	49.2	46.0	50.5
Pr <sub>6</sub> O <sub>11</sub>	5.1	4.5	5.1	5.0
Nd <sub>2</sub> O <sub>3</sub>	16.6	12.0	17.4	15.0
Y <sub>2</sub> O <sub>3</sub>	0.3	0.1	2.4	1.3

Bastnasite is a fluorocarbonate mineral found as an accessory mineral in several large deposits. The most important deposits containing bastnasite as a high grade accessory mineral are at Mountain Pass, California and Baiyunebo, China.<sup>25</sup> This mineral is mined from hard rock deposits. While chinese bastnasite is a by-product of iron ore mining, United States production is solely rare-earths. Monazite is phosphate mineral and one of the most abundant rare-earth minerals. It contains light-rare-earth elements and is enriched

in cerium.<sup>26</sup> This mineral usually appears associated to other minerals as zircon or rutile which are the driving force for exploiting the deposits. That is why monazite is treated as a by-product of the production of titanium and zirconium minerals. Australia is the major supplier of monazite of the world, followed by India, China or Brazil which also supply this mineral.<sup>27</sup> Loparite is a phosphate mineral that can be found in the Kola peninsula.<sup>28</sup>

### 1.3 Properties

CeO<sub>2</sub> presents a fluorite crystal structure with space group  $Fm\bar{3}m$  being stable from room temperature to the melting point. In this structure, Ce(IV) cations are coordinated to eight oxygens while each oxygen anion is coordinated by four cations. Some of its physical properties are listed in Table 1.2. Despite the fact that ceria exhibits few defects in the fluorite structure depending on the oxygen partial pressure, these defects modify the properties of the material for its potential use in catalysis, energy conversion and other applications. A complete reduction of this material lead to the hexagonal sesquioxide Ce<sub>2</sub>O<sub>3</sub> which presents a P3m1 structure.

Table 1.2: Some physical properties of pure stoichiometric CeO<sub>2</sub>

Property	Value
Melting point <sup>29</sup>	2750 K
Lattice parameter	$a_0 = 5.411 \text{ \AA}$
Thermal conductivity <sup>29</sup>	$12 \text{ W m}^{-1} \text{ K}^{-1}$
Electronic conductivity (25 °C) <sup>30</sup>	$2.48 \times 10^{-8} \text{ S cm}^{-1}$
Ionic conductivity (1000 °C in air) <sup>31</sup>	$3.13 \times 10^{-3} \text{ S cm}^{-1}$
Ionic conductivity (600 °C in air) <sup>31</sup>	$4.08 \times 10^{-5} \text{ S cm}^{-1}$

As aforementioned, oxygen vacancy formation is the key to some properties of this material. If an oxygen atom is removed from the lattice, two electrons are localized in the Ce *4f* band reducing two Ce(IV) to Ce(III) ions.<sup>32,33</sup> These two electrons in ceria can be described as small polarons, and the motion of electrons through the lattice is achieved via a thermally activated hopping process.<sup>34</sup> The formation of defects or vacancies in ceria can be considered a dynamic process because its concentration may change spontaneously or in response to physical parameters such as temperature, oxygen partial pressure, doping with other ions,<sup>35</sup> as well as an electric field,<sup>36</sup> or surface stress.<sup>37</sup>

For instance, CeO<sub>2</sub> is well known to release significant levels of oxygen at low oxygen partial pressures and elevated temperatures (e.g.  $\sim 10^{-15}$  atm O<sub>2</sub> at 800 °C) leading to a



mixed ionic electronic conductivity (MIEC). Ceria can accommodate a high concentration of vacancies by the substitution of some cations by lower valent elements in a similar way as occurs in zirconia. The effects of doping on the electrical properties of doped  $\text{CeO}_2$  have been well addressed by Guo *et al.*<sup>38</sup>

An electric field can be used to drive the redox process in  $\text{CeO}_2$ . This process was analyzed using high-resolution transmission electron microscopy by Wang *et al.*<sup>38</sup> These results could lead to the low-temperature operation of catalysts by means of an electric field for the purification of automobile emissions of pollutants, oxygen generation, and intermediate-temperature solid oxide fuel cells, as well as catalytic reforming. Some authors have observed how the application of an electric field reduces the operation temperature and the activation energy of some reactions.<sup>39</sup>

Modifications of the microstructure can also be used to increase the defect concentration and thus the conductivity of ceria. Two strategies are usually adopted: (1) to increase the density of grain boundaries, by moving from microcrystalline to nanocrystalline structures; (2) to create specific heterointerfaces, by employing epitaxial thin-film geometries.<sup>40</sup> Recently, doped-ceria has been used to prepare epitaxial-heterostructures using yttria stabilized zirconia (YSZ) as the second phase. Different authors have observed that increasing the number of nanometric layers leads to an enhancement of the conductivity by more than one order of magnitude.<sup>41</sup>

Particle size is also an important factor that should be taken into account. In ceria nanoparticles, the formation of more oxygen vacancies with a decrease in particle size has been reported.<sup>42,43</sup> The large surface area to volume ratio existing in a nanoparticle improves the catalytic performance of  $\text{CeO}_2$ . For instance, nanoparticles with a diameter below 5 nm seem to rise the catalytic activity of CO oxidation catalyst more than one order of magnitude compared to bulk ceria support.<sup>44</sup> Moreover, nanocrystalline  $\text{CeO}_2$  materials also possess some other new properties compared to the bulk material, such as the enhanced electronic conductivity,<sup>45,46</sup> the size-induced lattice relaxation,<sup>47,48</sup> the pressure-induced phase transformation,<sup>49</sup> and a blue shift in ultraviolet absorption spectra.<sup>50</sup>

## 1.4 Synthesis and structure

Microstructure can modify drastically the properties and potential applications of ceria materials, that is why a big effort has been devoted to prepare new ceria nanostructures which can improve the performance of this oxide. During the last two decades, new strategies, techniques and methods have been developed such as precipitation<sup>51</sup>, sol-gel,<sup>52</sup> solvothermal<sup>53,54</sup> or microemulsion method.<sup>55</sup> The nucleating seeds, kinetic control, temperature, and selective activation energy modulations of surfaces through the use of capping molecules have been found to be crucial in order to control the nucleation and growth of the crystal, and thus the shape, morphology and properties of the system. In

this section, one-, two-, and three-dimensional ceria nanostructures and its most important properties are presented.

### 1.4.1 One-dimensional nanostructures

Since first carbon nanotube was characterized in 1991,<sup>56</sup> one-dimensional (1D) nanostructures have been intensively investigated. It is recognized that 1D nanostructures may exhibit unique electrical, optical, magnetic, mechanical, and thermal properties that are obviously different from those of bulk materials, and they have been the focus of intense research owing to their fascinating physical and chemical properties. Nanowires, nanorods and nanotubes are excellent candidates for different applications because their unique morphological properties and as promising building blocks for nanoscale devices.

Wu *et al.* and La *et al.* were the two first groups to synthesize ceria nanowires and nanorods respectively using hard templates, such as alumina membranes.<sup>57,58</sup> Different mediator as solvents, surfactants, mineralizers, concentration or temperature can be used to control thermodynamically and kinetically the anisotropic growth of 1D ceria nanostructures. For instance, sodium bis(2-ethylhexyl) sulfosuccinate has been used as a structure-directing to synthesize ceria nanowires via a solution-phase route.<sup>59</sup> CeO<sub>2</sub> nanorods have also been prepared by solvothermal methods.<sup>60-63</sup> Some authors have achieved single crystalline nanorods with typical rectangular cross section with [110] as the preferential growth direction. These nanorods have well-defined reactive (001) and (110) planes and present high catalytic activity toward CO oxidation because of their specific crystal planes and high vacancy concentration.<sup>63</sup>

Ceria nanotubes (NTs) have been prepared via a two-step procedure: precipitation at 100 °C and aging at 0 °C for a long time (45 days).<sup>64</sup> New and faster methods have been developed in last years. Ceria NTs have been synthesized annealing layer-structured Ce(OH)<sub>3</sub> nanotubes in a reducing atmosphere.<sup>65</sup> Ce(OH)<sub>3</sub> has been also used as precursor to prepare nanotubes with large cavities and thin walls by a simple oxidation.<sup>66</sup> Moreover, ceria NTs have been reported to be active catalyst for the WGS reaction at low temperatures.<sup>67</sup> High porosity and oxygen storage capacity, and excellent reducibility are some of the properties found for these systems.<sup>64,66,68</sup> Although much has been learned about the synthesis of ceria NTs,<sup>69</sup> the mechanism of formation and its structural and electronic properties remain poorly understood.

### 1.4.2 Two- and three-dimensional nanostructures

New advances and progress in the synthesis of ceria materials is not only focused on 1D nanostructures. A huge amount of new two- and three-dimensional (2D and 3D) nanostructured ceria materials has been synthesized in last decade. From ceria nanocubes to flowerlike CeO<sub>2</sub> microspheres, the number and variety of new nanostructures are

impressive.<sup>70,71</sup> In this section we will try to overview some of the most important advances in this field.

2D nanosheets and nanoplates have received a lot of attention in recent years because of their special properties. Recently, a simple solution-phase synthetic method to prepare ultrathin ceria nanoplates in the presence of mineralizers has been reported.<sup>72</sup> Their morphology can be controlled by changing reaction parameters, such as precursor ratio, concentration, or reaction time. One of the most important properties of these nanostructures is their high theoretical surface-area to volume ratio. Moreover, these nanostructures preferentially exhibits (100) surfaces with a higher vacancy concentration and thus a higher oxygen storage capacity. The key point of this synthesis is the incorporation of sodium diphosphate which acts as a mineralizer, accelerates the crystallization and controls the morphology. Other groups have synthesized ultrathin single-crystalline ceria nanosheets using Ce(III) nitrate as precursor. These 2D nanostructures present a thickness of approximately 2.2 nm and a lateral dimension up to 4  $\mu\text{m}$ .<sup>73</sup>

Mesoporous ceria is a potential candidate for multiple applications because of its high surface area and the increased dispersion of active secondary components. Nevertheless, mesoporous ceria materials exhibit a poor thermal stability.<sup>74</sup> In order to solve this problem different synthetic methods have been proposed to obtain mesoporous ceria with an excellent thermal stability. Monodisperse flowerlike ceria microspheres has been synthesized using a hydrothermal method.<sup>70</sup> These microspheres present a 3D porous and hollow structures consisting on nanosheets as the petals which exhibit high surface area, large pore volume and higher hydrothermal stability. This synthetic method has been generalized to prepare doped ceria microspheres<sup>75</sup> which have demonstrated high reactivity in CO oxidation, hydrocarbon reforming and surprising performance in solid oxide fuel cells. In last years a huge variety of new approaches and nanostructures have been developed. Yang *et al.* have reported a thermal decomposition process to fabricate 3D ceria foams.<sup>76</sup> Highly ordered thermal stable mesoporous ceria with photocatalytic properties was synthesized via nanocasting using mesoporous silica.<sup>77,78</sup>  $\text{Ce}_{1-x}\text{Zr}_x\text{O}_2$  nanocages with different morphologies have been prepared with physical templates by Kirkendall effect.

As we pointed out previously, ceria nanoparticles are used as abrasive material to polish microelectronic devices. However, ceria nanocrystals present polyhedra shapes that scratch the silicon wafers and increase defect concentration.<sup>3</sup> New Ti-doped ceria nanocrystals with a spherical shape reduce polishing defects.<sup>3</sup> Recently, these results have been explained using molecular dynamics simulation.<sup>79</sup>

## 1.5 Applications

$\text{CeO}_2$  is a technologically important functional material for many applications. In this

section, a summary of some of its most important applications will be given.

### 1.5.1 CO oxidation

Loaded with noble metals, ceria has demonstrated an excellent performance as a three-way catalyst,<sup>5,6</sup> low-temperature water gas shift (WGS) catalyst,<sup>7,8</sup> and for preferential oxidation of CO in a large hydrogen excess (PROX).<sup>80</sup>

Since Haruta reported the high activity of supported gold nanoparticles for CO oxidation,<sup>81</sup> many researchers have tried to understand the origin of this surprising activity. There are many factors which modify the activity of Au-supported catalysts such as Au particle size, preparation method, pretreatment conditions, and choice of the support.<sup>44,82</sup> In particular, we are going to focus on how the support has a significant effect on the performance of the catalyst. It is possible to classify the support depending on its reducibility. While non-reducible supports as MgO don't modify the catalytic activity, reducible supports such as TiO<sub>2</sub> or CeO<sub>2</sub> enhance its efficiency. For instance, gold nanoparticles supported on flowerlike CeO<sub>2</sub> microspheres were used as catalyst for the CO oxidation reaction.<sup>83</sup> High dispersion was obtained with a nanoparticle size about 2-30 nm. Ceria microspheres produce an important decrease of the operating temperature compared to other supports. The CO gas stream over the Au-ceria starts rapidly its conversion into CO<sub>2</sub> at room temperature, reaching above 80% of conversion. The enhanced performance was attributed to its open three-dimensional porous structure, large pore volume and higher oxygen vacancy level in CeO<sub>2</sub> microspheres.

Positive effects of ceria supports can be improved by doping. Low-temperature reducibility is enhanced by doping with reducible elements, such as Pr and Sn.<sup>84-86</sup> While Pr- or Sn-doped flowerlike ceria catalysts exhibit excellent catalytic activities due to the variable valence states of Pr and Sn, the doping of Y, La or Zr in CeO<sub>2</sub> presents adverse effects on the activity of CO oxidation.<sup>75</sup> It seems that the doping with stable valence cations partially suppress the conversion of the redox Ce(IV)/Ce(III) couple and decrease the dynamic oxygen storage capacity (OSC) in ceria.

We can also tune the reactivity of the catalyst by controlling the support exposed planes. Recently, single-crystalline CeO<sub>2</sub> nanorods with a higher activity for CO oxidation than irregular nanoparticles were synthesized.<sup>63</sup> This improvement was assigned to the more reactive crystal planes (001) and (110) in nanorods. The shape-dependent OSC of ceria nanocrystals with various shapes have also been studied.<sup>62</sup>

The role of the support is even bigger in WGS reaction. It has been well established that water dissociation is one of the most important steps in the catalytic cycle, indeed, it is the rate limiting step if the support is a metal.<sup>87-89</sup> Reducible supports facilitate the dissociation of water and increase the rate of the reaction considerably.<sup>90,91</sup> Different authors have used CeO<sub>2</sub> based materials as support obtaining excellent results for water gas shift

reaction.<sup>92</sup> Recently a new family of highly active catalyst for WGS has been developed in which  $\text{TiO}_2$  is used as substrate and small non-stoichiometric ceria nanoclusters are adsorbed with the noble metal.<sup>93</sup> The amazing activity of this family of catalysts relies in the ability of the ceria nanocluster to adsorb and dissociate water.<sup>94</sup>

### 1.5.2 Steam reforming of alcohols

The use of biomass-derived alcohol for the production of hydrogen has significant interest for clean energy supply and environmental protection.<sup>97,98</sup>  $\text{CeO}_2$  materials has also been used as catalyst for steam reforming of ethanol producing  $\text{H}_2$ . In order to analyze the activity of these catalysts it is necessary to take into account not only the ethanol conversion but also the selectivity of the products. Steam reforming catalysts based on ceria produce a hydrogen-rich gas mixture in a wide temperature range (300-500 °C).<sup>70</sup> Thermal stable mesoporous ceria improves the stability and selectivity compared to other catalysts even at high temperatures. The  $\text{CeO}_2$  morphology plays again a key role on the catalytic activity of ethanol reforming. It has been found that 1D nanostructures (nanotubes and nanorods) which exposed (110) and (100) crystal planes, showed better  $\text{H}_2$  selectivity and activity compared to irregular  $\text{CeO}_2$  nanoparticles.<sup>99</sup>

### 1.5.3 Photocatalysis

Catalysis is one of the most widely cited applications for ceria materials. However, in the last two decades ceria is starting to be used as a photocatalyst too. Heterogeneous photocatalysis is an emerging technique valuable for renewable energy as well as for water and air purification and remediation.<sup>100</sup> In principle, its wide main gap is not ideal for photocatalytic purposes under visible or UV light. Nevertheless, synthetic procedure and adsorbates can modify the electronic structure and reduce the gap.

Organic-dye-free solar cells using nanometric ceria particles as the active component have been prepared.<sup>101</sup> Hierarchically structured mesoporous material with large pore volumes, high surface areas, and marked thermal stability was synthesized. It also exhibits a photovoltaic response which is directly derived from the nanometric particle size.

Efficient photocatalytic systems for water splitting is one strategic field urgently needed since it can eventually lead to the production of fuels using solar resources.<sup>102-104</sup> A big effort has been made in order to develop and produce efficient photocatalysis for visible-light water splitting. However, the number of semiconductors that have considerable photocatalytic activity under visible-light illumination is still limited. Moreover, the vast majority of the studies are carried out with  $\text{TiO}_2$  materials.<sup>105,106</sup> Nevertheless, there are some examples of ceria based materials which acts as photocatalyst for water splitting. For instance, photocatalytic activity of  $\text{Au-CeO}_2$  materials has been reported.<sup>107</sup> Interestingly, while the the photocatalytic activity under UV light is considerably reduced for  $\text{TiO}_2$  and

other semiconductors, the performance for Au-CeO<sub>2</sub> is better using visible light. Last year, amazing photocatalytic activity for Pt adsorbed on ceria-titania heterostructure has been reported by Rodriguez *et al.*<sup>108</sup> While the mixed oxide reduces the band gap and adsorbs in the UV-vis region, the platinum atoms seem to behave as electron traps that enhance the photocatalytic activity.

Photocatalytic hydrogen production has also been reported using ceria based materials. Ceria nanorods with (110) planes supported on titania have been compared to commercial CeO<sub>2</sub>, CdS and TiO<sub>2</sub> for photocatalytic hydrogen production. It has been reported that the activity of ceria nanorods is higher than those other commercial solids.<sup>109</sup>

Ceria nanomaterials have also potential application for environmental remediation. Recently, it has been demonstrated that ceria nanotubes exhibited a markedly enhanced photocatalytic activity and stability compared with the counterpart of CeO<sub>2</sub> nanoparticles and commercial TiO<sub>2</sub> toward the degradation of aromatic benzene.<sup>110</sup> This compound is a well-known toxic pollutant that commonly occurs in urban ambient air and is of concern regarding environmental health because of its toxic, mutagenic, and carcinogenic properties.

#### 1.5.4 Solid oxide fuel cells

Solid oxide fuel cells (SOFC) is one of the most promising, sustainable and environmental friendly technologies for the substitution of fossil fuels. However, to improve the chemical and mechanical stability, and reduce the operational cost require to lower the operating temperature of these devices. In fact, operating temperatures below 500 °C could facilitate the practical use of SOFC. Enhancement of ionic conductivity of the electrolyte is the key point to achieving this goal and one of the main current research issues.

Doped ceria materials have been intensively studied as solid electrolyte in these devices. However, during the last decade, a new generation of high ion conductance solid electrolyte based on epitaxial oxide heterostructures has substituted yttria stabilized zirconia (YSZ) and doped ceria oxides. There are two main groups of structures based on coupling: i) an ionic-conductor with an insulator (e.g. in LiI/Al<sub>2</sub>O<sub>3</sub> or AgCl/Al<sub>2</sub>O<sub>3</sub>), and ii) two ion-conducting oxides (e.g. in YSZ/Sm-CeO<sub>2</sub> or YSZ/Gd<sub>2</sub>Zr<sub>2</sub>O<sub>7</sub>). Huge ionic conductivity has been detected for YSZ/doped-ceria epitaxial heterostructures. Firstly, these phenomena were associated to the strain of the heterostructure lattice. However, the undoped ceria heterostructure presents the same conductivity as YSZ so it seems that dopants play a key role in the process.

It has been reported that ceria-based ion conductors have a high resistance to carbon deposition, which permits the direct supply of dry hydrocarbon fuels to the anode.<sup>111</sup> Different groups have reported anodes based on ceria. Gorte *et al.* prepared a composite anode of copper and ceria which is able to oxidate different hydrocarbons fuels ranging

from methane to toluene.<sup>112</sup> In this anode design, Cu is used as current collector and CeO<sub>2</sub> acts as oxidizing catalyst. It has also been reported that ceria nanoparticles can be added to a conventional Ni/YSZ anode to effectively enhance its sulfur tolerance.<sup>113</sup> Moreover, it has been demonstrated that the presence of ceria-based oxides in the anodes of solid oxides fuel cells with oxygen-ion-conducting electrolytes significantly lowers the activation overpotential for hydrogen oxidation. It has been pointed that the near-equilibrium H<sub>2</sub> oxidation reaction pathway was dominated by electrocatalysis at the oxide-gas interface with minimal contributions from the oxide-metal-gas triple-phase boundaries.<sup>114</sup> Some groups have tried to design anodes which can facilitate their practical use. For instance, a Ru-CeO<sub>2</sub> catalyst with a conventional anode has been combined allowing internal reforming of iso-octane without coking, making this SOFC a promising candidate for practical and efficient fuel cell applications.<sup>115</sup>

### 1.5.5 Sensors and oxygen permeation membranes

Ceria materials can be used as sensors in many areas such as environment, industry, transportation, medicine or agriculture in which the measurement and control of the oxygen content are critical. Different authors have prepared thin films of CeO<sub>2</sub> in which the electrical conductivity is dependent on the oxygen partial pressure and temperature.

Columnar CeO<sub>2</sub> nanostructures have been synthesized in order to be used as ethanol and NO<sub>2</sub> sensors.<sup>116</sup> These devices are able to exhibit isothermal conductance variation to 100 ppm ethanol and 1 ppm NO<sub>2</sub>. This particular ethanol concentration value is lower than the detection limit required for a breath analyzer (200 ppm, corresponding approximately to 0.6 g alcohol per liter in human blood). These nanodevices presents a sensitivity higher than previous sensors based on CeO<sub>2</sub> thin films which demonstrates the promise of development of nanosized ceria sensor devices.

Oxygen permeating ceramics with mixed ionic and electronic conductivity have received much interest for high temperature applications such as production of CO and H<sub>2</sub>, oxygen removal from steel melt, separation of oxygen from air in both coal gasification and oxy-fuel power plants.<sup>117</sup> Nanocrystalline CeO<sub>2</sub> thin films were synthesized on porous cerium oxide substrates and used for oxygen permeation membranes.<sup>117</sup>

### 1.5.6 Biomedical applications

Until now we have exposed technological applications of ceria and related materials. However, recent researches have demonstrated that ceria nanoparticles possess antioxidant activity, and the potential uses of these materials in biomedical applications, such as protection against radiation damage, oxidative stress, and inflammation.<sup>20,21,118,119</sup> These applications rely in the unique redox properties of ceria which reversibly switch from

Ce(III) to Ce(IV). Furthermore, conjugation with targeting ligands makes ceria nanoparticles an effective nanocatalyst and detection tool in immunoassays.<sup>120</sup> However, the safety of engineered nanomaterials must be well addressed before their use. It has been reported that ceria nanoparticles have very low toxicity and are long-lived which can extend their beneficial effects for long periods without redosing. Recently, some authors have reviewed possible toxic effects of very common oxides such as ZnO, TiO<sub>2</sub> and CeO<sub>2</sub>.<sup>121,122</sup> While ZnO induced toxicity in cells, leading to the generation of reactive oxygen species, TiO<sub>2</sub> and CeO<sub>2</sub> did not show any adverse effect. However CeO<sub>2</sub> suppressed reactive oxygen species production and induced cellular resistance to an exogenous source of oxidative stress.

Ceria nanoparticles have been employed for applications in spinal cord repair and other diseases of the central nervous system. The auto-catalytic anti-oxidant behavior and biocompatibility of this material have been evaluated.<sup>118</sup> Ceria nanoparticles exhibited ideal properties for life science applications with remarkable antioxidant activity and pseudo-infinite half-life. The auto-regenerative anti-oxidant property of these nanoparticles is the key to its neuroprotective action.

## 1.6 Theoretical approach

The accurate first-principles description of the electronic structure of *f*-electron systems, i.e. ceria materials, is currently regarded as one of the great challenges in condensed matter physics. Systems with electrons in *f* orbitals are characterized by the simultaneous presence of itinerant (delocalized) and highly localized *f*-states and interactions between them. Density functional theory (DFT) methods such as LDA or GGA approximation are inadequate for *f*-electrons systems. These methods don't correct the self-interaction error<sup>123</sup> which delocalizes the electrons and is specially severe for systems with partially occupied *d*- or *f*-states. For instance, LDA and GGA methods incorrectly predict the metallic behavior for reduced CeO<sub>2</sub> and Ce<sub>2</sub>O<sub>3</sub> where one electron should be localized in a *f*-state. This fact prevents the use of such methods to study ceria-based materials because Ce(III)-Ce(IV) redox conversion is crucial in most applications. However, hybrid functionals partially correct the self-interaction error by incorporating a certain portion of Hartree-Fock exact exchange, significantly improving the descriptions of *d*- or *f*-electron systems.<sup>124</sup> Hybrid functionals describe correctly qualitative CeO<sub>2</sub> materials properties but are computationally expensive so it is necessary to look for other methods in order to explore large systems. DFT+U method is cheaper but depends on the adjustable parameters *U* which is usually used only for correlated orbitals of metals in transition metal oxide. This parameter shifts orbital energies depending on its occupancy. The main shortcoming of DFT+U method is the non-universality of the approach. Structural and electronic properties of ceria, such as band gap or lattice constants, depend strongly on the



U value. Different U values between 2 to 6 have been used in order to describe correctly different experimental results as CO adsorption or band gap.<sup>124–127</sup> Moreover, the U value can modify not only quantitatively but also qualitatively the results. It has been found that the oxidation state of Au on CeO<sub>2</sub> (111) surface depends on the selected U value.<sup>128</sup>

Theoretical studies of ceria have grown considerably last years. Vacancy formation, metal adsorption, doping or ionic conduction are some of the most investigated topics related to ceria from a theoretical point of view. Localization of Ce(III) and its relationship with vacancies in defective ceria have been intensively studied by different authors. Due to the different models and approaches, there is some controversy related to which is the interaction between Ce(III) ions and the vacancies. While some authors have pointed that Ce(III) are located in next nearest neighbor positions, other authors have reported that nearest neighbor positions are the most stable.<sup>129–132</sup> Doping and oxygen migration has been also studied using DFT calculations. Different strategies has been proposed in order to decrease the vacancy formation energy and oxygen migration barrier at the same time using trivalent dopant metals.<sup>133,134</sup> Metal adsorption is another important field because of its applications in catalysis. Precious metal atoms and clusters adsorption have been modeled on different surfaces, clusters and 1D nanostructures.<sup>128,135–137</sup> The metal-ceria interaction is important in order to understand the catalytic process, predict and propose new high performance catalysts.

## 1.7 Motivation and objectives

Within this chapter we have tried to highlight the importance, versatility and potential of ceria-based materials. We have seen how it is possible to tailor its properties modifying the synthesis process. Moreover, ceria applications range a variety of fields of high technological impact. From theoretical quantum chemistry to catalysis, or from fuel cell to biomedical applications, ceria can be considered as a material with unique properties. That is why this thesis has as title Ceria for all seasons.

However, a generalized and wide use of ceria in new devices and applications has been hampered by its price. Prices for rare earth oxides have gone up in a surprising way during last twenty years. In fact, prices shot up to historical highs in 2011, even for the two most abundant of the light rare earth elements, lanthanum and cerium. However different analysts think that these prices are projected to collapse. Ceria prices have moved from 3.5 €/kg in 2008 to 139 €/kg in September 2011. However in 2012, the prices have decreased drastically to 58 €/kg and to 9.2 €/kg in 2013. Moreover is predicted this trend can continue until a historical minimum price of 0.8 €/kg in 2017. This trend is due to non-Chinese rare earth projects such as Mountain Pass in California and Mt. Weld in Western Australia that are coming on. As we have shown previously, research related to ceria has intensively increased during last two decades despite of the high prices of

the materials. Thus, the collapse of its price is going to stimulate even more not only the research related to ceria but also its commercial applications.

The main concern of this work is to study ceria properties and new applications. Because ceria exhibits different properties and many applications, we have tried to investigate ceria from different points of views. The thesis have been divided in 6 chapters. After presenting a selection of the most important methods and foundations in **Chapter 2**, we will investigate ceria as a strongly correlated system in **Chapter 3**. In this chapter, we will explore different methodologies and functionals in order to optimize the description of the material. We will focus on its structure, electronic properties and reactivity. **Chapter 4** is dedicated to dynamic processes involved in ceria materials which are also important for their applications. On one hand, electron mobility via polaron hopping determines the behavior of Ce(III) ions that are essential in catalysis. That is why we will study electron transfer (ET) reaction both in bulk and at the surface ceria within the two-state Marcus model. We will evaluate the most important parameters that characterize the ET process. On the other hand, ionic transport via oxygen migration is really important for solid electrolytes in fuel cells. In fact, ionic transport has been intensively studied for ceria and doped ceria bulk systems. However, the vacancy concentration is higher on the surface and the first atomic layers so we will study vacancy formation and migration in surface and subsurface positions. **Chapter 5** will be focused on new 1D and 2D ceria nanostructures. For this purpose, we will make use of the CRYSTAL09 code combined with helical-rototranslational symmetry to model mono, bi and tri layer ceria nanotubes, and analyze its stability and properties. We will also investigate 2D YSZ/doped-ceria epitaxial heterostructure and the origin of their huge ionic conductivity. Finally, ceria will be studied as catalyst and photocatalyst in **Chapter 6**. We will show new advances in a highly active family of water gas shift catalysts based on using  $\text{TiO}_2$  as substrate and small non-stoichiometric ceria nanoclusters adsorbed with the noble metals. Moreover, ceria/titania heterostructures will be modeled to understand its photocatalytic performance in water splitting reactions.

## References

1. Ahrens, T. J., *Global Earth Physics: a Handbook of Physical Constants*, American Geophysical Union **1995**.
2. Lide, D., *CRC Handbook of Chemistry and Physics*, CRC Publishing Co. **2007**.
3. Feng, X. D.; Sayle, D. C.; Wang, Z. L.; Paras, M. S.; Santora, B.; Sutorik, A. C.; Sayle, T. X. T.; Yang, Y.; Ding, Y.; Wang, X. D.; Her, Y. S., *Science* **2006**, *312*, 1504.
4. Armini, S.; Messemaeker, J. D.; Whelan, C. M.; Moinpour, M.; Maex, K., *J. Electrochem. Soc.* **2008**, *155*, H653.

5. Trovarelli, A., *Catal. Rev. Sci. Eng.* **1996**, 38, 439.
6. Kaspar, J.; Fornasiero, P.; Graziani, M., *Catal. Today* **1999**, 50, 285.
7. Fu, Q.; Weber, A.; Flytzani-Stephanopoulos, M., *Catal. Lett.* **2001**, 77, 87.
8. Fu, Q.; Saltsburg, H.; Flytzani-Stephanopoulos, M., *Science* **2003**, 301, 935.
9. Beie, H. J.; Gnorich, A., *Sensor. Actuat. B-Chem.* **1991**, 4, 393.
10. Jasinski, P.; Suzuki, T.; Anderson, H. U., *Sensor. Actuat. B-Chem.* **2003**, 95, 73.
11. Stoukides, M., *Catal. Rev. Sci. Eng.* **2000**, 42, 1.
12. Yin, X.; Hong, L.; Liu, Z. L., *J. Membrane Sci.* **2006**, 268, 2.
13. Steele, B. C. H., *Solid State Ionics* **2000**, 129, 95.
14. Sun, C.; Hui, R.; Roller, J., *J. Solid State Electr.* **2010**, 14, 1125.
15. Park, S. D.; Vohs, J. M.; Gorte, R. J., *Nature* **2000**, 404, 265.
16. Porqueras, I.; Person, C.; Corbella, C.; Vives, M.; Pinyol, A.; Bertan, E., *Solid State Ionics* **2003**, 165, 131.
17. Azens, A.; Kullman, L.; Ragan, D. D.; Granqvist, C. G.; Hjorvarsson, B.; Vaivars, G., *Appl. Phys. Lett.* **1996**, 68, 3701.
18. Ozer, N., *Sol. Energ. Mat. Sol. C.* **2001**, 68, 391.
19. Morimoto, T.; Tomonaga, H.; Mitani, A., *Thin Solid Films* **1999**, 351, 61.
20. Asati, A.; Santra, S.; Kaittanis, C.; Nath, S.; Perez, J. M., *Angew. Chem. Int. Edit.* **2009**, 48, 2308.
21. Tarnuzzer, R. W.; Colon, J.; Patil, S.; Seal, S., *Nano Lett.* **2005**, 5, 2573.
22. Tuller, H. L., *Solid State Ionics* **2000**, 131, 143.
23. Esposito, V.; Traversa, E., *J. Am. Ceram. Soc.* **2008**, 91, 1037.
24. Gschneider, K. A., *Fine Chemical for the Electronics Industry II: Chemical Applications for the 1990's*, Royal Society of Chemistry **1991**.
25. Drew, L.; Quingrun, M.; Weijun, S., *The Geology of the Byan Obo Iron-Rare Earth-Niobium Deposits, Inner Mongolia, China*, U. S. Geol. Surv. **1990**.
26. Mariano, A. N., *Geochemistry and Mineralogy of Rare Earth Elements*, Mineralogical Soc. of America, Review in Mineralogy **1990**.
27. Hedrick, J. B.; Templeton, D. A., *BuMines Minerals Yearbook* **1991**, page 14.
28. Habashi, F., *The Discovery and Industrialization of the Rare Earths*, CIM Bulletin **1994**.
29. Mogensen, M.; Sammes, N. M.; Tompsett, G. A., *Solid State Ionics* **2000**, 129, 63.
30. Lappalainen, J.; Tuller, H. L.; Lantto, V., *J. Electroceram.* **2004**, 13, 129.
31. Basu, S.; Devi, P. S.; Maiti, H. S., *J. Mater. Res.* **2004**, 19, 3162.
32. Bishop, S. R.; Stefanik, T. S.; Tuller, H. L., *Phys. Chem. Chem. Phys.* **2011**, 13, 10165.
33. Tuller, H. L.; Nowick, A. S., *J. Electrochem. Soc.* **1979**, 126, 209.

34. Tuller, H. L.; Nowick, A. S., *J. Phys. Chem. Solids* **1977**, 38, 859.
35. Mamontov, E.; Egami, T.; Brezny, R.; Koranne, M.; Tyagi, S., *J. Phys. Chem. B* **2000**, 104, 11110.
36. Gao, P.; Kang, Z.; Fu, W.; Wang, W.; Bai, X.; Wang, E., *J. Am. Chem. Soc.* **2010**, 132, 4197.
37. Sheldon, B. W.; Shenoy, V. B., *Phys. Rev. Lett.* **2011**, 106, 216104.
38. Guo, X.; Waser, R., *Prog. Mater. Sci.* **2006**, 51, 151.
39. Sekine, Y.; Haraguchi, M.; Tomioka, M.; Matsukata, M.; Kikuchi, E., *J. Phys. Chem. A* **2010**, 114, 3824.
40. Souza, R. A. D.; Ramadan, A.; Hoerner, S., *Energ. Environ. Sci.* **2012**, 5, 5445.
41. Azad, S.; Marina, O. A.; Wang, C. M.; Saraf, L.; Shutthanandan, V.; McCready, D. E.; El-Azab, A.; Jaffe, J. E.; Engelhard, M. H.; Peden, C. H. F.; Thevuthasan, S., *Appl. Phys. Lett.* **2005**, 86, 131906.
42. Deshpande, S.; Patil, S.; Kuchibhatla, S. V. N. T.; Seal, S., *Appl. Phys. Lett.* **2005**, 87, 133113.
43. Tsunekawa, S.; Sahara, R.; Kawazoe, Y.; Ishikawa, K., *Appl. Surf. Sci.* **1999**, 152, 53.
44. Carrettin, S.; Concepcion, P.; Corma, A.; Nieto, J. M. L.; Puentes, V. F., *Angew. Chem. Int. Edit.* **2004**, 43, 2538.
45. Chiang, Y. M.; Lavik, E. B.; Kosacki, I.; Tuller, H. L.; Ying, J. Y., *Appl. Phys. Lett.* **1996**, 69, 185.
46. Chiang, Y. M.; Lavik, E. B.; Kosacki, I.; Tuller, H. L.; Ying, J. Y., *J. Electroceram.* **1997**, 1, 7.
47. Zhou, X. D.; Huebner, W., *Appl. Phys. Lett.* **2001**, 79, 3512.
48. Zhou, X. D.; Huebner, W.; Anderson, H. U., *Appl. Phys. Lett.* **2002**, 80, 3814.
49. Wang, Z. W.; Saxena, S. K.; Pischedda, V.; Liermann, H. P.; Zha, C. S., *Phys. Rev. B* **2001**, 64, 012102.
50. Tsunekawa, S.; Fukuda, T.; Kasuya, A., *J. Appl. Phys.* **2000**, 87, 1318.
51. Zhang, F.; Chan, S. W.; Spanier, J. E.; Apak, E.; Jin, Q.; Robinson, R. D.; Herman, I. P., *Appl. Phys. Lett.* **2002**, 80, 127.
52. Laberty-Robert, C.; Long, J. W.; Lucas, E. M.; Pettigrew, K. A.; Stroud, R. M.; Doescher, M. S.; Rolison, D. R., *Chem. Mater.* **2006**, 18, 50.
53. Hirano, M.; Kato, E., *J. Am. Ceram. Soc.* **1999**, 82, 786.
54. Sun, C.; Chen, L., *Eur. J. Inorg. Chem.* **2009**, pages 3883–3887.
55. Masui, T.; Fujiwara, K.; Machida, K.; Adachi, G.; Sakata, T.; Mori, H., *Chem. Mater.* **1997**, 9, 2197.
56. Iijima, S., *Nature* **1991**, 354, 56.
57. Wu, G. S.; Xie, T.; Yuan, X. Y.; Cheng, B. C.; Zhan, L. D., *Mater. Res. Bull.* **2004**, 39, 1023.

58. La, R. J.; Hu, Z. A.; Li, H. L.; Shang, X. L.; Yang, Y. Y., *Mat. Sci. Eng. A-Struct.* **2004**, 368, 145.
59. Sun, C. W.; Li, H.; Wang, Z. X.; Chen, L. Q.; Huang, X. J., *Chem. Lett.* **2004**, 33, 662.
60. Sun, C. W.; Li, H.; Zhang, H. R.; Wang, Z. X.; Chen, L. Q., *Nanotechnology* **2005**, 16, 1454.
61. Vantomme, A.; Yuan, Z. Y.; Du, G. H.; Su, B. L., *Langmuir* **2005**, 21, 1132.
62. Mai, H. X.; Sun, L. D.; Zhang, Y. W.; Si, R.; Feng, W.; Zhang, H. P.; Liu, H. C.; Yan, C. H., *J. Phys. Chem. B* **2005**, 109, 24380.
63. Zhou, K. B.; Wang, X.; Sun, X. M.; Peng, Q.; Li, Y. D., *J. Catal.* **2005**, 229, 206.
64. Han, W. Q.; Wu, L. J.; Zhu, Y. M., *J. Am. Chem. Soc.* **2005**, 127, 12814.
65. Tang, C. C.; Bando, Y.; Liu, B. D.; Golberg, D., *Adv. Mater.* **2005**, 17, 3005.
66. Zhou, K.; Yang, Z.; Yang, S., *Chem. Mater.* **2007**, 19, 1215.
67. Han, W.; Wen, W.; Hanson, J. C.; Teng, X.; Marinkovic, N.; Rodriguez, J. A., *J. Phys. Chem. C* **2009**, 113, 21949.
68. Chen, G.; Xu, C.; Song, X.; Zhao, W.; Ding, Y.; Sun, S., *Inorg. Chem.* **2008**, 47, 723.
69. Lin, K.; Chowdhury, S., *Int. J. Mol. Sci.* **2010**, 11, 3226.
70. Sun, C.; Sun, J.; Xiao, G.; Zhang, H.; Qiu, X.; Li, H.; Chen, L., *J. Phys. Chem. B* **2006**, 110, 13445.
71. Yang, S.; Gao, L., *J. Am. Chem. Soc.* **2006**, 128, 9330.
72. Wang, D.; Kang, Y.; Doan-Nguyen, V.; Chen, J.; Kuengas, R.; Wieder, N. L.; Bakhtmutsky, K.; Gorte, R. J.; Murray, C. B., *Angew. Chem. Int. Edit.* **2011**, 50, 4378.
73. Yu, T.; Lim, B.; Xia, Y., *Angewandte Chemie-International Edition* **2010**, 49, 4484.
74. Carreon, M. A.; Gulians, V. V., *Eur. J. Inorg. Chem.* **2005**, pages 27–43.
75. Xiao, G.; Li, S.; Li, H.; Chen, L., *Micropor. Mesopor. Mat.* **2009**, 120, 426.
76. Xing, J.; Wang, H. F.; Yang, C.; Wang, D.; Zhao, H. J.; Lu, G. Z.; Hu, P.; Yang, H. G., *Angew. Chem. Int. Edit.* **2012**, 51, 3611.
77. Laha, S. C.; Ryoo, R., *Chem. Commun.* **2003**, pages 2138–2139.
78. Ji, P.; Zhang, J.; Chen, F.; Anpo, M., *J. Phys. Chem. C* **2008**, 112, 17809.
79. Sayle, D. C.; Feng, X.; Ding, Y.; Wang, Z. L.; Sayle, T. X. T., *J. Am. Chem. Soc.* **2007**, 129, 7924.
80. Manzoli, M.; Avgouropoulos, G.; Tabakova, T.; Papavasiliou, J.; Ioannides, T.; Boccuzzi, F., *Catal. Today* **2008**, 138, 239.
81. Haruta, M., *Journal of New Materials for Electrochemical Systems* **2004**, 7, 163.
82. Bond, G. C.; Thompson, D. T., *Catal. Rev.* **1999**, 41, 319.
83. Sun, C.; Li, H.; Chen, L., *J. Phys. Chem. Solids* **2007**, 68, 1785.
84. Song, Z.; Liu, W.; Nishiguchi, H.; Takami, A.; Nagaoka, K.; Takita, Y., *Appl. Catal. A-Gen.*

- 2007**, 329, 86.
85. Zhang, T.-Y.; Wang, S.-P.; Yu, Y.; Su, Y.; Guo, X.-Z.; Wang, S.-R.; Zhang, S.-M.; Wu, S.-H., *Catal. Commun.* **2008**, *9*, 1259.
  86. Sasikala, R.; Gupta, N. M.; Kulshreshtha, S. K., *Catal. Lett.* **2001**, *71*, 69.
  87. Gokhale, A. A.; Dumesic, J. A.; Mavrikakis, M., *J. Am. Chem. Soc.* **2008**, *130*, 1402.
  88. Liu, P.; Rodriguez, J. A., *J. Chem. Phys.* **2007**, *126*, 16705.
  89. Phatak, A. A.; Delgass, W. N.; Ribeiro, F. H.; Schneider, W. F., *J. Phys. Chem C* **2009**, *113*, 7269.
  90. Peng, S.; Ho, J., *Phys. Chem. Chem. Phys.* **2011**, *13*, 20393.
  91. Rodriguez, J. A.; Evans, J.; Graciani, J.; Park, J. B.; Liu, P.; Hrbek, J.; Sanz, J. F., *J. Phys. Chem. C* **2008**, *113*, 7364.
  92. Kim, H. Y.; Henkelman, G., *J. Phys. Chem. Lett.* **2012**, *4*, 216.
  93. Park, B.; Graciani, J.; Evans, J.; Stacchiola, D.; Senanayake, S. D.; Barrio, L.; Liu, P.; Sanz, J. F.; Hrbek, J.; Rodriguez, J. A., *J. Am. Chem. Soc.* **2010**, *132*, 356.
  94. Graciani, J.; Plata, J. J.; Sanz, J. F.; Liu, P.; Rodriguez, J. A., *J. Chem. Phys.* **2010**, *132*, 104703.
  95. Si, R.; Flytzani-Stephanopoulos, M., *Angew. Chem. Int. Edit.* **2008**, *47*, 2884.
  96. Boucher, M. B.; Goergen, S.; Yi, N.; Flytzani-Stephanopoulos, M., *Phys. Chem. Chem. Phys.* **2011**, *13*, 2517.
  97. Liguoras, D. K.; Kondarides, D. I.; Verykios, X. E., *Appl. Catal. B-Environ.* **2003**, *43*, 345.
  98. Deluga, G. A.; Salge, J. R.; Schmidt, L. D.; Verykios, X. E., *Science* **2004**, *303*, 993.
  99. Hsiao, W.-I.; Lin, Y.-S.; Chen, Y.-C.; Lee, C.-S., *Chem. Phys. Lett.* **2007**, *441*, 294.
  100. Litter, M. I., *Appl. Catal. B-Environ.* **1999**, *23*, 89.
  101. Corma, A.; Atienzar, P.; Garcia, H.; Chane-Ching, J. Y., *Nat. Mater.* **2004**, *3*, 394.
  102. Gust, D.; Moore, T. A.; Moore, A. L., *Accounts Chem. Res.* **2009**, *42*, 1890.
  103. Kudo, A.; Miseki, Y., *Chem. Soc. Rev.* **2009**, *38*, 253.
  104. Kamat, P. V., *J. Phys. Chem. C* **2007**, *111*, 2834.
  105. Yerga, R. M. N.; Galvan, M. C. A.; del Valle, F.; Villoria de la Mano, J. A.; Fierro, J. L. G., *Chemsuschem* **2009**, *2*, 471.
  106. Hernandez-Alonso, M. D.; Fresno, F.; Suarez, S.; Coronado, J. M., *Energ. Environ. Sci.* **2009**, *2*, 1231.
  107. Primo, A.; Marino, T.; Corma, A.; Molinari, R.; Garcia, H., *J. Am. Chem. Soc.* **2011**, *133*, 6930.
  108. Kundu, S.; Ciston, J.; Senanayake, S. D.; Arena, D. A.; Fujita, E.; Stacchiola, D.; Barrio, L.; Navarro, R. M.; Fierro, J. L. G.; Rodriguez, J. A., *J. Phys. Chem. C* **2012**, *116*, 14062.
  109. Lu, X.; Zhai, T.; Cui, H.; Shi, J.; Xie, S.; Huang, Y.; Liang, C.; Tong, Y., *J. Mater. Chem.*

- 2011, 21, 5569.
110. Tang, Z.-R.; Zhang, Y.; Xu, Y.-J., *Rsc Advances* **2011**, 1, 1772.
  111. Marina, O. A.; Mogensen, M., *Appl.Catal. A-Gen.* **1999**, 189, 117.
  112. He, H. P.; Gorte, R. J.; Vohs, J. M., *Electrochemical and Solid State Letters* **2005**, 8, A279.
  113. Kurokawa, H.; Sholkapper, T. Z.; Jacobson, C. P.; Jonghe, L. C. D.; Visco, S. J., *Elec. Solid State Lett.* **2007**, 10, B135.
  114. Chueh, W. C.; Hao, Y.; Jung, W.; Haile, S. M., *Nat. Mater.* **2012**, 11, 156.
  115. Zhan, Z. L.; Barnett, S. A., *Science* **2005**, 308, 844.
  116. Barreca, D.; Gasparotto, A.; Maccato, C.; Maragno, C.; Tondello, E.; Comini, E.; Sberveglieri, G., *Nanotechnology* **2007**, 18, 125502.
  117. Brinkman, K. S.; Takamura, H.; Tuller, H. L.; Iijima, T., *J. Electrochem. Soc.* **2010**, 157, B1852.
  118. Das, M.; Patil, S.; Bhargava, N.; Kang, J.-F.; Riedel, L. M.; Seal, S.; Hickman, J. J., *Biomaterials* **2007**, 28, 1918.
  119. Schubert, D.; Dargusch, R.; Raitano, J.; Chan, S. W., *Biochem. bioph. res. co.* **2006**, 342, 86.
  120. Perez, J. M.; Asati, A.; Nath, S.; Kaittanis, C., *Small* **2008**, 4, 552.
  121. Nel, A.; Xia, T.; Madler, L.; Li, N., *Science* **2006**, 311, 622.
  122. Xia, T.; Kovochich, M.; Liong, M.; Maedler, L.; Gilbert, B.; Shi, H.; Yeh, J. I.; Zink, J. I.; Nel, A. E., *Acs Nano* **2008**, 2, 2121.
  123. A. J. Cohen, P. M.-S.; Yang, W., *Science* **2008**, 321, 792.
  124. Da Silva, J. L. F.; Ganduglia-Pirovano, M. V.; Sauer, J.; Bayer, V.; Kresse, G., *Phys. Rev. B* **2007**, 75, 045121.
  125. Huang, M.; Fabris, S., *J. Phys. Chem. C* **2008**, 112, 8643.
  126. Castleton, C. M. W.; Kullgren, J.; Hermansson, K., *J. Chem. Phys.* **2007**, 127, 244704.
  127. Nolan, M.; Grigoleit, S.; Sayle, D. C.; Parker, S. C.; Watson, G. W., *Surf. Sci.* **2005**, 576, 217.
  128. Branda, M. M.; Castellani, N. J.; Grau-Crespo, R.; de Leeuw, N. H.; Hernandez, N. C.; Sanz, J. F.; Neyman, K. M.; Illas, F., *J. Chem. Phys.* **2009**, 131, 094702.
  129. Ganduglia-Pirovano, M. V.; Hofmann, A.; Sauer, J., *Surf. Sci. Rep.* **2007**, 62, 219.
  130. Ganduglia-Pirovano, M. V.; Silva, J. L. F. D.; Sauer, J., *Phys. Rev. Lett.* **2009**, 102, 026101.
  131. Shoko, E.; Smith, M. F.; McKenzie, R. H., *J. Phys. Chem. Solids* **2011**, 72, 1482.
  132. Nakayama, M.; Ohshima, H.; Nogami, M.; Martin, M., *PCCP* **2012**, 14, 6079.
  133. Andersson, D. A.; Simak, S. I.; Skorodumova, N. V.; Abrikosov, I. A.; Johansson, B., *P. Natl. Acad. Sci. USA* **2006**, 103, 3518.
  134. Tang, Y.; Zhang, H.; Cui, L.; Ouyang, C.; Shi, S.; Tang, W.; Li, H.; Lee, J.-S.; Chen, L., *Phys. Rev. B* **2010**, 82, 125104.

135. Vayssilov, G. N.; Lykhach, Y.; Migani, A.; Staudt, T.; Petrova, G. P.; Tsud, N.; Skala, T.; Bruix, A.; Illas, F.; Prince, K. C.; Matolin, V.; Neyman, K. M.; Libuda, J., *Nat.Mater.* **2011**, *10*, 310.
136. Campbell, C. T.; Parker, S. C.; Starr, D. E., *Science* **2002**, *298*, 811.
137. Plata, J. J.; Ruiz-Tagle, I.; Mrquez, A. M.; Sanz, J. F., *J. Phys. Chem. Lett.* **2012**, *3*, 2092.





## 2.1 Introduction to *ab-initio* methods: Hartree-Fock approximation

Describing the electronic structure of atoms, molecules or solids is ubiquitous to quantum mechanics, since electrons are very light particles and cannot be described quantitatively or qualitatively by classical mechanics. Wave function based quantum chemical methods can be characterized as being “ab-initio” methods (Latin: “from the beginning”) in which the solutions are generated without references to experimental data. This means that in these methods mathematical approximations to the full N-electron Schrödinger are built without the help of any adjustable parameters. One of the advantages of ab-initio methods is that they can be systematically improved towards the exact solution of the Schrödinger equation and they possess an intrinsic criterion for the quality of the current approximation.

The aim of quantum mechanics is solving the Schrödinger equation for the system under consideration which consists of a number  $K$  of nuclei and a number  $N$  of electrons. This system is determined by the Hamiltonian and will depend on the coordinates of the nuclei,  $R$ , and the electrons,  $r$ :

$$\hat{H}(R, r) \Psi(R, r) = E \Psi(R, r) \quad (2.1)$$

The total Hamiltonian operator can be written as kinetic and potential energy of the nuclei and the electrons

$$\hat{H}(R, r) = \hat{T}_n + \hat{T}_e + \hat{V}_{n,e} + \hat{V}_{e,e} + \hat{V}_{n,n} \quad (2.2)$$

where

$$T_n = -\frac{1}{2} \sum_{\alpha}^K \frac{\nabla_{\alpha}^2}{M_{\alpha}} \quad (2.3)$$

is the kinetic energy operator of the nuclei, and  $\nabla_{\alpha}^2 = \left( \frac{\delta^2}{\delta x_{\alpha}^2} + \frac{\delta^2}{\delta y_{\alpha}^2} + \frac{\delta^2}{\delta z_{\alpha}^2} \right)$ ,

$$T_e = -\frac{1}{2} \sum_i^N \nabla_i^2 \quad (2.4)$$

is the kinetic energy operator of the electrons,

$$V_{n,e} = - \sum_i^N \sum_{\alpha}^K \frac{Z_{\alpha}}{r_{i\alpha}} \quad (2.5)$$

is the Coulomb attraction between the nuclei possessing the charges  $Z_{\alpha}$  and the electrons,

$$V_{e,e} = \sum_{i=1}^N \sum_{j>i}^N \frac{1}{r_{ij}} \quad (2.6)$$

is the Coulomb repulsion between the electrons, and

$$V_{n,n} = \sum_{\alpha=1}^K \sum_{\beta>\alpha}^K \frac{Z_{\alpha}Z_{\beta}}{r_{\alpha\beta}} \quad (2.7)$$

is the Coulomb repulsion between the nuclei. Some aspects should be clarified about the Hamiltonian described above:

1. Atomic units have been used to describe the different operators that contribute to the Hamiltonian.
2. External electric or magnetic fields have not been included in the Hamiltonian.
3. The Hamiltonian given above is non-relativistic. Relativistic effects in quantum mechanical systems is beyond the scope of this chapter.

### 2.1.1 Born-Oppenheimer Approximation

If we try to solve the Schrödinger equation, we have a eigenvalue equation in  $3K + 3N$  independent variables which cannot be solved either analytically or numerically. For this reason, it is necessary to find approximate solutions, accurate enough to provide useful information. The first approximation was proposed by Born and Oppenheimer in 1927,<sup>1,2</sup> and consists in decoupling of the motion of the lighter and therefore "faster" electrons from the motion of the "slower" nuclei. This assumption leads to write the wave function  $\Psi(R, r)$  in the form of a product of an electronic wave function  $\Phi_e(r; R)$  and a nuclear wave function  $\chi_n(R)$ :

$$\Psi(R, r) = \Phi_e(r; R) \cdot \chi_n(R) \quad (2.8)$$

By means of Eq. 2.8 the total Schrödinger equation (Eq. 2.1) is decomposed into one equation for the electronic wave function  $\Phi_e(r; R)$

$$\hat{H}_e \Phi_e(r; R) = E_e(R) \Phi_e(r; R) \quad (2.9)$$

where

$$\hat{H}_e = \hat{H} - \hat{T}_n = \hat{T}_e + \hat{V}_{n,e} + \hat{V}_{e,e} + \hat{V}_{n,n} \quad (2.10)$$

and one equation for the wave function  $\chi_n(R)$  describing the motion of the nuclei

$$[\hat{T}_n + E_e(R) + \hat{C}(R)]\chi_n(R) = E\chi_n(R) \quad (2.11)$$

It has to be noted that  $\Phi_e(r; R)$  not only depends on  $r$  but also depends parametrically on the coordinates  $R$  of the nuclei. As consequence of this fact, electronic Schrodinger equation has to be solved for a given nuclear geometry. Because of this dependence,  $E_e(R)$

plays the role of the potential energy in the Schrödinger equation (Eq. 2.11) and it is usually called as “potential energy surface” (PES). The term  $\hat{C}(R)$  is an operator called “adiabatic diagonal correction” which acts on the nuclear wave function  $\chi_n(R)$ .

$$\hat{C}(R) = \int \Phi_e^*(r; R) T_n \Phi_e(r; R) dr - \sum_{\alpha} \frac{1}{M_{\alpha}} \int \Phi_e^*(r; R) \nabla_{\alpha} \Phi_e(r; R) dr \cdot \nabla_{\alpha} \quad (2.12)$$

If  $C(R)$  is neglected, this approximation is called the Born-Oppenheimer approximation, however, it is named adiabatic approximation if it is included. In most cases, the Born-Oppenheimer approximation works pretty well and it is only necessary to go beyond it in cases of degeneracies or at very high energies for the nuclear motion.

### 2.1.2 Requirements for the Electronic Wave Function

From now, we will stay within the Born-Oppenheimer approximation and will only be concerned with the electronic Schrödinger equation (Eq. 2.9). In order to simplify the notation, we will drop the subscript “el” and the nuclear coordinates  $R$  from  $\Phi_e(r; R)$ .

A wave function has to satisfy three requirements for describing the electronic structure of the system and to being an approximate or exact solution of the electronic Schrödinger equation (Eq. 2.9).

1. *Normalization.* This condition ensures that the probability for finding the system somewhere in space is unity.

$$\int \Phi^*(r) \Phi(r) dr = 1 \quad (2.13)$$

2. *Antisymmetry* with respect to the permutation of two electrons. As electrons are fermions, the solutions of the electronic Schrödinger equation must be antisymmetric with respect to a permutation of any two electrons in the system.

$$\Phi(1, 2, \dots, i, \dots, j) = -\Phi(1, 2, \dots, j, \dots, i) \quad (2.14)$$

3. *Electronic spin.* Electronic Hamiltonian (Eq. 2.10) commutes with the operators  $S_z$  and  $S^2$

$$[\hat{H}, \hat{S}_z] = 0, \quad [\hat{H}, \hat{S}^2] = 0 \quad (2.15)$$

where  $\hat{S}_z$  and  $\hat{S}^2$  are the N-electron spin operators

$$\hat{S}_z = \sum_i^N \hat{s}_{z_i}, \quad \hat{S}^2 = \sum_i^N \hat{s}_i^2 \quad (2.16)$$

This means that electronic wave functions have to be eigenfunctions of  $\hat{S}_z$  and  $\hat{S}^2$  with the eigenvalues  $M_S$  and  $S(S + 1)$ . From now, we will represent the wave function of an electron as a product of a spatial part and a spin function. There are only two possible spin functions  $\alpha$  and  $\beta$ . In order to simplify the notation, beta-spin is usually denoted by a bar above the orbital.

### 2.1.3 Slater Determinants

Electronic Hamiltonian (Eq. 2.10) contains one-electron terms, two-electron terms and the nuclear repulsion  $V_{n,n}$  which is independent of the electron coordinates.

$$\hat{H} = \sum_i \hat{h}(i) + \sum_{ij} g(ij) + V_{n,n} \quad (2.17)$$

$$\hat{h}(i) = -\frac{1}{2}\nabla_i^2 - \sum_{\alpha}^K \frac{Z_{\alpha}}{r_{i\alpha}}, \quad g(ij) = \frac{1}{r_{ij}} \quad (2.18)$$

Due to the presence of two-electron terms,  $g(ij)$ ,  $\hat{H}$  cannot be a sum of terms which only depends on one electron coordinates. That's why  $\hat{H}$  cannot be made separable and therefore its eigenfunctions are not just products of eigenfunctions of the one-particle Hamiltonian  $\hat{h}$  and its eigenvalues sums of eigenvalues of  $\hat{h}$ . Nevertheless, we can consider products of one-electron wave functions as valid trial wave functions.

$$\Phi(1, \dots, N) = \psi_a(1) \cdot \psi_b(2) \cdots \psi_N(N) \quad (2.19)$$

This product does not possess the required antisymmetry property, therefore we have to apply the antisymmetrizer operator and obtain

$$\Phi(1, \dots, N) = \mathcal{A}[\psi_a(1) \cdot \psi_b(2) \cdots \psi_N(N)] \quad (2.20)$$

Antisymmetrizer operator generates a determinant which can be written as<sup>3</sup>

$$\Phi(1, \dots, N) = |\psi_a(1) \cdot \psi_b(2) \cdots \psi_N(N)| \quad (2.21)$$

where  $|\dots|$  is the usual notation for a determinant including the normalization constant  $\mathcal{N}$ .

Now we can use this trial function to calculate its energy expectation value

$$\langle \Phi | H | \Phi \rangle = \sum_{i=1}^n 2\langle i | h | i \rangle + \sum_{i,j=1}^n [2\langle ii | jj \rangle - \langle ij | ji \rangle] \quad (2.22)$$

where it is possible to distinguish: One-electron integrals,

$$\langle i | h | i \rangle = \int \phi_i^*(1) h(1) \phi_i(1) dr_1 \quad (2.23)$$

two-electron Coulomb-integrals,

$$(ii|jj) = \int \phi_i^*(1)\phi_i(1)\frac{1}{r_{12}}\phi_j^*(2)\phi_j(2)dr_1dr_2 \quad (2.24)$$

and two-electron exchange-integrals

$$(ij|ji) = \int \phi_i^*(1)\phi_j(1)\frac{1}{r_{12}}\phi_j^*(2)\phi_i(2)dr_1dr_2 \quad (2.25)$$

While the Coulomb-integral  $(ii|jj)$  corresponds exactly to the classical Coulomb interaction between two charge distributions  $\phi_i^*(1)\phi_i(1)$  and  $\phi_j^*(2)\phi_j(2)$ , the exchange integral does not present a classical analogue and it derives from the antisymmetry requirement to the quantum mechanical wave function  $\Phi$ .

### 2.1.4 Hartree-Fock Theory

We are going to consider an electronic system containing an even number of electron,  $N = 2n$ , which is realized for most ground states of stable molecules and periodic systems. In such cases, a one-determinant wave function of the form

$$\Phi_{SCF} = |\phi_1\bar{\phi}_1\phi_2\bar{\phi}_2 \dots \phi_n\bar{\phi}_n| \quad (2.26)$$

will be a good approximation to the true ground state wave function of the N-electron Hamiltonian. In fact, the Hartree-Fock or self-consistent field (SCF) consists essentially in making the ansatz (Eq. 2.26) for the N-electron wave function of the system under consideration.<sup>4,5</sup>

The orbitals  $\phi_i$  which are occupied in  $\Phi_{SCF}$  have to be determined. The most simple choice could be selecting the eigenfunctions of one particle Hamiltonian  $h$ , however, this yields to a poor approximation. Variation principle has to be applied to the wave function in order to obtain a reasonable set of orbitals and the energy expectation value calculated with  $\Phi_{SCF}$  as a functional of the occupied orbitals  $\phi_i$ . Eq. 2.22 shows how to obtain it, however, this formula is only valid if the occupied orbitals form an orthogonal set. That means that the energy expectation value has to be varied under the constraint that the orbitals remain orthogonal during the variation. This requirement can be achieved employing the method of the Lagrange multipliers. Therefore, we have to search for the minimum of the functional

$$\mathcal{J}[\phi] = \sum_{i=1}^n 2\langle i|h|i\rangle + \sum_{i,j=1}^n [2(ii|jj) - (ij|ji)] - \sum_{i,j=1}^n 2\lambda_{ij}[(\phi_i|\phi_j) - \delta_{ij}] \quad (2.27)$$

Section 2.1. Introduction to *ab-initio* methods: Hartree-Fock approximation 27

by varying the orbitals  $\phi_i$  where  $\delta_{ij}$  are the unknown Lagrangean multipliers. Performing this variation one arrives at the following one-particle eigenvalue equation

$$[h_i + \sum_j^{occ} (2J_j - K_j)]\phi_i = \sum_j^n \delta_{ij}\phi_j \quad \forall \phi_i \quad (2.28)$$

where  $J_j$  and  $K_j$  are the Coulomb and exchange operators respectively.

Eq. 2.28 can be simplified by noting that the SCF wave function  $\Phi_{SCF}$  (Eq. 2.26) is invariant with respect to unitary transformations among the occupied orbitals  $\phi_i$ . This fact can be used to transform Lagrangean multipliers matrix into a diagonal matrix. Moreover, we define this diagonal elements as  $\epsilon_i$  and the Fock operator as

$$\hat{F}_i = \hat{h}_i + \sum_j^{occ} (2\hat{J}_{ji} - \hat{K}_{ji}) \quad (2.29)$$

Finally we obtain

$$\hat{F}_i\phi_i = \epsilon_i\phi_i \quad \forall \phi_i \quad (2.30)$$

which is the Hartree-Fock equation. Since  $\hat{J}$  and  $\hat{K}$  operators are built from the orbitals  $\phi_i$  which have to be determined by solving the Hartree-Fock equation, iterative schemes are necessary. Commonly, some guess,  $\phi_i^{(0)}$  are used to construct  $\hat{J}_{ji}^{(0)}$ ,  $\hat{K}_{ji}^{(0)}$  and  $\hat{F}_i^{(0)}$  operators. Then, Eq. 2.30 is solved, yielding the next set of orbitals and orbitals energy. This procedure is repeated till "self-consistency" is reached.

### 2.1.5 Roothaan SCF

Though the Hartree-Fock theory has been formulated in the early 1930s, for a long time only numerical calculations could be performed for small and highly symmetric systems, such as atoms and diatomic molecules.

The breakthrough for molecular calculations came in 1951 when Hall<sup>6</sup> and Roothaan<sup>7</sup> independently proposed to expand the Hartree-Fock orbitals into a set of atom centered basis functions. Firstly, atomic orbitals were used,<sup>8</sup> then Boys<sup>9</sup> proposed using Gaussian functions, now other functions are also employed.

Roothaan proposed to expand the unknown Hartree-Fock orbitals  $\phi_i$  into a finite set of known M basis functions  $\chi_\nu$ .

$$\phi_i = \sum_{\nu=1}^M c_{i\nu}\chi_\nu \quad (2.31)$$

Now, the coefficients  $c_{i\nu}$  determine the orbitals  $\phi_i$  and have to be calculated. Variation principle is used again to obtain the coefficients that minimize the energy with the Hartree-

Fock equation.

$$\sum_{\nu}^M F_{\mu\nu} c_{i\nu} = \epsilon_i \sum_{\nu}^M S_{\mu\nu} c_{i\nu} \quad \forall \mu = 1, \dots, M \quad (2.32)$$

or in matrix notation

$$FC = \epsilon SC \quad (2.33)$$

where the  $S$  matrix contains the overlap elements between basis functions,  $F$  contains the Fock matrix elements in the  $\chi_{\nu}$  basis and  $C$  contains the coefficients vectors,

$$S_{\mu\nu} = (\mu|\nu) = (\chi_{\mu}|\chi_{\nu}) = \int \chi_{\mu}^* \chi_{\nu} \quad (2.34)$$

$$F_{\mu\nu} = (\mu|h|\nu) + \sum_j \sum_{\rho,\sigma} c_{j\rho} c_{j\sigma} [2(\rho\sigma|\mu\nu) - (\rho\nu|\mu\sigma)] \quad (2.35)$$

As in Hartree-Fock equation (Eq. 2.30), Roothaan-Hall equation (Eq. 2.33) has to be solved iteratively, using first some guess coefficients to construct an initial Fock matrix. Using Eq. 2.33 a new set of orbitals is obtained and the process is repeated until self consistency is achieved. Eq. 2.30 and Eq. 2.33 are only equivalent if  $M \rightarrow \infty$ , in other words, if a complete one-electron basis set is employed.

## 2.2 Density Functional Theory methods

Density Functional Theory (DFT), is a quantum mechanical theory used to introduce the effects of correlation to study the ground state of large many-body systems. The key variable is electron density,  $\rho(\mathbf{r})$ , which is given by

$$\rho(\mathbf{r}) = N \int d^3 r_2 \int d^3 r_3 \dots \int d^3 r_N \Psi^*(\mathbf{r}, \mathbf{r}_2 \dots \mathbf{r}_N) \Psi(\mathbf{r}, \mathbf{r}_2 \dots \mathbf{r}_N) \quad (2.36)$$

Hartree-Fock approximation is based on calculating a molecular wavefunction, however the wavefunction is not a measurable feature of a molecule or atom, it is not an "observable". DFT is based not on the wavefunction, but rather on the electron probability density commonly called the electron density,  $\rho(\mathbf{r})$ . Whereas the many-body stationary wave function,  $\Psi(\mathbf{r}, \mathbf{r}_2 \dots \mathbf{r}_N)$ , is dependent on  $3N$  variables, the density is only a function of three variables and is a simpler quantity to deal with both conceptually and practically. DFT is computationally much less expensive than post-Hartree-Fock methods, that is the main reason of its popularity.



### 2.2.1 Early Approximations

DFT roots its basis on the Thomas-Fermi<sup>10,11</sup> method developed in 1927 which is a prototypical description of the ground-state properties of a many-electron system. The simplest approach is to consider the system to be classical, in which case the potential energy components are straightforwardly determined. The attraction between the electron density and the nuclei is

$$V_{n,e}[\rho(\mathbf{r})] = \sum_{\alpha}^K \int \frac{Z_{\alpha}}{|\mathbf{r} - \mathbf{r}_{\alpha}|} \rho(\mathbf{r}) d\mathbf{r} \quad (2.37)$$

and the self-repulsion of a classical charge distribution is

$$V_{e,e}[\rho(\mathbf{r})] = \int \int \frac{\rho(\mathbf{r}_1)\rho(\mathbf{r}_2)}{|\mathbf{r}_1 - \mathbf{r}_2|} d\mathbf{r}_1 d\mathbf{r}_2 \quad (2.38)$$

However, the kinetic energy of a continuous charge distribution is less obvious. To proceed, we first introduce the fictitious substance jellium. Jellium is a system composed of an infinite number of electrons moving in an infinite volume of a space that is characterized by a uniformly distributed positive charge. This electronic distribution, also called the uniform electron gas, has a constant non-zero density. Thomas and Fermi,<sup>10,11</sup> in 1927, used fermion statistical mechanics to derive the kinetic energy for this system as

$$T_{TF}[\rho] = C_F \int \rho^{5/3}(\mathbf{r}) d\mathbf{r} \quad (2.39)$$

where  $C_F$  is (in atomic units)

$$C_F = \frac{3}{10} (3\pi^2)^{2/3} \quad (2.40)$$

Finally, the energy of the system can be calculated as

$$E_{TF}[\rho(\mathbf{r})] = T_{TF}[\rho(\mathbf{r})] + V_{n,e}[\rho(\mathbf{r})] + V_{e,e}[\rho(\mathbf{r})] \quad (2.41)$$

In 1928, Dirac<sup>12,13</sup> and Bloch<sup>14</sup> improved this theory including an Exchange term,  $K(\mathbf{r})$  which is known as Thomas-Fermi-Dirac model (TFD). This theory remained rather inaccurate for most applications, for instance, the energies obtained with this model present an error between 10-15%. However, the most important problem of the method is the inability to describe the chemical bonding. In order to describe chemical bonds and molecules some authors proposed different  $K(\mathbf{r})$  terms derived from the exchange term proposed by Slater<sup>15</sup>

$$K[\rho(\mathbf{r})] = -\frac{9\alpha}{8} \left(\frac{3}{\pi}\right)^{1/3} \int \rho^{4/3}(\mathbf{r}) d\mathbf{r} \quad (2.42)$$

Given the differing values of  $\alpha$  in Eq.2.42 as a function of different derivations, many early workers try to fit it as an empirical value which usually are termed as  $X_\alpha$  calculations.<sup>16–18</sup> These new methods can describe chemical bonding however there were big differences compared with wavefunction methods.

Finally, in 1964, Hohenberg and Kohn (HK)<sup>19</sup> developed the existence of a one-to-one correspondence between the ground state electron density,  $\rho(\mathbf{r})$  and the ground state wavefunction of a many-particle system  $\Psi(\mathbf{r}, \mathbf{r}_2 \dots \mathbf{r}_N)$ . They proved that the energy of a quantum mechanical system is a unique function of  $\rho(\mathbf{r})$  and that the correct ground-state density minimizes it.

### 2.2.2 From The Hohenberg-Kohn theorems to Kohn-Sham approach

Nowadays DFT calculations are based on the Kohn-Sham approach,<sup>20</sup> the stage for which was set by two theorems published by Hohenberg and Kohn in 1964.<sup>19</sup> The first Hohenberg-Kohn theorem says that any ground state property of a molecule is a functional of the ground state electron density function  $\rho_0(\mathbf{r})$ . In other words, ground state wavefunction  $\Psi_0$  is a unique functional of  $\rho_0(\mathbf{r})$ .

$$\Psi_0 = \Psi_0[\rho_0] \quad (2.43)$$

The second Hohenberg-Kohn theorem is the DFT analogue of the wavefunction variation theorem: it says that any trial electron density function,  $\rho'$ , will give an energy higher than or equal to the true ground state energy.

$$E[\rho'] \geq E[\rho_0] \quad (2.44)$$

The Hohenberg-Kohn theorems were originally proved only for nondegenerate ground states, but have been shown to be valid for degenerate ground states too.

The main problem in Thomas-Fermi model and other first approximations are the poor representation of the kinetic energy. The key idea in the Kohn-Sham (KS) formalism is to split the kinetic energy functional into two parts, one which can be calculated exactly, and a small correction term. However, in contrast, orbitals have to be re-introduced, so the number of variables is again  $3N$  as in HF method and electron correlation re-emerges as a separate term. The KS model is closely related to the HF method, sharing identical formulas for the kinetic, electron-nuclear and Coulomb electron-electron energies.

First, the energy of a polielectronic system is defined as

$$\begin{aligned} E[\rho_0] &= \langle \Psi_0 | \hat{H} | \Psi_0 \rangle = \langle \Psi_0 | \hat{T} + \hat{V}_{ee} | \Psi_0 \rangle + \int \rho_0(\mathbf{r}) \hat{V}_{ext}(\mathbf{r}) d\mathbf{r} \\ &= F_{HK}[\rho_0] + \int \rho_0(\mathbf{r}) \hat{V}_{ext}(\mathbf{r}) d\mathbf{r} \end{aligned} \quad (2.45)$$

where  $\hat{T}$  represents the kinetic energy operator, and  $V_{ee}$  is the electron-electron potential. Both are called universal functionals because are identical for all the systems with  $N$  electrons. On the other hand,  $V_{ext}$  is th external potential and depends on the system.

The underlying problem is that there is not an exact expression for the functional  $F_{HK}[\rho_0]$  so an approximation has to be used. Kohn and Sham proposed a method based on using a fictitious or non-interacting model in which there is not interaction between the electrons. The potential, which is called Kohn-Sham potential  $V_{KS}$ , is also modified to maintain the electron density identical to the real system.

$$E[\rho_0] = F_{HK}[\rho_0] + \int \rho_0(\mathbf{r})V_{ext}(\mathbf{r})d\mathbf{r} \quad (2.46)$$

$$E_{KS}[\rho_0] = T_S[\rho_0] + \int \rho_0(\mathbf{r})V_{KS}(\mathbf{r})d\mathbf{r} \quad (2.47)$$

If Eq. 2.46 and 2.47 are combined, the following equation is obtained for the energy:

$$E[\rho_0] = T_S[\rho_0] + \int \rho_0(\mathbf{r})V_{ext}(\mathbf{r})d\mathbf{r} + \frac{1}{2} \int \frac{\rho_0(\mathbf{r}_1)\rho_0(\mathbf{r}_2)}{|\mathbf{r}_1 - \mathbf{r}_2|} d\mathbf{r}_1 d\mathbf{r}_2 + E_{xc}[\rho_0] \quad (2.48)$$

In Eq. 2.48,  $F_{HK}$  has been substituted by the kinetic energy of the non-interacting system. Moreover, two new terms appear; while the first one represents the classical Coulomb repulsion between electrons, the second one is called exchange-correlation functional. An exact expression for this last terms is still unknown.

The next step is to define the electron density. As we saw in HF theory, the ground state wavefunction of the system can be described as a Slater determinant which has been constructed from the occupied Kohn-Sham orbitals.

$$\Phi_S = \frac{1}{\sqrt{N!}} \det |\phi_1^{KS}, \phi_2^{KS} \dots \phi_N^{KS}| \quad (2.49)$$

Thus, electron density and the kinetic energy,  $T_S$  are defined as:

$$\rho_0(\mathbf{r}) = \sum_{i=1}^N |\phi_i^{KS}(\mathbf{r})|^2 \quad (2.50)$$

$$T_S[\rho_0] = \sum_{i=1}^N \langle \phi_i^{KS} | -\frac{1}{2} \nabla_i^2 | \phi_i^{KS} \rangle \quad (2.51)$$

Finally, KS orbitals are obtained from the solution of mono-electronic Kohn-Sham equations.

$$\left(-\frac{1}{2} \nabla_i^2 + \widehat{V}_{KS}(\mathbf{r})\right) \phi_i^{KS}(\mathbf{r}) = \varepsilon_i^{KS} \phi_i^{KS}(\mathbf{r}) \quad (2.52)$$

In order to solve KS equation is necessary to expand KS orbitals which are defined using a basis set,

$$\phi_i^{KS}(\mathbf{r}) = \sum_{\mu=1}^M \chi_{\mu}(\mathbf{r}) c_{\mu i}^{KS} \quad (2.53)$$

Now, KS equations can be re-written in matrix notation as,

$$\sum_{\nu} F_{\mu\nu}^{KS} C_{\nu p}^{KS} = \sum_{\nu} S_{\mu\nu} C_{\nu p}^{KS} \epsilon_p^{KS} \quad (2.54)$$

where

$$F_{\mu\nu}^{KS} = h_{\mu\nu} + \sum_{\mu,\nu} P_{\sigma\tau}^{KS} (\nu\mu|\tau\sigma) + \langle \nu|V_{XC}|\mu\rangle \quad (2.55)$$

$$P_{\mu\nu}^{KS} = \sum_{i=1}^{N/2} (C_{\sigma i}^{KS})^* C_{\tau i}^{KS} \quad (2.56)$$

$P_{\mu\nu}^{KS}$  is the KS density matrix and  $\langle \nu|V_{XC}|\mu\rangle$  is usually computed by numerical integration. The procedure to solve this equation is equivalent to HF equations. Firstly, we use a guess density which is used to construct KS equations. Then, the new KS orbitals and energies are obtained which are used again to built the new equations system. These steps are repeated until reaching the self-consistency.

The KS energy equation (Eq. 2.52) is exact: if we knew the density function and the exchange-correlation energy functional it would give the exact energy. The HF energy equation (Eq. 2.30), on the other hand, is an approximation that does not treat electron correlation properly. Even in the basis set limit, the HF equations would not give the correct energy, but the KS equations would. In wavefunction theory we know how to improve on HF-level results: by using perturbational theory or configuration interaction treatments to include electron correlation. However, in DFT there is not a systematic way of improving the exchange-correlation energy functional. It has been said that while solutions to the HF equations may be viewed as exact solutions to an approximate description, the KS equations are approximations to an exact description!

### 2.2.3 Exchange-correlation functionals

$E_{xc}[\rho_0]$  not only accounts for the difference between the classical and quantum mechanical electron-electron repulsion, it also includes the difference in kinetic energy between the non-interacting system and the real system. Formally, the functional dependence of  $E_{xc}[\rho_0]$  on the electron density is expressed as an interaction between the electron density and an “energy density”  $\epsilon_{xc}$  that is dependent on the electron density,

$$E_{xc}[\rho(\mathbf{r})] = \int \rho(\mathbf{r}) \epsilon_{xc}[\rho(\mathbf{r})] d\mathbf{r} \quad (2.57)$$

The energy density  $\varepsilon_{xc}$  is always treated as a sum of individual exchange and correlation contributions. For instance, within this formalism, Slater exchange<sup>15</sup> energy density can be derived from Eq. 2.42 as

$$\varepsilon_{xc}[\rho(\mathbf{r})] = -\frac{9\alpha}{8}\left(\frac{3}{\pi}\right)^{1/3}\rho^{1/3}(\mathbf{r}) \quad (2.58)$$

Finally, spin can be easily included in  $E_{xc}$  using individual functionals of  $\alpha$  and  $\beta$  densities. However, spin densities at any position are typically expressed in terms of the normalized spin polarization,  $\zeta$ , defined as

$$\zeta(\mathbf{r}) = \frac{\rho_{\alpha}(\mathbf{r}) - \rho_{\beta}(\mathbf{r})}{\rho_{\alpha}(\mathbf{r}) + \rho_{\beta}(\mathbf{r})} \quad (2.59)$$

### LD and LSD Approximations

In the Local Density Approximation (LDA) it is assumed that the density locally can be treated as a uniform electron gas, or equivalently that  $\rho(\mathbf{r})$  varies only very slowly with position

$$E_{xc}^{LDA}[\rho] = \int \rho(\mathbf{r})\varepsilon_{xc}^{hom}[\rho(\mathbf{r})]d\mathbf{r} \quad (2.60)$$

The LD approximation has an exchange component  $\varepsilon_x$  given by the Dirac formula

$$\varepsilon_x^{hom}[\rho(\mathbf{r})] = -\frac{3}{4}\left(\frac{3}{\pi}\right)^{1/3}\rho^{1/3} \quad (2.61)$$

The  $X_{\alpha}$  method which was derived by Slater is a special case of the LDA in which the correlation part of the exchange-correlation functional is neglected.

The correlation component is commonly based on the results of quantum Monte Carlo (MC) calculations for an homogeneous electron gas of different densities.<sup>21,22</sup> Analytic interpolation formulas have been constructed by Vosko, Wilk and Nusair (VWN)<sup>23</sup> and Perdew and Wang (PW)<sup>24</sup> in order to use these results in DFT calculations.

The spin-polarized version of LDA is termed as Local-Spin Density Approximation, LSDA and allows different spatial parts  $\rho_{\alpha}$  and  $\rho_{\beta}$ .

$$E_x^{LSDA}[\rho] = -2^{1/3}C_x \int (\rho_{\alpha}^{4/3}(\mathbf{r}) + \rho_{\beta}^{4/3}(\mathbf{r}))d\mathbf{r} \quad (2.62)$$

Spin polarization function and the total density can also be used as an alternative to derive LSDA

$$E_x^{LSDA}[\rho] = -\frac{1}{2}C_x\rho^{1/3}(\mathbf{r})[(1 + \zeta)^{3/4} + (1 - \zeta)^{3/4}] \quad (2.63)$$

LDA and LSDA almost always lead to the correct picture of binding trends across and down the periodic table. Structures, bond lengths, and vibration frequencies in many systems are reproduced satisfactorily, and the deviations from measurements of these and other quantities are often quite systematic. However, electron density in molecules and solids is far from being homogeneous, even having a cusp at the nucleus. Now we can enumerate some of the most important drawbacks of LDA and LSDA<sup>25</sup>:

1. Binding energies of molecules and cohesive energies of solids are usually overestimated. In weakly bound systems, these overestimations are often large, and the bond lengths are too short.
2.  $E_{xc}$  decays exponentially instead of with the inverse power of distance. This is one of the consequences of the incomplete self-interaction correction.
3. Negative ions are often unbound.
4. In semiconductors the band gap energy is underestimated.
5. LSDA fails in the description of the so-called strongly correlated systems, such as the insulating  $3d$ -transition metal oxides, which predicts them to be metallic.
6. Partially filled  $d$ - and  $f$ - bands, in general, require modifications of the LDA and LSDA approximations.

Despite its limitations, LDA and LSDA have been widely used by the scientific community, especially for the study of metals where the approximation of a slowly varying electron density is quite valid.

### Generalized Gradient Approximation

Hohenberg and Kohn introduced the local density approximation in the context of DF theory, but they also pointed out the need for modifications in systems where the density is not homogeneous. Most DFT calculations nowadays use exchange-correlation energy functionals that not only involve the LSDA, but also utilize both the electron density and its gradient.

$$E_{xc}^{GGA}[\rho] = \int \rho(\mathbf{r}) \epsilon_{xc}^{hom}[\rho(\mathbf{r}), \nabla\rho(\mathbf{r})] d\mathbf{r} \quad (2.64)$$

Such an approach was initially referred to as non-local DFT however, the first derivative of a function at a single position is a local property, so the more common term in modern nomenclature for functionals that depend on both the density and the gradient of the density is “gradient-corrected”. Including a gradient correction defines the “generalized

gradient approximation“, GGA. Typically, exchange and correlation terms are modeled separately and can be combined.

The approximation to improve exchange functionals has led to a clear dichotomy of views. The first implies that the search for a functional is so difficult that we should develop a reasonable form and fit its adjustable parameters to experimental data. Becke developed the first widely popular GGA exchange functional.<sup>26</sup> Usually abbreviated as B, this functional adopts a mathematical form that has correct asymptotic behavior at long range for the energy density, and it further incorporates a single empirical parameter the value of which was optimized by fitting to the exactly known exchange energies of the six noble gas atoms. There are several exchange functionals which follow the same methodology, including CAM, FT97, O, PW, mPW, and X.<sup>24,27,28</sup> The second approach seeks to build on the positive features of the LSD approximation by incorporating exact constraints and hoping that the added features will automatically improve the description of reality. These exchange functionals have been developed based on rational function expansions of the reduced gradient and contain no empirically optimized parameters. Some of them are: B86, LG, P, PBE, RPBE, mPBE.<sup>29,30</sup>

The same dichotomy appears in correlation functionals. While P86, and PW91<sup>31,32</sup> correlation functionals contain no empirical parameters, LYP correlation functional<sup>33</sup> does not correct the LDA expression. LYP correlation functional contains four empirical parameters fitted to the helium atom. Among all the correlation functionals discussed, this is the only one that provides an exact cancellation of the self-interaction error in one-electron systems. In fact, the combination of Becke exchange with LYP correlation functional outperformed correlated ab initio methods (MP2 and QCSID) in calculations of atomization energies for 32 molecules.<sup>34</sup>

GGA generally leads to improved bond angles, lengths, and energies. In particular, the strengths of hydrogen bonds and other weak bonds between closed shell systems are significantly better than local density results. However, the self-interaction problem remains, and some asymptotic requirements for isolated atoms are not satisfied

### Meta-GGA methods

As was done for LD and LSD approximations, GGA can be improved allowing the exchange and correlation functionals to depend on higher order derivatives of the electron density. In Meta-GGA, exchange-correlation functional also depends on the Laplacian of the density. Alternatively, it can be taken to depend on the orbital kinetic energy density because both magnitudes carry the same information, since they are related via the orbitals and the effective potential. Several Meta-GGA functionals for exchange, correlation, or both have been developed including B95, B98, ISM, KCIS, PKZB,  $\tau$ HCTH, TPSS, and VSXC.<sup>35-41</sup>

### Hybrid methods

Hybrid methods are based on the adiabatic connection<sup>42</sup> which ensures that an exact connection can be made between the exchange-correlation energy and the corresponding hole potential connecting the non-interacting reference and the actual system. The crudest approximation is the Half and Half method, HH.<sup>43</sup>

$$E_{xc}^{HH} = 0.5E_x^{HF} + 0.5(E_x^{LSDA} + E_c^{LSDA}) \quad (2.65)$$

Hybrid functionals are the only functionals which are fully nonlocal. That is, exact exchange depends on the density at points  $\mathbf{r}'$  around  $\mathbf{r}$ . Hybrid functionals have historically provided some of the most accurate energies and structures in DFT.

B3LYP is the most used hybrid functional, in which three adjustable parameters are used to fit calculated values to a molecular data base.<sup>44</sup>

$$E_{xc}^{B3LYP} = (1 - a)E_x^{LSDA} + aE_x^{HF} + b\Delta E_x^{B8} + (1 - c)E_c^{LSDA} + cE_c^{LYP} \quad (2.66)$$

where  $a$ ,  $b$ , and  $c$  were optimized to 0.20, 0.72, and 0.81, respectively. Others combinations can be done using different correlation and exchange functional, for instance B3PW91, in which PW91 correlation functional is used instead of LYP functional. Another popular hybrid functional that performs quite well is the PBE0 functional,<sup>45</sup>

$$E_{xc}^{PBE0} = aE_x^{HF} + (1 - a)E_x^{PBE} + E_c^{PBE} \quad (2.67)$$

The most important advantage of hybrid functionals is that they tend to improve the quality of DFT calculations. However, they are more computationally expensive than other methods due to the fully non-local nature of the exchange. In order to speed up the exact exchange computation, Hyde, Scuseria and Ernzerhof have exploited the fact that the range of the exchange interaction decays exponentially in insulators, and algebraically in metals. Following this idea, the HSE method<sup>46</sup> applies a screened Coulomb potential to the exchange interaction in order to screen the long-range part of the HF exchange:

$$E_{xc}^{HSE} = aE_x^{HF,sr} + (1 - a)E_x^{PBE,sr} + E_x^{PBE,lr} + E_c^{PBE} \quad (2.68)$$

where  $E_x^{HF,sr}$  is the short-range Hartree-Fock exchange,  $E_x^{PBE,sr}$  and  $E_x^{PBE,lr}$  are the short-range and long-range components of PBE exchange, and  $a = 0.25$  is the Hartree-Fock mixing parameter.

## 2.3 Strongly correlated systems

Strongly correlated systems usually contain transition metal or rare-earth metal ions with partially filled  $d$  or  $f$  shells. Because of the orbital-independent potentials in LSDA and



GGA, they cannot properly describe such systems. In previous subsection, we described how LSDA method underestimates band gap energies and predicts metallic behavior for transition metal oxides. However, these oxides are Mott insulators and the  $d$  or  $f$  electrons are well localized. To describe these strongly correlated systems properly, orbital-dependent potentials should be used for  $d$  and  $f$  electrons. Nowadays, there are several approaches that incorporate the strong correlations between  $d$  or  $f$  electrons as self-interaction correction (SIC) method,<sup>47</sup> GW approximation<sup>48</sup> or LDA+U method<sup>49</sup> which is the most employed.

### 2.3.1 Self-interaction corrected functionals

In the DF formalism each electron interacts with itself via the Coulomb electrostatic potential, and this unphysical interaction would be exactly cancelled by a contribution from the exchange-correlation functional. This is called the self-interaction problem. In the LSD approximation this cancellation is imperfect, but rather good. Some authors have developed corrected LSDA functionals referred to as self-interaction corrected (SIC) functionals in order to solve this problem.<sup>47</sup> If LSDA methodology is used, the SIC functional take the formalism

$$E^{SIC} = E^{LSDA}[\rho^\alpha(\mathbf{r}), \rho^\beta(\mathbf{r})] + \sum_{i\sigma} \delta_{i\sigma} \quad (2.69)$$

where  $E^{LSDA}$  is the LSDA energy functional and  $\delta_{i\sigma}$  is the self-interaction correction (SIC) for the orbital with spin and charge density  $\rho_{i\sigma}(\mathbf{r})$  which contains two terms. The first term is the self-interaction energy and the second is the xc-energy within LSDA of a fully spin-polarized system with density  $\rho_{i\sigma}(\mathbf{r})$ .

However, if we compared SIC and LSDA results, ionization and transfer energies of atoms are not improved. In fact, some authors have proposed that the improved total energies obtained with SIC functional are due to a better description of the correlation of the core electrons which play a relatively minor role in most chemical and physical processes of interest.<sup>50</sup>

### 2.3.2 DFT+U

LDA+U<sup>49</sup> acronym is used for methods that involve LSDA- and GGA- type calculations coupled with an additional orbital-dependent interaction. In LDA+U methods, the electrons are divided in two classes: delocalized electrons, usually  $s$  and  $p$  electrons and localized  $d$  and  $f$  electrons. In order to describe this  $d$ - $d$  or  $f$ - $f$  interaction, and orbital dependent term is used,  $\frac{1}{2}U \sum_{i \neq j} n_i n_j$ , where  $n_i$  and  $n_j$  denote the occupancy of  $d$  and  $f$  orbitals. The total energy in LSDA+U framework is defined as<sup>25</sup>

$$E^{LSDA+U}[\rho^\sigma(\mathbf{r}), \{n^\sigma\}] = E^{LSDA}[\rho^\sigma(\mathbf{r})] + E^U[\{n^\sigma\}] - E_{dc}[\{n^\sigma\}] \quad (2.70)$$

where  $\sigma$  denotes the spin index,  $\rho^\sigma(\mathbf{r})$  is the electron density for spin- $\sigma$  and  $\{n^\sigma\}$  is the density matrix of  $d$  or  $f$  electrons for spin- $\sigma$ . The first term corresponds to the LSDA energy functional, the second term is the electron-electron Coulomb interaction energy and the last term is the double-counting term which removes an averaged LSDA energy contribution of these  $d$  or  $f$  electrons from the LSDA energy. This last term can be described as

$$E_{dc}[\{n^\sigma\}] = \frac{1}{2}UN(N-1) - \frac{1}{2}J[N^\alpha(N^\alpha-1) + N^\beta(N^\beta-1)] \quad (2.71)$$

where  $N^\sigma = Tr(n_{m,m'}^\sigma)$  and  $N = N^\alpha + N^\beta$ .  $U$  and  $J$  are called the screened Coulomb and exchange parameters respectively.

In the simplest approximation, the exchange and non-sphericity are neglected, so Eq. 2.70 can be written as

$$E^{LSDA+U} = E^{LSDA} + \frac{1}{2}U \sum_{i \neq j} n_i n_j - \frac{1}{2}UN(N-1) \quad (2.72)$$

The energy of each orbital can be derived from Eq. 2.72, as

$$\varepsilon_i^{LSDA+U} = \varepsilon_i^{LSDA} + U\left(\frac{1}{2} - n_i\right) \quad (2.73)$$

In this first approximation, orbital energies are shifted depending on its occupancy. While occupied orbital ( $n_i=1$ ) are shifted  $-U/2$ , unoccupied orbitals are shifted  $+U/2$  which produces a widening of the band gap.

In a sense the LDA+U method is similar to the philosophy both of the self-interaction corrected (SIC) functional and the hybrids functionals. It is similar to SIC because the energy of the orbitals in which U parameter is applied is free of self-interaction of the localized orbitals by construction. These are the orbitals for which the self-interaction error of LDA is largest. On the other hand it is similar to the hybrids functionals because it uses a fraction of screened exchange, although not in a global sense but by correcting only a particular set of orbitals.

This work is based on the rotationally invariant formalism developed by Dudarev et al.<sup>51</sup> In this approach, the Coulomb and exchange parameters are combined into a single parameter  $U_{eff} = U - J$ . Within this formalism, orbitals are shifted  $\pm \frac{U-J}{2}$  depending on its occupancy. This method has been widely applied to the study of transition metal oxide and other strong correlated materials successfully. However  $U$  and  $J$  parameters are usually determined empirically.

## 2.4 Important aspects

### 2.4.1 Basis set

There are different kinds of approximations when we have to choose the basis set to build the KS orbitals. The linear combination of atomic orbitals (LCAO) approximation takes atomic orbitals centered in the nuclei as the basis set. The most important advantage of this method relies in the small quantity of functions that are needed to obtain an acceptable description of the orbitals. However, it has some shortcomings, such as the difficulty of knowing the degree of convergence of the basis set or how the results are affected by the basis set superposition error (BSSE).<sup>63</sup>

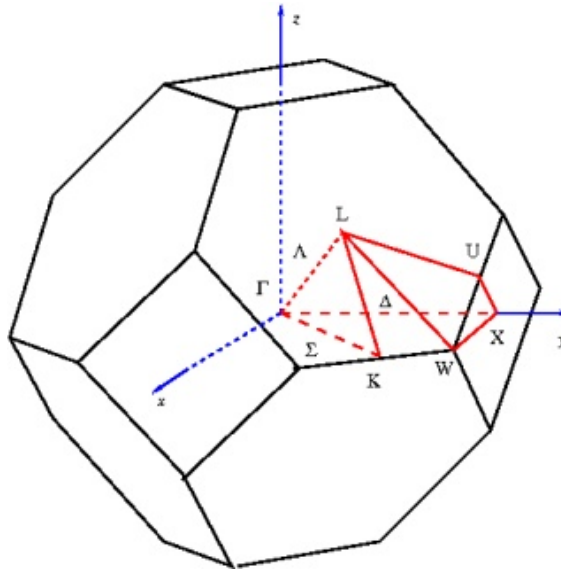


Figure 2.1: Some important symmetry points of the first Brillouin zone for a fcc crystal.

On the other hand, the plane waves (PW) approximation uses these functions to describe the KS orbitals. The use of plane waves is frequently employed in solid state DFT calculations due to the 3D periodicity present in the systems under study. The expansion of the wave function is based on the Bloch theorem,<sup>52</sup> so it is described as the product of a plane wave and a periodic function  $U_n(\mathbf{r})$

$$\phi_n(\mathbf{r}) = e^{i\mathbf{k}\mathbf{r}} U_n(\mathbf{r}) \quad (2.74)$$

The periodic part of the wave function can be expressed using a set of plane waves in

which the wave vectors are the reciprocal lattice vectors of the crystal

$$U_n(\mathbf{r}) = \sum_G c_{c,G} e^{i\mathbf{G}\mathbf{r}} \quad (2.75)$$

where  $\mathbf{G}$  is the reciprocal lattice vector which is defined as  $\mathbf{G}\mathbf{l} = 2\pi m$  for all values of  $\mathbf{l}$ , where  $\mathbf{l}$  is a lattice vector and  $m$  an integer number. Therefore, the wavefunction for each electron can be described as the sum of plane waves.

$$\phi(\mathbf{r}) = \sum_G c_{c,G+k} e^{i(\mathbf{G}+\mathbf{k})\mathbf{r}} \quad (2.76)$$

where  $\mathbf{k}$  is the wave vector limited to the first Brillouin zone (see fig. 2.1). Thus, the eigenvalue of the orbitals energy is periodic,  $E_{nk} = E_{n(k+\mathbf{G})}$ , and this periodicity depends on the reciprocal lattice vectors. The coefficients,  $c$ , are usually obtained analytically or numerically. In principle, this Fourier series is infinite, but in practice it is truncated. by including plane waves with a kinetic energy lower than a given cutoff energy ( $E_{cut}$ ).<sup>53</sup>

This approach is far from a framework in which each atom of the network has its corresponding atomic functions, however, there are advantages in terms of the mathematical development. For example, properties can be easily converged by controlling only the cutoff energy. Moreover, computed energies are not affected by BSSE.

## 2.4.2 Pseudopotentials

Although plane waves could be used as basis functions for general use, it is needed a huge amount of them to describe the rapid oscillations of the atomic wave functions near the nuclei. These oscillations can not be underestimated as they reflect the atomic nature of the orbitals near the nuclei. In other words, the PW describes well the translational symmetry of matter and describes the smooth variations of the density in the valence region, but are unable to provide a good description of the region near the nuclei.

A first approach to the problem consists in constructing PW representing valence levels forcing them to be orthogonal to the core levels for a given  $\mathbf{k}$ . This technique is known as the orthogonalized plane waves method.<sup>54</sup> Orthogonalized plane waves (OPW) oscillate in the core region while they behave as PW in the external region.

Despite having focused our discussion on the core, the chemical properties of matter are really influenced by the outer electrons, while the electrons of the inner layers are chemically inert. Therefore, we can approximate that the distribution of the core electrons does not change when the atoms are in different chemical environments. Thus core electrons may be regarded as essentially fixed. This is the essence of the pseudopotential approximation: the strong core potential is replaced by a pseudopotential, whose ground state wavefunction mimics the all electron valence wavefunction outside a selected core radius.

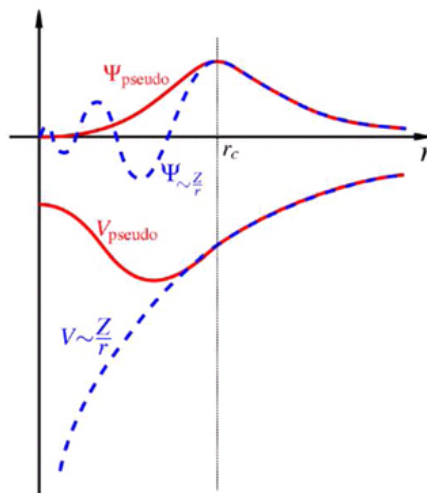


Figure 2.2: Scheme of the all electron (blue) and pseudoelectron (red) wavefunction.

During a long period, the evolution of pseudopotentials has been carried out following these purposes:

1. The pseudopotential should be as soft as possible, meaning that it should allow expansion of the valence pseudo-wavefunctions using as few planewaves as possible.
2. They should be as transferable as possible (meaning that a pseudopotential generated for a given atomic configuration should reproduce others accurately), thereby helping to assure that the results will be reliable in solid state applications, where the crystal potential is necessarily different from an atomic potential
3. The pseudo-charge density must reproduce the valence charge density as precisely as possible.

The concept of norm-conservation represents a significant improvement in achieving these objectives. With the "norm-conserving" pseudopotentials (HSC), the pseudo-wavefunctions (and potential) are constructed to be equal to the actual valence wavefunctions (and potential) outside some core radius,  $r_c$ . Inside  $r_c$ , the pseudo-wavefunctions differ from the true wavefunctions, but the norm is constrained to be the same (see fig. 2.2). In summary, the main features of these pseudopotentials are:

1. The eigenvalues which have been calculated including all electrons (AE) and using the HSC pseudopotentials, are equal to the valence levels.
2. The valence orbitals calculated with HSC and AE should be very similar beyond a cutoff radius,  $r_c$ .
3. The pseudo-wavefunction (and potential) is constructed in order to be equal to the current wavefunction beyond a cutoff radius ( $r_c$ ). However, within this radius, it differs from the wavefunction but it retains the norm-conserving behavior.<sup>55,56</sup>
4. Imposition of norm-conservation ensures not only that the logarithmic derivative of the pseudo- and AE wavefunction match at the reference energy, but also that the first derivative with respect to  $E$  matches as well. Thus, the difference between the pseudo- and AE logarithmic derivative is second order in the deviation from the reference, and this helps ensure transferability for norm-conserving pseudopotentials.

Among all the steps necessary to construct these pseudopotentials, perhaps the most delicate and decisive step is the choice of the  $r_c$ . The value should be between the outermost node of the valence wavefunction and its end. Small values of  $r_c$  result in hard pseudopotentials that require a large amount of planewaves but very portable. By contrast, large  $r_c$  generate soft pseudopotentials much less transferable. In addition, values of  $r_c$  too close to the external node may involve numerical instabilities.

While the  $r_c$  for transition metals is usually large enough for using a soft pseudopotential, this does not hold for the lighter elements whose  $r_c$  must be very small, requiring a higher number of plane waves. In order to solve this problem and generate pseudopotentials as soft as possible, Vanderbilt *et al.*<sup>57,58</sup> proposed a completely different approach compared to the methodology applied for "norm-conserving" pseudopotentials. In this new approach, the wave pseudofunction must be equal to the all-electron wavefunction out of the  $r_c$ . However, within  $r_c$  has to be as smooth as possible. Although removing the "non-conserving" condition involves some difficulties, the pseudopotentials obtained are much softer because the  $r_c$  that can be taken is greater.

This new methodology presents three main difficulties. Removing the norm-conserving condition implies a nontrivial overlap within the secular equation. Moreover, the pseudo-charge density should be calculated carefully because it can derive to erroneous charges. Finally, these "ultrasoft" pseudopotentials are less transferable, however, Vanderbilt potentials are designed for the calculation of big systems in which the cost of generating the pseudopotential is negligible compared to the cost of the calculation.

We have explained how pseudopotentials make possible the use of planewaves and reduce the number of them that have to be used. However, pseudopotentials also carry some disadvantages. First, information of the core functions and their associated electron

density is lost. Moreover, delocalized character of the planewaves prevent the chemical interpretation of some phenomena such as X-ray photoelectrons spectroscopy or NMR coupling constants and shielding.

### 2.4.3 APW and PAW method

Pseudopotentials reduce the number of planewaves required as we said before but they can influence the calculation of certain properties, such hyperfine parameters, and electric field gradients. A different approach is the augmented-plane-wave method (APW), which was developed by Slater.<sup>59</sup> In APW method, space is divided into atom-centered augmentation spheres inside which the wavefunctions are taken as some atom-like partial waves, and a bonding region outside the spheres, where some envelope functions are defined. The atom-like partial waves that reside inside the radii of the spheres,  $r_{apw}$ , are constructed with atomic functions which contain spherical harmonics. The bonding region, ( $r > r_{apw}$ ), is described with planewaves. The partial waves and the envelope functions are then matched at the boundaries of the spheres. The main problem of APW method is the diagonalization of the secular matrix which must be solved numerically. That's why, this method is computationally very expensive. In 1975, Andersen proposed the so called linear methods which consist on describing each term which depends on the energy as a Taylor series. This method was called linearized augmented plane wave (LAPW) method.<sup>60</sup>

Pseudopotentials and LAPW methods has been used to describe solids during last decades. However, new approaches has been developed recently which results in faster and more accurate calculations. One of this method is the projector augmented wave (PAW) method which was developed by Blöchl.<sup>61</sup> This method combines pseudopotential approximation and the LAPW method. PAW method is analogous to pseudopotentials in that introduces projectors acting on smooth valance functions that are the primary objects in the calculation. It also introduces auxiliary localized functions like the "ultrasoft" pseudopotential method. However, the localized functions actually keep all the information on the core states like planewaves and APW method. Thus many aspects of the calculations are identical to pseudopotential calculations.

## 2.5 Some properties

### 2.5.1 Bader Charges

Previous sections have been dedicated to explain how to find the ground state of a system and its energy. However, many other properties can be obtained from the wavefunction. Although the quantum-mechanical description of a molecule consists in a positive nuclei surrounded by a cloud of electrons, chemistry needs the description and localization of

bonds between the atoms in order to analyze and rationalize the properties of system. At this point it is reasonable to ask how it is possible to define an atom, and if their population is linked to others using their wave function.

The atomic charge is a concept often used to discuss and analyze structural and reactivity differences. There are three methods commonly used to describe the charges of the atoms:

- Divide the wave function in terms of basis sets.
- Adjustment schemes.
- Divide the electron density in atomic domains.

There is some controversy explaining the inability to exactly know the charge of one atom within an polielectronic system. Many authors focus the discussion on the absence of a quantum mechanical operator associated with the charge,<sup>62</sup> but other authors focus their explanation in the impossibility of defining an atom in a molecule.<sup>63</sup>

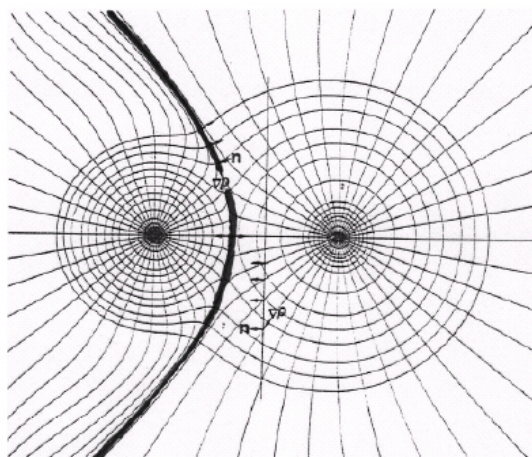


Figure 2.3: Electron density and  $\nabla\rho$  in a diatomic system

One of the most rigorous schemes of dividing the volume of a molecule in atomic subspaces is the "Atoms in Molecules" theory (AIM) developed by R. Bader.<sup>64,65</sup> The electron density is a function of three spatial coordinates and can be analyzed in terms of its topology. For example, a maximum of the electron density function identifies a core,



which can be treated as a point which attracts the electron density. The density gradient at each point, points in the direction of the nuclei which attracts it more strongly. In this way, it is possible to rigorously define density subspaces associated with the different nuclei (see fig. 2.3). Once defined these subspaces it is only necessary to integrate the electron density contained in them to know the atomic charge. Besides analyzing the derivative of the electron density, the theory developed by Bader also uses the Laplacian density to locate different critical points (bonds, rings or cages) which allow us to study the nature of the bond and predict and explain the structure and reactivity of the system.

### 2.5.2 Transition states search: CI-NEB method

The calculation of the minima of the potential energy surface (PES) of the ground state is not enough to fully describe the system because these points only give us information of thermodynamic processes. There are a variety of situations where the dynamics of chemical reactions play a major role, both from a scientific as technological point of view. For this reason, in this section, we are going to pay attention to how DFT calculations can be used to determine the kinetics of chemical processes. The best way to address the problem is by analyzing the PES that define the system  $E(\mathbf{R}_1, \dots, \mathbf{R}_N)$ . The PES is usually constituted by several local minima,  $E_1, E_2, E_3, \dots$ . First, we can consider an elementary process in which the system evolve from a minimum,  $E_i$ , to another minimum,  $E_j$ , without passing through any minimum. Other important points at the PES are the saddle point which represent a maximum in all directions except in a direction that connects two minima. These saddle points are defined as transition states and combined with two minima define the reaction path. These paths are characterized by:

1. They are the reaction paths with a higher statistical weight.
2. The forces which act on the atoms at any point along the path, point in the direction of the reaction path.
3. The energy is stationary for any degree of freedom perpendicular to the reaction path.

Several methods have been developed to find the minimum energy path and the transition state that characterizes it. These algorithms are based on maximizing a degree of freedom while minimizing the others. However, the challenge relies on knowing what is the degree of freedom to maximize. Here, we will describe the nudged elastic band (NEB) method.<sup>69</sup> This algorithm is widely applied for the calculation of transition states using DFT and plane waves.

This algorithm takes a set of geometries or initial images ( $\mathbf{R}_0, \mathbf{R}_1, \mathbf{R}_2, \dots, \mathbf{R}_N$ ) in which  $\mathbf{R}_0$  and  $\mathbf{R}_N$  are the minimum of the PES. It is considered that these images are connected

by springs or oscillators which generate an elastic band. We have to minimize the force acting on the springs in order to find the reaction path. The forces which act on each spring can be divided into two groups; those forces with the same direction as the reaction path, and the forces which are perpendicular to the path.

$$\mathbf{F}_i = \mathbf{F}_{i\parallel} + \mathbf{F}_{i\perp} = \mathbf{F}_{i\parallel} - \nabla E(\mathbf{R}_i)|_{\perp} \quad (2.77)$$

where the forces which are perpendicular to the reaction path are described as:

$$\nabla E(\mathbf{R}_i)|_{\perp} = \nabla E(\mathbf{R}_i) - \nabla E(\mathbf{R}_i)\hat{\tau}_i \quad (2.78)$$

where  $E$  is the energy of the system, and  $\hat{\tau}_i$  is the normalized local tangent at the image  $i$ . Moreover, the spring force may be expressed as:

$$\mathbf{F}_{i\parallel} = k(|\mathbf{R}_{i+1} - \mathbf{R}_i| - |\mathbf{R}_i - \mathbf{R}_{i-1}|)\hat{\tau}_i \quad (2.79)$$

where  $k$  is the force constant of the spring. The algorithm attempts to minimize the energy so that the force described in equation 2.77 becomes zero.

The most important drawback of the method is the dependence with respect to the initial images because it is very difficult for one of these relaxed images to match the transition state. In order to solve this problem, the Climbing Image Nudged Elastic Band (CI-NEB) algorithm is used.<sup>70</sup> This technique is a modification of NEB method described above which does not present an extra computational cost. CI-NEB algorithm identifies which is the image with a higher energy and treats it differently than the others images. Forces which act on this image are described as follows,

$$\begin{aligned} \mathbf{F}_{i_{max}} &= -\nabla E(\mathbf{R}_{i_{max}}) - 2\nabla E(\mathbf{R}_{i_{max}})|_{\parallel} \\ &= -\nabla E(\mathbf{R}_{i_{max}}) - 2\nabla E(\mathbf{R}_{i_{max}})\hat{\tau}_{i_{max}}\hat{\tau}_{i_{max}} \end{aligned} \quad (2.80)$$

This expression describes the force due to the potential with the parallel component of the inverted elastic band. Minimizing the energy leads to a situation in which the perpendicular forces to the reaction path are null and the parallel forces are maximum, thereby determining the transition state.

### 2.5.3 Electron transfer processes

Electron transfer (ET) reactions consist in the transference of an electron from a donor,  $D$ , to an acceptor,  $A$ .  $D$  and  $A$  may be two metal complexes surrounded by solvent molecules, two subunits of the same compound separated by bridging ligands or metallic centers linked by anions, for instance,  $O^{2-}$ . The ET treatment discussed here is based on “Marcus” two-state model. We denote the initial electronic state as  $\psi_A = D \cdots A$  and the final

electronic state as  $\psi_B = D^+ \cdots A^-$ , where “ $\cdots$ ” indicates that the donor and acceptor are in close proximity, just few angstroms.

ET can be considered as a Frank-Condon process<sup>71,72</sup> because electron motion is instantaneous compared to the frequency of the nuclear motion. In order to move the electron from donor to acceptor, the D and A energy levels must match. This requirement is achieved by reorganizing the nuclei of the reactant atoms and surrounding material. Because ET involves nuclear reorganization, this process is described in terms of potential energy surface as a function of reaction coordinates, (see fig. 2.4).<sup>73</sup> The dashed lines represent the two adiabatic states, which are eigenfunctions of the electronic hamiltonian,  $H_{el}$ , while the continuous lines represent the diabatic states which are not eigenfunctions of  $H_{el}$ .

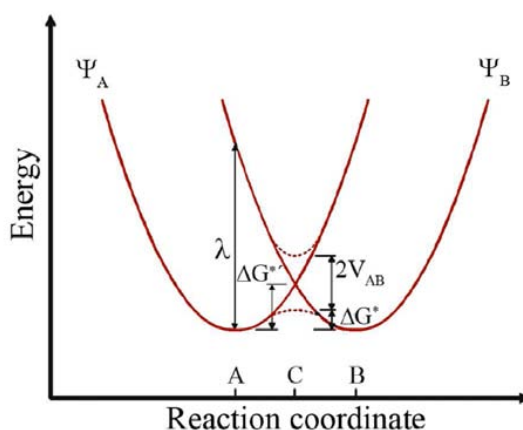


Figure 2.4: General profile for a ET reaction.

The electronic coupling matrix element,  $V_{AB}$ , the reorganization energy,  $\lambda$ , and the activation energy,  $\Delta G^{*}$  are the three key parameter which allow us describe the ET process. In this section we are going to focus on the  $V_{AB}$  calculation because it determines adiabatic or non-adiabatic nature of the ET process.  $V_{AB}$  is half of the energy splitting between the upper and the lower adiabatic surfaces at the crossing seam,  $C$ . There are different strategies to calculate this parameter using ab initio calculations.<sup>74,75</sup> In this work, we have used the so-called quasi-diabatic or corresponding orbital method.<sup>76</sup> This method is based on the approach of using two diabatic states to describe the ET system. At the intersection, the splitting can be obtained by solving the secular equation

$$\begin{vmatrix} H_{AA} - E & H_{AB} - ES_{AB} \\ H_{BA} - ES_{BA} & H_{BB} - E \end{vmatrix} = 0 \quad (2.81)$$

where  $H_{ij} = \langle \psi_i | H_{el} | \psi_j \rangle$  and  $i$  and  $j$  are equal to A and B,  $H_{el}$  is the electronic Hamiltonian,  $S_{AB} = \langle \psi_A | \psi_B \rangle$ , and  $E$  is the energy eigenvalue. The two roots of the secular equation give the upper and lower adiabatic surfaces. Half of the energy difference between the two adiabatic surfaces at the intersection is given by

$$V_{AB} = \frac{|H_{AB} - S_{AB}(H_{AA} + H_{BB})/2|}{1 - S_{AB}^2} \quad (2.82)$$

Many authors have used UHF solutions as diabatic functions  $\psi_A$  and  $\psi_B$ . The more strongly localized these wavefunctions are, the more suitable they would be for this approach. The corresponding orbital transformation makes easier the calculation of the  $H_{AB}$  and  $S_{AB}$ . The overlap matrix  $\mathbf{D} = \mathbf{B}^\dagger \mathbf{S} \mathbf{A}$  is calculated from the atomic orbital overlap matrix,  $\mathbf{S}$ , and the eigenvectors for the two diabatic states,  $\mathbf{A}$ ,  $\mathbf{B}$ . However, the  $\mathbf{S}$  is not diagonal, which makes more difficult the calculation of  $H_{AB}$  and  $S_{AB}$ . Corresponding orbitals are the orbitals which diagonalize the overlap matrix. In order to achieve it, the two diabatic states,  $\mathbf{A}$ ,  $\mathbf{B}$  are subjected to a linear transformation. This bi-orthogonalization of the overlap matrix simplifies the evaluation of the Hamiltonian using Slater's rules.<sup>77</sup> The corresponding orbital method is available in different quantum chemistry packages as HONDO or NWChem.<sup>78,79</sup>

As we said before,  $V_{AB}$  value determines the nature of the ET. If the interaction between both states is weak and, therefore,  $V_{AB}$  is small, the ET takes place by tunneling which is referred to as non-adiabatic or diabatic process. However, if the interaction is strong, two new adiabatic states are formed from the diabatic ones. In this case, the system evolves on the lower surface from the reactants to the products which is called an adiabatic ET. Adiabaticity can be determined from the value of the transmission coefficient  $\kappa$ , which is given by<sup>80</sup>

$$\kappa = \frac{2P}{1 + P} \quad (2.83)$$

where  $P$  is the probability for conversion of the reactants into products upon a single passage through the intersection region.  $P$  can be calculated using Landau-Zerner two state model.<sup>81,82</sup>

$$P = 1 - \exp\left(-\frac{\nu_{el}}{2\nu_n}\right) \quad (2.84)$$

where  $\nu_{el}$  is the frequency of the ET at the intersection and  $\nu_n$  is the nuclear vibration frequency. From the Landau-Zerner model for classical harmonic motion

$$\frac{\nu_{el}}{2\nu_n} = \frac{2\pi V_{AB}^2}{\hbar\nu |S_A - S_B|} \quad (2.85)$$

where  $\nu$  is the average velocity of the system moving through the intersection, and  $S_A$  and  $S_B$  are the slopes of the two potential energy surfaces at the intersection.

## References

1. Born, M.; Oppenheimer, J. R., *Ann. Physik* **1927**, *84*, 457.
2. Kolos, W.; Wolniewicz, L., *J. Chem. Phys.* **1964**, *41*, 3663.
3. Slater, J. C., *Phys. Rev* **1929**, *34*, 1293.
4. Hartree, D. R., *Proc. Cambridge Phil. Soc.* **1928**, *24*, 89.
5. Fock, V., *Z. Physik* **1930**, *61*, 126.
6. Hall, G. G., *Proc. Roy. Soc.* **1951**, *A205*, 541.
7. Roothaan, C. C. J., *Rev. Mod. Phys.* **1951**, *23*, 69.
8. Barnett, M. P.; Coulson, C. A., *Phil. Trans. Roy. Soc.* **1951**, *A243*, 221.
9. Boys, S. F., *Proc. Roy. Soc.* **1950**, *A200*, 542.
10. Thomas, L. H., *Proc. Camb. Phil. Soc.* **1927**, *23*, 542.
11. Fermi, E., *Z. Phys.* **1928**, *48*, 73.
12. Dirac, P. A. M., *P. N. A. Proc. Roy. Soc.* **1928**, *117*, 610.
13. Dirac, P. A. M., *Proc. Cambridge Phil. Soc.* **1930**, *26*, 376.
14. Bloch, F., *Z. Physik* **1929**, *57*, 545.
15. Slater, J. C., *Phys. Rev* **1951**, *82*, 538.
16. Slater, J. C., *Solid-State and Molecular Theory: A Scientific Biography*, Wiley **1975**.
17. Slater, J. C., *Phys. Rev.* **1951**, *81*, 385.
18. Teller, E., *Rev. Mod. Phys.* **1962**, *34*, 627.
19. Hohenberg, P.; Kohn, W., *Phys. Rev.* **1964**, *136*, B864.
20. Kohn, W.; Sham, L. J., *Phys. Rev.* **1965**, *140*, A1133.
21. Ceperly, D. M.; Alder, J., *Phys. Rev. Lett.* **1980**, *45*, 566.
22. Ortiz, G.; Ballone, P., *Phys. Rev. B* **1994**, *50*, 1391.
23. Vosko, S. J.; Wilk, L.; Nusair, M., *Can. J. Phys.* **1980**, *58*, 1200.
24. Perdew, J. P.; Wang, Y., *Phys. Rev. B* **1992**, *45*, 13244.
25. Anisimov, V. I.; Aryasetiawan, F.; Lichtenstein, A. I., *Condens. Matter* **1997**, *9*, 767.
26. Becke, A. D., *Phys. Rev. A* **1988**, *33*, 3098.
27. Filippi, C.; Umrigar, C. J.; Taut, M., *J. Chem. Phys.* **1994**, *100*, 1290.
28. Filatov, M.; Thiel, W., *Mol. Phys.* **1997**, *91*, 847.
29. Perdew, J. P.; Burke, K.; Ernzerhof, M., *Phys. Rev. Lett.* **1996**, *77*, 3865.
30. Hammer, B.; Hansen, L. B.; Norskov, J. K., *Phys. Rev. B* **1999**, *59*, 7413.
31. Perdew, J., *Phys. Rev. B* **1986**, *33*, 8822.
32. Perdew, J. P.; Chevary, J. A.; Vosko, S. H.; Jackson, K. A.; Pederson, M. R.; Singh, D. J.;

- Fiolhais, C., *Phys. Rev. B* **1992**, *46*, 6671.
33. Lee, C.; Yang, W.; Parr, R. G., *Phys. Rev. B* **1988**, *37*, 785.
  34. Johnson, B. G.; Gill, P. M. W.; Pople, J. A., *J. Chem. Phys.* **1992**, *97*, 7846.
  35. Becke, A. D.; Roussel, M. R., *Phys. Rev. A* **1989**, *39*, 3761.
  36. Becke, A. D., *J. Chem. Phys.* **1989**, *104*, 1040.
  37. Voorhis, T. V.; Scuseria, G. E., *J. Chem. Phys.* **1998**, *109*, 400.
  38. Boese, A. D.; Handy, N. C., *J. Chem. Phys.* **2002**, *116*, 9559.
  39. Perdew, J. P.; S. Kurth, A. Z.; Blaha, P., *Phys. Rev. Lett.* **1999**, *82*, 2544.
  40. Tao, J.; Perdew, J. P.; Staroverov, V. N.; Scuseria, G. E., *Phys. Rev. Lett.* **2003**, *91*, 146401.
  41. Tao, J.; Perdew, J. P.; Staroverov, V. N.; Scuseria, G. E., *J. Chem. Phys.* **2004**, *120*, 6898.
  42. Harris, J., *Phys. Rev. A* **1984**, *29*, 1648.
  43. Becke, A. D., *J. Chem. Phys.* **1993**, *98*, 1372.
  44. Becke, A. D., *J. Chem. Phys.* **1993**, *98*, 5648.
  45. Adam, C.; Barone, V., *Chem. Phys. Lett.* **1998**, *198*, 113.
  46. Heyd, J.; Scuseria, G. E., *J. Chem. Phys.* **2006**, *125*, 224106.
  47. and O. Gunnarsson, A. S., *Phys.Rev. Lett.* **1990**, *25*, 1148.
  48. Heidin, L., *Phys.Rev.* **1965**, *139*, A796.
  49. Anisimov, V. I.; Zaanen, J.; Andersen, O. K., *Phys.Rev. B* **1991**, *44*, 943.
  50. Gunnarsson, O.; Jones, R. O., *Solid State Commun.* **1981**, *37*, 249.
  51. Dudarev, S. L.; Botton, G. A.; Savrasov, S. Y.; Humphreys, C. J.; Sutton, A. P., *Phys. Rev. B* **1998**, *57*, 1505.
  52. Ashcroft, N. W.; Mermin, N. D., *Solid State Physics*, Saunders College Publishing **1976**.
  53. Payne, M. C.; Teter, M. P.; Allan, D. C.; Arias, T. A.; Joannopoulos, J. D., *Rev. Mod. Phys.* **1992**, *64*, 1045.
  54. Herring, C., *Phys. Rev.* **1940**, *57*, 1169.
  55. Topp, W. C.; Hopfield, J. J., *Phys. Rev. B* **1973**, *7*, 1295.
  56. Starkloff, T.; Joannopoulos, J. D., *Phys. Rev. B* **1977**, *16*, 5212.
  57. Vanderbilt, D., *Phys. Rev. B* **1990**, *41*, 7892.
  58. Laasonen, K.; Car, R.; Lee, C.; Vanderbilt, D., *Phys. Rev. B* **1991**, *43*, 6796.
  59. Slater, J. C., *Phys. Rev.* **1951**, *51*, 846.
  60. Andersen, O. K., *Phys. Rev. B* **1975**, *12*, 3060.
  61. Blochl, P. E., *Phys. Rev. B* **1994**, *71*, 1085.
  62. Cramer, C. J., *Essentials of Computational Chemistry.*, Wiley, VCH. **2004**.
  63. Jensen, F., *Introduction to Computational Chemistry*, Wiley, VCH. **2007**.

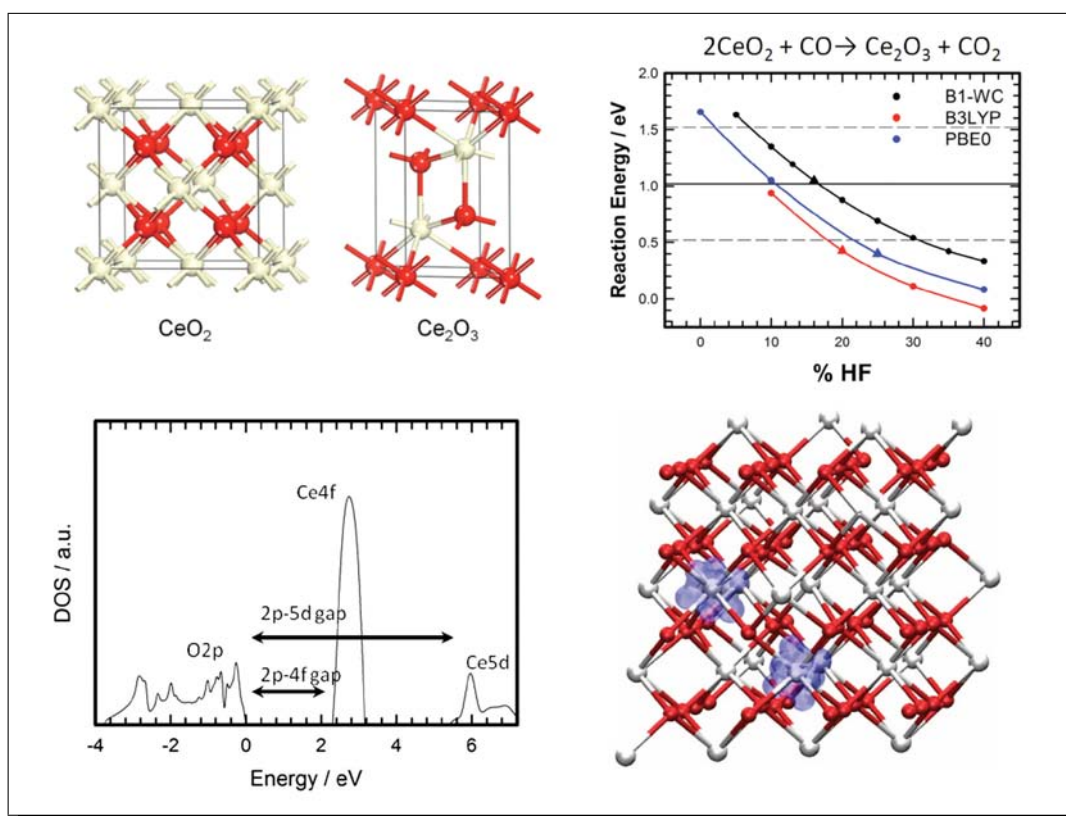
64. Bader, R. F. W., *Acc. Chem. Res.* **1985**, *18*, 9.
65. Bader, R. F. W., *Chem. Rev.* **1991**, *91*, 893.
66. Henkelman, G.; Arnaldsson, A.; Jonsson, H., *Comp. Mat. Sci.* **2006**, *36*, 354.
67. Sanville, E.; Kenny, S. D.; Smith, R.; Henkelman, G., *J. Comp. Chem.* **2007**, *28*, 899.
68. Tang, W.; Sanville, E.; Henkelman, G., *J. Phys., Cond. Mat.* **2009**, *21*, 084204.
69. Henkelman, G.; Jonsson, H., *J. Chem. Phys.* **2000**, *113*, 9978.
70. Sheppard, D.; Terrell, R.; Henkelman, G., *J. Chem. Phys* **2008**, *128*, 134106.
71. Franck, J., *Trans. Faraday Soc.* **1925**, *21*, 536.
72. Condon, E. U., *Phys. Rev.* **1928**, *32*, 858.
73. Marcus, R. A., *J. Chem. Phys.* **1956**, *24*, 966.
74. Amini, A.; Harriman, A., *J. Photochem. Photobiol. C* **2003**, *4*, 155.
75. Rosso, K. M.; Dupuis, M., *Theor. Chem. Acc.* **2006**, *116*, 124.
76. Farazdel, A.; Dupuis, M.; Clement, E.; Aviram, A., *J. Am. Chem. Soc.* **1990**, *112*, 4206.
77. King, H. F.; Stanton, R. E.; Kim, H.; Wyatt, R. E.; Park, R. G., *J. Chem. Phys.* **1967**, *47*, 1936.
78. Dupuis, M.; Rys, J.; King, H. F., *J. Chem. Phys.* **1990**, *65*, 111.
79. Dupuis, M., *Comp. Phys. Comm.* **2001**, *134*, 150.
80. Newton, M. D.; N.Sutin, *Ann. Rev. Phys. Chem.* **1984**, *35*, 437.
81. Landau, L., *Phys. Z. Sowjet.* **1932**, *1*, 89.
82. Zerner, C., *Proc. Roy. Soc.* **1932**, *A137*, 696.





CHAPTER  
**THREE**

Ceria as strongly correlated oxide



## 3.1 Introduction

As we have shown, ceria and related materials are complex systems from a theoretical and computational point of view. It is quite convenient to analyze which methods describe correctly the different properties of ceria. This will be the subject of this chapter and become essential to understand and predict the properties of these materials. Stoichiometric cerium oxide in which all the metallic center are Ce(IV) and the  $f$ -states are empty is not a problem for semilocal functionals. However, LDA or GGA are not able to describe even qualitatively the electronic structure of reduced ceria materials which contain Ce(III) and  $f$ -electrons. As we said, this problem is owing to the self-interaction error, which is intrinsic to semilocal functionals.<sup>1</sup> While the self-interaction Coulomb term is exactly canceled by the self-exchange term in HF theory, it is not canceled completely in DFT methods because it is not known exactly the expression for the exchange correlation functional. That's why these methods tends to over-delocalize  $f$ -electrons<sup>2</sup> and produce artificial metallic behavior,<sup>3</sup> systematic underestimation of energy barriers for chemical reactions<sup>4</sup> and artificially lower defect formation energy in reduced ceria.<sup>5</sup>

Nowadays, there are two different strategies or methods to solve these shortcomings. On one hand, DFT+U which corrects the on-site Coulomb correlation effects by a Hubbard-type U term is the cheapest solution.<sup>6</sup> On the other, hybrids functionals which include a percentage of exact HF exchange.<sup>7</sup> In this chapter we will analyze both options. First, different hybrids density functionals will be applied to the CeO<sub>2</sub> and Ce<sub>2</sub>O<sub>3</sub> bulk phases. The performance of five functionals: Half-and-half functional, PBE0, B3LYP, and the recently introduced B1-WC hybrid functional will be compared. Moreover, a new approach to study ceria using DFT+U method will be proposed in which a U parameter not only for the  $4f$  Ce orbitals but also for  $2p$  O orbitals are used.

### 3.1.1 The Wu-Cohen functional

A nonempirical density functional generalized gradient approximation (GGA) has been presented recently by Wu and Cohen.<sup>8</sup> This functional gives better results for lattice constants, crystal structures and metal surface energies than PBE functional.<sup>8</sup> In this functional, the exchange part of the PBE functional has been modified in order to achieve a smoother variation than other functionals such as PBE or PW91 of the electron density of the valence electrons. In order to achieve that, the exchange enhancement factor ( $F_X$ ) has been redefined to recover the fourth order parameter of the gradient expansion equation of Svendsen and von Barth for slowly varying density systems.<sup>9</sup>

Although there is some controversy over the method in which fourth-order term is recovered,<sup>10,11</sup> WC functional obtains lattice parameters more accurately than other previously used GGA functional especially if there are heavy atoms in the system.<sup>12</sup>

The electron density varies faster in molecules and atoms, so WC functional should describe molecular properties less accurate than other functionals. However, WC results for molecules are quite similar to PBE results.<sup>12</sup>

In the same way that B3LYP functional is constructed from Becke exchange functional and LYP correlation GGA functionals, it is possible to add an exact HF exchange percentage to WC GGA functional in order to develop a new hybrid functional. For the first time, Bilc *et al.* have used the B1-WC functional which combines the accurate description of the lattice parameter of WC functional and an exact HF exchange percentage to describe properly the band-gap.<sup>13</sup> This functional is constructed in the same way as the B3LYP functional,<sup>7</sup>

$$E_{xc}^{B1WC} = E_x^{LDA} + A(E_x^{HF} - E_x^{LDA}) + (1 - A)(E_x^{WC} - E_x^{LDA}) - E_c^{PBE} \quad (3.1)$$

where A is the unique adjustable parameter which is around 0.16 in order to describe the properties of ferroelectric materials.

It has been reported that lattice parameter and cell volume are the key factors to describe the adsorption of metal atoms on ceria surface.<sup>14</sup> In addition, the description of the 4*f* band that appears in the partially reduced CeO<sub>2</sub> band gap plays a very important role in all kinds of phenomena that occur on the surface. That's why the functional B1-WC may be suitable for ceria based systems in which is essential a good description of both properties.

### **3.2 Comparative Study on the Performance of Hybrid DFT Functionals in Highly Correlated Oxides: The Case of $\text{CeO}_2$ and $\text{Ce}_2\text{O}_3$**

# JCTC

Journal of Chemical Theory and Computation

## Comparative Study on the Performance of Hybrid DFT Functionals in Highly Correlated Oxides: The Case of $\text{CeO}_2$ and $\text{Ce}_2\text{O}_3$

Jesús Graciani,<sup>†</sup> Antonio M. Márquez,<sup>†</sup> José J. Plata,<sup>†</sup> Yanaris Ortega,<sup>†</sup>  
Norge C. Hernández,<sup>‡</sup> Alessio Meyer,<sup>§</sup> Claudio M. Zicovich-Wilson,<sup>||</sup> and  
Javier Fdez. Sanz<sup>\*†</sup>

*Departamento de Química Física, Facultad de Química, Universidad de Sevilla, 41012 Sevilla, Spain; Departamento de Física Aplicada I, Universidad de Sevilla, 41011 Sevilla, Spain; Dipartimento IFM, Università di Torino, Via P. Giuria, 7, I-10125 Torino, Italy and Unità INFN di Torino, Sezione F, via Giuria 5, I-10125 Torino, Italy; and Facultad de Ciencias, Universidad Autónoma del Estado de Morelos, Av. Universidad 1001, 62209 Cuernavaca, México*

Received August 3, 2010

**Abstract:** The outstanding catalytic properties of cerium oxides rely on the easy  $\text{Ce}^{3+} \leftrightarrow \text{Ce}^{4+}$  redox conversion, which however constitutes a challenge in density functional based theoretical chemistry due to the strongly correlated nature of the 4f electrons present in the reduced materials. In this work, we report an analysis of the performance of five exchange-correlation functionals (HH, HHLYP, PBE0, B3LYP, and B1-WC) implemented in the CRYSTAL06 code to describe three properties of ceria: crystal structure, band gaps, and reaction energies of the  $\text{CeO}_2 \rightarrow \text{Ce}_2\text{O}_3$  process. All five functionals give values for cell parameters that are in fairly good agreement with experiment, although the PBE0 hybrid functional is found to be the most accurate. Band gaps,  $2p\text{-}4f\text{-}5d$  in the case of  $\text{CeO}_2$  and  $4f\text{-}5d$  in the case of  $\text{Ce}_2\text{O}_3$ , are found to be, in general, overestimated and drop off when the amount of Hartree–Fock exchange in the exchange-correlation functional decreases. In contrast, the reaction energies are found to be underestimated, and increase when the amount of HF exchange lowers. Overall, at its standard formulation, the B1-WC functional seems to be the best choice as it provides good band gaps and reaction energies, and very reasonable crystal parameters.

### 1. Introduction

Cerium oxides, either  $\text{CeO}_2$  or nonstoichiometric  $\text{CeO}_{2-x}$ , hereafter referred to generically as ceria, have traditionally played the role of a support material in components of catalysts used in several chemical processes. Typical ex-

amples of industrial applications are the three-way catalysts in automotive catalytic converters, fluid-cracking catalysts in refineries, and ethylbenzene dehydrogenation catalysts used during the production of styrene.<sup>1,2</sup> Ceria is also an active component in low-temperature CO and VOC oxidation catalysts, wet-oxidation of organic pollutants in water, hydrocarbon-reforming and the water-gas-shift reaction. Initially, the promoting effect of ceria was attributed to the enhancement of the metal dispersion and the stabilization toward thermal sintering.<sup>3,4</sup> However, subsequent work has shown that ceria can act as a chemically active component as well, working as an oxygen reservoir able to deliver it in the presence of reductive gases and to incorporate it upon interaction with oxidizing gases.<sup>5–7</sup> Its ability to store, release, and transport oxygen ions indicates

\* Corresponding author e-mail: sanz@us.es.

<sup>†</sup> Departamento de Química Física, Facultad de Química, Universidad de Sevilla.

<sup>‡</sup> Departamento de Física Aplicada I, Universidad de Sevilla.

<sup>§</sup> Dipartimento IFM, Università di Torino and Unità INFN di Torino.

<sup>||</sup> Facultad de Ciencias, Universidad Autónoma del Estado de Morelos.

that ceria is not just a mere spectator but it takes part in the catalytic reaction. For instance, in the case of oxidation reactions catalyzed by vanadia, the catalytic activity appears to be highly enhanced when supported on ceria as compared to more inert supports as silica and alumina.<sup>8–11</sup> Similar behavior is clearly seen in the case of the water–gas shift reaction, where experiments carried on Rh/CeO<sub>2</sub> and on pure CeO<sub>2</sub><sup>12,13</sup> reveal striking differences. Also, the very recent work of Park et al.<sup>14</sup> and of Rodriguez et al.<sup>15,16</sup> illustrates the importance of stabilizing Ce<sup>3+</sup> centers and the role of the ceria nanoparticles.

The outstanding properties of ceria, and, consequently, the broad use in heterogeneous catalysis are due to its facile Ce<sup>3+</sup> ↔ Ce<sup>4+</sup> redox conversion,<sup>17</sup> however, the adequate description of the electronic configuration of Ce<sup>3+</sup> ions constitutes a challenge in density functional based theoretical chemistry due to the strongly correlated nature of the 4*f* electrons. Indeed, the 4*f* electrons in Ce<sub>2</sub>O<sub>3</sub> are localized and the material behaves like a typical antiferromagnetic Mott–Hubbard insulator.<sup>18</sup> However, due to the well-known lack of cancellation of the Coulomb self-interaction, DFT approaches within the LDA or GGA frameworks predict metallic behavior.<sup>19–26</sup> To circumvent this problem within the DFT framework, the use of hybrid functionals, in particular the Heyd–Scuseria–Ernzerhof (HSE06) hybrid<sup>27</sup> has been recently reported for both fully reduced bulk Ce<sub>2</sub>O<sub>3</sub>,<sup>23,28</sup> and partially reduced CeO<sub>2</sub> (111) surfaces.<sup>29</sup> Alternatively, a much less demanding computational approach makes use of a Hubbard-like term to account for the strong *on-site* Coulomb interactions. Indeed, the choice of *U* is a delicate point as the physical idea behind the method is to improve the electron correlation description of an electron pair in a given orbital, and it is clear that the optimum *U* value for LDA and GGA can be different. Also, the *U* parameter has to be large enough to properly localize the 4*f* electron of Ce<sup>3+</sup>, but without introducing undesired artifacts, such as overestimated band-gaps, and finally, as recently suggested by Castleton et al.,<sup>25</sup> the *U* value might be different for different properties under study. This latter aspect is not of minor importance as, for instance, the *U* value that better gives the lattice parameters must not necessarily provide the best energies or band gaps. Finally, one has to mention the possibility of using a *U* value determined in a self-consistent way: *U*<sub>eff</sub> = 5.30 and 4.50 eV for LDA and GGA, respectively.<sup>30,31</sup> However, there is no guarantee that a self-consistent *U* will systematically improve calculated results. In this context, it is also worth mentioning that a recent work on lanthanide oxides using a many-body perturbation theory in the *GW@LDA+U* approach exhibits only a weak dependence on *U* in a physically meaningful range of *U* values.<sup>32</sup>

In spite of the empirical choice of the *U* parameter,<sup>21,22</sup> the DFT+*U* approach has been shown to be an effective, widely used, theoretical tool in the study of structure and reactivity of ceria surfaces. However, for accurate energies and properties, an approach without external semiempirical input appears to be preferable. For instance, let us consider the case of CeO<sub>2</sub> fluorite structure for which the experimental value is *a*<sub>0</sub> ≈ 5.41 Å (5.406 Å<sup>33</sup> or 5.411 Å<sup>34</sup>). The LDA+*U* (*U*<sub>eff</sub> = 5.30 eV) value is *a*<sub>0</sub> = 5.40 Å, in good agreement

with the experiment, while GGA (PBE+*U*, *U*<sub>eff</sub> = 4.5 eV)<sup>23</sup> moderately overestimates it: *a*<sub>0</sub> = 5.49 Å. This 1.3% error of the GGA represents a 4.5% increase in the equilibrium volume and it has been shown to be critical in the determination of the charge state of gold atoms deposited on CeO<sub>2</sub> (111) surfaces.<sup>35–37</sup> In its turn, a very accurate *a*<sub>0</sub> value results from hybrid DFT calculations: 5.39 and 5.40 Å from plane-wave calculations with the PBE0 and HSE hybrid functionals, respectively,<sup>23</sup> or 5.41 Å from calculations using a Gaussian-Type Orbitals (GTO) basis set and the HSE functional.<sup>28</sup>

The performance of both the DFT+*U* and the hybrid DFT approaches to describe the electronic properties of ceria has been analyzed in a series of papers. For instance, Hay et al.<sup>28</sup> compared the suitability of LDA, GGA and meta-GGA DFT functionals with HSE06 hybrid calculations using a GTO basis set. Furthermore, Da Silva et al.<sup>23</sup> compared PBE0 and HSE functionals using a plane wave basis set, and more recently, Kullgren et al.<sup>38</sup> have reported on the performance of B3LYP calculations. In the latter work, it was shown for instance that B3LYP performs slightly better than PBE0 for the electronic properties but slightly worse for the structural properties.

The work reported so far on the performance of the DFT functionals to describe the electronic properties of ceria makes it clear that hybrid functionals are better suited than DFT+*U* techniques to correctly render the structural and electronic properties of reduced ceria-based systems. Unfortunately, periodic hybrid DFT calculations face a number of computational problems that make them computationally demanding. Briefly, if we consider the plane-wave and GTO implementations, we find that energy calculations are reasonably fast when using GTO but geometry optimization becomes slow because the calculation of energy gradients in a GTO basis set becomes, generally speaking, the limiting step regardless the functional used. The choice of the basis set is also a key question especially for the 4*f* shell. In contrast, geometry optimizations are in general much more efficient when using a plane-wave basis set, but here the limiting step is the calculation of the energy with the hybrid functional due to the difficulty to estimate the nonlocal Fock exchange contribution. Finally, one must realize that hybrid DFT is sensitive to an additional factor because the amount of Fock exchange included in the potential is also an external input which largely affects the final description.<sup>39,40</sup>

Despite the recent efforts devoted to elucidate the properties of reduced ceria samples, and the ability of hybrid functionals to describe them, the body of literature about the subject still is scarce. In particular, most of the work has mainly been focused on structural and electronic aspects, while the energetic aspects, which are of major interest in chemistry, had not been in general considered. Moreover, a complete analysis of the dependence of the 4*f* band splitting, as well as the different band-gaps, cell parameters, and heats of formation on the amount of the exact exchange has not been yet reported. Indeed, as reported by Moreira et al. in their work on NiO,<sup>40</sup> the fraction of Fock exchange introduced in the hybrid functional does alter not only the

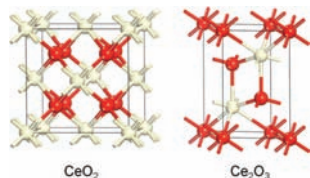


**Figure 1.** Left: Fluorite type structure of  $\text{CeO}_2$  (face-centered cubic,  $Fm\bar{3}m$ ). Right: the sesquioxide A-type structure of  $\text{Ce}_2\text{O}_3$  (hexagonal,  $P3m1$ ). Red and white balls indicate O and Ce atoms, respectively.

band-gaps but also the lattice constant, and the elastic constants and bulk modulus.

In view of the importance of this class of material, and the lack of information about the suitability of hybrid functionals to render a specific property, we have carried out in the present work a systematic analysis of the performance of five functionals commonly used in the literature, and that are implemented in the CRYSTAL06 code, namely the Perdew–Burke–Ernzerhof PBE0, the half and half HH, the modified half and half HHLYP, the widely used in computational chemistry B3LYP, and the recently proposed B1-WC functional. Using a purely ab initio periodic framework and treating oxidized and reduced ceria on an equal footing, we focus on the response of these functionals on three different sets of data: (i) structure: lattice parameters for  $\text{CeO}_2$  and  $\text{Ce}_2\text{O}_3$ ; (ii) band gaps:  $2p$ – $4f$ – $5d$  in the case of  $\text{CeO}_2$  and  $4f$ – $5d$  in the case of  $\text{Ce}_2\text{O}_3$ ; and (iii) reaction energies involved in the  $\text{CeO}_2/\text{Ce}_2\text{O}_3$  redox process. Moreover, bearing in mind the aforementioned sensitivity of the hybrid functionals to the fraction of exchange included, a systematic analysis of the behavior of the PBE0, B3LYP, and B1-WC functionals that incorporate different amounts of exact Fock exchange is also reported.

## 2. Computational Details

Two different structures were studied in this work, the  $\text{CeO}_2$  fluorite crystal ( $Fm\bar{3}m$ ) and the  $\text{Ce}_2\text{O}_3$  A-type crystal ( $P3m1$ ). Their unit cells are shown in Figure 1. All of the calculations were performed using a developing version of the CRYSTAL06 code,<sup>41</sup> where the Fock (and Kohn–Sham, KS) equations<sup>42</sup> for the valence electron density are solved in a periodic framework. In this framework, the crystalline orbitals are represented as linear combinations of Bloch functions (BFs) and are evaluated over a regular three-dimensional mesh in the reciprocal space. Each BF is built from atom-centered atomic orbitals (AOs) that are contractions (linear combinations with constant coefficients) of Gaussian-type functions (GTFs), each GTF being the product of a Gaussian times a real solid spherical harmonic.

Five hybrid DFT functionals were used in this work: PBE0,<sup>43</sup> HH, HHLYP,<sup>44</sup> B3LYP,<sup>45–47</sup> and the recently proposed B1-WC functional.<sup>48</sup> Self-consistent-field (SCF) closed shell calculations were performed to obtain the ground electronic state in the case of  $\text{CeO}_2$ , while in the case of  $\text{Ce}_2\text{O}_3$  spin-polarized calculations were performed in order

to discriminate between the ferromagnetic and antiferromagnetic states of this oxide. In the latter, multiple solutions of the SCF take place depending on the accommodation of the unpaired electrons over the Ce  $4f$  AOs. A recent implementation in the CRYSTAL program allows us to favor the convergence into a given symmetry adapted electronic configuration through a proper definition of the initial guess. In  $\text{Ce}_2\text{O}_3$  calculations, the most stable configuration for the  $4f$  electrons in Ce has been chosen. This is an antiferromagnetic state where both  $\alpha$  and  $\beta$  electrons occupy a mixing between  $(2z^2 - 3x^2 - 3y^2)z$  and  $(x^2 - 3y^2)x$  components of the  $4f$  AOs of Ce.

The PBE0 is a combination of the GGA exchange–correlation functional PBE<sup>49</sup> ( $E_{\text{XC}}^{\text{PBE}}$ ) and the exact Hartree–Fock (HF,  $E_{\text{X}}^{\text{HF}}$ ) exchange following the expression:

$$E_{\text{XC}}^{\text{PBE0}} = E_{\text{XC}}^{\text{PBE}} + 1/4(E_{\text{X}}^{\text{HF}} - E_{\text{X}}^{\text{PBE}}) \quad (1)$$

The HH, HHLYP, B3LYP, and B1-WC follow the expression:

$$E_{\text{XC}} = (1-A)(E_{\text{X}}^{\text{LDA}} + BE_{\text{X}}^{\text{BECKE/WC}}) + AE_{\text{X}}^{\text{HF}} + (1-C)E_{\text{C}}^{\text{VWN}} + CE_{\text{C}}^{\text{LYP/PBE}} \quad (2)$$

where  $E_{\text{X}}^{\text{LDA}}$  is the exchange contribution by using the Dirac–Slater functional<sup>50</sup> and  $E_{\text{C}}^{\text{VWN}}$  is the correlation energy coming from the use of the Vosko–Wilk–Nusair parametrization of the Ceperley–Alder free electron gas correlation results.<sup>51</sup> In the case of HH, HHLYP, and B3LYP functional,  $E_{\text{X}}^{\text{BECKE/WC}}$  stands for the Becke’s exchange,<sup>52</sup> and  $E_{\text{C}}^{\text{LYP/PBE}}$  represents the Lee–Yang–Parr correlation energy.<sup>46</sup> In the case of the B1-WC functional,  $E_{\text{X}}^{\text{BECKE/WC}}$  stands for the Wu–Cohen<sup>53</sup> GGA exchange, and  $E_{\text{C}}^{\text{LYP/PBE}}$  is the correlation energy contribution from the PBE.<sup>49</sup> Concerning the three weight parameters,  $A = 0.2$ ,  $B = 0.9$ , and  $C = 0.81$  for B3LYP. These parameters are set to  $A = 0.5$  and  $C = 1.0$  when we deal with the HH ( $B = 0.0$ ) and HHLYP ( $B = 1.0$ ) functional. In the case of using the B1-WC functional,  $A = 0.16$  and  $B = C = 1.0$ .

Although calculations using the HSE06 functional are not performed in this work, we will also briefly outline it since is closely related to the PBE0 and largely used in the comparisons reported here. In the HSE functional, the spatial decay of the HF exchange interaction is accelerated by partitioning the Coulomb potential for exchange into short-range (SR) and long-range (LR) components:<sup>27</sup>

$$E_{\text{XC}}^{\text{HSE}} = aE_{\text{X}}^{\text{HF,SR}}(\omega) + (1-a)E_{\text{X}}^{\text{PBE,SR}}(\omega) + E_{\text{X}}^{\text{PBE,LR}}(\omega) + E_{\text{C}}^{\text{PBE}} \quad (3)$$

where the mixing coefficient  $a$  is set to 0.25, and the screening factor  $\omega$  defines the separation range. This enables a substantial lowering of the computational cost for calculations in extended systems. Note that in the limit  $\omega = 0$ , HSE reduces to the hybrid functional PBE0, and when  $\omega \rightarrow \infty$ , HSE becomes identical with PBE.

Inner electrons of Ce atom were replaced by an effective core potential developed by the Stuttgart–Dresden group.<sup>54</sup> The Ce electrons explicitly treated were the  $4s^2 4p^6 4d^{10} 5s^2 5p^6 4f^4 6s^2 5d^1$ , with a  $(10\text{sp}7\text{d}8\text{f})/[4\text{sp}2\text{d}3\text{f}]$  basis

**Table 1.** Calculated and Experimental Lattice Parameters (in Å) for CeO<sub>2</sub> and Ce<sub>2</sub>O<sub>3</sub>

method	CeO <sub>2</sub>		Ce <sub>2</sub> O <sub>3</sub>			refs
	a <sub>0</sub>	error	a <sub>0</sub>	error	c <sub>0</sub>	
B3LYP	5.47	0.06	3.89	0.00	6.17	0.11
HH	5.34	-0.07	3.83	-0.06	5.93	-0.13
HHLYP	5.42	0.01	3.88	-0.01	6.14	0.08
PBE0	5.40	-0.01	3.86	-0.03	6.04	-0.02
B1-WC	5.38	-0.03	3.84	-0.05	5.93	-0.13
GGA(PBE)+U(U = 4.5)			3.87	-0.02	5.93	-0.13
GGA(PW91)+U(U = 3.0)	5.48	0.07	3.92	0.03		
HSE	5.41	0.00	3.87	-0.02	6.06	0.00
PBE0	5.39	-0.02	3.87	-0.02	6.07	0.01
Experiment	5.41		3.89		6.06	33,34

set optimized to properly describe oxides where the metal features III and IV oxidation states. The corresponding exponents and coefficients can be found in ref 55. For O an all-electron basis set proposed in ref 56 for ionic crystals was adopted. The two most external *sp* and *d* exponents have been reoptimized for cerium oxide, their resulting values being 0.4798717, 0.1801227, and 0.2991812 bohr<sup>-2</sup>, respectively.

Other technical parameters were set as follow. With the aim of obtaining an enough level of accuracy when evaluating the Coulomb and exchange series the five thresholds had the values of 10<sup>-8</sup>, 10<sup>-8</sup>, 10<sup>-8</sup>, 10<sup>-8</sup>, and 10<sup>-20</sup>. The Brillouin zone was sampled using a 6 × 6 × 6 Monkhorst-Pack<sup>57</sup> grid, corresponding to 16 reciprocal space irreducible points at which the KS matrix was diagonalized. The SCF calculations were considered to be converged when the energy changes between the iterations were smaller than 10<sup>-8</sup> hartree. The exchange-correlation contribution to the energy was evaluated by numerical integration over the cell volume.<sup>58</sup> Radial and angular points of the atomic grid were generated through Gauss-Legendre and Lebedev quadrature schemes. A grid pruning was adopted, as discussed in ref 58. In the present study, a (75, 974)p grid was used, such that it contains 75 radial points and a variable number of angular points, with a maximum of 974 on the Lebedev surface in the most accurate integration region. Full optimization (lattice constants and atomic positions) of CeO<sub>2</sub> and Ce<sub>2</sub>O<sub>3</sub> were carried out using a convergence criterion of 3 × 10<sup>-4</sup> hartree/bohr for the root-mean-square values of forces and 1.2 × 10<sup>-3</sup> bohr in the root-mean-square values of atomic displacements. The Fermi level in the DOS plots is taken directly from CRYSTAL, and estimated in accordance with the zero-th level of the electrostatic energy in the multipolar Ewald-type expansion.<sup>59</sup>

### 3. Results and Discussion

**3.1. Crystal Structure.** By and large, DFT methods are known to predict fairly well the crystal structure of a wide variety of inorganic compounds. In general, the deviations of lattice parameters, both positive and negative, are in the range 2–3%,<sup>60</sup> hence it seems reasonable to adopt a value of 2.5% as accuracy criterion. Table 1 displays the computed lattice parameters for CeO<sub>2</sub> and Ce<sub>2</sub>O<sub>3</sub> for each one of the functionals tested in this work. For comparison, some values chosen from the recent literature are also shown in this Table. In general, all computed values are found to correctly

reproduce the experimental lattice parameters for both oxides, fulfilling the proposed accuracy criterion. The a<sub>0</sub> parameter for CeO<sub>2</sub> seems to be only modestly influenced by the exchange-correlation functional chosen. The largest errors correspond to the values computed with the B3LYP functional, the HH functional, or with the GGA+U approach (~1.3%, 0.06–0.07 Å), although they are well below the required accuracy criterion. Alternatively, the smallest errors are found for the HHLYP, HSE and PBE0 functionals (less than 0.4%).

The a<sub>0</sub> and c<sub>0</sub> lattice parameters for Ce<sub>2</sub>O<sub>3</sub> show a similar behavior: the computed values are quite insensitive to the functional chosen, with all calculated values within the proposed error bar. The HH functional is, again, the one with the largest errors with respect to the experimental values, underestimating by 1.5% and 1.9% the lattice parameters. It is worth pointing out that, except for the HSE functional,<sup>23</sup> the percent errors on the computed c<sub>0</sub> lattice parameter are larger than the errors found for the calculated a<sub>0</sub> values. As in the case of the lattice parameter of CeO<sub>2</sub>, the smallest average errors are found for the HHLYP, HSE, and PBE0 functionals (less than 0.6% on average). Finally, it is worth mentioning here that the computed values with the PBE0 functional are practically the same, no matter the kind of basis set used: plane waves<sup>23</sup> or localized atomic orbitals (this work).

**3.2. Electronic Structure.** *3.2.1. Electronic Structure of CeO<sub>2</sub>.* In CeO<sub>2</sub>, the valence and conduction band are mainly composed by O 2*p* and Ce 5*d* states, respectively, while the Ce 4*f* states lie within the gap. All valence Ce states, including the 4*f* states, are empty, and the system is a wide gap insulator (see Figure 2, top). All local, semi local, and hybrid functionals produce an insulating solution, in agreement with the above picture of the CeO<sub>2</sub> electronic structure. Besides this qualitative agreement, the theoretical description of the electronic structure of CeO<sub>2</sub> is quite sensitive to the approach used, as can be deduced from the different band gaps reported in Table 2. As expected, both LDA and PBE underestimate the main band gap (O 2*p*–Ce 5*d*).<sup>23</sup> However, it is interesting to note that all DFT+U approaches reported in the literature also underestimate this band gap, and the results are not much sensitive to the specific value of the *U* parameter.<sup>22,23</sup> This can be easily explained since the *U* parameter acts only on the Ce 4*f* states, thus not modifying the relative positions of the valence and conduction bands, that have predominantly O 2*p* and Ce 5*d*



60 *J. Chem. Theory Comput.*, Vol. 7, No. 1, 2011

Graciani et al.

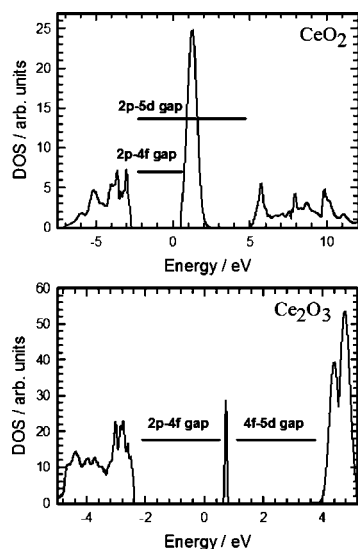


**Figure 2.** Total density of states (DOS) for CeO<sub>2</sub> (top) and Ce<sub>2</sub>O<sub>3</sub> (bottom).

**Table 2.** Calculated and Experimental Band Gaps (in eV) for CeO<sub>2</sub>

method	O 2p–Ce 5d	O 2p–Ce 4f	Ce 4f–Ce 5d
B3LYP	8.16	3.70	3.54
HH	10.64	7.50	1.91
HHLYP	10.75	7.18	2.51
PBE0	8.52	4.30	3.10
B1-WC	7.48	3.18	3.09
LDA <sup>23</sup>	5.61	2.0	2.25
PBE <sup>23</sup>	5.64	2.0	2.5
PBE0 <sup>23</sup>	7.93	4.5	2.25
HSE <sup>23</sup>	6.96	3.5	2.25
HSE <sup>28</sup>	7.0	3.3	-
DFT+U <sup>22,23</sup>	~ 5	-	-
Experiment <sup>61,62,28</sup>	~ 6–8	2.6–3.9	-

character. Alternatively, all hybrid functionals are found to produce larger values of the O 2p - Ce 5d gap. Particularly, the HH and HHLYP functionals result in an overly large error (~3–4 eV) with respect to the experimental value<sup>61</sup> for this band gap. This behavior might be ascribed to an excessive weight (50%) of the exact exchange in these two functionals. Among the different hybrid possibilities tested in this work, the B1-WC functional is the one that produces the smallest O 2p–Ce 5d gap, 7.48 eV, in close agreement with XPS and BIS experimental data,<sup>62</sup> which indicate a conduction band about 3 eV wide centered at about 7.5 eV. The smaller gap found for B1-WC agrees with the fact that it is the one incorporating the lowest HF exchange fraction. However, it is worth noting that although the HF fraction in B1-WC is lower than that of the screened HSE hybrid, the latter gives a gap even smaller (~7 eV), in excellent agreement with the experimental data.

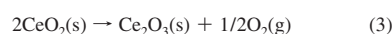
**Table 3.** Calculated and Experimental Band Gaps (in eV) for Ce<sub>2</sub>O<sub>3</sub>

method	O 2p–Ce 5d	O 2p–Ce 4f	Ce 4f–Ce 5d
B3LYP	6.61	2.17	4.08
HH	9.4	1.83	7.19
HHLYP	9.78	1.13	8.25
PBE0	7.08	2.34	4.54
B1-WC	5.94	3.00	2.78
PBE0 <sup>23</sup>	6.75	3.25	3.50
HSE <sup>23</sup>	5.75	3.25	2.50
experiment <sup>18</sup>	-	-	2.40

The results found for the O 2p–Ce 4f gap closely follow the behavior previously discussed for the main band gap. The HH and HHLYP functionals produce band gaps that are too large, mainly because the excessive weight of the exact exchange pushes upward all virtual levels. Among the remaining results, the B1-WC hybrid functional (with the lowest HF fraction) produces the lowest band gap, 3.18 eV, again in close agreement with available experimental data,<sup>62</sup> and with the HSE values (3.3–3.5 eV), which also fall in the experimental range. The use of the PBE0 approach results in a band gap slightly larger than the experimental data, a behavior already reported and discussed.<sup>23</sup>

**3.2.2. Electronic Structure of Ce<sub>2</sub>O<sub>3</sub>.** In contrast to CeO<sub>2</sub>, in Ce<sub>2</sub>O<sub>3</sub> one electron per Ce atom populates the Ce band, resulting in a narrow 4f occupied band that develops in the O 2p–Ce 5d gap, some 2.4 eV below the conduction band<sup>18</sup> that is formed mainly by a mixing of Ce 5d and Ce 4f states (see Figure 2, bottom). Overall, the effect of the inclusion of the exact exchange in the hybrid functionals is similar to those found in CeO<sub>2</sub>. The HH and HHLYP functionals result in too large band gaps, with all virtual levels too high in energy. With respect to the remaining hybrid functionals used in this paper, again the B1-WC produces the best result for the Ce 4f–Ce 5d gap (2.78 eV). This value agrees reasonably with the experimental value available (2.40 eV) and is slightly higher than the one estimated using the HSE functional (2.50 eV), which actually is the best to reproduce the experiment. In any case, except for the aforementioned cases of the HH and HHLYP functionals, the computed electronic structure of Ce<sub>2</sub>O<sub>3</sub> is in semiquantitative agreement with the experimental information. Finally, if we compare the PBE0 band gaps obtained either with plane-wave or GTO basis sets noticeable differences might be seen, indicating that the electronic structure is more implementation dependent than the lattice parameters.

**3.3. Reaction Energies.** Given the active and crucial role played by CeO<sub>2</sub> and Ce<sub>2</sub>O<sub>3</sub> oxides in many heterogeneous chemical reactions, generally traced back to their oxygen storage capacity, we have also investigated the performance of different hybrid functionals on the computation of some reaction energies involving cerium oxides. The suitability to predict the relevant thermodynamic properties has been investigated by computing the energetics of two reduction reactions involving CeO<sub>2</sub> and Ce<sub>2</sub>O<sub>3</sub>, namely:



Hybrid DFT Functionals in Highly Correlated Oxides



The reaction enthalpies have been calculated as

$$\Delta H_1 = E(\text{Ce}_2\text{O}_3) + 1/2 E(\text{O}_2) - 2 E(\text{CeO}_2) \quad (5)$$

$$\Delta H_2 = E(\text{Ce}_2\text{O}_3) + E(\text{CO}_2) - 2E(\text{CeO}_2) - E(\text{CO}) \quad (6)$$

where  $E(X)$  represents the computed total energies of  $X = \text{CeO}_2$  (solid),  $\text{Ce}_2\text{O}_3$  (solid),  $\text{O}_2$  (gas),  $\text{CO}_2$  (gas), and  $\text{CO}$  (gas) per formula unit. The experimental values have been obtained from the corresponding heats of formation of reactants and products.<sup>63</sup> The computed reduction energies, along with the experimental values are reported in Table 4. Zero-point vibrational energy contributions have not been included. A major problem that we encounter which makes it hard to extract any conclusions with respect to the reliability of the different functionals is that the experimental heats of formation of cerium oxides are not easy to measure. This problem is related to difficulties in the preparation of defect-free oxides in a well-defined oxidation state. Comparing the most recent reported data for reaction 3, shown in Table 4, with other values available in the recent literature (3.57 eV),<sup>2</sup> the uncertainty in the experimental value might be estimated to be  $\sim 0.5$  eV. With this caution in mind we can, anyhow, comment on the values computed in this work with different hybrid functionals. The estimated reaction energies for reaction 3 show a dispersion (standard deviation) of 0.67 eV, with an average value of 3.92 eV, in close agreement with the last reported experimental value. Excluding the HHLYP value, that shows the larger absolute error with respect to the experimental value, the average reaction energy increases to 4.12 eV (slightly larger than the experiment) and the dispersion is reduced to 0.50 eV, similar to the experimental error bar. Thus, regarding the computed reaction energies for reaction 3 we can say that all theoretical values fit within the experimental error bar, being the HH and PBE0 functional the ones that produce the data with the smaller deviation with respect to the currently accepted experimental reaction enthalpy. However, we can see once again a significant difference between the PBE0 estimated values obtained using plane-waves or GTO as basis set.

In the case of reaction 4, we can assume a similar error bar for the experimental value reported. Similar comments

**Table 4.** Computed and Experimental Reaction Energies (in eV) for  $2 \text{CeO}_2 \rightarrow \text{Ce}_2\text{O}_3 + 1/2 \text{O}_2$  and  $2 \text{CeO}_2 + \text{CO} \rightarrow \text{Ce}_2\text{O}_3 + \text{CO}_2$

method	$2 \text{CeO}_2 \rightarrow \text{Ce}_2\text{O}_3 + 1/2 \text{O}_2$		$\text{CeO}_2 + \text{CO} \rightarrow \text{Ce}_2\text{O}_3 + \text{CO}_2$	
	$\Delta H$	error	$\Delta H$	error
B3LYP	3.52	-0.47	0.44	-0.58
HH	4.37	0.38	0.93	-0.09
HHLYP	2.88	-1.11	-0.16	-1.18
PBE0	3.66	-0.33	0.40	-0.62
B1-WC	4.45	0.46	1.05	0.03
PBE0 <sup>23</sup>	3.14	-0.85		
HSE <sup>23</sup>	3.16	-0.83		
LDA+U <sup>23</sup>	3.04	-0.95		
PBE+U <sup>23</sup>	2.29	-1.70		
experiment <sup>63</sup>	3.99		1.02	

*J. Chem. Theory Comput., Vol. 7, No. 1, 2011* 61

can be made with respect to the computed theoretical values. Excluding again the value obtained with the HHLYP functional (that predicts an exothermic reaction), the calculated average reaction energy will be 0.80 eV, in close agreement with the experimental reaction enthalpy of 1.02 eV. The standard deviation of the theoretical values is, in this case, only 0.36 eV, well within the experimental error bar. In this case, the HH and B1-WC functionals produce the theoretical values in better agreement with the experimental data.

In summary, we can state that, excluding the HHLYP functional, all tested functionals produce values for the reaction energy that are within the experimental error bar of 0.5 eV.

**3.4. Effect of the Fock Exchange.** In addition, to evaluate the performance of different hybrid functionals in the description of the geometric and electronic structure of  $\text{CeO}_2$  and  $\text{Ce}_2\text{O}_3$ , and in selected reaction energies involving ceria, we have also investigated to what extent the amount of HF exchange affects the three properties that we are looking at in this work: the cell parameters, the band gaps, and the reaction energies involved in the  $\text{Ce}^{3+} \leftrightarrow \text{Ce}^{4+}$  redox process. Taking into account the results we have obtained so far, we have limited this analysis to the B3LYP, PBE0, and B1-WC functionals.

**3.4.1. Cell Parameters.** Figure 3 shows the influence of the amount of exact exchange in the computed values of the lattice parameters of  $\text{CeO}_2$  and  $\text{Ce}_2\text{O}_3$ . Starting with the  $a_0$  parameter of  $\text{CeO}_2$ , the computed lattice parameter decreases in all cases on increasing the percentage of HF exchange. This first result is in contrast with that reported on NiO, where the lattice constant was found to increase when the amount of exact exchange was raised.<sup>40</sup> For the PBE0 functional, the value computed with the standard amount of exact exchange (25%) is already very close to the experimental value, while for the B3LYP functional, the experimental lattice parameter is only reached at  $\sim 55\%$  of exact exchange and for the B1-WC functional the most accurate value is obtained at 0% of exact exchange.

With respect to the lattice parameters of  $\text{Ce}_2\text{O}_3$ , we find that the  $a_0$  parameter is quite insensitive to the amount of exact exchange in the three functionals tested. Only for the B3LYP functional, the experimental value of  $a_0$  is reached (for 10–20% of HF exchange), while for PBE0 and B1-WC the computed value is always below the experimental one. The  $a_0$  lattice parameter remains almost invariant with the B1-WC functional: the absolute change is less than 0.01 Å in the tested range (10–50% of HF exchange). The value of  $c_0$  is more sensitive than that of  $a_0$  to the fraction of HF exchange included in the hybrid functional. For the B3LYP and PBE0 functionals, the computed value decreases on increasing the participation of HF exchange, while for the B1-WC functional  $c_0$  increases slightly. In the case of the PBE0 functional, the value closest to the experimental data is reached at about 10% of exact exchange, even though, with the standard value of HF exchange the error is only  $-0.35\%$ , which is quite accurate and keeps the advantages of using a standard definition of the functional. In the case of the B3LYP functional, the experimental value of  $c_0$  is

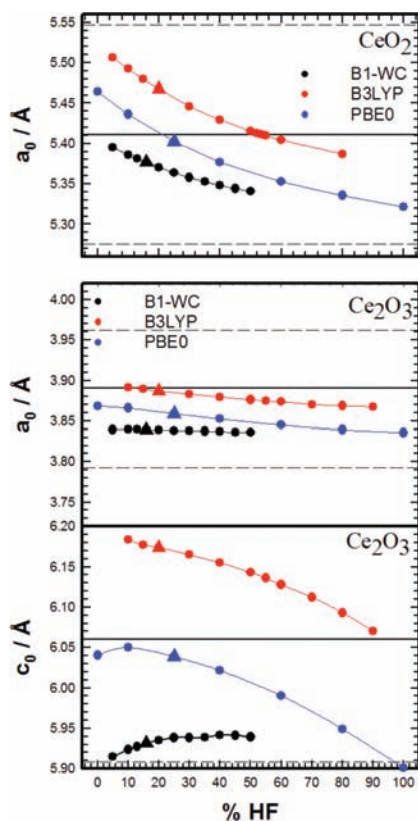


**Figure 3.** Dependency of the computed lattice parameters for  $\text{CeO}_2$  (top) and  $\text{Ce}_2\text{O}_3$  ( $a_0$ , middle and  $c_0$ , bottom) on the amount of exact exchange in the B3LYP, PBE0, and B1-WC functionals. The triangles denote the standard HF percent for each functional. The horizontal lines show the experimental value (full) and the acceptable error bars (dashed).

not reached for any amount of exact exchange, being only approximated when the amount of HF exchange is increased up to 90%. The variation of  $c_0$  with the percentage of HF exchange in the B1-WC functional is (as it did happen with  $a_0$ ) quite small. The computed lattice parameter increases only slightly in the tested range of exact exchange, the total increment being less than 0.05 Å.

In summary, the analysis of the variations in the cell structure suggests that overall the PBE0 at its original formulation is the more appropriate choice to simultaneously render the three parameters. Although in the case of the sesquioxide the B3LYP answer for  $a_0$  is very good, it needs to incorporate a large amount of Fock exchange to get closer to the experimental  $c_0$  value. In the general comparison the B1-WC functional seems to perform satisfactorily with small variations.

**3.4.2. Band Gaps.** The evolution of the computed band gaps with the amount of Fock exchange included in the functional shows, for the three functionals tested, a marked

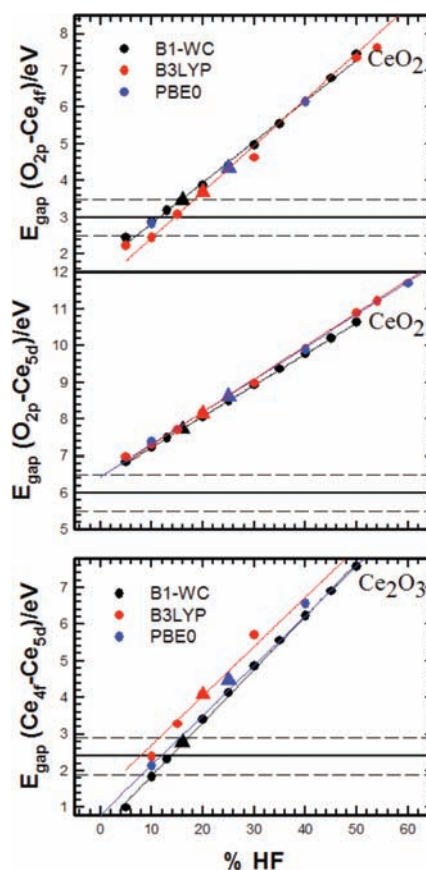


**Figure 4.** Dependency of the computed band gaps for  $\text{CeO}_2$  (top and middle) and  $\text{Ce}_2\text{O}_3$  (bottom) on the percentage of exact exchange in the B3LYP, PBE0, and B1-WC functionals. Refer to Figure 3 for labeling.

linear behavior (see Figure 4). In all cases, and in agreement with the well-known trend,<sup>40,64</sup> the computed band gaps increase with the amount of exact exchange, the increment being practically linear, showing similar slopes, with many of the fitting lines overlapping. A direct consequence of this behavior is that similar values of the band gaps are computed for similar contributions of the Fock exchange, regardless of the functional utilized. The O 2p–Ce 4f experimental band gap of  $\text{CeO}_2$  is, thus, most approximated in the 10–15% range of exact exchange. On the contrary, the computed O 2p–Ce 5d band gap of  $\text{CeO}_2$  is always larger than the experimental value of 6.0 eV,<sup>61</sup> but it approaches the ~7.0–7.5 eV value<sup>62</sup> obtained from XPS and BIS data, for about 10% Fock exchange. In the case of  $\text{Ce}_2\text{O}_3$ , the experimental value is, again, more closely approached in the 10–15% range of exact exchange and the computed value increases linearly with increasing contribution of the HF exchange in the functional. It is particularly striking again

Hybrid DFT Functionals in Highly Correlated Oxides

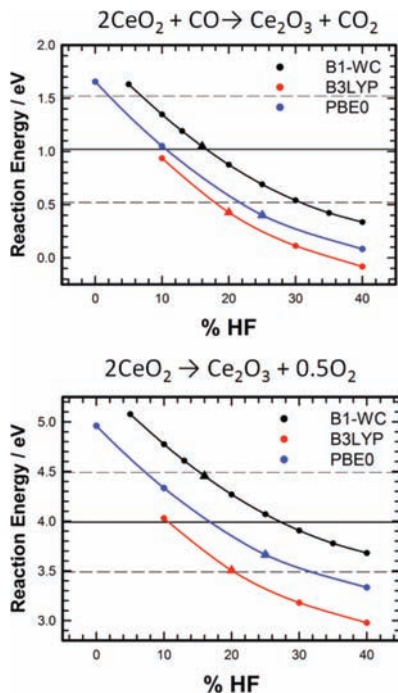


**Figure 5.** Dependency of the computed reaction energies on the percentage of exact exchange in the B3LYP, PBE0, and B1-WC functionals. Refer to Figure 3 for labeling.

that, regardless of the functional used, all experimental band gaps are nearly approximated in a similar range of HF exchange, around 10–15%. This can be interpreted in the sense that the different band gaps (the relative position of the bands) are mostly dependent on the exchange functional and basically independent of the correlation functional utilized.

Summarizing again, when we analyze the plots for the three band gaps reported in Figure 4, the B1-WC functional is the one that gives a better result. Only this functional at its original formulation is able to reproduce band gaps within the  $\pm 0.5$  eV error bar, even though the O  $2p$ –Ce  $5d$  gap still is overestimated.

**3.4.3. Energetics.** The dependence on the computed reduction energies for reactions 3 and 4 on the percentage of HF exchange included in the functional is shown in Figure 5. In both cases, the estimated reaction energies are decreased on increasing the contribution of exact exchange and show a similar dependency as demonstrated by the curve fitted to the computed reaction energies. It is always possible to adjust the contribution of HF exchange to reproduce the experimental reaction energy. For the reduction of  $\text{CeO}_2$  with CO, reaction 4, amounts of HF exchange of 10–15% seem to give the best agreement with the experimental reaction energy. For reaction 3, however, the dispersion of the computed reaction energy is larger and, as result, the percentage of HF exchange required to for the experimental

*J. Chem. Theory Comput., Vol. 7, No. 1, 2011* 63

**Table 5.** Summary of the Effect of the Fock Exchange Contribution on the Structure, Band Gaps and Reaction Energies<sup>a</sup>

property	error limit	B3LYP(20)	PBE0(25)	B1WC(16)
structure (cell parameters)	2.5%	[0–100]	[0–100]	[0–100]
band-gaps $\text{CeO}_2$	0.5 eV	[10–18]	[8–16]	[8–16]
band-gaps $\text{Ce}_2\text{O}_3$	0.5 eV	[4–12]	[8–16]	[10–16]
energy for reaction 3	0.5 eV	[8–20]	[8–32]	[16–50]
energy for reaction 4	0.5 eV	[2–18]	[2–22]	[7–30]
the whole set		[10–12]	[8–16]	16

<sup>a</sup> Values that fulfill the accuracy criteria are in brackets, and the standard fractions between parentheses.

value also spawns a larger range:  $\sim 10\%$  for B3LYP,  $\sim 18\%$  for PBE0, and  $\sim 28\%$  for the B1-WC functional. At its original formulation, the B1-WC functional is once again the best well-behaved functional as it is very accurate for reaction 4 and within the bar error in the case of reaction 3.

A complete view of the final ranges of possible HF fractions for which the different calculated values fall within the error bars might be obtained inspecting Table 5. As can be seen, the fraction for a given functional giving results within the error bars for lattice constants, band gaps, and energetics may differ, however, the three hybrids with the same nominal fraction of roughly 10–16% give results in fairly good agreement with the experimental data.

#### 4. Conclusions

In this work, we report an analysis of the performance of five exchange-correlation functionals implemented in the CRYSTAL06 code to describe three properties of ceria that include crystal structure, band gaps, and reaction energies involved in the  $\text{Ce}^{3+} \leftrightarrow \text{Ce}^{4+}$  redox process. Concerning the cell parameters, all five functionals give values that are within the 2.5% error, usually found for a vast majority of inorganic crystals, although the PBE0 hybrid functional is found to be the most accurate, giving parameters also very close to those estimated using the HSE screened functional. In general, when the fraction of HF exchange increases, a moderate lowering in the cell parameters is observed. Things change when we look at the band gaps of both cerium dioxide and sesquioxide. First the HH and HHLYP functionals lead to band gaps too large as they incorporate too much HF exchange that pushes the empty states too high. It is shown that for any functional used, the gaps are overestimated, and the agreement improves lowering the amount of the HF exchange. In this case, the overall best answer is provided by the B1-WC functional, which actually, among the functionals here considered, incorporates the lowest amount of HF exchange in its original formulation. The suitability to render the reaction energies normally involved in the rich ceria chemistry has been evaluated estimating the energetics associated to the  $\text{CeO}_2 \rightarrow \text{Ce}_2\text{O}_3$  reduction process. For the two reactions considered, the reaction energies are in general underestimated, and lower when the amount of HF exchange increases, which is in contrast with the gaps behavior. Overall, the B1-WC functional is once again the most well-behaved functional to reproduce the correct energetics.

64 *J. Chem. Theory Comput.*, Vol. 7, No. 1, 2011

Graciani et al.

In summary, the present work shows that as far as the structure is concerned, any of the functionals that we have considered, in the original formulation, are accurate enough, giving parameters within the usual error bar. In general, the cell parameters are found to depend only moderately on the HF exchange fraction. However, caution should be taken in the case that the structure might favor a given state or property, in which case the PBE0 functional should be the choice. In the case of band gaps and reaction energies, a stronger dependency on the amount of HF exchange is observed. Its lowering improves band gaps and reaction energies with both PBE0 and B3LYP functional. Otherwise, at its standard formulation, the B1-WC functional (the one with the smallest fraction of HF exchange), seems to be the best choice as it provides good band gaps and reaction energies, and very reasonable crystal parameters.

**Acknowledgment.** This work has been supported by the Spanish Ministry of Science and Innovation, MICINN (Grant Nos. MAT2008-04918, CSD2008-0023), and the Junta de Andalucía (P08-FQM-3661). Computational time on the Barcelona Supercomputing Center/Centro Nacional de Supercomputación is gratefully acknowledged.

#### References

- (1) Trovarelli, A. *Catal. Rev. Sci. Eng.* **1996**, *38*, 439.
- (2) Trovarelli, A. *Catalysis by Ceria and Related Materials; Catalytic Science Series*; Imperial College Press: London, 2002; Vol. 2.
- (3) Dictor, R.; Roberts, S. *J. Phys. Chem.* **1989**, *93*, 5846.
- (4) Su, E. C.; Rothschild, W. G. *J. Catal.* **1986**, *99*, 506.
- (5) Yao, H. C.; Yu Yao, Y. F. *J. Catal.* **1984**, *86*, 254.
- (6) Engler, B.; Koberstein, E.; Schubert, P. *Appl. Catal.* **1989**, *48*, 71.
- (7) Miki, T.; Ogawa, T.; Haneda, M.; Kakuta, N.; Ueno, A.; Tateishi, S.; Matsuura, S.; Sato, M. *J. Phys. Chem.* **1990**, *94*, 6464.
- (8) Daniell, W.; Ponchel, A.; Kuba, S.; Anderle, F.; Weingand, T.; Gregory, D. H.; Knozinger, H. *Top. Catal.* **2002**, *20* (1–4), 65–74.
- (9) Wachs, I. E. *Catal. Today* **2005**, *100*, 79–94.
- (10) Dinse, A.; Frank, B.; Hess, C.; Habel, D.; Schomacker, R. *J. Mol. Catal. A* **2008**, *289*, 28–37.
- (11) Ganduglia-Pirovano, M. V.; Popa, C.; Sauer, J.; Abbott, H.; Uhl, A.; Baron, M.; Stacchiola, D.; Bondarchuk, O.; Shaikhutdinov, S.; Freund, H.-J. *J. Am. Chem. Soc.* **2010**, *132*, 2345.
- (12) Shido, T.; Iwasawa, Y. *J. Catal.* **1992**, *136*, 493.
- (13) Shido, T.; Iwasawa, Y. *J. Catal.* **1993**, *141*, 71.
- (14) Park, J. B.; Graciani, J.; Evans, J.; Stacchiola, D.; Ma, S. G.; Liu, P.; Nambu, A.; Sanz, J. F.; Hrbek, J.; Rodriguez, J. A. *Proc. Natl. Acad. Sci.* **2009**, *106*, 4975.
- (15) Rodriguez, J. A.; Graciani, J.; Evans, J.; Park, J. B.; Yang, F.; Stacchiola, D.; Senanayake, S. D.; Ma, S.; Perez, M.; Liu, P.; Sanz, J. F.; Hrbek, J. *Angew. Chem., Int. Ed.* **2009**, *48*, 8047.
- (16) Park, J. B.; Graciani, J.; Evans, J.; Stacchiola, D.; Senanayake, S. D.; Barrio, L.; Liu, P.; Sanz, J. F.; Hrbek, J.; Rodriguez, J. *J. Am. Chem. Soc.* **2010**, *132*, 356.
- (17) Trovarelli, A.; de Leitenburg, C.; Boaro, M.; Dolcetti, G. *Catal. Today* **1999**, *50*, 353.
- (18) Prokofiev, A.; Shelykh, A.; Melekh, B. *J. Alloys Compd.* **1996**, *242*, 41.
- (19) Yang, Z.; Woo, T. K.; Baudin, M.; Hermansson, K. *J. Chem. Phys.* **2004**, *120*, 7741.
- (20) Nolan, M.; Grigoleit, S.; Sayle, D. C.; Parker, S. C.; Watson, G. W. *Surf. Sci.* **2005**, *576*, 217.
- (21) Andersson, D. A.; Simak, S. I.; Johansson, B.; Abrikosov, I. A.; Skorodumova, N. V. *Phys. Rev. B* **2007**, *75*, 035109.
- (22) Loschen, C.; Carrasco, J.; Neyman, K.; Illas, F. *Phys. Rev. B* **2007**, *75*, 035115.
- (23) Da Silva, J. L. F.; Ganduglia-Pirovano, M. V.; Sauer, J.; Bayer, V.; Kresse, G. *Phys. Rev. B* **2007**, *75*, 045121.
- (24) Da Silva, J. L. F. *Phys. Rev. B* **2007**, *76*, 193108.
- (25) Castleton, C. W. M.; Kullgren, J.; Hermansson, K. *J. Chem. Phys.* **2007**, *127*, 244704.
- (26) Kresse, G.; Blaha, P.; Da Silva, J. L. F.; Ganduglia-Pirovano, M. V. *Phys. Rev. B* **2005**, *72*, 237101.
- (27) Heyd, J.; Scuseria, G. E. *J. Chem. Phys.* **2006**, *125*, 224106.
- (28) Hay, P. J.; Martin, R. L.; Uddin, J.; Scuseria, G. E. *J. Chem. Phys.* **2006**, *125*, 034712.
- (29) Ganduglia-Pirovano, M. V.; Da Silva, J. L. F.; Sauer, J. *Phys. Rev. Lett.* **2009**, *102*, 026101.
- (30) Fabris, S.; de Gironcoli, S.; Baroni, S.; Vicario, G.; Balducci, G. *Phys. Rev. B* **2005**, *72*, 237102.
- (31) Cococcioni, M.; de Gironcoli, S. *Phys. Rev. B* **2005**, *71*, 035105.
- (32) Jiang, H.; Gomez-Abal, R. I.; Rinke, P.; Scheffler, M. *Phys. Rev. Lett.* **2009**, *102*, 126403.
- (33) Duclos, S. J.; Vohra, Y. K.; Ruoff, A. L.; Jayaraman, A.; Espinosa, G. P. *Phys. Rev. B* **1988**, *38*, 7755.
- (34) Gerward, L.; Olsen, J. S. *Powder Diffr.* **1993**, *8*, 127.
- (35) Branda, M. M.; Hernández, N. C.; Sanz, J. F.; Illas, F. *J. Phys. Chem. C* **2010**, *114*, 1934.
- (36) Hernández, N. C.; Grau-Crespo, R.; de Leeuw, N. H.; Sanz, J. F. *Phys. Chem. Chem. Phys.* **2009**, *11*, 5246.
- (37) Branda, M. M.; Castellani, N. J.; Grau-Crespo, R.; de Leeuw, N. H.; Cruz Hernandez, N.; Sanz, J. F.; Neyman, K. M.; Illas, F. *J. Chem. Phys.* **2009**, *131*, 94702.
- (38) Kullgren, J.; Castleton, Ch. W. M.; Müller, C.; Muñoz-Ramo, D.; Hermansson, K. *J. Chem. Phys.* **2010**, *132*, 054110.
- (39) Martin, R. L.; Illas, F. *Phys. Rev. Lett.* **1997**, *79*, 1539.
- (40) Moreira, I. de P. R.; Illas, F.; Martin, R. L. *Phys. Rev. B* **2002**, *65*, 155102.
- (41) Dovesi, R.; Saunders, V. R.; Roetti, C.; Orlando, R.; Zicovich-Wilson, C. M.; Pascale, F.; Civarelli, B.; Doll, K.; Harrison, N. M.; Bush, I. J.; D’Arco, P.; Llunell, M. *CRYSTAL06 User’s Manual*; Università di Torino: Torino, 2006.
- (42) Parr, R. G.; Yang, W. *Density Functional Theory of Atoms and Molecules*; Oxford University Press: New York, 1989.
- (43) Adamo, C.; Barone, V. *Chem. Phys. Lett.* **1998**, *298*, 113.
- (44) Becke, A. D. *J. Chem. Phys.* **1993**, *98*, 1372.
- (45) Becke, A. D. *J. Chem. Phys.* **1993**, *98*, 5648.
- (46) Lee, C.; Yang, W.; Parr, R. G. *Phys. Rev. B* **1998**, *37*, 785.

Hybrid DFT Functionals in Highly Correlated Oxides

- (47) Miehlich, B.; Savin, A.; Stoll, H.; Preuss, H. *Chem. Phys. Lett.* **1989**, *157*, 200.
- (48) Bile, D. I.; Orlando, R.; Rignanese, G. M.; Íñiguez, J.; Ghosez, P. *Phys. Rev. B* **2008**, *77*, 165107.
- (49) Perdew, J. P.; Burke, K.; Ernzerhof, M. *Phys. Rev. Lett.* **1996**, *77*, 3865.
- (50) Dirac, P. A. M. *Proc. Cambridge Phil. Soc.* **1930**, *26*, 376.
- (51) Vosko, S. H.; Wilk, L.; Nusair, M. *Can. J. Phys.* **1980**, *58*, 1200.
- (52) Becke, A. D. *Phys. Rev. A* **1988**, *38*, 3098.
- (53) Wu, Z.; Cohen, R. E. *Phys. Rev. B* **2006**, *73*, 235116.
- (54) Dolg, M.; Stoll, H.; Preuss, H. *J. Chem. Phys.* **1989**, *90*, 1730.
- (55) The CRYSTAL web page: <http://www.crystal.unito.it>
- (56) Corà, F. *Mol. Phys.* **2005**, *103*, 2483.
- (57) Monkhorst, H. J.; Pack, J. D. *Phys. Rev. B* **1976**, *13*, 5188.
- J. Chem. Theory Comput.*, Vol. 7, No. 1, 2011 **65**
- (58) Pascale, F.; Zicovich-Wilson, C. M.; López Gejo, F.; Civarelli, B.; Orlando, R.; Dovesi, R. *J. Comput. Chem.* **2004**, *25*, 888.
- (59) Saunders, V. R.; Freyria-Fava, C.; Dovesi, R.; Salasco, L.; Roetti, C. *Mol. Phys.* **1992**, *77*, 629.
- (60) Sholl, D. S.; Steckel, J. A. In *Density Functional Theory: A Practical Introduction*; John Wiley and Sons: Hoboken, NJ, 2009, p 222.
- (61) Marabelli, F.; Wachter, P. *Phys. Rev. B* **1987**, *36*, 1238.
- (62) Wuilloud, E.; Delley, B.; Schneider, W. D.; Baer, Y. *Phys. Rev. Lett.* **1984**, *53*, 202.
- (63) Lide, D. R., Ed. *CRC Handbook of Chemistry and Physics*, 9th ed.; CRC Press, Boca Raton, Florida, U.S.A., 2009).
- (64) Muscat, J.; Wander, A.; Harrison, N. M. *Chem. Phys. Lett.* **2001**, *342*, 397.
- CT100430Q

### 3.3 Improving the Density Functional Theory+U Description of CeO<sub>2</sub> by Including the Contribution of the O 2p Electrons

## Communication: Improving the density functional theory+ $U$ description of $\text{CeO}_2$ by including the contribution of the O $2p$ electrons

José J. Plata, Antonio M. Márquez, and Javier Fdez. Sanz<sup>a)</sup>

*Departamento de Química Física, Facultad de Química, Universidad de Sevilla, 41012 Sevilla, Spain*

(Received 7 November 2011; accepted 3 January 2012; published online 23 January 2012)

Density functional theory (DFT) based approaches within the local-density approximation or generalized gradient approximation frameworks fail to predict the correct electron localization in strongly correlated systems due to the lack of cancellation of the Coulomb self-interaction. This problem might be circumvented either by using hybrid functionals or by introducing a Hubbard-like term to account for the on site interactions. This latter DFT+ $U$  approach is less expensive and therefore more practical for extensive calculations in solid-state computational simulations. By and large, the  $U$  term only affects the metal electrons, in our case the Ce  $4f$  ones. In the present work, we report a systematic analysis of the effect of adding such a  $U$  term also to the oxygen  $2p$  electrons. We find that using a set of  $U^f = 5$  eV and  $U^p = 5$  eV effective terms leads to improved description of the lattice parameters, band gaps, and formation and reduction energies of  $\text{CeO}_2$ . © 2012 American Institute of Physics. [doi:10.1063/1.3678309]

Cerium oxides constitute a class of materials widely used in catalysis both as support and active phases. Typical examples of industrial applications are the three-way catalysts in automotive catalytic converters, fluid-cracking catalysts in refineries, and ethylbenzene dehydrogenation in the production of styrene.<sup>1</sup> Either  $\text{CeO}_2$  or non-stoichiometric  $\text{CeO}_{2-x}$ , hereafter referred to generically as ceria, are also an active component in a number of processes such as low-temperature CO and VOC oxidation catalysts, wet-oxidation of organic pollutants in water, hydrocarbon reforming and the water-gas-shift reaction. Although the promoting effect of ceria was initially attributed to the enhancement of the metal dispersion and the stabilization towards thermal sintering,<sup>2,3</sup> subsequent work has shown that ceria can act as a chemically active component as well, working as an oxygen reservoir able to deliver it in the presence of reductive gases and to incorporate it upon interaction with oxidizing gases.<sup>4-6</sup>

The broad use in heterogeneous catalysis of ceria relies on its facile  $\text{Ce}^{3+} \leftrightarrow \text{Ce}^{4+}$  redox conversion;<sup>7</sup> however, the adequate description of the electronic configuration of  $\text{Ce}^{3+}$  ions constitutes a challenge in density functional based theoretical chemistry due to the strongly correlated nature of the  $4f$  electrons. Indeed, the  $4f$  electrons in  $\text{Ce}_2\text{O}_3$  are localized and the material behaves like a typical antiferromagnetic Mott-Hubbard insulator.<sup>8</sup> However, due to the well-known lack of cancellation of the Coulomb self-interaction, density functional theory (DFT) approaches within the local-density approximation (LDA) or generalized gradient approximation (GGA) frameworks predict metallic behavior.<sup>9-16</sup> To circumvent this problem within the DFT framework, the use of hybrid functionals, has been recently reported using both plane waves and Gaussian-Type Orbitals (GTO) as basis set.<sup>13,17,18</sup> Such functionals, in particular HSE, PBE0, and B1-WC, are

found to correctly reproduce lattice constants and band gaps, although its general use is limited by the high computational cost involved in extensive solid state (periodic) calculations. That is why a more pragmatic but much less computationally demanding approach that makes use of a Hubbard-like term,  $U$ , to account for the strong *on-site* Coulomb interactions is generally used in surface reactivity studies. The choice of  $U$  is a subtle point, as it has to be large enough to properly localize the  $4f$  electron of  $\text{Ce}^{3+}$ , but without introducing undesired artifacts, such as overestimated band-gaps. Usually its value is selected by fitting a given property,<sup>11,12</sup> from linear-response calculations,<sup>19,20</sup> or even on a self-consistent basis,<sup>21,22</sup> although, as suggested by Castleton *et al.*,<sup>15</sup> the optimal  $U$  value might be different for different properties under study. For instance, let us consider the case of  $\text{CeO}_2$  fluorite structure for which the experimental lattice parameter value is  $a_0 \approx 5.41$  Å (5.406 Å (Ref. 23) or 5.411 Å (Ref. 24)). The LDA+ $U$  ( $U_{\text{eff}} = 5.30$  eV) value is  $a_0 = 5.40$  Å, in good agreement with the experiment, while GGA (PBE+ $U$ ,  $U_{\text{eff}} = 4.5$  eV) (Ref. 13) moderately overestimates it:  $a_0 = 5.49$  Å. This 1.3% error of the GGA represents a 4.5% increase in the equilibrium volume and it has been shown to be critical in the determination of the charge state of gold atoms deposited on  $\text{CeO}_2$  (111) surfaces.<sup>25-27</sup>

In spite of these limitations, the DFT+ $U$  is currently the method of choice in the analysis of structure and reactivity of surfaces of reducible metal oxides, in particular in ceria, where including the  $U$  Ce  $4f$  term provides a consistent treatment of reduced Ce ions. The common approach to setup DFT+ $U$  calculations in a metal oxide is to select a  $U$  parameter for the metal ( $U_{\text{eff}} = 4.5$ – $5.5$  eV in the case of Ce  $4f$  orbitals) and to perform the calculations at just a little extra cost. Yet, the price to pay concerns not only some inaccuracies in the structure but also in the energetics as will be shown later. Additional effects might be introduced, in particular the inter-site correction, or DFT+ $U$ + $V$  approach, lately

<sup>a)</sup> Author to whom correspondence should be addressed. Electronic mail: sanz@us.es.



### Section 3.3. Improving DFT+U description of CeO<sub>2</sub>

041101-2 Plata, Marquez, and Sanz

J. Chem. Phys. **136**, 041101 (2012)

implemented by Campo *et al.*,<sup>28</sup> and successfully applied to NiO among other materials. Recently Park *et al.*,<sup>29</sup> based on earlier ideas of Nekrasov *et al.*,<sup>30</sup> showed that, in the case of reduced titania, adding a correction on the oxygen 2*p* orbitals dramatically improved the description. By employing the so-called LDA+*U<sup>d</sup>*+*U<sup>p</sup>* approach, systematic shifts for both the valence and conduction bands were observed. In the present communication, we extend these ideas to cerium oxide with the aim to estimate a set of *U<sub>eff</sub>* parameters for both the Ce 4*f* and O 2*p* electrons that could improve the GGA+*U* description of the dioxide and sesquioxide.

Periodic DFT+*U* calculations were carried out with the Vienna *ab initio* simulation package (VASP).<sup>31–33</sup> This code solves the Kohn–Sham equations for the valence electron density within a plane wave basis set and makes use of the projector augmented wave (PAW) method to describe the interaction between the valence electrons and the atomic cores.<sup>34,35</sup> The valence electron density is defined by the twelve (*5s<sup>2</sup>5p<sup>6</sup>6s<sup>2</sup>5d<sup>1</sup>4f<sup>1</sup>*) electrons of each Ce atom and the six (*2s<sup>2</sup>2p<sup>4</sup>*) electrons of each O atom. The plane-wave expansion includes all plane waves with kinetic energy smaller than a cut-off value set to 500 eV, which ensures adequate convergence with respect to the basis set.

The GGA functional proposed by Perdew *et al.* (PW91) (Refs. 36 and 37) was selected. The Hubbard-like term was introduced according to the formalism due to Dudarev *et al.*,<sup>38</sup> which makes use of a single *U<sub>eff</sub>* parameter, hereafter denoted simply as *U<sup>f</sup>* and *U<sup>p</sup>*, to design the effective values used for the Ce 4*f* and O 2*p* electrons, respectively. CeO<sub>2</sub> and Ce<sub>2</sub>O<sub>3</sub> were represented by minimal 1 × 1 × 1 cells. For the numerical integration within the Brillouin zone, Monkhorst-Pack generated grids of special *k*-points were used: 12 × 12 × 12 for CeO<sub>2</sub> and 12 × 12 × 6 for Ce<sub>2</sub>O<sub>3</sub>.<sup>39</sup>

We start our analysis by exploring the behavior of the GGA+*U<sup>f</sup>*+*U<sup>p</sup>* approach in the description of the lattice parameters in the CeO<sub>2</sub> fluorite type structure. In a preliminary step, we examined the variations of the lattice constant *a*<sub>0</sub> when the *U* parameters are systematically set to *U<sup>f</sup>* = 3, 4.5, 5, 6 y 7 eV, and *U<sup>p</sup>* = 0, 3, 4, 5, 6, 7, 8, 9 y 12 eV as depicted in Figure 1. In general for a given *U<sup>f</sup>*, increasing *U<sup>p</sup>* leads to smaller values *a*<sub>0</sub>, closer to the experimental value of 5.41 Å. For instance, the set *U<sup>f</sup>* = 5 eV and *U<sup>p</sup>* = 12 eV (hereafter, we will denote this couple of values by just the figures, i.e., in this case: 5+12) leads to *a*<sub>0</sub> = 5.45 Å, better than the (5+0) result of 5.48 Å, but still overestimated. In contrast, for a given *U<sup>p</sup>*, increasing the value of *U<sup>f</sup>* also increases the lattice parameter in agreement with that observed for the case in which *U<sup>p</sup>* = 0.<sup>12</sup> For the sake of comparison, we have gathered in Table I a series of values from this work and other taken from the literature. Any way, the conclusion to be drawn from this systematic analysis is that the inclusion of an additional Hubbard-like on-site parameter on the O 2*p* electrons slightly affects the CeO<sub>2</sub> structure, and only relatively large values of *U<sup>p</sup>* are able to reduce the *a*<sub>0</sub> by a few hundredths of Å.

Let us now analyze the effect of the *U<sup>p</sup>* parameter on the band gaps of CeO<sub>2</sub>, a well-know issue as GGA approaches tend to underestimate the band gaps. In Figure 2, the DOS for CeO<sub>2</sub> is depicted together with the gaps labeling, whose

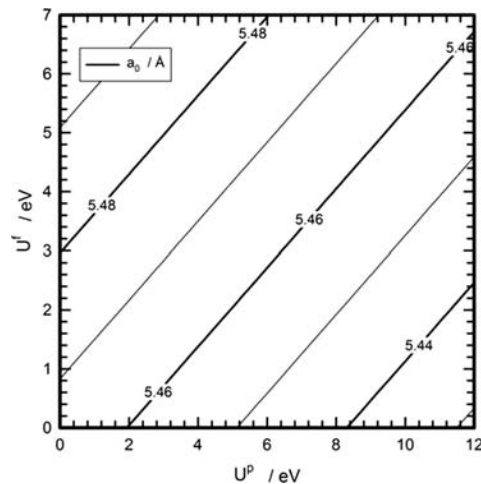


FIG. 1. Dependency of the CeO<sub>2</sub> lattice parameter, *a*<sub>0</sub>, on the *U<sup>f</sup>* and *U<sup>p</sup>* values.

evolution against the *U* values is plotted in Figure 3. Starting with the 2*p*-4*f* gap, one can see that for a given *U<sup>f</sup>*, increasing *U<sup>p</sup>* also increases the gap. For the set (5+5) the gap is 2.3 eV, still below the experimental value that is in the 2.6–3.9 eV range.<sup>40</sup> The behavior observed for the 2*p*-5*d* gap is essentially the same, as it rises when the value of *U<sup>p</sup>* increases. For the couple (5+5) this band gap amounts to 5.4 eV, once again smaller than the experimental value of 6–8 eV.<sup>40,41</sup>

Although the above discussion seems to suggest that the larger the *U<sup>p</sup>* value, the shorter the lattice constant of CeO<sub>2</sub>, the larger the band gaps, and consequently the better the agreement, one can wonder whether such high values are not penalizing the description of other properties that we can look at, namely its formation and reduction energies, as well as the cell parameters of Ce<sub>2</sub>O<sub>3</sub>. To this aim, we have first

TABLE I. Calculated and experimental lattice parameters (in Å) for CeO<sub>2</sub> and Ce<sub>2</sub>O<sub>3</sub>.

GGA+( <i>U<sup>f</sup></i> + <i>U<sup>p</sup></i> )	Ce <sub>2</sub> O <sub>3</sub>		References		
	CeO <sub>2</sub> <i>a</i> <sub>0</sub>	<i>a</i> <sub>0</sub>		<i>c</i> <sub>0</sub>	
(3+0)	5.48	3.92	6.08	This work	
(5+0)	5.49	3.93	6.08		
(3+5)	5.46	3.91	6.08		
(5+5)	5.47	3.90	6.05		
(5+6)	5.47	3.90	6.06		
(5+12)	5.45	3.88	6.01		
(7+7)	5.48	3.91	6.04		
(4.5+0)	5.48	3.92	6.08		[12]
PBE(4.5+0)		3.87	5.93		[14]
HSE	5.41	3.87	6.06		[13]
PBE0	5.39	3.87	6.07		[13]
	5.40	3.86	6.04		[18]
B1-WC	5.38	3.84	5.93		[18]
Experiment	5.41	3.89	6.06		[23 and 24]

041101-3 CeO<sub>2</sub>: Including a  $U$  term for O 2p electrons

J. Chem. Phys. **136**, 041101 (2012)

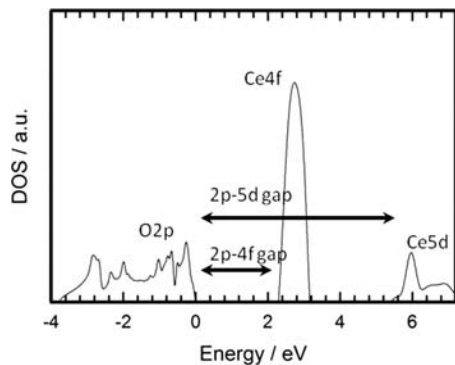


FIG. 2. Total density of states (DOS) for CeO<sub>2</sub> with the definition of the band gaps. Obtained with the (5+5) set.

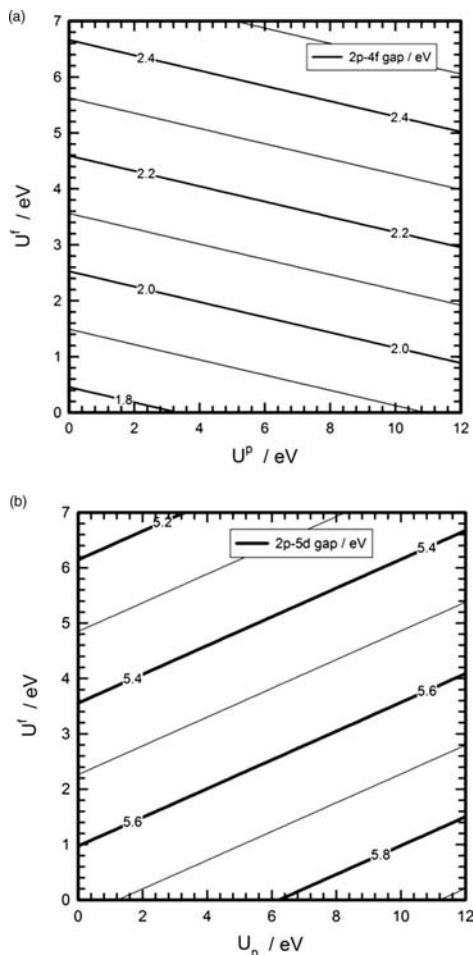


FIG. 3. Dependency of the CeO<sub>2</sub> band gaps on the  $U^f$  and  $U^p$  values.

TABLE II. Energy (eV) of CeO<sub>2</sub> formation and its reduction: CeO<sub>2</sub> → Ce<sub>2</sub>O<sub>3</sub> + 1/2 O<sub>2</sub>.

Method	$-E_{\text{form}}$	$E_{\text{red}}$	References
(5+0)	9.79	4.83	This work
(3+5)	10.09	3.03	
5+5	9.04	4.01	[13]
5+6	8.88	3.94	
5+12	7.84	3.46	[13 and 18]
PBE+U		2.29	
PBE0	11.15	3.14–3.66	[42]
Experiment	10.44	3.99	

estimated these energies for a series of  $U^f$  and  $U^p$  figures as reported in Table II. As can be seen, compared to the experimental formation energy of  $-10.44$  eV,<sup>42</sup> the theoretical estimates agree reasonably well, although they are quite sensitive to the  $U$  parameters. At first glance, the (3+5) set would be the choice, however, taking in to account the reduction energies, the (5+5) and (5+6) pairs seem to be more adequate. It is worth to note that in contrast with the behavior observed with gaps and lattice parameters, increasing  $U^p$  beyond 5–6 eV decreases these energies, the description getting worse. We can now analyze how the variation of  $U$  parameters affects the lattice constants of the sesquioxide Ce<sub>2</sub>O<sub>3</sub>. The trends observed are similar to those found in CeO<sub>2</sub>, thus for a given  $U^p$  (for instance  $U^p = 0$ ) increasing values of  $U^f$  lead to larger  $a_0$ , with  $c_0$  practically unchanged. In contrast, for a given  $U^f$ , increasing  $U^p$  decreases  $a_0$ . For instance, going from (3+0) to (3+5) decrease  $a_0$  from 3.92 to 3.91 Å. Also, on going from (5+5) to (5+12)  $a_0$  decreases from 3.90 to 3.88 Å, and  $c_0$  from 6.05 to 6.01 Å. Compared to the experimental values 3.89 and 6.06 Å, it appears that the couples (5+5) and (5+6) perform reasonably well.

A further question that might be examined concerns the oxygen vacancy formation energy, an issue that has deserved considerable theoretical work,<sup>43</sup> and that, besides the theoretical approach itself, needs to deal with the defect concentration. To this aim, we used a larger cell consisting of 32 CeO<sub>2</sub> units, and in this case the Brillouin zone was integrated over a  $2 \times 2 \times 2$  grid of special k-points. Using the (5+5) couple, the calculations were done in two steps: in the first one, the four Ce atoms around the vacancy were kept to be symmetrically equivalent obtaining a vacancy formation energy of 3.05 eV. This delocalized structure was then allowed to relax leading to a more stable configuration in which two Ce atoms neighboring the hole were bearing one 4f electron each. This localized structure was found to be more stable, the vacancy formation energy being 2.64 eV, significantly lower than that estimated by Nolan *et al.*,<sup>44</sup> 3.39 eV, using the same functional (PW91) and also the same supercell (Ce<sub>32</sub>O<sub>64</sub>), with a  $U^f$  of 5 eV. It appears then that the use of the  $U^p$  parameter in this case decreases this energy by a 20%. Our value is also close to that recently reported by Kehoe *et al.*,<sup>45</sup> 2.23 eV, using a very similar theoretical setup. It should be noted that them all are underestimated when compared with experimentally determined formation energies (3.94–4.98 eV)<sup>46</sup> as previously reported.<sup>47</sup> On the other hand, the spin electron density for

Section 3.3. Improving DFT+U description of CeO<sub>2</sub>

041101-4 Plata, Marquez, and Sanz

J. Chem. Phys. **136**, 041101 (2012)

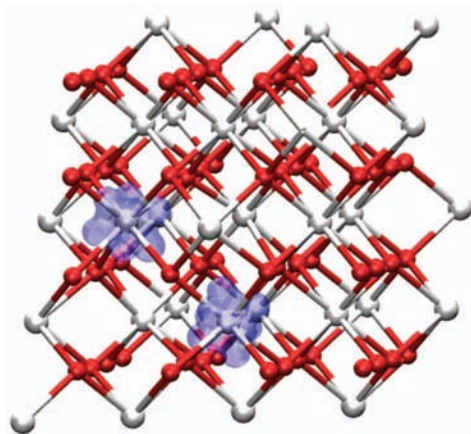


FIG. 4. Electron spin density of bulk CeO<sub>2</sub> after removing an oxygen atom showing the formation of two Ce<sup>III</sup> centers localized around the vacancy.

this localized structure is shown in Figure 4. The structure around the hole appears to be slightly distorted, with Ce<sup>III</sup>-O bond distances of 2.42 Å, i.e., larger than the non-defective bond distance (2.36 Å).

In summary, the present work shows that, within the DFT+U formalism, adding a Hubbard-like parameter not only to the cerium 4*f* electrons but also to the oxygen 2*p* electrons leads to a moderately improved description of some critical aspects that concern structure, electronic properties, and thermochemistry of both CeO<sub>2</sub> and Ce<sub>2</sub>O<sub>3</sub>.

This work has been supported by the Spanish Ministry of Science and Innovation, MICINN (Grants MAT2008-04918 and CSD2008-0023). Computational time on the Barcelona Supercomputing Center/Centro Nacional de Supercomputación is gratefully acknowledged. We thank Dr. M. Nolan for helpful discussions.

<sup>1</sup>A. Trovarelli, *Catalysis by Ceria and Related Materials* (Imperial College Press, London, UK, 2002).  
<sup>2</sup>R. Dicter and S. Roberts, *J. Phys. Chem.* **93**, 5846 (1989).  
<sup>3</sup>E. C. Su and W. G. Rothschild, *J. Catal.* **99**, 506 (1986).  
<sup>4</sup>H. C. Yao and Y. F. Yu Yao, *J. Catal.* **86**, 254 (1984).  
<sup>5</sup>B. Engler, E. Koberstein, and P. Schubert, *Appl. Catal.* **48**, 71 (1989).  
<sup>6</sup>T. Miki, T. Ogawa, M. Haneda, N. Kakuta, A. Ueno, S. Tateishi, S. Matsuura, and M. Sato, *J. Phys. Chem.* **94**, 6464 (1990).  
<sup>7</sup>A. Trovarelli, C. de Leitenburg, M. Boaro, and G. Dolcetti, *Catal. Today* **50**, 353 (1999).  
<sup>8</sup>A. Prokofiev, A. Shelykh, and B. Melekh, *J. Alloys Compd.* **242**, 41 (1996).  
<sup>9</sup>Z. Yang, T. K. Woo, M. Baudin, and K. Hermansson, *J. Chem. Phys.* **120**, 7741 (2004).  
<sup>10</sup>M. Nolan, S. Grigoleit, D. C. Sayle, S. C. Parker, and G. W. Watson, *Surf. Sci.* **576**, 217 (2005).

<sup>11</sup>D. A. Andersson, S. I. Simak, B. Johansson, I. A. Abrikosov, and N. V. Skorodumova, *Phys. Rev. B* **75**, 035109 (2007).  
<sup>12</sup>C. Loschen, J. Carrasco, K. Neyman, and F. Illas, *Phys. Rev. B* **75**, 035115 (2007); *Phys. Rev. B* **84**, 199906(E) (2011).  
<sup>13</sup>J. L. F. Da Silva, M. V. Ganduglia-Pirovano, J. Sauer, V. Bayer, and G. Kresse, *Phys. Rev. B* **75**, 045121 (2007).  
<sup>14</sup>J. L. F. Da Silva, *Phys. Rev. B* **76**, 193108 (2007).  
<sup>15</sup>C. W. M. Castleton, J. Kullgren, and K. J. Hermansson, *J. Chem. Phys.* **127**, 244704 (2007).  
<sup>16</sup>G. Kresse, P. Blaha, J. L. F. Da Silva, and M. V. Ganduglia-Pirovano, *Phys. Rev. B* **72**, 237101 (2005).  
<sup>17</sup>P. J. Hay, R. L. Martin, J. Uddin, and G. E. Scuseria, *J. Chem. Phys.* **125**, 034712 (2006).  
<sup>18</sup>J. Graciani, A. M. Márquez, J. J. Plata, Y. Ortega, N. C. Hernández, C. Zicovich-Wilson, M. Alessio, and J. F. Sanz, *J. Chem. Theory Comput.* **7**, 56 (2011).  
<sup>19</sup>S. Fabris, S. de Gironcoli, S. Baroni, G. Vicario, and G. Balducci, *Phys. Rev. B* **72**, 237102 (2005).  
<sup>20</sup>M. Cococcioni and S. de Gironcoli, *Phys. Rev. B* **71**, 035105 (2005).  
<sup>21</sup>H. J. Kulik, M. Cococcioni, D. A. Scherlis, and N. Marzari, *Phys. Rev. Lett.* **97**, 103001 (2006).  
<sup>22</sup>H. Hsu, K. Umamoto, M. Cococcioni, and R. Wentzcovitch, *Phys. Rev. B* **79**, 125124 (2009).  
<sup>23</sup>S. J. Duclos, Y. K. Vohra, A. L. Ruoff, A. Jayaraman, and G. P. Espinosa, *Phys. Rev. B* **38**, 7755 (1988).  
<sup>24</sup>L. Gerward and J. S. Olsen, *Powder Diffr.* **8**, 127 (1993).  
<sup>25</sup>M. M. Branda, N. C. Hernández, J. F. Sanz, and F. Illas, *J. Phys. Chem. C* **114**, 1934 (2010).  
<sup>26</sup>N. C. Hernández, R. Grau-Crespo, N. H. de Leeuw, and J. F. Sanz, *Phys. Chem. Chem. Phys.* **11**, 5246 (2009).  
<sup>27</sup>M. M. Branda, N. J. Castellani, R. Grau-Crespo, N. H. de Leeuw, N. C. Hernández, J. F. Sanz, K. M. Neyman, and F. Illas, *J. Chem. Phys.* **131**, 94702 (2009).  
<sup>28</sup>V. L. Campo, Jr. and M. Cococcioni, *J. Phys.: Condens. Matter* **22**, 055602 (2010).  
<sup>29</sup>S. G. Park, B. Magyar-Köpe, and Y. Nishi, *Phys. Rev. B* **82**, 115109 (2010).  
<sup>30</sup>I. A. Nekrasov, M. A. Korotin, and V. I. Anisimov, e-print arXiv:cond-mat/0009107v1.  
<sup>31</sup>G. Kresse and J. Hafner, *Phys. Rev. B* **47**, 558 (1993).  
<sup>32</sup>G. Kresse and J. Hafner, *Phys. Rev. B* **48**, 13115 (1993).  
<sup>33</sup>G. Kresse and J. Hafner, *Phys. Rev. B* **49**, 14251 (1994).  
<sup>34</sup>P. Blochl, *Phys. Rev. B* **50**, 17953 (1994).  
<sup>35</sup>G. Kresse and D. Joubert, *Phys. Rev. B* **59**, 1758 (1999).  
<sup>36</sup>J. P. Perdew, J. A. Chevary, S. H. Vosko, K. A. Jackson, M. R. Pederson, D. J. Singh, and C. Fiolhais, *Phys. Rev. B* **46**, 6671 (1992).  
<sup>37</sup>J. P. Perdew, J. A. Chevary, S. H. Vosko, K. A. Jackson, M. R. Pederson, D. J. Singh, and C. Fiolhais, *Phys. Rev. B* **48**, 4978 (1993).  
<sup>38</sup>S. L. Dudarev, G. A. Botton, S. Y. Savrasov, C. J. Humphreys, and A. P. Sutton, *Phys. Rev. B* **57**, 1505 (1998).  
<sup>39</sup>H. J. Monkhorst and J. D. Pack, *Phys. Rev. B* **13**, 5188 (1976).  
<sup>40</sup>E. Wuilloud, B. Delley, W. D. Schneider, and Y. Baer, *Phys. Rev. Lett.* **53**, 202 (1984).  
<sup>41</sup>F. Marabelli and P. Wachter, *Phys. Rev. B* **36**, 1238 (1987).  
<sup>42</sup>*CRC Handbook of Chemistry and Physics*, 9th ed., edited by D. R. Lide (CRC Press, Boca Raton, Florida, USA, 2009).  
<sup>43</sup>M. V. Ganduglia-Pirovano, A. Hofmann, and J. Sauer, *Surf. Sci. Rep.* **62**, 219–270 (2007).  
<sup>44</sup>M. Nolan, J. E. Fearon, and G. W. Watson, *Solid State Ion.* **177**, 3069 (2006).  
<sup>45</sup>A. B. Kehoe, D. O. Scanlon, and G. W. Watson, *Chem. Mater.* **23**, 4464 (2011).  
<sup>46</sup>Y. M. Chiang, E. B. Lavik and D. A. Blom, *Nanostruct. Mater.* **9**, 633 (1997).  
<sup>47</sup>M. Nolan, S. Parker, and G. W. Watson, *Surf. Sci.* **595**, 223 (2005).

### 3.4 GW approximation

Despite this computational effort, it is difficult to conclude which functional or  $U^f$  and  $U^p$  parameters are the best choice in order to describe the electronic structure of ceria. This is related to the wide range of values for the experimental band gap. Many-body perturbation theory (MBPT) in the GW approach can be considered as a first step towards a systematic ab initio understanding of the electronic structure of ceria. It has been reported that the GW approach is able to predict transition metal oxides band gaps within an error below 0.5 eV in most of these compounds.<sup>15</sup> Thus, these results can be used as a reference to elucidate which of the previous approaches is the most appropriate for the theoretical study of big ceria systems.

The GW approach corresponds to the first order term of a systematic expansion in MBPT<sup>16</sup> and has become the method of choice for the description of quasiparticle band structures in weakly correlated solids.<sup>17</sup> The screened Coulomb interaction  $W$  captures the screening among itinerant electrons while at the same time treats exchange at the exact exchange level. The GW method is typically applied in a perturbative manner (denoted as  $G_0W_0$ ) in which the quasiparticle (QP) energies  $\epsilon_{nk}^{QP}$  are calculated as a first-order correction to the eigenenergies  $\epsilon_{nk}$  and eigenvectors  $\psi_{nk}$  of a reference single particle Hamiltonian  $\hat{H}_0$ .<sup>17</sup> We have used the HSE method as starting point for  $G_0W_0$  which can be denoted as  $G_0W_0@HSE$ .

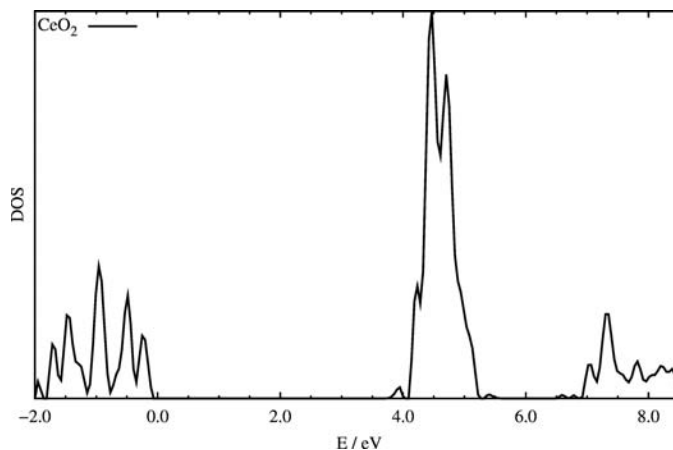


Figure 3.1: Total density of states (DOS) for CeO<sub>2</sub> using  $G_0W_0@HSE$  approach

The density of states of bulk ceria using  $G_0W_0@HSE$  is depicted in figure 3.1. The  $2p-5d$  gap is around 6.46 eV while the  $2p-4f$  gap is 3.78 eV. These values are close to

previous results published by Scheffler *et al.* using a  $G_0W_0@PBE+U$  approach.<sup>18</sup> They obtained 4.5 and 6.0 eV for  $2p-4f$  and  $2p-5d$  gap respectively without any dependence on the  $U$  value. Both data are quite close to the experimental results obtained by Wuilloud *et al.*<sup>19</sup>

### 3.5 Conclusions

Different methods have been used in this chapter to reproduce structural and electronic properties of ceria and related materials. Hybrid functionals reduce the problem of the self-interaction error, however the amount of exact exchange and the functional have to be chosen carefully. While all hybrid functionals can describe accurately the crystal structure of  $CeO_2$  and  $Ce_2O_3$  oxides, high deviations were found for the band gaps. A big amount of exact HF exchange produces an overestimation of the band gap, so the agreement with the experimental gap is obtained for these functionals with a lower amount of HF exchange. Because of the wide range of values that we can find in experimental results, we have calculated the electronic structure of ceria using a  $G_0W_0@PBE+U$  approach. These results are quite similar to the values that were obtained using HSE and B1-WC functionals. The energetics associated to ceria reduction process was also evaluated being the B1-WC once again, the most well-behaved functional to reproduce the correct energetics.

Hybrid functionals describe correctly  $CeO_2$  and reduced ceria, however, this approach is quite expensive to study big systems using planewaves. Here, we have proposed a new DFT+ $U$  approach in which a  $U$  parameter for the  $2p$  oxygen states is also used. The combination of  $U_f$  and  $U_p$  leads to a moderately improved description of the lattice parameters, band gap and reaction energies and partially corrects the self-interaction error. We have found that the best combination of both parameters is  $U_f = 5$  and  $U_p = 5$  quite close to the combination proposed recently by Keating *et al.*<sup>20</sup>

### References

1. Perdew, J. P.; Zunger, A., *Phys. Rev. B* **1981**, *23*, 5048.
2. Mori-Sánchez, P.; Cohen, A. J.; Yang, W., *Phys. Rev. Lett.* **2008**, *100*, 146401.
3. Seidl, A.; Gorling, A.; Volg, P.; Majewki, J. A.; Levy, M., *Phys. Rev. B* **1996**, *53*, 3764.
4. Zhao, Y.; Truhlar, D. G., *J. Chem. Phys. A* **2005**, *109*, 5656.
5. Ganduglia-Pirovano, M. V.; Sauer, A.; Sauer, J., *Surf. Sci. Rep.* **2007**, *62*, 219.
6. Anisimov, V. I.; Zaanen, J.; Andersen, O. K., *Phys. Rev. B* **1991**, *44*, 943.
7. Becke, A. D., *J. Chem. Phys.* **1993**, *98*, 5648.

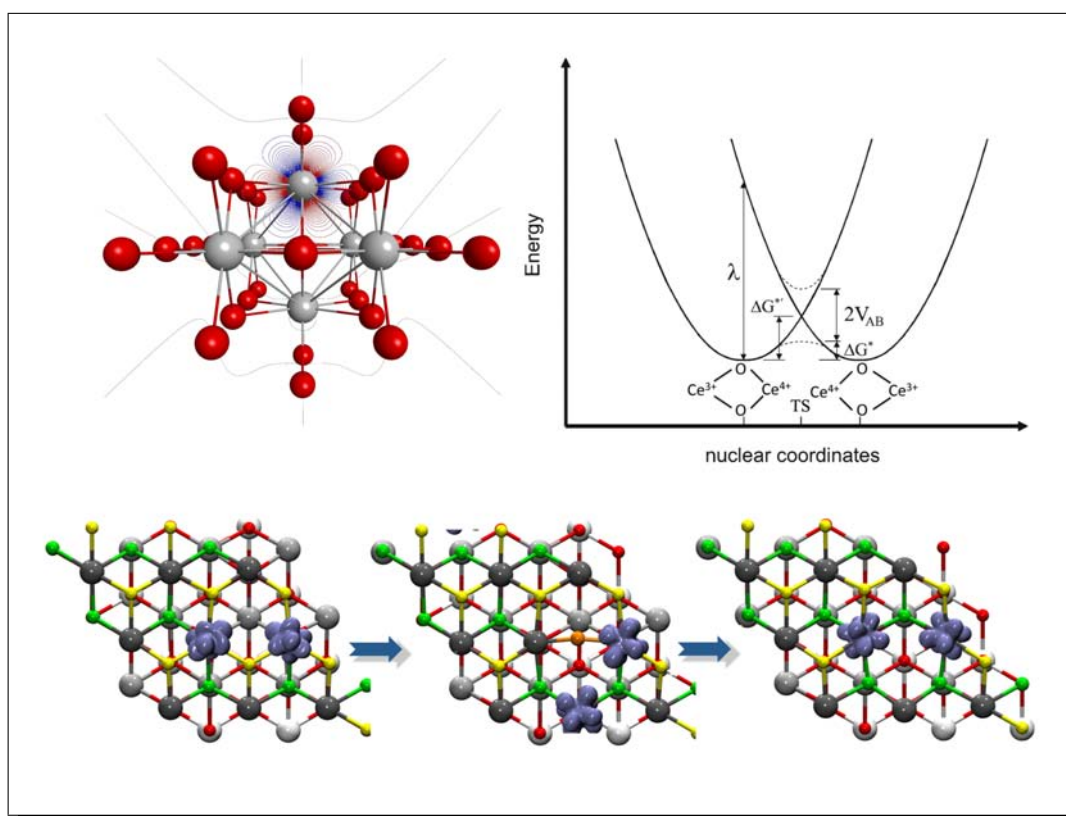
8. Wu, Z.; Cohen, R. E., *Phys.Rev. B* **2006**, *73*, 235116.
9. Svendsen, P. S.; Barth, U. V., *Phys.Rev. B* **1996**, *54*, 17402.
10. Zhao, Y.; Truhlar, D. G., *Phys. Rev. B* **2008**, *78*, 197101.
11. Wu, Z.; Cohen, R. E., *Phys.Rev. B* **2008**, *78*, 197102.
12. Tran, F.; Laskowski, R.; Blaha, P.; Schwarz, K., *Phys. Rev. B* **2007**, *75*, 115131.
13. Bilc, D. I.; Orlando, R.; Shaltaf, R.; Rignanese, G.; niguez, J. I.; Ghosez, P., *Phys. Rev. B* **2008**, *77*, 165107.
14. Branda, M. M.; Castellani, N. J.; Grau-Crespo, R.; de Leeuw, N. H.; Hernandez, N. C.; Sanz, J. F.; Neyman, K. M.; Illas, F., *J. Chem. Phys.* **2009**, *131*, 094702.
15. Schilfgaarde, M. V.; Kotani, T.; Faleev, S., *Phys. Rev. Lett.* **2006**, *96*, 226402.
16. Heidin, L., *Phys. Rev.* **1965**, *139*, A796.
17. Aryasetiawan, F.; Gunnarsson, O., *Rep. Prog. Phys.* **1998**, *61*, 237.
18. Jiang, H.; Gomez-Abal, R. I.; Rinke, P.; Scheffler, M., *Phys. Rev. Lett* **2009**, *102*, 126403.
19. Wuilloud, E.; Delley, B.; Schneider, W. D.; Baer, Y., *Phys. Rev. Lett* **1984**, *53*, 202.
20. Keating, P. R.; Scanlon, D. O.; Morgan, B. J.; Galea, N. M.; Watson, G. W., *J. Phys. Chem. C* **2012**, *116*, 2443.

---

CHAPTER  
**FOUR**

---

Ceria as ionic and electronic conductor



## 4.1 Introduction

In the previous chapter, different methodological approaches were used in order to describe the crystal and electronic structure of ceria. However, the technological applications of ceria are related to the ability of this material to act as an oxygen storage material and the easy  $\text{Ce}^{3+}/\text{Ce}^{4+}$  equilibrium. The oxygen dynamics at ceria surface is closely related to the electronic properties of this material.

In this regard, the ion diffusion processes play a key role on the use of  $\text{CeO}_2$  as an oxygen storage material and is the basis for its use as solid electrolyte or anode in SOFC.<sup>1-3</sup> Oxygen vacancy formation in ceria results in the partial reduction of the material as the two electrons left by the removal of the neutral O atom reduce two  $\text{Ce}^{4+}$  to  $\text{Ce}^{3+}$ . These two electrons located in  $\text{Ce}^{3+}$  cations are responsible for the electronic conductivity of this solid. Both, electronic and ionic conductivity are important for the correct fuel cell operation. The electrolyte in solid oxide fuel cells serves as a medium through which ions diffuse reach the anode surface. Here, they electrochemically oxidize the fuel and produce two electrons that, after doing some work in an external circuit reach the cathode where they reduce molecular oxygen into oxygen anions that enter into the solid electrode again.

In catalysis and photocatalysis the  $\text{Ce}^{3+}$ - $\text{Ce}^{4+}$  redox conversion, the formation of oxygen vacancies at the ceria surface and their interplay with electron transfer processes are also important factors that influence the efficiency of many applications.<sup>4-8</sup>

For these reasons this chapter will be dedicated to electron transfer process and oxygen migration in ceria materials. Initially *ab initio* quantum theory methods will be employed to understand the nature of the electron transfer process between adjacent  $\text{Ce}^{3+}$  and  $\text{Ce}^{4+}$  centers in bulk ceria. The electron transfer process will be examined within the two-state Marcus model in order to calculate the most important parameters that characterize this process. Later on the principal characteristics of ionic conductivity will be analyzed on ceria (111) surface. Recent studies have demonstrated that the concentration of vacancies is higher at the surface than in the bulk. Thus, the understanding of oxygen migration at the surface is highly important to rationalize the ionic conductivity process. Finally, ion and electron conduction sometimes cannot be analysed separately because coupling effects between motion of cations and electrons have been reported in some transition metal oxides.<sup>9-13</sup> In last years, experimental results<sup>14,15</sup> have suggested that ceria and doped-ceria material are in this group of oxides. Thus we will end this chapter by examining the coupling between these two processes in the ceria (111) surface.



## 4.2 Electron Mobility via Polaron Hopping in Bulk Ceria: A First-Principles Study

José J. Plata, Antonio Márquez, and Javier Fdez. Sanz

Published in *J. Phys. Chem. C*, **2013**

DOI:10.1021/jp402594x

**Abstract:** The outstanding catalytic properties of cerium oxides, and, consequently, the broad use in heterogeneous catalysis rely on the easy  $\text{Ce}^{3+} \leftrightarrow \text{Ce}^{4+}$  redox conversion. Within the two-state model of Marcus, the electron transfer associated to the redox process is governed by the electronic coupling matrix element  $V_{AB}$  that accounts for the interaction between the diabatic electronic states at the crossing seam. Here we present a computational analysis based on ab initio quantum mechanics theory that allows for a characterization of negative polaron structures and intrinsic polaron hopping in perfect bulk  $\text{CeO}_2$ . The relevant parameters inherent to the model: reorganization energy, activation barrier and electronic coupling for the  $4f \rightarrow 4f$  electron hopping are estimated for several models. Our analysis predicts an activation barrier of 0.4 eV and a transmission coefficient  $\kappa = 0.81$  confirming the earlier proposed adiabatic theory of small polaron and hopping conductivity in reduced bulk ceria.

### Introduction

Cerium oxide is one of the most used materials in catalysis both as support and active phases. Typical examples of industrial applications are the three-way catalysts in automotive catalytic converters, fluid-cracking catalysts in refineries, and ethylbenzene dehydrogenation in the production of styrene.<sup>16</sup> Either  $\text{CeO}_2$  or non-stoichiometric  $\text{CeO}_{2-x}$ , hereafter generically referred to as ceria, are also an active component in a number of processes such as low-temperature CO and VOC oxidation catalysts,<sup>17</sup> wet-oxidation of organic pollutants,<sup>18</sup> hydrocarbon reforming,<sup>19</sup> and the water-gas-shift reaction.<sup>20</sup> Although the promoting effect of ceria was initially attributed to the enhancement of the metal dispersion and the stabilization towards thermal sintering,<sup>21,22</sup> subsequent work has shown that ceria can act as a chemically active component as well, working as an oxygen reservoir able to deliver it in the presence of reductive gases and to incorporate it upon interaction with oxidizing gases.<sup>23–25</sup>

The outstanding catalytic properties of ceria rely on its ability to undergo rapid and repeatable  $\text{Ce}^{3+} \leftrightarrow \text{Ce}^{4+}$  redox cycles depending on the conditions in the reactor stream. Stoichiometric  $\text{CeO}_2$  is an insulator and its electronic structure might be described as a formally fully occupied O  $2p$  band and empty  $4f$  and  $5d$  states, with an experimental band gap of 6–8 eV between the O  $2p$  and Ce  $5d$  states,<sup>26,27</sup> although there is agreement with the

facts that the valence band contains a non-negligible admixture of  $f$ -symmetry orbitals.<sup>28</sup> When  $\text{CeO}_2$  is reduced (metal doping, for instance) or exposed to reducing conditions ( $\text{O}_2$  deficient atmosphere and high temperature), the in gap  $4f$  states are occupied, leading to states strongly localized at Ce sites. In the limit, the configuration of the sesquioxide  $\text{Ce}_2\text{O}_3$ , described as a Mott insulator, is reached. Therefore, we might conceive that partially reduced cerium oxide phases consist of a distribution of  $\text{Ce}^{3+}$  and  $\text{Ce}^{4+}$  centers that may easily interconvert,<sup>29</sup> which, actually, involves oxidation and reduction of the Ce  $4f$  levels. On the other hand, the capability to store and mobilize oxygen within the ceria matrix should also be related with this interconversion between  $\text{Ce}^{3+}$  and  $\text{Ce}^{4+}$  centers, which, in fact, involves electron transport through the material.

The electronic conduction in cerium oxide has been attributed to the formation of small-polarons that diffuse according to a hopping mechanism. From electrical conductivity measurements performed by Naik and Tien,<sup>30</sup> it was reported that in nonstoichiometric ceria the electrons are localized and the high temperature electrical conduction occurs by a hopping mechanism in which electrons jump from a  $\text{Ce}^{3+}$  ion to a neighboring  $\text{Ce}^{4+}$  ion. The small-polaron model developed by Holstein and Friedman<sup>31,32</sup> satisfactorily explains the observed temperature dependence of the high temperature drift mobility. A similar conclusion was drawn from the work of Tuller and Nowick,<sup>33</sup> that showed ceria to be perhaps the clearest case of small polaron hopping conductivity. The mobility in  $\text{CeO}_{2-x}$  was found to be activated, with activation energy  $E_a = 0.40$  eV at small  $x$  and increasing to 0.52 eV at  $x = 0.25$ . Moreover, the so-called hopping integral,  $t$ , a key quantity in the analysis of the electron mobility of a system, has been investigated. However, depending of the methods to compute this value, a large discrepancy has been reported.<sup>34</sup>

From a theoretical point of view the study of electron transfer hopping in ceria has been hampered by the intrinsic difficulty in the explicit treatment of  $4f$  electrons in a solid-state context. Here we must recall that the Ce  $4f$  electrons in reduced ceria are localized, and that to render this situation in a density functional theory approach needs to incorporate either the exchange, via a hybrid xc-functional, or an explicit Hubbard type term (DFT+U). In fact, and as far as we know, ab initio computations of the electron transfer integral in an  $f$ - $f$  system have never been reported. This is contrast with the  $d$ - $d$  systems, some of which have been analyzed by Dupuis and coworkers.<sup>35-38</sup> Notice on the other hand, that the  $\text{Ce}^{\text{III}}(4f^1)$ - $\text{Ce}^{\text{IV}}(4f^0)$  electron hopping is the simplest case among the possible  $f$ - $f$  systems.

In this paper, we report a first-principles study of the electron mobility parameters in perfect bulk cerium oxide as a first step to obtain an inclusive theoretical characterization of charge transport in ceria. Our aim is to present a computational description of the structure of negative polaron arrangements and polaron hopping in perfect  $\text{CeO}_2$ . According to the theoretical model described below, several quantities are needed for such a characterization. For instance, choosing the Marcus terminology<sup>39,40</sup> we must provide an estimate for the

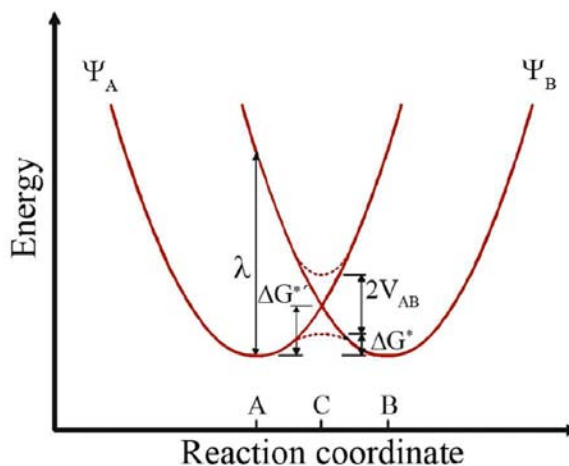


Figure 4.1: General description of the main features of the Marcus model for a symmetric electron transfer.  $\Psi_A$  and  $\Psi_B$  stands for the diabatic wavefunctions. The adiabatic activation barrier is denoted by  $\Delta G^*$ , estimated by subtracting to the diabatic barrier  $\Delta G^{*}$  the electronic coupling matrix element, defined as half the energy splitting at the intersection point.

electronic coupling,  $V_{AB}$ , the adiabatic barrier,  $\Delta G^*$ , and the reorganization energy  $\lambda$  (see Figure 4.1). Because one of our concerns refers to the suitability and reliability of our approach for the present system, we use a variety of computational techniques making use of both embedded cluster and periodic approaches. The paper is arranged as follows. First we summarize the theoretical foundations that are rooted in the Marcus two-state model for electron transfer, or in its equivalent description of polaron movement in solids as formulated by Emin and Holstein<sup>41,42</sup> and Austin and Mott,<sup>43</sup> (EHAM). In Section 3 the computational methods and models are described. Section 4 reports the results and discussion, and finally, the conclusions are outlined in Section 5.

### Theoretical framework

As noted by Deskins and Dupuis,<sup>38</sup> there is a parallelism between the EHAM theory and the two-state Marcus model that we briefly review here. The electron transfer (ET) process between adjacent cerium cations in oxidation states +3 and +4 is schematically represented in Figure 4.2. At the top of this figure the negative polaron is localized on the left, corresponding to a local electronic configuration of  $\text{Ce}^{III}(4f^1)\text{-Ce}^{IV}(4f^0)$ , and

conforming a nuclear arrangement labeled as  $q_A$ . At the bottom, the polaron is on the right,  $\text{Ce}^{IV}(4f^0)\text{-Ce}^{III}(4f^1)$ , and the nuclear arrangement is denoted as  $q_B$ . The structure at the middle,  $q_C$ , corresponds to the transition state, where the electron charge is shared by the two cations. Because of the lower positive charge of  $\text{Ce}^{III}$  centers, the interatomic distance  $\text{Ce}^{III}\text{-O}$  is expected to be larger than in the case of  $\text{Ce}^{IV}\text{-O}$ , therefore, passing from A to B involves an antisymmetric breathing vibration mode. The idealized energy profiles for the process following a generic reaction coordinate are represented in Figure 4.1. The two curves are assumed to be parabolic with minima at  $q_A$  and  $q_B$ , while the transition state is at  $q_C$ , that corresponds to the crossing point between the two localized wavefunctions  $\Psi_A$  and  $\Psi_B$ . The other highlighted parameter in Figure 4.1 is the reorganization energy  $\lambda$  that corresponds to the energy of the final state  $\Psi_B$  at the geometric configuration  $q_A$ .

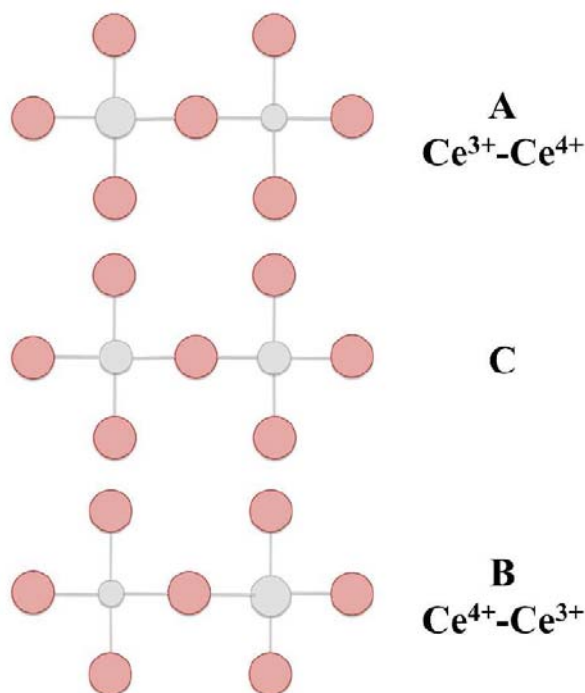


Figure 4.2: Schematic description of the electron transfer between two Ce ions. At the top,  $q_A$ , the electron is occupying a  $4f$  orbital localized on the left Ce ion. At the bottom,  $q_B$ , the electron is localized on the right Ce ion. At the transition state  $q_C$ , the electron is shared between the two cations.

The adiabatic or non-adiabatic nature of the ET process relies on the relative value of the time it takes the electron to jump between two adjacent centers,  $t_{el}$ , which in turn is related to the electron transfer integral,  $J$ , or electronic coupling  $V_{AB}$ . Briefly, in the adiabatic process the electron coupling is strong,  $V_{AB}$  is large, and the activation barrier lowers by this amount, in which case the main mechanism occurs via thermal hopping. If the electron transfer integral is small, the process is non-adiabatic and the ET mainly takes place by tunneling. In summary, whatever the process is, adiabatic or non-adiabatic, the electronic coupling element  $V_{AB}$  plays the crucial role.

Within the Marcus theory the electronic coupling matrix element  $V_{AB}$  is defined as half the energy difference between the two adiabatic states at the crossing seam,  $2 V_{AB} = E^- - E^+$ , where  $E^-$  and  $E^+$  are the energies of upper and lower states respectively. However, to estimate this quantity one may follow different strategies depending on the actual states used for this purpose. We can choose the localized states  $\Psi_A$  and  $\Psi_B$ , and the formula:

$$V_{AB} = \frac{|H_{AB} - S_{AB}(H_{AA} + H_{BB})/2|}{1 - S_{AB}^2} \quad (4.1)$$

where  $H_{AA} = \langle \Psi_A | H | \Psi_A \rangle$ ,  $H_{AB} = \langle \Psi_A | H | \Psi_B \rangle, \dots$  are the matrix elements of the full Hamiltonian on the basis of diabatic states, and  $S_{AA} = \langle \Psi_A | \Psi_A \rangle$ ,  $S_{AB} = \langle \Psi_A | \Psi_B \rangle, \dots$  the overlap elements. In the present work we used this strategy using the technique reported by Farazdel *et al.*<sup>44</sup> Also using orthogonalized diabatized states one can compute directly the off diagonal term of the  $2 \times 2$  Hamiltonian representation  $H_{AB}$ , to several orders of perturbation which renders more accurate estimates of the transfer integral.<sup>45,46</sup> On the other hand, one can formally compute the adiabatic energies  $E^+$  and  $E^-$  although now the difficulty relies on the calculation of the ground and first excited state to the same degree of accuracy. This latter point is of outstanding importance because the electronic coupling elements  $V_{AB}$  use to be small quantities, many times of the order of a few hundreds wavenumbers, and therefore reliable estimates are needed. We will see in the next section how the symmetry of the system can be exploited to achieve such a calculation.

### Models and Computational Methods

The present work makes use of both periodic and embedded cluster calculations to explore the different properties of the system. Firstly periodic calculations were performed to analyze the local structure of the negative polaron that results when a cerium atom in perfect  $\text{CeO}_2$  is populated with an extra electron. Also using a periodic model, we estimated the energy barrier of the electron hopping process. These calculations were undertaken using the CRYSTAL09 code<sup>47</sup> and CGTOs basis sets. The  $\text{CeO}_2$  fluorite crystal ( $\text{Fm}\bar{3}\text{m}$ ) was represent by a  $2 \times 2 \times 2$  supercell containing 96 atoms. Inner electrons of Ce atom were replaced by an effective core potential developed by the Stuttgart-Dresden

group.<sup>48</sup> The Ce electrons explicitly treated were the  $4s^2 4p^6 4d^{10} 5s^2 5p^6 4f^1 6s^2 5d^1$ , with a  $(10sp7d8f)/[4sp2d3f]$  basis set optimized to properly describe oxides where the metal features III and IV oxidation states.<sup>49</sup> For O an all-electron  $(8s6sp1d)/[1s3sp1d]$  basis set proposed for ionic crystals was adopted.<sup>50</sup> The two most external sp and d exponents have been re-optimized for cerium oxide, their resulting values being 0.4798717, 0.1801227 and 0.2991812 bohr<sup>-2</sup>, respectively.<sup>51,52</sup>

Spin-polarized density functional, DFT, calculations were performed using the Perdew-Burke-Ernzerhof PBE0 functional,<sup>53</sup> that has been shown to perform adequately when both Ce<sup>III</sup> and Ce<sup>IV</sup> ions are present.<sup>51</sup> This hybrid functional is a combination of the GGA exchange-correlation functional PBE<sup>54</sup> and the exact Hartree-Fock (HF, EXHF) exchange following the expression:  $E_{XC}^{PBE0} = E_{XC}^{PBE} + 1/4(E_X^{HF} - E_X^{PBE})$ . However, near the crossing seam such admixture led to delocalized solutions, therefore, we decided to keep the reaction path exploration at the UHF level of theory. The calculations were performed in the reciprocal space, and a  $4 \times 4 \times 4$  Monkhorst-Pack grid,<sup>55</sup> corresponding to 36 reciprocal space irreducible points, was used to sample the Brillouin zone. The SCF procedure was considered converged when the energy changes between the iterations were smaller than 10<sup>-8</sup> hartree. To analyze the polaronic structure, the ions positions were fully optimized until gradients were lesser than 0.00045 hartree/bohr. The lattice parameter at the UHF level of theory was found to be 5.37 Å in agreement with that obtained from PBE0 calculations, 5.40 Å.<sup>51</sup>

Using the structures obtained in the above described ab initio optimizations, model clusters were designed following two lines. In the first one, two molecular clusters were used. The minimal model consisted of a pair of cerium octahedra (minimal dimer cluster), having formula Ce<sub>2</sub>O<sub>4</sub>(H<sub>2</sub>O)<sub>10</sub> that will be labeled as small. This cluster, shown in Figure 4.3, is stoichiometric, represents the smallest structural unit able to exhibit the pair Ce<sup>III</sup>-Ce<sup>IV</sup>, and has D<sub>2h</sub> symmetry at the crossing seam. To include in the calculations additional effects of environment atoms a larger molecular model of gross formula Ce<sub>6</sub>O<sub>12</sub>(H<sub>2</sub>O)<sub>20</sub>, labeled as big and D<sub>2h</sub> was built from the bulk calculations. Again, the oxygen atoms were kept at their optimized positions and saturated with hydrogen atoms in order to have stoichiometric non-charged clusters. The second type of finite models was of the embedded cluster type. A Ce<sub>6</sub>O<sub>32</sub> cluster was excised from the bulk, and embedded in an array of point charges (PC) to incorporate the effect of the Madelung potential in the calculations. To avoid the excess of polarization of the outer oxygen atoms, the nearest layer of counterions was represented by Ce total ion potentials (TIPs), giving place to a model of formula Ce<sub>6</sub>O<sub>32</sub>(CeTIP)<sub>30</sub>PC. The whole system was symmetrized to preserve D<sub>2h</sub> symmetry and will be labeled big+PC.

The calculation of the electronic coupling matrix element  $V_{AB}$  started by determining the geometry at the crossing point. Once the geometry of the system with, for instance, the extra electron localized on the left, so the pair Ce<sup>III</sup>-Ce<sup>IV</sup>, is determined, the crossing-point

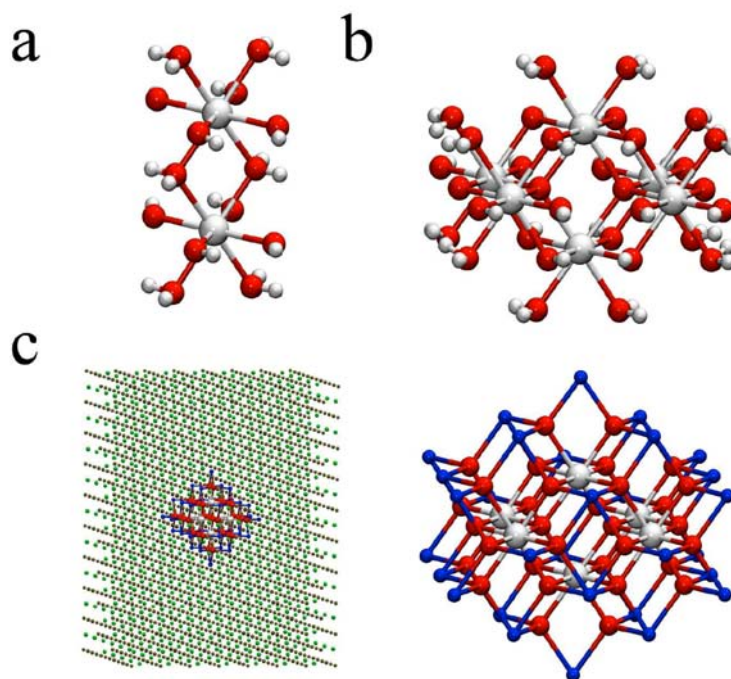


Figure 4.3: Structure of the cluster models used to compute the electronic coupling  $V_{AB}$ . a: small; b: big; c: big+PC. Red spheres are oxygen atoms and small light spheres hydrogen atoms. In model c, the blue spheres stand for Ce TIPS, The array of charges is also shown on the bottom left part of the figure

configuration for the system might be estimated using the linearized reaction coordinate approximation. If the electron-transfer reactant and product potential-energy surfaces are assumed to be parabolic, a reasonable approximation of the reaction coordinate is given by

$$q(\alpha) = \alpha q_A + (1 - \alpha)q_B \quad (4.2)$$

where  $0 \leq \alpha \leq 1$ , and if  $\alpha = 0.5$  then  $q(\alpha) = q_C$ . Broken symmetry ( $C_{2v}$ ) Hartree-Fock solutions for the cerium dimer cluster holding the electron localized left and right are then obtained and used to compute  $V_{AB}$  using the approach of Farazdel *et al.*<sup>44</sup> The calculations were performed using a home-adapted version of HONDO program. The effective core potential and basis sets used were essentially the same that in the periodic approach unless that the basis set for oxygen (and hydrogen) atoms was the standard DZP. Notice that the  $C_2$  axis of the reduced symmetry cluster falls along the Ce-Ce axis, so the according to Figure 4.3, we should speak in terms of up and down instead of left and right localization.

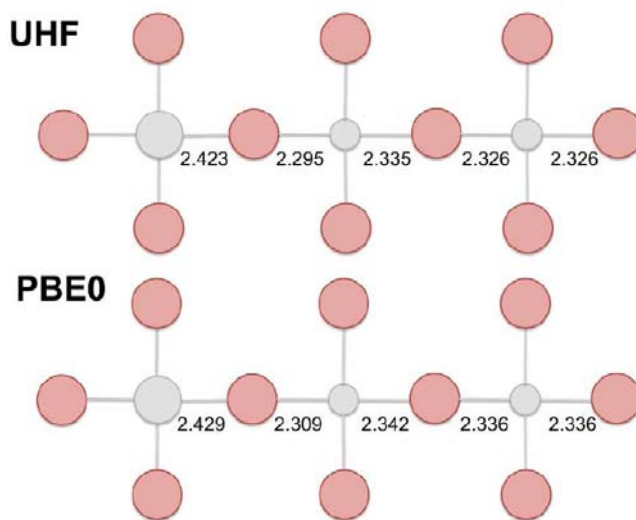


Figure 4.4: Schematic representation showing the structure of the polaron obtained from DFT and UHF calculations.

## Results and Discussion

### *Polaron structure and reorganization energy*

We start the section analyzing the deformation induced in the cerium ion  $\text{Ce}^{IV}$  coordination shell when it is reduced to  $\text{Ce}^{III}$ . The PBE0 optimization leads to a Ce-O interatomic distance of 2.429 Å, that compared with that of perfect  $\text{CeO}_2$  (2.338 Å)<sup>51</sup> shows a noticeable lengthening, which, on the other hand agrees with the lowering of the electrostatic interaction. This interatomic distance falls within those reported for  $\text{Ce}_2\text{O}_3$  bulk: 2.321, 2.435 Å.<sup>51</sup> The expansion of the coordination shell around the  $\text{Ce}^{III}$  center is accompanied by a shortening of the neighboring O- $\text{Ce}^{IV}$  interatomic distance, 2.309 Å, as depicted in the scheme of Figure 4.4. The next neighbor  $\text{Ce}^{IV}$ -O distances are computed to be 2.342, 2.336 and 2.336 Å, recovering thus the usual value of bulk ceria. These results indicate that the perturbation induced by the reduction almost exclusively involves the first coordination shell around the concerned Ce center, which is consistent with the small polaron nature experimentally proposed.<sup>30,33</sup> Population analysis of this structure confirms that the extra electron is occupying a Ce 4*f* orbital. As shown in the scheme of Figure 4.4, the optimization at the UHF level of theory leads to values very close to those obtained from DFT calculations.

Using an adequate initial guess we were able to obtain a converged UHF wavefunction for this configuration when the electron is localized on one of the neighboring Ce atoms.



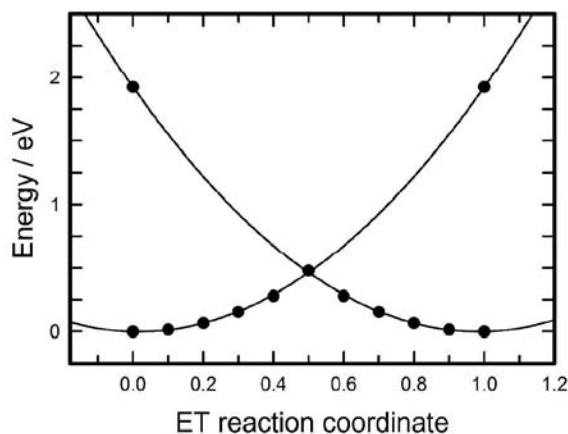


Figure 4.5: Electron transfer energy profiles along the ideal reaction coordinate  $q$ .

Formally speaking, the difference of energy associated to these states gives the reorganization energy  $\lambda$ , which in the present case is found to be 1.92 eV. This value might be considered as an upper bound and is in reasonable agreement with that of 1.4 eV obtained from the experimental optical absorption coefficient of reduced ceria samples.<sup>56</sup> On the other hand, employing this optimized structure and the linearized reaction coordinate approximation aforementioned we performed a series of static calculations to reach the crossing point and estimate the diabatic barrier. The results are summarized in Figure 4.5 where the parabolic shape of the potential curves is clearly observed (coefficient of determination for a square fitting  $R^2=1.0018$ ). The diabatic barrier was found to be 0.48 eV, that is, just a fourth of  $\lambda$ , as ideally expected.

#### *Electronic coupling matrix element*

The determination of  $V_{AB}$  from cluster models and equation (1) involves first obtaining localized wavefunctions at the crossing seam. In principle the highly symmetric  $4f$  atomic orbital that bears the extra electron may correspond to any of the four possible symmetry species that result after splitting under the reduced symmetry ( $C_{2v}$ ). Because these states may be close in energy we were compelled to obtain the four different solutions and therefore to perform four electronic coupling type calculations. The localized nature of the solutions was verified for every model, and the shape of the active orbitals for the lowest solutions each symmetry is reported in Figure 4.6. For the small model cluster, the  $A_1$  symmetry state is found to be the lowest state, while the other states are found to lie more than 0.1 eV higher. The electronic coupling matrix element for this state is 65 meV or 522

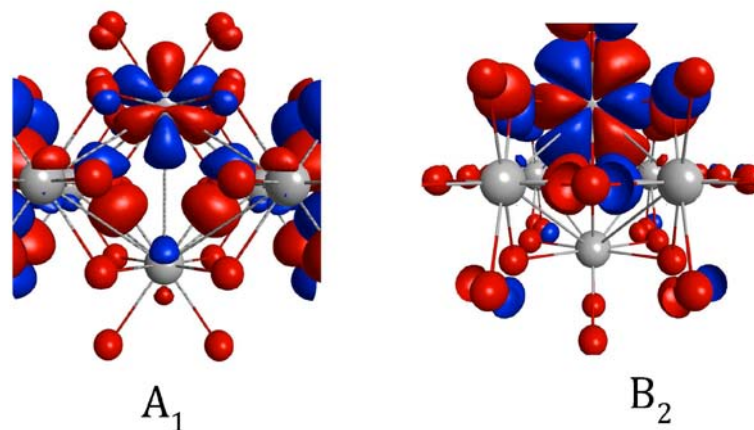


Figure 4.6: Shape of the active orbitals obtained for the small cluster model.

$\text{cm}^{-1}$ , a relatively small value. For the states of the other symmetries the coupling is even smaller, ranging between 2 and 34 meV. Increasing the model cluster leads to variations in the ordering of the states and also in the estimated coupling. Thus, for the big model the lowest state still has  $A_1$  symmetry, however for the big+PC model the  $B_2$  state is found to be the ground state, though almost degenerate with the  $A_1$  state. This result agrees with the periodic calculations in which a  $B_2$  state was found to be one of the precursor states. If we now analyze the dependence of the electronic coupling with the model we can see that changing the model cluster also changes the coupling. Thus, one can see that for  $A_1$  states the estimated values are quite stable indicating that even the simplicity of the small model cluster captures the main physical factors affecting the coupling. The same can be roughly said of the  $B_2$  symmetry states. However, for the two other symmetries one can see that at least the big model cluster is needed. The largest differences found are when passing from the small to the big cluster models, while the addition of the electrostatic field through the point charges is of lesser importance in the coupling, although appears to be essential to stabilize the  $B_2$  component, and correctly account for the ground state.

One further aspect that may be considered concerns the adequacy of the extrapolating procedure to estimate crossing seam geometry. Although in principle a geometry optimization could be performed, it has been shown that, in general, the electronic coupling slightly depends on the geometry. In the present work no attempts to carry out such optimization were envisaged, however, preliminary calculations at different geometries were done. For instance, in the case of the small cluster model, the electronic coupling was calculated for a configuration in which both Ce and O atoms were kept frozen at the experimental bulk

positions of  $\text{CeO}_2$ . The values of  $V_{AB}$  obtained were 61, 2, 26 and 18 meV, that are quite close to those obtained incorporating the polaronic distortion at the crossing point. This low dependency of the ET matrix element on the geometry agrees with that observed in the mixed valence  $\text{Cu}^I\text{-Cu}^{II}$  system.<sup>57</sup>

Let us now consider the results obtained with the adiabatic strategy. As the largest coupling is that of  $A_1$  states, we will focus on this symmetry in the following discussion. If the full  $D_{2h}$  symmetry is allowed in the SCF procedure at the crossing seam, the open shell orbital, SOMO, is of  $A_g$  symmetry. This molecular orbital actually corresponds to a symmetric (g or gerade) combination of the two  $A_1$  localized active orbitals, one of which is shown in Figure 4.6. For the antisymmetric (ungerade) combination of the pair of active orbitals one obtains u-symmetry molecular orbitals. The shape of these molecular orbitals is shown in Figure 4.7. As the associated states are of different symmetry one can in principle achieve convergence in the SCF procedure, and according to the Marcus theory we have assumed that half the difference of energy between the ground state ( $A_g$ ) symmetry and the lowest root of u-type symmetry, a  $B_{3U}$  state, corresponds to the electronic coupling matrix element. Because of the stability observed in the coupling matrix element for  $A_1$  states with respect to the cluster model, we have limited our analysis to the small model. Also, we have explored several exchange-correlation functionals, in particular B3LYP,<sup>58–60</sup> HSE06,<sup>61</sup> and M06,<sup>62</sup> besides the PBE0 approach. These calculations were performed using the same basis sets and theoretical setup but using Gaussian09 program. The values obtained for  $V_{AB}$  are: 85, 83, 68 and 88 meV for the functionals PBE0, B3LYP, HSE06, and M06 respectively. As can be seen these values appear to be steady, though somewhat larger than that obtained using the diabatic approach (65 meV). This behavior has been already reported in the calculation of the electronic coupling in other metal transition dimer clusters. For instance, hole-doped  $\text{La}_2\text{CuO}_4$  perovskites, where the B3LYP computations led to an ET matrix element of 217 meV, noticeably larger than that obtained using the diabatic procedure, 189 meV, but underestimated with respect to the value of 262 meV using a selected CI (DDCI).<sup>63</sup>

The analysis of the values calculated for the electronic coupling is generally performed on the basis of through-bond and through-space contributions although this evaluation can only be made on very simple models. However, in order to put our results in context first, it is worth comparing them with those found for related systems. The closest (and simplest) system is the  $3d^1\text{-}3d^0$  present in reduced titanium dioxide extensively investigated by Deskins and Dupuis.<sup>38</sup> These authors considered electron transfer in both anatase and rutile phases, along different directions, obtaining values ranging between 10 and 200 meV. The differences were attributed to there factors: the Ti-Ti distance, the degree of oxygen bridging, and the orientation of active d orbitals. Yet, the gross analysis was consistent with the well-known decay of the electronic coupling with distance, as one of its main ingredients relies on the overlap between donor and acceptor pairs. In particular,

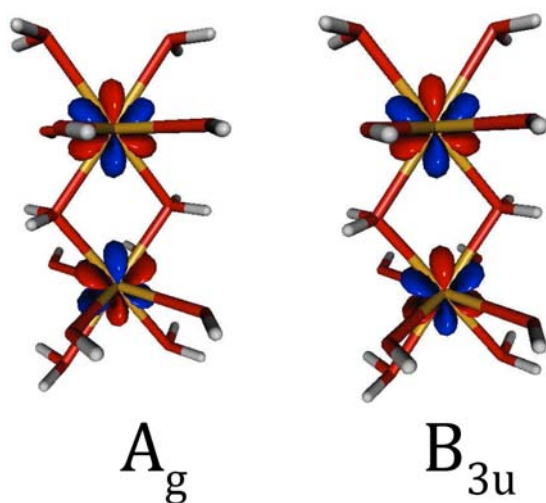


Figure 4.7: Shape of the highest occupied molecular orbital,  $A_g$ , and its antisymmetric counterpart of  $B_{3u}$  symmetry for the small cluster model.

for those cases where Ti atoms are linked by two bridging oxygens, the ET coupling element lowers from 200 meV (rutile [001] direction, Ti-Ti distance of 2.97 Å), to 30 meV (anatase, [201] direction, Ti-Ti distance of 3.09 Å). Since in our case two oxygen atoms link two Ce atoms, with a Ce-Ce distance of 3.80 Å, our estimate of 64 meV appears to be reasonable. A similar conclusion might be inferred when we compare with the results obtained for a related system, the  $\text{Cu}^I(3d^{10})\text{-Cu}^{II}(3d^9)$  where the ET process also involves only one d electron.<sup>57</sup> For this system the metal-metal distance was 3.1 Å and a comparable calculation gave an ET element of 189 meV. Let us now compare with other values of the electronic coupling derived from experimental data. Taking a value for  $\lambda$  of 0.88 eV and the mobility reported by Tuller et al.,<sup>33</sup> Shoko et al.<sup>35</sup> estimated an ET integral of 20 meV. However, this value was suggested to be too low, as using the Harrison method a much larger hopping integral was obtained ( $\sim 100$  meV). Beyond the approximations assumed in these estimations, we suggest that the discrepancy is due to the small value of the reorganization energy used for the calculation. Although our value for  $\lambda$  (1.96 eV) calculated at the UHF level might be overestimated, it is interesting to note that assuming  $T=1000$  °C, the estimated value for the ET hopping integral is 79 meV, remarkably close to the value of 65 meV obtained using the diabatic UHF wavefunctions.

To end up with this discussion let us analyze the adiabatic barriers for the ET process. For the ET matrix element we can take the mean of the values determined from the

adiabatic DFT approach (81 meV). For the diabatic barrier we can chose as a reasonable approximation the difference between the UHF energies computed at the crossing seam and at the minima reported in the energy profiles of Figure 4.5 (0.48 eV). Disregarding ZPE corrections we can estimate an adiabatic barrier of 0.40 eV, which is agreement with the 0.42-0.50 eV range experimentally determined.<sup>30,33</sup> On the other hand, the adiabatic or diabatic behavior of the ET transfer is governed by the transmission probability  $\kappa$ . This coefficient gives the probability of passing from the initial state to the final state and is given by  $\kappa = 2P_{12}^0 / (1 + P_{12}^0)$ ,<sup>64</sup> where  $P_{12}^0$  is the probability of conversion to the final state per passage through the crossing seam. A value near 1 for  $\kappa$  indicates adiabatic transfer. For a self-exchange process,<sup>65</sup> the probability  $P_{12}^0$  might be estimated through the Landau and Zener expresin:<sup>66,67</sup>

$$P_{12}^0 = 1 - \exp[-(V_{AB}^2/h\nu_0)(\pi^3/\lambda k_B T)^{1/2}] \quad (4.3)$$

Here  $\nu_0$  is a typical frequency for nuclear motion, and in our case it corresponds to the specific phonon mode describing the antiphase breathing mode of the oxygen atoms bound to the Ce<sup>III</sup> site. Taking for this quantity the experimental accepted value of 595 cm<sup>-1</sup> for longitudinal optic-mode phonon,<sup>26,68</sup> we obtain a coefficient transmission  $\kappa = 0.81$ , i.e. close to the ideal adiabaticity. This finding agrees with the adiabatic theory of small polaron and reinforces the proposed hopping conductivity mechanism in which electrons jump from a Ce<sup>3+</sup> ion to a neighboring Ce<sup>4+</sup> ion.

## Conclusions

Ab initio quantum theory has been employed to determine and characterize the nature of the electron transfer process between adjacent Ce<sup>3+</sup> and Ce<sup>4+</sup> centers in bulk ceria. Using a supercell model, periodic boundary conditions and DFT calculations with the PBE0 xc-functional, we have demonstrated that the reorganization that takes place when a Ce<sup>4+</sup> is reduced to Ce<sup>3+</sup> involves almost exclusively the first coordination shell with an increasing in the Ce(III)-O interatomic distance of 0.09 Å. This result allows us to confirm the small polaron nature of reduced ceria previously proposed. The analysis of the spin and electronic density shows a strongly localized charge distribution around the Ce<sup>3+</sup> ions. Within the two-state Marcus model, we have estimated the electronic coupling matrix element or electron transfer integral,  $V_{AB}$ , following two approaches. Using diabatic wavefunctions determined at the Hartree-Fock level of theory we obtain for this quantity a value of 65 meV. The analysis of the active orbitals nicely shows the strong localized nature of the 4*f* states. Using an adiabatic approach enabled us to estimate  $V_{AB}$  from DFT calculations employing several exchange-correlation functionals. The obtained values fall in the 68-88 meV range (mean value  $V_{AB} = 81$  meV).

From the energy profiles determined at the UHF level of theory for the electron transfer process along an idealized reaction path we obtained a reorganization energy  $\lambda$  of 1.96

eV, and an adiabatic barrier for the polaron hopping of 0.40 eV, in very good agreement with activation energy estimated from conductivity experiments performed on reduced ceria. Finally, the transmission coefficient  $\kappa$  was estimated to be 0.81, indicating that the electron transfer process is mainly adiabatic, confirming the earlier proposed adiabatic theory of small polaron and hopping conductivity in defective bulk ceria.

### 4.3 Transport properties in $\text{CeO}_{2-x}$ (111) surface: from charge distribution to ion-electron collaborative migration.

José J. Plata, Antonio Márquez, and Javier Fdez. Sanz

**Abstract:** Charge distribution and ion and electron migration have been theoretically studied in reduced  $\text{CeO}_2$  (111) surface by means of density functional calculations including on-site localization corrections (DFT+U). The analysis of the charge distribution shows that nearest-neighbor and next-nearest-neighbor configurations of  $\text{Ce}^{3+}$  and oxygen vacancies are the most stable arrangements for both surface and subsurface oxygen vacancies. Electron transfer between  $\text{Ce}^{3+}$  and  $\text{Ce}^{4+}$  centers correspond to a polaron hopping involving the exchange of a  $4f$  electron across the surface, with activation energies of about 0.3 eV. Activation barriers for oxygen atom migration on the surface strongly depend on the charge of the ions surrounding the atom that actually moves. Namely, the migration is particularly facile when the migration occurs crossing the line through  $\text{Ce}^{4+}$  ions. The present results afford a quantitative depiction of the low barrier for the oxygen diffusion across the cerium oxide surface.

#### Introduction

Cerium oxide or ceria ( $\text{CeO}_2$ ) has been one of the most studied materials during the last decade because of its outstanding properties in a variety of technological applications. This material is used as catalyst in a diversity of processes such as automotive exhaust converters, water-gas shift reaction, production and purification of hydrogen, or crude oil refining.<sup>16,69–72</sup> Initially, the promoting effect of ceria was attributed to the enhancement of the metal dispersion and the stabilization of the support towards thermal sintering.<sup>21,22</sup> However, subsequent work has shown that ceria can act as a chemically active component as well, working as an oxygen reservoir able to release it in the presence of reductive gases and to stock it upon interaction with oxidizing gases.<sup>23,25,73</sup> On the other hand, due to its relatively high oxygen ion conductivity, ceria is an interesting material as electrolyte in high temperature devices, such as solid oxide fuel cells, or oxygen gas sensors.<sup>73,74</sup>

The suitability of ceria in this broad range of technological fields is due to the well-known ability of cerium to cycle between  $\text{Ce}^{3+}$  and  $\text{Ce}^{4+}$  oxidation states, on one side, and the easiness to create oxygen vacancies, on the other side. This ability, related to the reducibility of the material, is accompanied by a facile electron transfer across the bulk and surface, together with an easy oxygen transport, and later healing of the defects under oxidizing conditions. Understanding the behavior of surface reactive sites is essential in order to establish the reaction mechanisms, and a great effort has been made in recent

years to describe the charge distribution in  $\text{CeO}_{2-x}$  materials and thus rationalize the processes involved in ionic and electron migration.<sup>34</sup>

Electron mobility in ceria was first experimentally studied by Tuller and Nowick,<sup>33</sup> that from electrical conductivity measurements proposed a small polaron hopping mechanism in which electrons jump from a  $\text{Ce}^{4+}$  ion to a neighboring  $\text{Ce}^{4+}$  ion, according to the model developed by Holstein and Friedman.<sup>31,32</sup> The mobility in  $\text{CeO}_{2-x}$  was found to be activated, with an activation energy  $E_a = 0.40$  eV at small  $x$  and increasing to 0.52 eV at  $x = 0.25$ . A similar conclusion was drawn from the work of Naik and Tien,<sup>75</sup> though at very low vacancies concentration the activation energy reported was lower: 0.20 eV. From a theoretical point of view, the so-called hopping integral,  $t$ , a key quantity in the analysis of the electron mobility of a system, has been investigated. However, depending of the method to compute this value, a large discrepancy has been reported.<sup>34</sup> In a recent work we have described an ab initio prediction of this quantity based on quantum chemical calculations.<sup>75</sup> In bulk ceria the electron coupling matrix element or hopping integral was estimated to be 0.08 eV, with an adiabatic activation barrier for the polaron hopping of 0.4 eV. Moreover the transmission coefficient  $\kappa$  was estimated to be 0.81, indicating that the electron transfer process is mainly adiabatic, confirming the earlier proposed adiabatic theory of small polaron and hopping conductivity in defective bulk ceria.

Oxygen transport in ceria materials has been experimentally and theoretically studied too.<sup>16</sup> On one hand, experiments have been performed in order to analyze the diffusion of oxygen vacancies in ceria and doped ceria. One of the most common techniques used to obtain activation energy for oxygen diffusion is the ac impedance analysis of the measured electrical conductivity. The barriers obtained range from 0.5 to 0.9 eV, a rather high value that together with the low concentration of vacancies in pure ceria makes it not specially suited as solid electrolyte. Ceria doped with lower valence cations contains intrinsic oxygen vacancies, which improve the conductivity, and actually doping ceria with rare-earth trivalent cations is the usual technique to improve the conductivity.<sup>76</sup> From a theoretical point of view, oxygen transport in ceria has been analyzed in several works. For instance, Andersson et al.<sup>77</sup> analyzed the connection between defect association and ionic conductivity using density functional theory based calculations, DFT, within a generalized gradient approach, GGA. Dholabhai et al.<sup>78</sup> included a Hubbard like term in the computational approach, DFT+U, in order to elucidate oxygen vacancy migration in bulk ceria and Pr-doped ceria. However, ionic and electron conduction cannot be in general analyzed separately because coupling effects between motion of cations and electrons have been reported in some transition metal oxides.<sup>12,13,79</sup> In last years, experimental results have suggested that ceria and doped-ceria material are in this group of oxides in which there is a relation between electronic and ionic currents.<sup>15,80,81</sup> In fact, charge distribution of  $\text{Ce}^{3+}$  and vacancies have been intensively discussed. Nakayama et al.<sup>82</sup> calculated high association energies (0.49-0.80 eV) between the oxygen vacancies and



$\text{Ce}^{3+}$  ions, and therefore the formation of isolated vacancies would be negligible in bulk. However, other authors assumed that  $\text{Ce}^{3+}$  ions show a preference for next nearest neighbor positions instead of nearest neighbor sites at low concentration of defects in bulk and (111) surface.<sup>34,83,84</sup>

In a recent work Chueh *et al.*<sup>1</sup> performed a spectroscopy study to quantify simultaneously the concentration of  $\text{Ce}^{3+}$  species on the surface and in the bulk of Sm-doped ceria. They showed that the surface  $\text{Ce}^{3+}$  concentration is substantially enhanced from the bulk, especially at low bulk oxygen nonstoichiometries, and is only weakly dependent on temperature and oxygen activity. Likewise, the reduced surfaces have high oxygen vacancy concentration, meaning that  $\text{Ce}^{3+}$  segregation is accompanied not only by electron transfer but also by oxygen diffusion through the first surface layers.

In light of the crucial and distinctive role exhibited by the surface in the charge transport process in reduced ceria, we decided to undertake a theoretical analysis of the electron mobility and oxygen migration in a defective ceria surface. We used DFT+U methodology in which the U parameter is also applied to O 2p orbital ( $U^p$ ). This strategy was reported to improve the description of some oxides as  $\text{CeO}_2$  and  $\text{Ce}_2\text{O}_3$ .<sup>85–87</sup> In this study, we start by analyzing the charge distribution and vacancy formation in reduced (111) ceria. Then the energy barriers associated with the electron hopping between  $\text{Ce}^{3+}$  and  $\text{Ce}^{4+}$  ions are estimated for several vacancy arrangements. In a third step we compute the barriers for oxygen migration. The whole analysis shows some coupling between polaron hopping and oxygen diffusion, suggesting that, for specific arrangements, the polaron hopping somehow assists the vacancy migration at the surface.

### Computational details and surface model

Periodic DFT+U spin polarized calculations were carried out with the Vienna *ab initio* simulation package (VASP).<sup>88–90</sup> This code solves the Kohn-Sham equations for the valence electron density within a plane-wave basis set and makes use of the projector augmented wave (PAW) method to describe the interaction between the valence electrons and the atomic cores.<sup>91,92</sup> The valence electron density is defined by the twelve ( $5s^25p^66s^25d^14f^1$ ) electrons of each Ce atom and the six ( $2s^22p^4$ ) electrons of each O atom. The plane-wave expansion includes all plane waves with kinetic energy smaller than a cut-off value set to 500 eV, which ensures adequate convergence with respect to the basis set. The GGA functional proposed by Perdew *et al.*<sup>93,94</sup> (PW91) was selected. To take into account the on-site Coulomb correction a Hubbard-like term was introduced according to the formalism due to Dudarev *et al.*,<sup>95</sup> which makes use of a single  $U_{eff}$  parameter, hereafter denoted simply as  $U_f$  and  $U_p$ , to design the effective values used for the Ce 4f and O 2p electrons, respectively. For Ce and O we have used a  $U^f$  and  $U^p$  of 5 eV which leads to a moderately improved description of some critical aspects that concern structure,

electronic properties, and thermochemistry of both  $\text{CeO}_2$  and  $\text{Ce}_2\text{O}_3$ .<sup>51,87</sup>

Forces on the ions were calculated through the Hellmann-Feynman theorem, including the Harris-Foulkes correction to forces.<sup>96</sup> This calculation of forces allows one to employ the conjugated gradient scheme in geometry optimization. Iterative relaxation of the atomic positions was stopped when the forces on the atoms were  $< 0.01 \text{ eV/\AA}$ . The barriers for vacancy-oxygen migration were located using the climbing image version of the nudged elastic band (NEB) algorithm.<sup>97</sup> Barriers for the polaron hopping were calculated using a linear interpolation scheme. This method is based on the appropriate localization of electrons on initial and final site, and has been successfully used in previous studies.<sup>38,75,98</sup> This method captures the physics of the key phonon mode associated with the polaron transfer, the antiphase breathing polaronic expansion around the reduced metal site, and the contraction around the oxidized metal site.

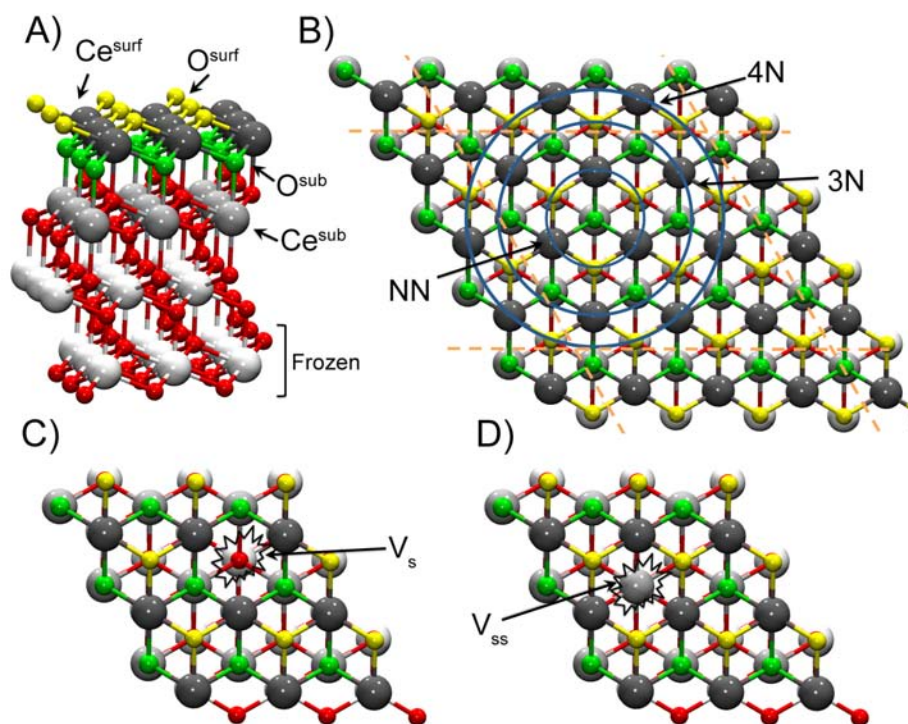


Figure 4.8: A) Model of the  $(3 \times 3)$ , four-layer thick,  $\text{CeO}_2$  (111) surface. B) Top view of  $\text{CeO}_2$  (111) surface supercell. Blue circles show different kind of neighbors around subsurface oxygen. C) and D) Top view of reduced surface with subsurface ( $V_{ss}$ ) and surface ( $V_s$ ) vacancies respectively. Atom colors: red=O, white=Ce, green=subsurface O ( $\text{O}^{sub}$ ), yellow=surface O ( $\text{O}^{surf}$ ), grey= subsurface Ce ( $\text{Ce}^{sub}$ ), dark grey=surface Ce ( $\text{Ce}^{surf}$ ).

The bulk ceria lattice constant is taken from previous work<sup>87</sup> in which the same theoretical approximations of this work were used. The resulting parameter is 3.47 Å, which is within 2% of the experimental value ( $a_0 = 3.41$  Å). The  $\text{CeO}_2$  (111) surface was described by a slab model with three-dimensional boundary conditions. We used a (3x3) supercell in which three different kinds of cerium ions can be distinguished on the surface depending on the proximity to an oxygen vacancy: nearest neighbor (NN or 2N), next-nearest neighbor (3N) and next-next-nearest neighbor (4N). The cell was 12 atomic layers thick or four  $\text{CeO}_2$  trilayers. The supercell model and different sites and arrangements are depicted in Figure 4.8. In all cases, the lower  $\text{CeO}_2$  trilayer was kept frozen while the rest of the atoms were allowed to fully relax their atomic positions. The supercell model is separated from their images by a vacuum of 15 Å, considered enough to avoid interaction between the slabs. To sample the Brillouin zone a  $2 \times 2 \times 1$  grid of k-points generated by the Monkhorst-Pack scheme was used. Two kinds of defects were considered, surface and subsurface oxygen vacancies, which have been reported as the most stable defects in the (111) surface.<sup>84</sup>

## Results and discussion

### Charge distribution

To analyze the charge distribution in reduced ceria (111) surface, we first computed oxygen vacancy formation energies ( $E_{vf}$ ) in surface ( $O_{surf}$ ) and subsurface ( $O_{sub}$ ) sites. For these calculations, we took molecular  $\text{O}_2(\text{g})$  and stoichiometric surface energies as references. Vacancy creation generates two  $\text{Ce}^{3+}$  ions, with electronic configuration  $4f$ , which can couple ferromagnetic (FM) or antiferromagnetically (AF). However, we limit the study to FM states that have been recently reported as slightly more stable due to superexchange mechanism.<sup>99</sup> The results obtained for different arrangements are reported in Table 4.1. One can observe that, in general, the vacancy formation energies are lower when the vacancy is located at the subsurface oxygen layer, in agreement with previous calculations.<sup>83,84,100</sup> The  $\text{Ce}^{3+}$  ions tend to remain apart each other, and located at the surface sites, reflecting that they can relax more efficiently than if they were located at the subsurface. The most stable site for the vacancy corresponds to a 3N\_3N arrangement, in agreement with previous PBE+U calculations.<sup>83</sup> On the other hand, the  $E_{vf}$  values estimated using the  $U^p$  on-site term are found slightly smaller compared to previous HSE or DFT+U calculations, which is in agreement with bulk results.<sup>87</sup> However, the relative stability between different possible configurations remains essentially unchanged. For both the surface and the subsurface defects the 3N\_3N configuration is the most stable, indicating that the 3N sites are the preferential distribution for  $\text{Ce}^{3+}$  on the reduced surface. NN or 3N site preference has been studied in lanthanide trivalent-doped systems in which two different effects were described.<sup>77</sup> On one hand, the Coulomb interactions between

the vacancy and dopant charged defects are stronger (negative) for NN than 3N site. This interaction decreases slowly in the lanthanide series from left to the right. On the other hand, elastic contributions related to lattice deformations are stronger (positive) and decrease faster than Coulomb interactions for NN sites. When both contributions are taken into account, this model predicts 3N preference from  $\text{La}^{3+}$  to  $\text{Pm}^{3+}$ - $\text{Sm}^{3+}$  (including  $\text{Ce}^{3+}$ ) while the other trivalent cations of the series prefer NN sites.

Table 4.1: Table1. Vacancy formation energies ( $E_{vf}$ ) on the  $\text{CeO}_2$  (111) surface. The s prefix was used to label  $\text{Ce}^{3+}$  ions at the subsurface  $\text{Ce}^{sub}$  sites.

$E_{vf}$					
Surface vacancy			Subsurface vacancy		
Configuration	This work	PBE+U <sup>a</sup>	Configuration	This work	PBE+U <sup>b</sup>
3N_3N	2.18	2.06 <sup>c</sup>	3N_3N	1.81	1.87 <sup>c</sup>
NN_3N	2.24	2.16 <sup>c</sup>	NN_3N	1.90	2.00 <sup>c</sup>
NN>NN	2.31	2.22 <sup>c</sup>	3N_4N	1.94	-
3N_s3N	2.32	-	s3N_s3N	1.95	-
3N_s3N	2.32	-	3N_sNN	2.10	2.08 <sup>c</sup>
3N_4N	2.33	-	NN_sNN	2.17	2.40 <sup>c</sup>
NN_4N	2.44	2.28 <sup>c</sup>	3N_s3N	2.23	-
NN_s3N	2.47	2.45 <sup>c</sup>	3N_s3N	2.26	2.38 <sup>c</sup>
s3N_s3N	2.65	2.59	s3N_sNN	2.34	-

<sup>a</sup>Values calculated using a 3x3 supercell. <sup>100</sup> <sup>b</sup>Values calculated employing a 2x2 supercell. <sup>84</sup> <sup>c</sup>Similar defect-formation energies have been calculated using a 3x4 supercell. <sup>83</sup>

### Electron mobility

To explore the electron mobility near the surface we computed the adiabatic activation barriers for electron transfer between  $\text{Ce}^{3+}$  and  $\text{Ce}^{4+}$  ions in the defective surface. To cover all possible situations in the surface, we estimated three different barriers for both surface and subsurface vacancy arrangements, which essentially differ by the proximity to the vacancy. In a first step, we analyzed the  $\text{Ce}^{3+}$ - $\text{Ce}^{4+}$  electron hopping far away from the vacancy ( $3\text{N}_3\text{N} \rightarrow 3\text{N}_3\text{N}$ ). A pathway closer to the vacancy was modeled calculating the barrier for electron transfer from a 3N site to a NN site ( $3\text{N}_3\text{N} \rightarrow \text{NN}_3\text{N}$ ). Finally, an immediate electron hopping directly across the vacancy was considered ( $\text{NN}_3\text{N} \rightarrow \text{NN}_3\text{N}$ ), as shown in Figure 4.9. The adiabatic activation barriers computed for the three pathways for both surface and subsurface oxygen vacancies are reported in Table 4.2. The largest barriers correspond to the first case, in which the  $\text{Ce}^{3+}$  and  $\text{Ce}^{4+}$  ions exchanging

the electron are located well away from the vacancy, and would be representative of a sort of isolated  $\text{Ce}^{3+}\text{-Ce}^{4+}$  pairs. The estimated barriers are 0.45 and 0.50 eV, larger than the experimental data. However, when the polaron is located at the surroundings of the vacancy, a significant lowering of the barrier (30-50%) can be observed. This behavior is found for both surface and subsurface vacancy models. The computed barriers now fall in the 0.28-0.37 eV range, in very good agreement with the experiment. On the other hand, our values appear to be somewhat larger than those recently found by Nakayama *et al.* that for a bulk model using a PBEsol+U approach, a jellium background and dipole corrections reported barriers for the electron transfer lower than 0.2 eV. To check whether the differences are due to the different setup in the calculations we carried out a computation of the barrier in a bulk model described by a  $2 \times 2 \times 2$  supercell containing an oxygen vacancy (95 atoms). To avoid  $\text{Ce}^{3+}\text{-Ce}^{3+}$  coupling effects one of these reduced Ce atoms was substituted by a  $\text{Ce}^{3+}$  pseudopotential, which allows one to perform the calculations for an electronic doublet without including the jellium background. The result of this calculation gave an activation barrier for the polaron hopping of 0.31 eV, in agreement with the values above reported, and consistently lower than the barrier for the perfect crystal (0.40 eV). Such a lowering of electron transfer barrier near a vacancy also is qualitatively in agreement with the findings reported by Nakayama *et al.*

Table 4.2: Activation energy (eV) for polaron hopping in the  $\text{CeO}_2$  (111) surface.

Path	$V_s$	$V_{ss}$
NN_3N→NN_3N	0.30	0.28
3N_3N→NN_3N	0.37	0.29
3N_3N→3N_3N	0.45	0.50

The findings obtained so far theoretically corroborates that the presence of vacancies facilitate the electron mobility experimentally observed. This phenomenon should be related to the breathing polaronic expansion and contraction of the bridging oxygen atoms between  $\text{Ce}^{3+}$  and  $\text{Ce}^{4+}$  ions. If the oxygen vacancy is in the contiguity to one of the Ce atoms involved in the electron transfer, the relaxation is expected to be easier than when it is in the vicinity of a fully coordinated ion. Experimental data suggest that electron conductivity is highly depending on the surface area and the vacancy concentration. Litzelman and Tuller reported that electron conductivity is  $p\text{O}_2$  dependent while ionic conductivity is not.<sup>101</sup> In fact, electron conductivity is higher at low  $p\text{O}_2$  levels, in which the concentration of vacancies increases. Also, Tschope analyzed how electronic conductivity increase upon reduction of the grain size of polycrystalline cerium oxide.<sup>102</sup> A reduction of the grain size derives in more grain boundaries and surface area in which

$E_{vf}$  is lower than in bulk, and therefore, an increase in the surface concentration of vacancies is expected. Both experimental works show that the electronic conductivity increases when surface vacancy concentration is higher, which is in agreement with the model here proposed.

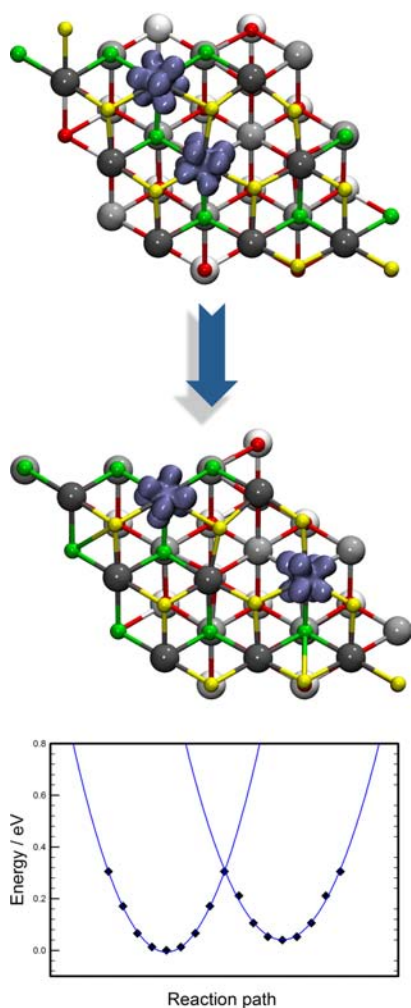


Figure 4.9: Top. Spin density isosurfaces (dark blue) for polaron migration from NN<sub>3N</sub> site to NN<sub>3N</sub> site, labeled as Ce<sup>3+</sup>-Ce<sup>3+</sup> in defective CeO<sub>2</sub> (111) surface. Bottom. Reaction energy profile for polaron transfer.

### Ionic transport

Oxygen migration has been intensively studied not only for its applications in solid fuel cell but also for its importance in the oxidation catalytic process in which the surface act as oxygen reservoir. Oxygen or vacancy migration barriers have been computed in reduced  $\text{CeO}_{2-x}$  bulk systems, with estimated values in the 0.40-0.70 eV range.<sup>77,78,82</sup> However, studies of vacancy migration on the surface are much more scarce, and in fact, as far as we can ascertain, the ionic mobility in the (111) surface has never been studied. In the present simulations we will consider the oxygen migration between surface and subsurface, which actually would represent the first (or the last) step in the oxygen exchange across the surface. The starting point will be the most stable vacancy, i.e. located at the subsurface. For an oxygen ion to move from the surface towards the subsurface it has to follow a path through two cerium atoms. The distance between a pair of  $\text{Ce}^{4+}$  ions in the stoichiometric surface is 3.80 Å. However, this interatomic distance will be different for the reduced surface, as  $\text{Ce}^{3+}$  features larger ionic radius. Since the charge is also different, the energy profiles along the reaction coordinate will depend, therefore, on the nature of the pair ( $\text{Ce}^x\text{-Ce}^x$ ) across which the oxygen atom migrates. To take into account this diversity four different possibilities were considered. In the first, labeled  $\text{Ce}^{3+}\text{-Ce}^{3+}$ , the oxygen moves through a pair of  $\text{Ce}^{3+}$  ions. The second refers to the movement of the oxygen atom crossing the line  $\text{Ce}^{3+}\text{-Ce}^{4+}$ . In the two remaining possibilities the oxygen makes its way between  $\text{Ce}^{4+}$  ions, in which case the  $\text{Ce}^{3+}$  ion might be located far from the vacancy ( $\text{Ce}^{4+}\text{-Ce}^{4+}$ )<sup>A</sup>, or close to the vacancy ( $\text{Ce}^{4+}\text{-Ce}^{4+}$ )<sup>B</sup>. The transition states for these four oxygen migrations were located using the well-known NEB algorithm and the activation energies are reported in Table 4.3. As can be seen, the activation energy involving two trivalent Ce ions is significantly high, 0.73 eV, close to that previously estimated from bulk ceria models. Substitution of a trivalent ion by a tetravalent ion involves a drastic lowering ( $E_a = 0.39$  eV), with further reduction when the migration takes place across two  $\text{Ce}^{4+}$  ions ( $E_a = 0.27$  and 0.12 eV). The analysis of the charge distribution along the reaction paths reveals that in the  $\text{Ce}^{3+}\text{-Ce}^{3+}$  pathway, oxygen atom migration is accompanied by a electron shift from one of the closest  $\text{Ce}^{3+}$  ions (NN) towards a  $\text{Ce}^{4+}$  ion located at site 3N. This kind of assisted mechanism is depicted in Figure 4.10, where one can see that in the transition state structure, one of the  $4f^1$  electrons has also moved. Such a concerted mechanism has been also reported for oxygen migration in bulk ceria by Nakayama *et al.* Indeed, instead of surmounting a high barrier through two  $\text{Ce}^{3+}$  ions, an initial electron shift allows for a much easier relaxation of the transition state structure. It should be noticed however that, in the surface, even with the assisted mechanism, the barrier is considerably high, and the preferred migration will always proceed through ( $\text{Ce}^{4+}\text{-Ce}^{4+}$ ) pairs. This statement is also reinforced with the fact that 3N\_3N and NN\_3N arrangements are energetically favored. For oxygen atom to migrate it will find its way

through a ( $\text{Ce}^{4+}\text{-Ce}^{4+}$ ) pair even though a preliminary electron transfer (easier and faster) is needed. In this sense, the oxygen migration might be viewed as an electron-hopping assisted mechanism.

Table 4.3: Activation energy,  $E_a$  for oxygen migration in the  $\text{CeO}_2$  (111) surface.

Path	$E_a / \text{eV}$
$\text{Ce}^{3+}\text{-Ce}^{3+}$	0.73
$\text{Ce}^{3+}\text{-Ce}^{4+}$	0.39
$(\text{Ce}^{4+}\text{-Ce}^{4+})(\text{A})$	0.27
$(\text{Ce}^{4+}\text{-Ce}^{4+})(\text{B})$	0.12

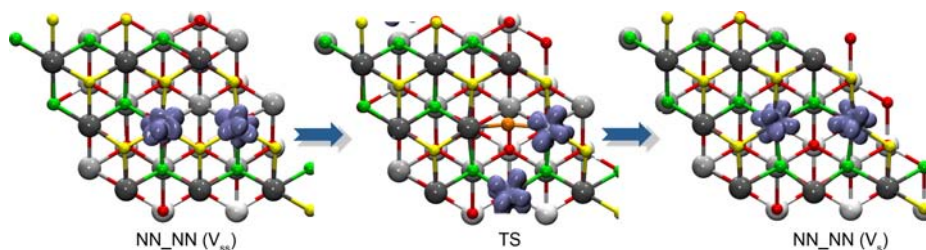


Figure 4.10: Top. Isosurfaces (dark blue) and reaction path of the (FM) spin density for oxygen migration from NN\_NN ( $V_{ss}$ ) site to NN\_NN ( $V_s$ ) site in defective  $\text{CeO}_2$  (111) surface. In the transition state structure the oxygen that moves from the surface to the subsurface is colored in orange.

## Conclusions

A theoretical study of the charge distribution and ion and electron motilities in reduced  $\text{CeO}_2$  (111) has been performed using DFT calculations that include on-site Hubbard-like corrections on both Ce and O atoms (DFT+U). The analysis of the electron density shows that  $\text{Ce}^{3+}$  ions prefer to be located at nearest-neighbor and next-nearest-neighbor arrangements with respect to the oxygen vacancies. With respect to the position of oxygen vacancies, they are found to be more stable in the subsurface layer than in the outermost layer of the surface, in agreement with previous calculations.

The electron transfer between  $\text{Ce}^{3+}$  and  $\text{Ce}^{4+}$  ions, responsible for the electron mobility, is an activated process whose barrier depends on the proximity of the oxygen vacancy. When the  $\text{Ce}^{3+}\text{-Ce}^{4+}$  pair is located well apart from the defect, the estimated barriers



are 0.45 and 0.50 eV, values that are closed to that found for non-defective bulk ceria. However, when the polaron is located at the surroundings of the vacancy, a significant lowering of the activation energy can be observed for both surface and bulk models, with barriers in the 0.28-0.37 eV range. This result is in agreement with experimental data suggesting that the electron conductivity is highly dependent of properties that modify the number of oxygen vacancies.<sup>101,102</sup>

With respect to the oxygen migration, the energy profiles indicate that the lowest pathway involves oxygen atom making its way through a ( $\text{Ce}^{4+}$ - $\text{Ce}^{4+}$ ) pair toward the adjacent vacancy. Under these conditions the estimated barrier may be as low as 0.12 eV. However, the activation energy significantly increases when the oxygen moves to a vacancy traversing between ( $\text{Ce}^{3+}$ - $\text{Ce}^{4+}$ ) or ( $\text{Ce}^{3+}$ - $\text{Ce}^{3+}$ ) pairs. In such a case it would be preferable to transfer an electron to a nearby  $\text{Ce}^{4+}$  to facilitate the oxygen migration.

In summary, charge transport in ceria might be viewed as a collaborative movement of electron transfer and ionic migration. Electron transfer is facilitated by the presence of oxygen vacancies, while oxygen (vacancy) migration is much easier when the atomic displacement occurs through non-reduced  $\text{Ce}^{4+}$  ions. This coupling between electronic and ionic conductivity is consistent with previous experimental results in which the measurements of Onsager cross coefficient and the ionic and electronic charge of transport reveal that both carriers do not migrate independently.<sup>14,15</sup>

## References

1. Chueh, W. C.; Hao, Y.; Jung, W.; Haile, S. M., *Nat. Mater.* **2012**, *11*, 156.
2. Jasinski, P.; Suzuki, T.; Anderson, H. U., *Sensor. Actuat. B-Chem.* **2003**, *95*, 73.
3. He, H. P.; Gorte, R. J.; Vohs, J. M., *Electrochem. Solid State Lett.* **2005**, *8*, A279.
4. Deluga, G.; Salge, J.; Schmidt, L.; Verykios, X., *Science* **2004**, *303*, 993.
5. Rodriguez, J.; Ma, S.; Liu, P.; Hrbek, J.; Evans, J.; Prez, M., *Science* **2007**, *318*, 1757.
6. Esch, F.; Fabris, S.; Zhou, L.; Montini, T.; Africh, C.; Fornasiero, P.; Comelli, G.; Rosei, R., *Science* **2005**, *309*, 752.
7. Corma, A.; Atienzar, P.; Garca, H.; Chane-Ching, J.-Y., *Nat. Mater.* **2004**, *3*, 394.
8. Li, Y.; Sun, Q.; Kong, M.; Shi, W.; Huang, J.; Tang, J.; Zhao, X., *J. Phys. Chem. C* **2011**, *115*, 14050.
9. Yoo, H.-I.; Martin, M., *Ceram. Trans.* **1991**, *24*, 103.
10. Lee, J.-H.; Yoo, H.-I., *J. Electrochem. Soc.* **1994**, *141*, 2789.
11. Schroeder, M.; Martin, M., *Zeitschrift fur Physikalische Chemie* **1998**, *207*, 1.
12. Lee, D.-K.; Yoo, H.-I., *Phys. Rev. Lett.* **2006**, *97*.
13. Yoo, H.-I.; Lee, D.-K., *Solid State Ionics* **2008**, *179*, 837.

14. Park, W.-S.; Yang, I.; Yoo, H.-I., vol. 13 **2008** pages 327–336.
15. Chatzichristodoulou, C.; Park, W.-S.; Kim, H.-S.; Hendriksen, P.; Yoo, H.-I., *PCCP* **2010**, *12*, 9637.
16. Trovarelli, A., *Catalysis by Ceria and related Materials*, World Scientific **2002**.
17. Gamarra, D.; Belver, C.; Fernandez-Garcia, M.; Martinez-Arias, A., *J. Am. Chem. Soc.* **2007**, *129*, 12064.
18. Zhong, L.-S.; Hu, J.-S.; Cao, A.-M.; Liu, Q.; Song, W.-G.; Wan, L.-J., *Chem. Mater.* **2007**, *19*, 1648.
19. Cambolis, A.; Matralis, H.; Trovarelli, A.; Papadopoulou, C., *App. Catal. A Gen.* **2010**, *377*, 12.
20. Park, J. B.; Graciani, J.; Evans, J.; Stacchiola, D.; Ma, S.; Liu, P.; Nambu, A.; Sanz, J. F.; Hrbek, J.; Rodriguez, J. A., *Proc. Natl. Acad. Sci. U.S.A.* **2009**, *106*, 4975.
21. Dictor, R.; Roberts, S., *J. Phys. Chem.* **1989**, *93*, 5846.
22. Su, E. C.; Rothschild, W. G., *J. Catal.* **1986**, *99*, 506.
23. Yao, H. C.; Yao, Y. F. Y., *J. Catal.* **1984**, *86*, 254.
24. Engler, B.; Koberstein, E.; Schubert, P., *Appl. Catal.* **1989**, *48*, 71.
25. Miki, T.; Ogawa, T.; Haneda, M.; Kakuta, N.; Ueno, A.; Tateishi, S.; Matsuura, S.; Sato, M., *J. Phys. Chem.* **1990**, *94*, 6464.
26. Marabelli, F.; Wachter, P., *Phys. Rev. B* **1987**, *36*, 1238.
27. Wuilloud, E.; Delley, B.; Schneider, W. D.; Baer, Y., *Phys. Rev. Lett.* **1984**, *53*, 202.
28. Ganduglia-Pirovano, M. V.; Hofmann, A.; Sauer, J., *Surf. Sci. Rep.* **2007**, *62*, 219.
29. Trovarelli, A.; de Leitenburg, C.; Boaro, M.; Dolcetti, G., *Catal. Today* **1999**, *50*, 353.
30. Naik, I. K.; Tien, T. Y., *J. Phys. Chem. Solids* **1978**, *39*, 311.
31. Friedman, L.; Holstein, T., *Ann. Phys.* **1963**, *21*, 494.
32. Holstein, T., *Ann. Phys.* **1959**, *8*, 325.
33. Tuller, H. L.; Nowick, A. S., *J. Phys. Chem. Solids* **1977**, *38*, 859.
34. Shoko, E.; Smith, M. F.; McKenzie, R. H., *J. Phys. Chem. Solids* **2011**, *72*, 1482.
35. Iordanova, N.; Dupuis, M.; Rosso, K. M., *J. Chem. Phys.* **2005**, *122*, 144305.
36. Iordanova, N.; Dupuis, M.; Rosso, K. M., *J. Chem. Phys.* **2005**, *123*, 074710.
37. Rosso, K. M.; Dupuis, M., *J. Chem. Phys.* **2004**, *120*, 7050.
38. Deskins, N. A.; Dupuis, M., *Phys. Rev. B* **2007**, *75*, 195212.
39. Marcus, R. A.; Sutin, N., *Biochim. Biophys. Acta* **1985**, *811*, 265.
40. Marcus, R. A., *Rev. Mod. Phys.* **1993**, *65*, 599.
41. Holstein, T., *Ann. Phys.* **2000**, *281*, 725.
42. Emin, D.; Holstein, T., *Ann. Phys. (N.Y.)* **1969**, *53*, 439.

43. Austin, I. G.; Mott, N. F., *Adv. Phys.* **2001**, *50*, 757.
44. Farazdel, A.; Dupuis, M.; Clementi, E.; Aviram, A., *J. Am. Chem. Soc.* **1990**, *112*, 4206.
45. Sanz, J. F.; Malrieu, J. P., *J. Phys. Chem.* **1993**, *97*, 99.
46. Calzado, C. J.; Sanz, J. F.; Castell, O.; Caballol, R., *J. Phys. Chem. A* **1997**, *101*, 1716.
47. Dovesi, R.; Saunders, V. R.; Roetti, R.; Orlando, R.; Zicovich-Wilson, C. M.; Pascale, F.; Civalleri, B.; Doll, K.; Harrison, N. M.; Bush, I. J.; D'Arco, P.; LLunell, M., *CRYSTAL09 user's manual*, Universidad de Torino **2009**.
48. Dolg, M.; Stoll, H.; Preuss, H., *J. Chem. Phys.* **1989**, *90*, 1730.
49. *The CRYSTAL web page* ??? <http://www.crystal.unito.it>.
50. Cora, F., *Mol. Phys.* **2005**, *103*, 2483.
51. Graciani, J.; Marquez, A. M.; Plata, J. J.; Ortega, Y.; Hernandez, N. C.; Meyer, A.; Zicovich-Wilson, C. M.; Sanz, J. F., *J. Chem. Theo. Comput.* **2011**, *7*, 56.
52. Plata, J. J.; Ruiz-Tagle, I.; Marquez, A. M.; Sanz, J. F., *J. Phys. Chem. Lett.* **2012**, *3*, 2092.
53. Adamo, C.; Barone, V., *Chem. Phys. Lett.* **1998**, *298*, 113.
54. Perdew, J. P.; Burke, K.; Ernzerhof, M., *Phys. Rev. Lett.* **1996**, *77*, 3865.
55. Monkhorst, H. J.; Pack, J. D., *Phys. Rev. B* **1976**, *13*, 5188.
56. Allen, G. C.; Wood, M. B.; Dyke, J. M., *J. Inorg. Nucl. Chem.* **1973**, *35*, 2311.
57. Calzado, C. J.; Sanz, J. F., *J. Am. Chem. Soc.* **1998**, *120*, 1051.
58. Miehlich, B.; Savin, A.; Stoll, H.; Preuss, H., *Chem. Phys. Lett.* **1989**, *157*, 200.
59. Becke, A. D., *J. Chem. Phys.* **1993**, *98*, 5648.
60. Lee, C. T.; Yang, W. T.; Parr, R. G., *Phys. Rev. B* **1988**, *37*, 785.
61. Heyd, J.; Scuseria, G. E., *J. Chem. Phys.* **2006**, *125*, 224106.
62. Zhao, Y.; Truhlar, D. G., *Theo. Chem. Acc.* **2007**, *120*, 215.
63. Sanz, J. F.; Calzado, C. J.; Marquez, A., *Int. J. Quantum Chem.* **2000**, *76*, 458.
64. Ulstrup, J., *Lecture Notes in Chemistry*, Springer **1979**.
65. Brunschwig, B. S.; Logan, J.; Newton, M. D.; Sutin, N., *J. Am. Chem. Soc.* **1980**, *102*, 5798.
66. Zener, C., *P. R. Soc. Lond. A-Conta.* **1933**, *140*, 660.
67. Landau, L., *Phys. Z. Sowjeunion* **1932**, *2*, 24.
68. Mochizuki, S., *Phys. Status Solidi B* **1982**, *114*, 189.
69. Kaspar, J.; Fornasiero, P.; Graziani, M., *Catal. Today* **1999**, *50*, 285.
70. Rodriguez, J. A.; Graciani, J.; Evans, J.; Park, J. B.; Yang, F.; Stacchiola, D.; Senanayake, S. D.; Ma, S.; Perez, M.; Liu, P.; Sanz, J. F.; Hrbek, J., *Angew. Chem. Int. Ed.* **2009**, *48*, 8047.
71. Graciani, J.; Plata, J. J.; Sanz, J. F.; Liu, P.; Rodriguez, J. A., *J. Chem. Phys.* **2010**, *132*, 104703.

72. Gorte, R. J., *AIChE J.* **2010**, *56*, 1126.
73. Inaba, H.; Tagawa, H., *Solid State Ionics* **1996**, *83*, 1.
74. Wachsman, E. D.; Lee, K. T., *Science* **2011**, *334*, 935.
75. Marquez, J. J. P. A. M.; Sanz, J. F., *J. Phys. Chem. C* **2012**, *3*.
76. Park, S. D.; Vohs, J. M.; Gorte, R. J., *Nature* **2000**, *404*, 265.
77. Andersson, D. A.; Simak, S. I.; Skorodumova, N. V.; Abrikosov, I. A.; Johansson, B., *Proc. Natl. Acad. Sci. U.S.A.* **2006**, *103*, 3518.
78. Dholabhai, P. P.; Adams, J. B.; Crozier, P.; Sharma, R., *J. Chem. Phys.* **2010**, *132*, 094104.
79. Yoo, H.-I.; Lee, C.-E., *Solid State Ionics* **2009**, *180*, 326.
80. Chatzichristodoulou, C.; Hendriksen, P. V., *J. Electrochem. Soc.* **2010**, *157*, B481.
81. Chatzichristodoulou, C.; Hendriksen, P. V.; Hagen, A., *J. Electrochem. Soc.* **2010**, *157*, B299.
82. Nakayama, M.; Ohshima, H.; Nogami, M.; Martin, M., *PCCP* **2012**, *14*, 6079.
83. Li, H.-Y.; Wang, H.-F.; Gong, X.-Q.; Guo, Y.-L.; Guo, Y.; Lu, G.; Hu, P., *Phys. Rev. B* **2009**, *79*, 193401.
84. Ganduglia-Pirovano, M. V.; Silva, J. L. F. D.; Sauer, J., *Phys. Rev. Lett.* **2009**, *102*, 026101.
85. Morgan, B. J.; Watson, G. W., *Phys. Rev. B* **2009**, *80*, 233102.
86. Keating, P. R. L.; Scanlon, D. O.; Morgan, B. J.; Galea, N. M.; Watson, G. W., *J. Phys. Chem. C* **2012**, *116*, 2443.
87. Marquez, J. J. P. A. M.; Sanz, J. F., *J. Chem. Phys.* **2012**, *136*.
88. Kresse, G.; Hafner, J., *Phys. Rev. B* **1993**, *47*, 558.
89. Kresse, G.; Hafner, J., *Phys. Rev. B* **1993**, *48*, 13115.
90. Kresse, G.; Hafner, J., *Phys. Rev. B* **1994**, *49*, 14251.
91. Blochl, P. E., *Phys. Rev. B* **1994**, *50*, 17953.
92. Kresse, G.; Joubert, D., *Phys. Rev. B* **1999**, *59*, 1758.
93. Perdew, J. P.; Chevary, J. A.; Vosko, S. H.; Jackson, K. A.; Pederson, M. R.; Singh, D. J.; Fiolhais, C., *Phys. Rev. B* **1992**, *46*, 6671.
94. Perdew, J. P.; Chevary, J. A.; Vosko, S. H.; Jackson, K. A.; Pederson, M. R.; Singh, D. J.; Fiolhais, C., *Phys. Rev. B* **1993**, *48*, 4978.
95. Dudarev, S. L.; Botton, G. A.; Savrasov, S. Y.; Humphreys, C. J.; Sutton, A. P., *Phys. Rev. B* **1998**, *57*, 1505.
96. Harris, J., *Phys. Rev. B* **1985**, *31*, 1770.
97. Sheppard, D.; Terrell, R.; Henkelman, G., *J. Chem. Phys.* **2008**, *128*, 134106.
98. Maxisch, T.; Ceder, G., *Phys. Rev. B* **2006**, *73*, 174112.
99. Han, X.; Lee, J.; Yoo, H., *Phys. Rev. B* **2009**, *79*, 100403.
100. Jerratsch, J. F.; Shao, X.; Nilius, N.; Freund, H.-J.; Popa, C.; Ganduglia-Pirovano, M. V.;

- Burow, A. M.; Sauer, J., *Phys. Rev. Lett.* **2011**, *106*, 246801.
101. Litzelman, S. J.; Tuller, H. L., *Solid State Ionics* **2009**, *180*, 1190.
102. Tschope, A., *J. Electroceramics* **2005**, *14*, 5.
103. Burbano, M.; Norberg, S. T.; Hull, S.; Eriksson, S. G.; Marrocchelli, D.; Madden, P. A.; Watson, G. W., *Chem. Mater.* **2012**, *24*, 222.

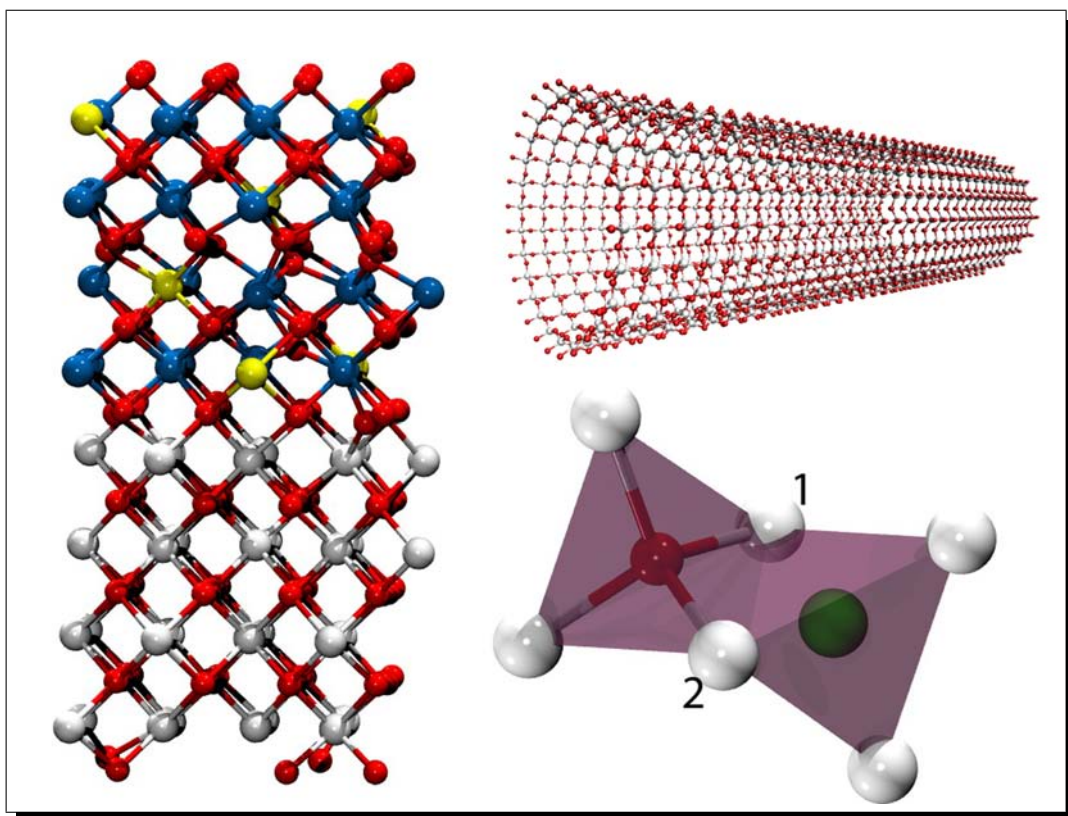


---

CHAPTER  
**FIVE**

---

Ceria as nanostructure



## 5.1 Introduction

In the recent years, development of new ceria nanomaterials has received much attention in the literature as new synthetic techniques has enabled the prepararion of low dimensional nanostructures such as nanorods, nanotubes, nanoplates, nanocages or epitaxial heterostructures which exhibit excelent properties for different technological applications.<sup>1–14</sup> However, fabrication of nanocrystalline systems with the desired dimension and shape to provide the desired activity and efficiency for catalytic purposes is still an ultimate challenge in modern material research.

The success of ceria as a catalyst is strongly related to the easy  $\text{Ce}^{3+}/\text{Ce}^{4+}$  conversion. As a consequence, surface oxygen vacancies are easily stabilized and ceria can behave as an oxygen buffer in many oxidizing reactions. These properties are strongly related to the surface structure, specifically to the nature of the exposed surface planes of  $\text{CeO}_2$ .<sup>15–18</sup> In fact, the effect of the structure of the exposed crystal plane has been found to strongly affect the activity of ceria supported gold particles in WGS and low temperature CO oxidation reactions.<sup>19–21</sup> For this reason, the development of new ceria nanostructures controlling their structure and exposed planes has recently led to the appearance of more active and efficient ceria-based catalysts.<sup>22,23</sup>

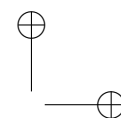
Taking into account all these considerations, ceria nanotubes are strong candidates to be the basis for highly active ceria based catalyst. Nanotubes exhibit high specific surface area and can be tuned to expose a desired plane. Moreover it has been reported that ceria nanotubes presents high density of oxygen vacancies and  $\text{Ce}^{3+}$  ions.<sup>24</sup> In fact, highly active metal clusters supported on ceria nanotubes where reported recently for different oxidation reactions.<sup>25–28</sup> However, the mechanism of formation and stabilization of these 1D nanostructure is not well known yet.

Solid oxide fuel cell (SOFC) is among the most promising, sustainable and environmental friendly technologies for power generation. Their main disadvantage is their high working temperature (800 – 1000 °C) wich introduces difficulties related to materials and structure stabilities. A current objective is, thus, to reduce the operating temperature to about 500 – 700 °C by increasing the ionic conductivity of the solid electrolyte. Different strategies are being pursued simultaneously to reach this goal. Rare earth doped ceria are promising electrolyte materis due to their high electronic conductivity at low temperatures.<sup>29</sup> Nanocrystalline materials are also actively investigated as increases of about 2-3 orders of magnitude in ionic conductivity have been found compared to microcrystalline systems.<sup>30–33</sup> This is related to the high number of surface atoms that expose these systems that are active sites for reactions and allow to enhance the ionic conductivity across the interfaces. Moreover, many of these systems develop mixed ionic/electronic conductivity properties which also makes them anode candidates in SOFCs.

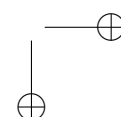
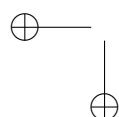
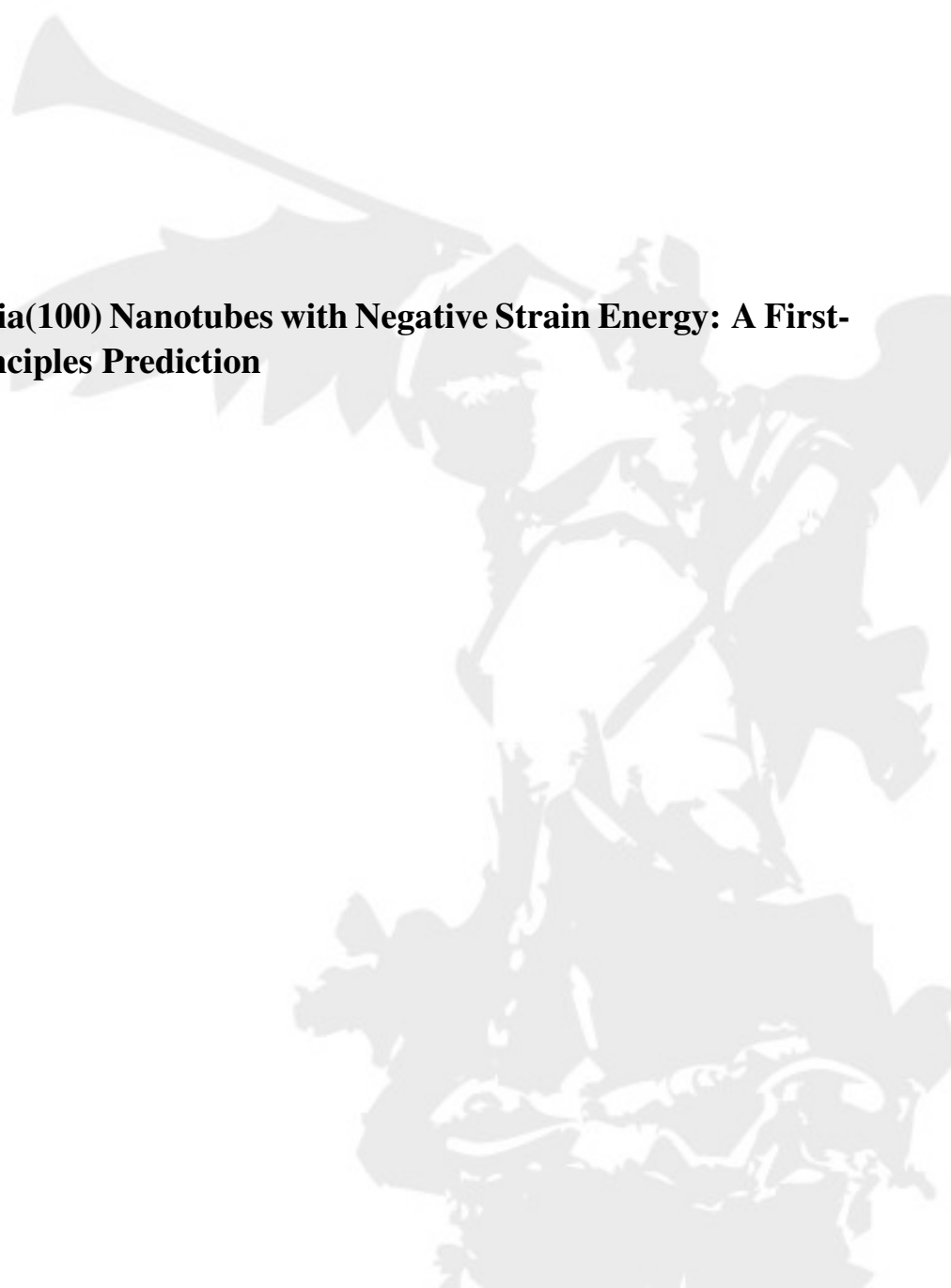
In this chapter we will analyze the formation and stabilization and rationalize the



properties of some low dimensional  $\text{CeO}_2$  nanostructures. Ceria (100) nanotubes (NT) will be studied in order to explore their stability, geometric, and electronic structure. The stability of these systems will be rationalized in terms of reduction of NT strain and bond covalency reinforcement. Moreover, gold adsorption on ceria nanotubes will be evaluated to analyze its potential use as catalyst. The second part of this chapter will be dedicated to ceria epitaxial heterostructures on yttria stabilized zirconia (YSZ). First, the effect of the strain lattice on the oxygen migration barrier in the zirconia phase will be evaluated. Later on,  $\text{Ce}^{3+}$  and vacancy stabilization will be explored. Finally, we will rationalize the enhancement of the ionic conductivity of these nanostructures based on the properties of doped ceria layers.



## 5.2 Ceria(100) Nanotubes with Negative Strain Energy: A First-Principles Prediction



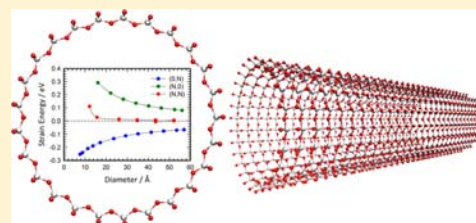
## Ceria(100) Nanotubes with Negative Strain Energy: A First-Principles Prediction

José J. Plata, Igor Ruiz-Tagle,<sup>†</sup> Antonio M. Márquez, and Javier Fdez. Sanz\*

Departamento de Química Física, Facultad de Química, Universidad de Sevilla, E-41012 Sevilla, Spain

**ABSTRACT:** Over the past decade, one-dimensional (1D) ceria nanotubes (NTs) have been synthesized and reported as promising candidates for catalysis. Here, for first time, we address the structural and electronic properties of a family of ceria single-walled NTs by means of state-of-the-art periodic density functional theory (DFT) calculations using a hybrid functional. Strain energies were found to be negative in almost the whole diameter range for the (0,N) series, indicating the stability of these NTs relative to the ceria flat layer. Both O2p–Ce4f and O2p–Ce5d band gaps are found to widen with respect to the bulk values. Gold atoms have been deposited on both the outer and inner surfaces of a prototypical NT, the interaction energy being of  $\sim 1.4$  eV. These surfaces appear to be easily reducible with the formation of cationic Au<sup>+</sup> species, which make them especially attractive for catalytic purposes.

**SECTION:** Physical Processes in Nanomaterials and Nanostructures



Cerium oxide (either CeO<sub>2</sub> or nonstoichiometric CeO<sub>2-x</sub>), commonly referred to as ceria, is one of the most important rare earth materials, and has been extensively studied for many technological applications such as heterogeneous catalysis, luminescence, fuel cells, and solar cells due to its chemical stability, high oxygen storage capacity, and so forth.<sup>1–3</sup> Ceria nanoparticles supported on either another (reducible) metal oxide (TiO<sub>2</sub>),<sup>4,5</sup> or a metal such as Cu (the inverted catalyst), have also been considered and actually found to display a high catalytic activity in the water–gas shift (WGS) reaction.<sup>6</sup>

It is recognized that one-dimensional (1D) nanostructures may exhibit unique electrical, optical, magnetic, mechanical, and thermal properties that are obviously different from those of bulk materials, and they have been the focus of intense research owing to their fascinating physical and chemical properties. Recently, 1D ceria nanostructures as nanowires, nanorods, or nanotubes (NTs), have been synthesized.<sup>7,8</sup> Moreover, ceria NTs have been reported to be active catalyst for the WGS reaction at low temperatures.<sup>9</sup> High porosity and oxygen storage capacity, and excellent reducibility are some of the properties found for these systems.<sup>10–12</sup> Although much has been learned about the synthesis of ceria NTs,<sup>13</sup> the mechanism of formation and its structural and electronic properties remain poorly understood. In fact, as far as we can ascertain, this type of 1D ceria nanostructures have never been studied from a quantum chemical point of view, and only classical atomistic simulations have been reported.<sup>14</sup> In this study, for the first time, periodic density functional theory (DFT) calculations using a hybrid functional were carried out to model and analyze the stability, structure, and electronic properties of ceria NTs. As a preliminary study focused on the catalytic behavior of these systems, the interaction between gold atoms and ceria

NTs was also studied in order to predict the possible applications and properties as catalyst.

Catalytic and optical performance of nanometer-sized cerium oxide strongly depends on its morphology and crystallographic orientation. Ceria (100) layers are one of the possible wall structures found in CeO<sub>2</sub>-based NTs.<sup>15</sup> This surface is reconstructed because of a dipole moment perpendicular to the surface, so a removal and shift of 50% of the terminating oxygen species is performed.<sup>16</sup> The reconstructed surface presents three different atomic layers corresponding to one layer of 4-fold coordinated Ce atoms in between two O layers. The O layers consist of rows of 2-fold coordinated or bridging oxygen atoms (O<sub>b</sub>) perpendicular to each other. Three rollup vectors were chosen to obtain single-walled monolayer nanotubes (SWNTs) with different chirality: (N,0), (0,N) and (N,N), as depicted in Figure 1a. Different oxygen terminations are generated depending on the folding. The (N,0) and (0,N), which actually are not chiral, differ in the orientation of the outer/inner O<sub>b</sub> rows (see Figure 1b). Thus, the (N,0) rollup leads to O<sub>b</sub> rows perpendicular to the growing vector of the NT in the outer layer (<sup>out</sup>O<sub>b</sub>) and parallel in the inner layer (<sup>in</sup>O<sub>b</sub>). The opposite arrangement is obtained in the case of the (0,N) rollup. For the (N,N) rollup mode, rows of oxygen atoms forming a 45° angle (diag) with the growing vector of the NT are obtained; in this case, the NT is chiral.

The outstanding catalytic properties of ceria rely on its facile Ce<sup>3+</sup> ↔ Ce<sup>4+</sup> redox conversion;<sup>17</sup> however, the strongly correlated nature of the 4f electrons means that pure GGA

Received: June 5, 2012

Accepted: July 23, 2012

Published: July 23, 2012

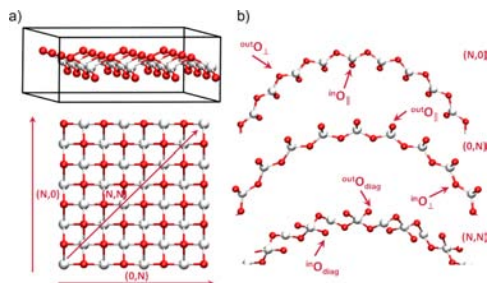


**Figure 1.** (a) Rollup vectors for the ceria NTs and top view of the one-layer (001) ceria nanosheet. Side-view pictured at the top showing the oxygen rows. (b) Oxygen terminations for the different growing modes. Atom colors: red = O, white = Ce.

functionals are not well suited to model oxidized and reduced ceria. In this work, we use the hybrid B1-WC functional,<sup>18</sup> which has been found to consistently describe structural and electronic properties of ceria materials.<sup>19</sup> To model the NTs, we took advantage of the helical rototranslational symmetry recently implemented in the periodic CRYSTAL09 code.<sup>20</sup> The symmetry is used for the automatic generation of the structure, for the calculation of one and two-electron integrals and for the diagonalization of the Fock matrix, where each irreducible representation is treated separately.<sup>21,22</sup> The calculations setup is similar to that previously reported in ref 19, and additional information is given in the Computational Details section. In order to measure the stability of the NT, we compute the strain energies,  $E_s$ , defined as  $E_s = E_{CeO_2}^{NT} - E_{CeO_2}^{NS}$ , where  $E_{CeO_2}^{NT}$  is the energy of one  $CeO_2$  unit in the NT, and  $E_{CeO_2}^{NS}$  is the energy of one  $CeO_2$  unit in the nanosheet.<sup>22</sup>

The strain energy for the (N,0), (0,N) and (N,N) NTs are reported in Figure 2a. In general, the strain originating from the curvature of the NT is expected to increase when its diameter is reduced, and the (N,0) and (N,N) series show this trend. However, while the (N,N) curve quickly converges to zero, the (N,0) curve shows higher strain energy values and a slower decay to zero. Both structures presented positive strain energy values in the whole range, indicating that they are not stable compared to the ceria (100) nanosheet. Interestingly, the behavior of the (0,N) series is completely different from that observed for the two other series. First, the values of the strain energy are negative, i.e., more stable than the 1-layer ceria nanosheet. Second, the higher the curvature of the NT, the lower the strain energy obtained, which is quite a peculiar behavior since, as commented above, one could expect that rolling a flat slab leads to less stable structures. This behavior has also been theoretically observed in single-layered  $SrTiO_3$  NTs,<sup>23</sup> and shows how the modification of the rollup vector dramatically modifies the stability of the structure.

To elucidate the factors affecting the stability of these systems, we have carefully analyzed the structural and electronic properties of each series. If we compare the (N,0) and (0,N) strain energies, the curves look like mirror images. In fact, their structures just differ in the  $O_b$  termination at the inner and outer surfaces.  $O_b$  rows in the inner and outer surface are perpendicular and parallel, respectively, to the growing vector of the NT in (0,N) systems, while the situation is the opposite for (N,0) structures. This suggests that oxygen termination may

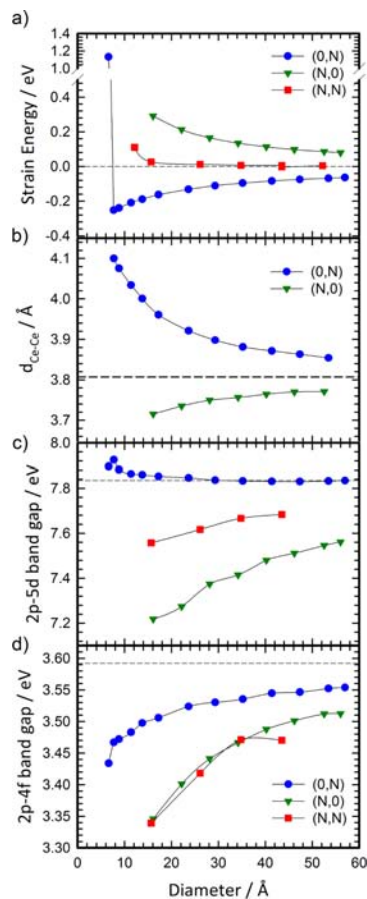


**Figure 2.** Properties of single-walled monolayer ceria (001) NT versus the NT diameter. (a) Strain energy; (b) interatomic Ce–Ce distance; (c) O2p–Ce5d band gap; (d) O2p–Ce4f band gap. Horizontal dashed lines correspond to the values computed for the ceria nanosheet.

determine the stability of the structure. Over all the structures considered, the Ce–O interatomic distance changes less than 0.020 Å with respect to the nanosheet; however, the Ce–O–Ce angle and Ce–Ce distance are strongly modified depending on the rollup mode, as shown in Figure 2b. While for the (N,0) NT series the Ce–Ce distance increases when the diameter grows, this distance lowers for the (0,N) NT series. An almost mirror image relationship between both curves was again observed.

To rationalize this behavior, we first realize that (N,0) and (0,N) modes actually correspond to upward and downward folding of the same sheet (Figure 1a). Depending on the up/down mode, the outer  $O_b$  rows are perpendicular or parallel to the growing vector. A Mulliken population gives an average net charge for these atoms of  $-1.24$  |e|. Since these rows of bridging oxygen atoms are facing each other, it is reasonable to

assume that the repulsion between these negatively charged atoms is the main reason for the energy differences observed between the series. The interbridge distance decreases in the (N,0) rollup, while it increases in the (0,N) mode. To gain a deeper insight into the structure, we have reported in Figure 3

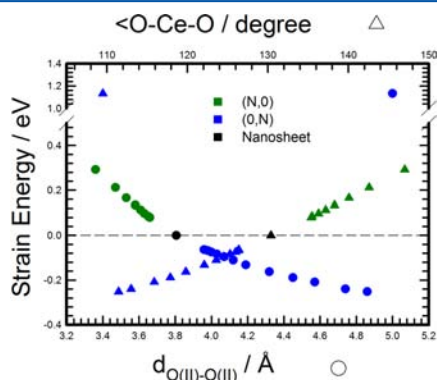


Figure 3. Strain energy of ceria (001) NTs versus the  $O_{||}-O_{||}$  interatomic distance (circles) and  $O_{\perp}-Ce-O_{\perp}$  bond angle (triangles).

strain energies against some relevant structural parameters in such a way that both growth modes might be viewed in the same plot. Figure 3 shows the dependence of the strain energy on the distance between parallel oxygen rows. As indicated above, these are in the inner layer in the (N,0) NTs and in the outer layer in the (0,N) NTs. If we start from the nanosheet (3.805 Å, the reference in Figure 3), decreasing this value (lowering the diameter in the (N,0) series) leads to a higher strain energy partly due to the larger repulsion between  $O_{||}$ . Concomitantly, the  $O_{\perp}-Ce-O_{\perp}$  angle increases, which also adds to the instability. On the contrary, when the distance between parallel oxygen atoms increases (i.e., the diameter in the (0,N) NTs decreases), the electrostatic repulsion between these atoms lowers and so does the strain energy. The minimum is obtained for the (0,7) NT, where the  $O_{\perp}-Ce-O_{\perp}$  angles are slightly higher than the tetrahedral value. For the (0,6) NT, the energy suddenly raises mainly due to the quasi-linearity of the  $Ce-O_{\perp}-Ce$  bond angles needed to accommodate the Ce atoms in such a reduced circle. Indeed, this angle grows when the diameter lowers until near  $170^{\circ}$  for the (0,6) NT.

To analyze the dependence of the electronic properties on the NT diameter, we have estimated the density of states (DOS) for the three series. Plots for the relevant band-gaps are reported in Figure 2c,d. As can be observed, the  $O2p-Ce4f$  gap increases with the diameter of the NT in the three series; however, different trends were obtained for  $O2p-Ce5d$  gaps. For the (N,0) and (N,N) series, this band gap increases with the diameter, according to the lowering of the strain energy. Yet, it monotonously decreases with the diameter converging to the value found for the nanosheet (dashed line) for the (0,N) family, which is the structure with negative strain energy values. This finding suggests that this behavior could be related to the stability of the NT and tentatively accounted for taking into account that in this case the  $Ce-O$  distance is slightly reduced when the diameter lowers, leading, therefore, to a better overlap

between Ce and O orbitals. Consequently, a reinforcement of the covalency occurs, widening the gap between the bands corresponding to the involved orbitals, the Ce 5d (formally empty) and the O 2p orbitals. In summary, the stability found for (0,N) NTs might be due to both structural reasons (the presence of  $O_{\perp}$  in the inner surface and  $O_{||}$  in the outer surface) and electronic reasons (the reinforcement of the covalency between O 2p and Ce 5d orbitals). Moreover, due to quantum confinement, both  $O2p-Ce4f$  and  $O2p-Ce5d$  band gaps are found to widen with respect to bulk values computed with the same functional (3.18 and 7.48 eV),<sup>19</sup> although, compared with  $TiO_2$  NTs, the increments are relatively small.<sup>22</sup>

To model the interaction of coinage metals with these ceria nanostructures, we considered the deposition of single gold atoms on a prototypical NT. To this aim, we chose one of the most stable NT, the (0,8), with a diameter of 8.8 Å. We took a supercell consisting of four units that, with a length of 15.288 Å, ensures that Au-Au lateral interactions are minimized. Au atoms were added both at the inner and outer surfaces, and several sites were explored, and in both cases two stable sites were found. In site  $O_{top}$ , the Au atom binds on top of an oxygen atom, although in the optimized structure it appears to be somewhat tilted toward the  $O_{||}$  row. In the second site, the Au atom bridges two parallel oxygen atoms forming a quasi-linear  $O-Au-O$  bond, normal to the growing direction: the  $^{out}O_{||}-^{out}O_{||}(L)$  site in Figure 4. The labeling used for the

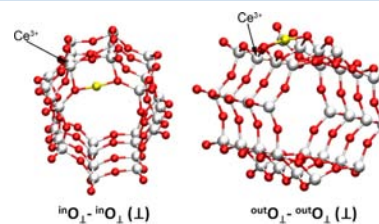


Figure 4. Most stable structure of gold atoms (yellow) adsorbed on inner and outer surfaces of ceria (0,8) NT.

inner surface follows a similar scheme. Adsorption basis set superposition error (BSSE)-corrected energies and gold population analyses obtained from spin-polarized calculations are shown in Table 1. The interaction energies at the bridging sites are large, falling in the range 1.15–1.43 eV, while the atop position gives place to weaker interaction. In the table, data obtained for the deposition of gold on a two-layer nanosheet have also been included. As can be seen, the energetics obtained for the nanosheet and the outer surface of the NT is quite similar. These values are noticeably larger than those

Table 1. Computed Adsorption Energies (in eV) and Charge of Gold Deposited on the (0,8) NT and the Two-Layer Ceria Nanosheet

surface	position	$E_{ads}/\text{eV}$	charge/ el
outer	$O_{top}$	-0.64	0.29
	$^{out}O_{  }-^{out}O_{  }(L)$	-1.43	0.87
inner	$^{in}O_{\perp}-^{in}O_{\perp}(  )$	-1.15	0.90
	$^{in}O_{\perp}-^{in}O_{\perp}(L)$	-1.38	0.88
nanosheet	$O_{top}$	-0.34	0.63
	$O_b-O_b$	-1.45	0.92

estimated for the CeO<sub>2</sub>(111) surface from DFT+U calculations.<sup>24–26</sup> When the charge of gold is analyzed, one can see that there is a clear reduction of the surface, and gold atoms are found to be almost monopositive in the most stable sites. A correlation between the charge and the interaction energy is observed too. The oxidation of the gold atom is consistent with the increment in the electron population found in a neighboring atom, as indicated in Figure 4. The Mulliken net charge computed for this atom decreases after gold deposition from +2.48 lel to +2.15 lel, mainly involving the 4f orbitals, and the bond-distances of the neighboring oxygen ions are found to be slightly lengthened. This oxidation of gold atoms is also in contrast with the almost negligible oxidation of gold observed in the CeO<sub>2</sub>(111) surface from DFT+U calculations.<sup>24</sup> Moreover, the reducibility of the NTs might be analyzed by comparing the vacancy formation energy,  $E_{\text{vac}}$ , with those of low-index ceria surfaces. For the (0,8) NT, we estimate an  $E_{\text{vac}}$  of 2.18 eV, close to that reported for the CeO<sub>2</sub>(100) surface (2.27 eV), which in turn is smaller than that estimated for the CeO<sub>2</sub>(111) surface (2.60 eV) from DFT+U calculations.<sup>27</sup>

In summary, negative strain energies have been predicted using DF calculations with a hybrid functional for single walled monolayer ceria NTs. The NT stability has been interpreted on the basis of interactions between terminating surface oxygen atoms. The reduction of NT strain and the reinforcement of covalency have been identified as the main factors determining the NT stability. Gold atoms show different behavior depending on the adsorption site (inside or outside the NT). Compared to CeO<sub>2</sub>(111) surface, we found that gold atoms are more easily oxidized upon deposition, and therefore high catalytic activity is expected for these systems in processes where either the reducibility of the support or the presence of cationic gold are expected to be key factors.

#### ■ COMPUTATIONAL DETAILS

Inner electrons of Ce atom were replaced by an effective core potential developed by the Stuttgart–Dresden group.<sup>28</sup> The Ce electrons explicitly treated were the 4s<sup>2</sup>4p<sup>6</sup>4d<sup>10</sup>5s<sup>2</sup>5p<sup>6</sup>4f<sup>1</sup>6s<sup>2</sup>5d<sup>1</sup>, with a (10sp7d8f)/[4sp2d3f] basis set optimized to properly describe oxides where the metal features III and IV oxidation states. The corresponding exponents and coefficients can be found in ref 29. For O, an all-electron basis set proposed for ionic crystals was adopted.<sup>30</sup> The two most external sp and d exponents have been reoptimized for cerium oxide, their resulting values being 0.4798717, 0.1801227, and 0.2991812 bohr<sup>-2</sup>, respectively. Inner electrons of Au atom were replaced by an effective core potential developed by Hay and Wadt.<sup>31</sup> The Au electrons explicitly treated were the 5s<sup>2</sup>5p<sup>6</sup>5d<sup>10</sup>6s<sup>1</sup>, with a (8s4p3d)/[3s2p2d] basis set.<sup>32</sup> The reciprocal space was sampled according to a regular sublattice determined by the shrinking factor 6 6 (four independent k-points in the irreducible part of the Brillouin zone). Full optimization (lattice constants and atomic positions) of CeO<sub>2</sub> NTs was carried out using a convergence criterion of  $3 \times 10^{-4}$  hartree/bohr for the root-mean-square values of forces and  $1.2 \times 10^{-3}$  bohr in the root-mean-square values of atomic displacements. The counterpoise method was applied to correct for the BSSE in adsorption energy values. Mulliken population analysis was also performed in order to quantify charge transfer effects.

#### ■ AUTHOR INFORMATION

##### Corresponding Author

\*E-mail: sanz@us.es.

#### Notes

The authors declare no competing financial interest.

<sup>†</sup>On leave from Departamento de Ciencias Químicas, Universidad Andrés Bello, Santiago de Chile, Chile.

#### ■ ACKNOWLEDGMENTS

This work was funded by the Ministerio de Economía y Competitividad (Spain, Grants MAT2012-31526 and CSD2008-0023). Computational resources were provided by the Barcelona Supercomputing Center/Centro Nacional de Supercomputación (Spain). I.R.-T. acknowledges the financial support of Chilean grants: The Millennium Nucleus Project P07-006-F, UNAB DI-12-09/1 and Conicyt fellowship No. 2108064, and the Junta de Andalucía (P08-FQM-3661) for supporting his stay at the University of Seville.

#### ■ REFERENCES

- (1) Inaba, H.; Tagawa, H. Ceria-based solid electrolytes. *Solid State Ionics* **1996**, *83*, 1–16.
- (2) Kaspar, J.; Fornasiero, P.; Graziani, M. Use of CeO<sub>2</sub>-based oxides in the three-way catalysis. *Catal. Today* **1999**, *50*, 285–298.
- (3) Trovarelli, A. In *Catalysis by Ceria and Related Materials*; Imperial College Press: 2002; Vol. 2.
- (4) Park, J. B.; Graciani, J.; Evans, J.; Stacchiola, D.; Ma, S. G.; Liu, P.; Nambu, A.; Sanz, J. F.; Hrbek, J.; Rodriguez, J. A. High catalytic activity of Au/CeO<sub>2</sub>/TiO<sub>2</sub>(110) controlled by the nature of the mixed-metal oxide at the nanometer level. *Proc. Natl. Acad. Sci. U.S.A.* **2009**, *106*, 4975–4980.
- (5) Park, J. B.; Graciani, J.; Evans, J.; Stacchiola, D.; Senanayake, S. D.; Barrio, L.; Liu, P.; Sanz, J. F.; Hrbek, J.; Rodriguez, J. A. Gold, Copper, and Platinum Nanoparticles Dispersed on CeO<sub>2</sub>/TiO<sub>2</sub>(110) Surfaces: High Water-Gas Shift Activity and the Nature of the Mixed-Metal Oxide at the Nanometer Level. *J. Am. Chem. Soc.* **2010**, *132*, 356–363.
- (6) Rodriguez, J. A.; Graciani, J.; Evans, J.; Park, J. B.; Yang, F.; Stacchiola, D.; Senanayake, S. D.; Ma, S.; Perez, M.; Liu, P.; Fdez Sanz, J.; Hrbek, J. Water-Gas Shift Reaction on a Highly Active Inverse CeO<sub>2</sub>/Cu(111) Catalyst: Unique Role of Ceria Nanoparticles. *Angew. Chem., Int. Ed.* **2009**, *48*, 8047–8050.
- (7) Pan, C.; Zhang, D.; Shi, L. CTAB assisted hydrothermal synthesis, controlled conversion and CO oxidation properties of CeO<sub>2</sub> nanoplates, nanotubes, and nanorods. *J. Solid State Chem.* **2008**, *181*, 1298–1306.
- (8) Macedo, A. G.; Fernandes, S. E. M.; Valente, A. A.; Ferreira, R. A. S.; Carlos, L. D.; Rocha, J. Catalytic Performance of Ceria Nanorods in Liquid-Phase Oxidations of Hydrocarbons with tert-Butyl Hydroperoxide. *Molecules* **2010**, *15*, 747–765.
- (9) Han, W.; Wen, W.; Hanson, J. C.; Teng, X.; Marinkovic, N.; Rodriguez, J. A. One-Dimensional Ceria as Catalyst for the Low-Temperature Water-Gas Shift Reaction. *J. Phys. Chem. C* **2009**, *113*, 21949–21955.
- (10) Zhou, K.; Yang, Z.; Yang, S. Highly reducible CeO<sub>2</sub> nanotubes. *Chem. Mater.* **2007**, *19*, 1215–1217.
- (11) Han, W.; Wu, L.; Zhu, Y. Formation and oxidation state of CeO<sub>2-x</sub> nanotubes. *J. Am. Chem. Soc.* **2005**, *127*, 12814–12815.
- (12) Chen, G.; Xu, C.; Song, X.; Zhao, W.; Ding, Y.; Sun, S. Interface reaction route to two different kinds of CeO<sub>2</sub> nanotubes. *Inorg. Chem.* **2008**, *47*, 723–728.
- (13) Lin, K.; Chowdhury, S. Synthesis, Characterization, and Application of 1-D Cerium Oxide Nanomaterials: A Review. *Int. J. Mol. Sci.* **2010**, *11*, 3226–3251.
- (14) Martin, P.; Parker, S. C.; Sayle, D. C.; Watson, G. W. Atomistic modeling of multilayered ceria nanotubes. *Nano Lett.* **2007**, *7*, 543–546.
- (15) Tang, C.; Bando, Y.; Liu, B.; Golberg, D. Cerium oxide nanotubes prepared from cerium hydroxide nanotubes. *Adv. Mater.* **2005**, *17*, 3005–3009.

- (16) Nolan, M.; Grigoletti, S.; Sayle, D.; Parker, S.; Watson, G. Density functional theory studies of the structure and electronic structure of pure and defective low index surfaces of ceria. *Surf. Sci.* **2005**, *576*, 217–229.
- (17) Trovarelli, A.; de Leitenburg, C.; Boaro, M.; Dolcetti, G. The utilization of ceria in industrial catalysis. *Catal. Today* **1999**, *50*, 353–367.
- (18) Wu, Z.; Cohen, R. More accurate generalized gradient approximation for solids. *Phys. Rev. B* **2006**, *73*, 235116.
- (19) Graciani, J.; Márquez, A. M.; Plata, J. J.; Ortega, Y.; Hernández, N. C.; Meyer, A.; Zicovich-Wilson, C. M.; Sanz, J. F. Comparative Study on the Performance of Hybrid DFT Functionals in Highly Correlated Oxides: The Case of CeO<sub>2</sub> and Ce<sub>2</sub>O<sub>3</sub>. *J. Chem. Theory Comput.* **2011**, *7*, 56–65.
- (20) Dovesi, R.; Saunders, V. R.; Roetti, R.; Orlando, R.; Zicovich-Wilson, C. M.; Pascale, F.; Civalieri, B.; Doll, K.; Harrison, N. M.; Bush, I. J.; D'Arco, P.; Lunell, M. In *CRYSTAL09 User's Manual*; University of Torino: Torino, Italy, 2009; .
- (21) Noel, Y.; D'Arco, P.; Demichelis, R.; Zicovich-Wilson, C. M.; Dovesi, R. On the Use of Symmetry in the Ab Initio Quantum Mechanical Simulation of Nanotubes and Related Materials. *J. Comput. Chem.* **2010**, *31*, 855–862.
- (22) Ferrari, A. M.; Szieberth, D.; Zicovich-Wilson, C. M.; Demichelis, R. Anatase(001) 3 ML Nanotubes, The First TiO<sub>2</sub> Nanotube With Negative Strain Energies: A DFT Prediction. *J. Phys. Chem. Lett.* **2010**, *1*, 2854–2857.
- (23) Piskunov, S.; Spohr, E. SrTiO<sub>3</sub> Nanotubes with Negative Strain Energy Predicted from First Principles. *J. Phys. Chem. Lett.* **2011**, *2*, 2566–2570.
- (24) Branda, M. M.; Hernández, N. C.; Sanz, J. F.; Illas, F. Density Functional Theory Study of the Interaction of Cu, Ag, and Au Atoms with the Regular CeO<sub>2</sub> (111) Surface. *J. Phys. Chem. C* **2010**, *114*, 1934–1941.
- (25) Branda, M. M.; Castellani, N. J.; Grau-Crespo, R.; de Leeuw, N. H.; Hernández, N. C.; Sanz, J. F.; Neyman, K. M.; Illas, F. On the difficulties of present theoretical models to predict the oxidation state of atomic Au adsorbed on regular sites of CeO<sub>2</sub>(111). *J. Chem. Phys.* **2009**, *131*, 094702.
- (26) Hernández, N. C.; Grau-Crespo, R.; de Leeuw, N. H.; Sanz, J. F. Electronic charge transfer between ceria surfaces and gold adatoms: a GGA plus U investigation. *Phys. Chem. Chem. Phys.* **2009**, *11*, 5246–5252.
- (27) Nolan, M.; Parker, S. C.; Watson, G. W. The electronic structure of oxygen vacancy defects at the low index surfaces of ceria. *Surf. Sci.* **2005**, *595*, 223–232.
- (28) Dolg, M.; Stoll, H.; Preuss, H. Energy-adjusted ab initio pseudopotentials for the rare-earth elements. *J. Chem. Phys.* **1989**, *90*, 1730–1734.
- (29) CRYSTAL web page: <http://www.crystal.unito.it> (accessed July 26, 2012).
- (30) Cora, F. The performance of hybrid density functionals in solid state chemistry: the case of BaTiO<sub>3</sub>. *Mol. Phys.* **2005**, *103*, 2483–2496.
- (31) Hay, P.; Wadt, W. Ab initio effective core potentials for molecular calculations - potentials for K to Au including the outermost core orbitals. *J. Chem. Phys.* **1985**, *82*, 299–310.
- (32) Wehrich, R.; Anusca, I. Halfantiperovskites II: on the Crystal Structure of Pd<sub>3</sub>Bi<sub>2</sub>S<sub>7</sub>. *Z. Anorg. Allg. Chem.* **2006**, *632*, 335–342.

### 5.3 Influence of Dopants on the Conductivity of Ceria/Zirconia Heteroepitaxial Structures

José J. Plata, Antonio Márquez, and Javier Fdez. Sanz

**Abstract:** In this paper, a systematic computational study of epitaxial YSZ/CeO<sub>2</sub> system was carried out. The influence of lattice strain, interface effects, stoichiometry, and specially presence of dopants on the conductivity have been evaluated. Lattice strain and interface effects are found to reduce the migration barrier at YSZ phase and the vacancy formation energy respectively. Nevertheless, they alone cannot explain the huge enhancement of the conductivity experimentally observed in these systems. Dopants seems to be the key factor that changes drastically the properties of the system. Ceria doping increases the vacancy concentration at the interface and can considerably reduce the oxygen migration barrier. Finally some considerations for best dopant selection are discussed and a smart design of new heterostructured materials for solid electrolyte in SOFCs is proposed.

#### Introduction

Solid oxide fuel cells (SOFC) is one of the most promising, sustainable and environmental friendly technologies for power generation. Their main disadvantage is their high working temperature (800 – 1000 °C) which introduces structural instabilities in the constituent materials. A high effort is, thus, being directed towards the development of new nanostructured materials that allow to reduce the working temperature at intermediate ranges (500 – 700 °C). To this end, enhancement of the ionic conductivity of the solid electrolyte is a key point and one of the main current research issues.<sup>34</sup> During the last decade, a new generation of high ion conductivity solid electrolyte based on epitaxial oxide heterostructures<sup>35–38</sup> has substituted yttria stabilized zirconia (YSZ) and doped ceria oxides.<sup>39,40</sup> There are two main groups of structures based on coupling *i*) an ionic-conductor with an insulator (e.g. in LiI/Al<sub>2</sub>O<sub>3</sub> or AgCl/Al<sub>2</sub>O<sub>3</sub>)<sup>41–44</sup> and *ii*) two ion-conducting oxides (e.g. in YSZ/Sm-CeO<sub>2</sub> or YSZ/Gd<sub>2</sub>Zr<sub>2</sub>O<sub>7</sub>).<sup>33,45</sup> Barriocanal *et al.* have reported colossal ionic conductivity at YSZ/SrTiO<sub>3</sub> (STO) interface heterostructures in which YSZ thickness is a few nanometers.<sup>32</sup> Conductivity measurements as high as 40 S cm<sup>-1</sup> at 550 K were obtained. This is eight orders of magnitude higher than the conductivity in bulk YSZ. This observation has led to an important discussion in the literature, indeed, and some authors attribute this phenomena to the electron conduction in the STO layers.<sup>46–48</sup>

Nowadays, the mechanism of ionic conductivity at oxide interfaces is not well known. Some authors have attributed this behavior to the space charge region at the interface originated in the redistribution of ionic and electronic defects.<sup>49</sup> However, heterostructures



made of doped oxides build up very narrow space charge regions, so the accumulation of charge carriers at this region should not affect significantly the conductivity.<sup>38</sup> Based on this argument other authors have explained high ionic conductivity in these heterostructures by means of the strain produced in the interface due to the different lattice parameters of the two oxides.<sup>50–52</sup> Depending on the mismatch degree between the two adjacent phases, the interface can be classified as coherent, semicoherent or incoherent. Misfit dislocations are created at incoherent and semicoherent interfaces in order to reduce the interfacial strain caused by the mismatch. These lower packing density regions can act as a diffusion pathway for ionic conduction.<sup>53</sup> On the contrary, coherent interfaces do not produce misfit dislocations and the mismatch is compensated by the elastic strain which causes the ionic mobility.<sup>54</sup> Strain lattice is difficult to evaluate and only in a few examples have been possible to correlate lattice elastic strain with interfacial conductivity. Interfacial strain can also relax through the formation of defects in the interface as grain boundaries which modify the conductivity of the system. Yildiz *et al.*<sup>54</sup> have studied oxygen diffusivity in strained YSZ by means of Density Functional Theory (DFT) and kinetic Monte Carlo (KMC). They observed as a moderate increasing of the strain in the system reduces drastically the oxygen migration barrier. However, this factor alone is not enough to explain the colossal conductivity reported by Barriocanal *et al.* for the YSZ/STO interface.<sup>32</sup>

The substrate in which the heterostructure is constructed, is another issue to take into account when investigating the interfacial conductivity. Traversa *et al.* have used MgO, which is a good insulator even at high temperatures, as substrate with a thin film of STO as buffer to prepare YSZ/CeO<sub>2</sub> heterostructures.<sup>33,46</sup> This method ensures that the obtained measurements do not incorporate contributions to the conductivity from the substrate or the formation of new grain boundaries and misfit dislocations. Surprisingly, while YSZ/Sm–CeO<sub>2</sub> presents an enhancement of ionic conductivity compared with YSZ bulk,<sup>33</sup> YSZ/CeO<sub>2</sub> heterostructures have a negligible effect on the transport properties of YSZ bulk.<sup>46</sup> DFT calculations performed to investigate defect formation in this interface<sup>55</sup> have shown that vacancy formation and the presence of dopants at the interface seems to be more favorable than in strained bulk phases. However there are many unsolved questions about the mechanism of interfacial conductivity.

In this paper, DFT+U calculations have been performed over a realistic model of the YSZ/CeO<sub>2</sub> interface. In YSZ intrinsic oxygen vacancy migration is first investigated in models of the strained thin film. Then, the energetics of Ce<sup>3+</sup> cations formation, that is simultaneous to vacancy creation, and oxygen migration at the interface, are evaluated. Finally, doping effects on vacancy concentration and oxygen migration are studied in order to understand the influence of dopants in the interfacial conductivity.

### Computational Details and Interface Model

Periodic DFT+U calculations were carried out with the Vienna ab initio simulation package (VASP).<sup>56-58</sup> This code solves the Kohn-Sham equations for the valence electron density within a plane wave basis set and makes use of the projector augmented wave (PAW) method to describe the interaction between the valence electrons and the atomic cores.<sup>59,60</sup> The valence electron density is defined by the twelve ( $5s^25p^66s^25d^14f^1$ ) electrons of each Ce atom, twelve ( $4s^24p^65s^24d^2$ ) electrons of each Zr and the six ( $2s^22p^4$ ) electrons of each O atom.

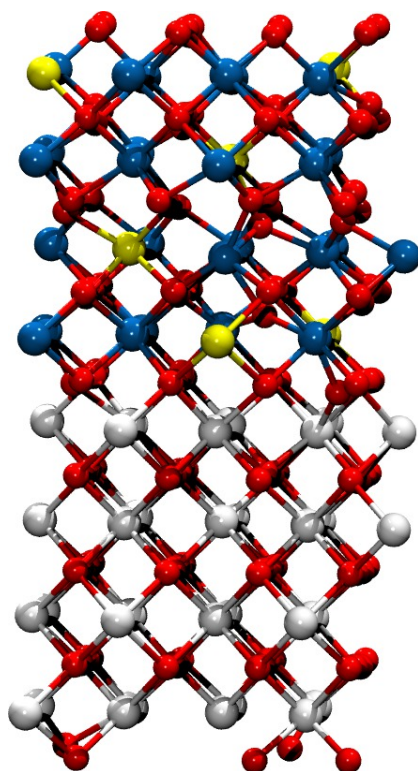


Figure 5.1: Fully relaxed YSZ/CeO<sub>2</sub> heterostructure model. Atom color: O=red; Ce=white; Zr=blue; Y=yellow

In these calculations the energy was computed using the GGA functional proposed by Perdew et al.<sup>61,62</sup> (PW91) and the electronic states were expanded using a plane wave basis set with a cutoff of 500 eV which ensures adequate convergence with respect to the basis set size. The Hubbard-like term was introduced according to the formalism of

Dudarev *et al.*<sup>63</sup> which makes use of a single  $U_{\text{eff}}$  parameter, hereafter denoted simply as  $U_f$  and  $U_p$ , to design the effective values used for the Ce  $4f$  and O  $2p$  electrons, respectively. For Ce and O we have used  $U_f$  and  $U_p$  values of 5 eV which leads to a moderately improved description of some critical aspects that concern structure, electronic properties, and thermochemistry of both  $\text{CeO}_2$  and reduced ceria.<sup>64</sup> Given that the O  $U_p$  parameter is applied to all oxygen atoms we have also included a  $U_d$  parameter for the  $4d$  levels of Zr atoms. In this case, an  $U_d$  value of 2 eV was chosen in order to reproduce lattice parameter of cubic yttria.

According to system size all the calculations were performed at the  $\Gamma$  point of the Brillouin zone. The convergence of the energy with this setup was confirmed in a previous paper.<sup>54</sup> Forces on the ions were calculated through the Hellmann-Feynman theorem, including the Harris-Foulkes correction to forces.<sup>65</sup> Iterative relaxation of the atomic positions was stopped when the forces on the atoms were  $< 0.01$  eV/Å. The barriers for vacancy-oxygen migration were located using the climbing image version of the nudged elastic band algorithm.<sup>66</sup>

Our model consisted on a 3D fully relaxed supercell which contained 2 oxide layers with 96 atoms each one. The YSZ phase was taken from a previous model developed by Yildiz *et al.*<sup>54</sup> and consisted in 9%  $\text{Y}_2\text{O}_3$  doped YSZ made of 26 Zr, 6 Y and 61 O atoms in the YSZ layer. The three vacancies and six Y dopant atoms were distributed homogeneously to enable the stability of the cubic phase (see Figure 5.1). The ceria phase consisted on 32  $\text{CeO}_2$  units in which 2 Ce cations are substituted by two trivalent cations if the phase was doped. The interface was built as a ceria-zirconia stacking of both phases along the  $[100]$  direction.

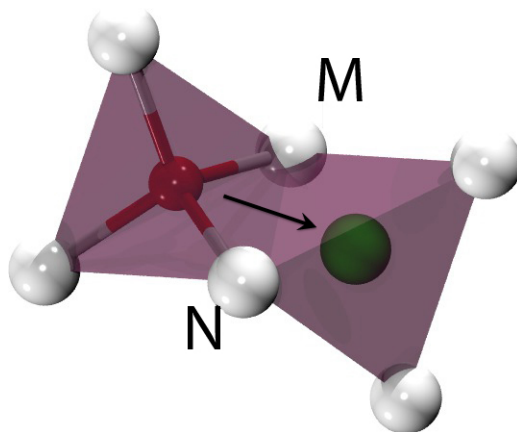


Figure 5.2: Migration path of the oxygen vacancy. M and N are the cations at the shared edge. Colors: Oxygen= red; Vacancy= green

## Results and discussion

### YSZ vacancy migration

YSZ presents fluorite crystal structure with the yttrium and zirconia cations on a face-centered-cubic cation lattice and oxygen and vacancies on a simple cubic anion lattice. Each cation is at the center of a cube of eight anions and each oxygen ion or vacancy is at the center of a cation tetrahedron. In this structure, oxygen ions migrates by hopping across and edge of a tetrahedron between two cations as shown in Figure 5.2. Thus, the migration barrier depends on the neighboring atoms which form the tetrahedra, specially atoms M and N which are in the shared edge. Because of that, migration path barriers were computed in the YSZ phase taking into account different combinations for the two cationic sites that are involved. Computed barriers have been represented in Figure 5.3 as a function of the sum of the ionic radii of the two cations that are in the shared edge ( $R_1+R_2$ ). Three different combinations can be considered in YSZ phase if we focus on the two cations of this shared edge,  $Zr^{4+}-Y^{3+}$ ,  $Zr^{4+}-Zr^{4+}$ , and  $Y^{3+}-Y^{3+}$ . The lowest barrier found is 0.19 eV for a  $Zr^{4+}-Zr^{4+}$  combination which is quite close to other barriers found for strained YSZ bulk by Yidiz *et al.*<sup>54</sup> while the highest barrier is observed for the  $Y^{3+}-Y^{3+}$  configuration ( $\approx 1.5$  eV).<sup>54</sup>

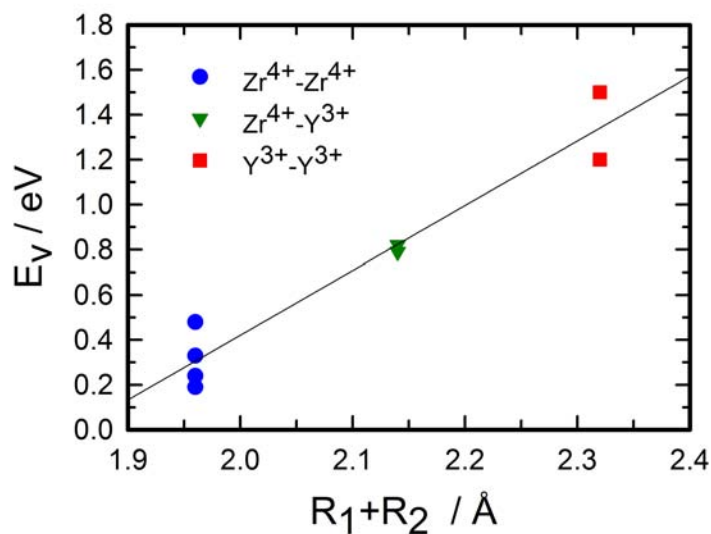


Figure 5.3: Activation energy for oxygen migration at the YSZ layer as a function of the radius of the two cations in the tetrahedra shared edge.

Data on Figure 5.3 clearly shows that the larger the ionic radius of these two cations the higher the migration barrier. As in the transition state (TS) the oxygen anion is located in between the two cations the available space for hopping gets reduced with increasing cation size and, thus, the barrier for oxygen anion hopping is increased. This phenomena has been reported previously in YSZ and other fluorite-like structured solids as ceria.<sup>54,67</sup>

### Interface vacancy migration

The strain which is produced by the heteroepitaxial structure decreases the barrier for oxygen migration in the YSZ layers and should increase the ionic conductivity of the system.<sup>54</sup> However this is not enough to produce the huge enhancement of the ionic conductivity reported in the experiments.<sup>32,33</sup> For this reason we have also explored the oxygen ions diffusion at the interface. Migration barriers were computed taking into account different cation combinations as it was done in the previous section. As migration takes place at the interface, one of the cations that are placed on the shared edge of both tetrahedra is  $\text{Ce}^{4+}$  while the second site is occupied by either  $\text{Zr}^{4+}$  or  $\text{Y}^{3+}$  cations. Thus,  $\text{Ce}^{4+}-\text{Y}^{3+}$  and  $\text{Ce}^{4+}-\text{Zr}^{4+}$ , cation combinations have been considered. Moreover, as oxygen vacancies are a common defect in ceria specially at surfaces and interfaces, the presence of  $\text{Ce}^{3+}$  cations at the interface must be taken into account. Thus, an extra vacancy has been generated at the interface in order to obtain  $\text{Ce}^{3+}$  cations and two new different cation combinations for the migration:  $\text{Ce}^{3+}-\text{Y}^{3+}$  and  $\text{Ce}^{3+}-\text{Zr}^{4+}$ .

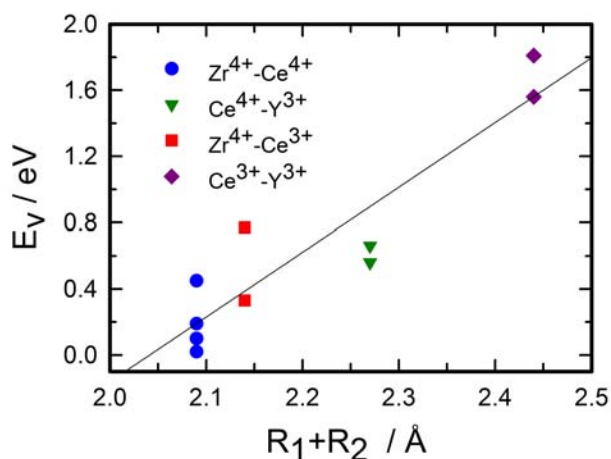


Figure 5.4: Activation energy for oxygen migration at the interface as a function of the radius of the two cations in the tetrahedra shared edge.

Computed oxygen migration barriers at the interface are depicted in Figure 5.4. The same trend that was observed in YSZ phase is obtained at the interface: the larger the cation size, the higher the barrier. However two important differences must be pointed out. First, the smallest barrier found is  $\approx 0.05$  eV which is considerably smaller than the barriers which were obtained in the YSZ layer. Thus, the enhancement of the conductivity in these heterostructures can be attributed to an interfacial phenomenon. Second, the presence of  $\text{Ce}^{3+}$  ions increases considerably the barrier. The average values for the barriers with  $\text{Ce}^{4+}\text{-Zr}^{4+}$  and  $\text{Ce}^{4+}\text{-Y}^{3+}$  combinations are 0.19 and 0.61 eV respectively while these values increase to 0.55 and 1.69 eV when replacing  $\text{Ce}^{4+}$  by  $\text{Ce}^{3+}$ . This fact could explain recent experimental results in which a negligible effect on the transport properties of YSZ/ $\text{CeO}_2$  epitaxial structures can be assigned to the interfacial conductivity.<sup>46</sup> In order to evaluate the concentration and stabilization of  $\text{Ce}^{3+}$  at the interface, vacancy formation energies have been computed at the different layers of heterostructure (see Table 5.1).

Table 5.1: Vacancy formation energy,  $E_v$  in different oxygen layer of YSZ/ $\text{CeO}_2$  system.

Layer	I+2	I+1	I	I-1	I-2
$E_v / \text{eV}$	2.42	2.19	1.72	2.18	4.00

There are five non-equivalent oxygen layers in our model, so five different configuration were explored. All the configurations were labeled as  $\text{I}\pm\text{X}$ , where  $\pm$  symbol indicates the phase in which the vacancy has been generated (+ for the ceria phase and - for the YSZ phase) and  $X$  the relative position of the layer taking as reference the oxygen interface layer. The  $\text{Ce}^{3+}$  cations were located in adequate positions trying to minimize the vacancy formation energy. Thus they were placed in the same layer of the vacancy if the vacancy is in then ceria layer in the interfacier layer if the vacancy is located at the YSZ phase. The vacancy formation energy at the middle layer of the ceria phase (I+2), is  $\approx 2.4$  eV which is quite close to values reported using the same set up for bulk ceria.<sup>64</sup> However, vacancy formation at the YSZ phase is significantly higher than for equivalent positions in the ceria phase,  $\approx 4$  eV. The vacancy formation energy decreases considerably for  $\text{I}\pm 1$  positions, 2.18 – 2.19 eV. Nevertheless, the most stable site for vacancy formation is the interface where the vacancy creation energy drastically decreases to 1.72 eV. These data suggest that oxygen vacancy and thus  $\text{Ce}^{3+}$  ions are strongly stabilized at the interface. Therefore two main consequences can be extracted. First, the vacancy concentration at the interface is going to be higher than in the separated oxides. This fact can explain the increase in conductivity at the interface of the heterostructure compared to the separated phases. Second,  $\text{Ce}^{3+}$  cations will be located at the interface and this will result in and increased oxygen hopping barrier. This fact agrees with previous results reported by Traversa *et*

*al.*<sup>46</sup> in which a negligible effect on the transport properties of YSZ/CeO<sub>2</sub> heterostructure is observed if this system it is compared with other YSZ bades systems.

### Doped ceria

While YSZ/CeO<sub>2</sub> does not exhibit a enhancement of the ionic conductivity,<sup>46</sup> YSZ/doped-CeO<sub>2</sub> systems were reported to drastically increase the conductivity of YSZ by some orders of magnitude.<sup>33</sup> Different trivalent cations have been used for doping ceria, however lanthanide elements has been the most employed group.<sup>29,33,45</sup> The first YSZ/doped-CeO<sub>2</sub> epitaxial heterostructure was reported by Azad *et al.*<sup>45</sup> and used Gd<sup>3+</sup> ions. Some years later the YSZ/Sm-doped CeO<sub>2</sub> (YSZ/SDC) epitaxial heterostructure was synthesized and characterized.<sup>33</sup> Both systems present a significant increase in conductivity at the interface.

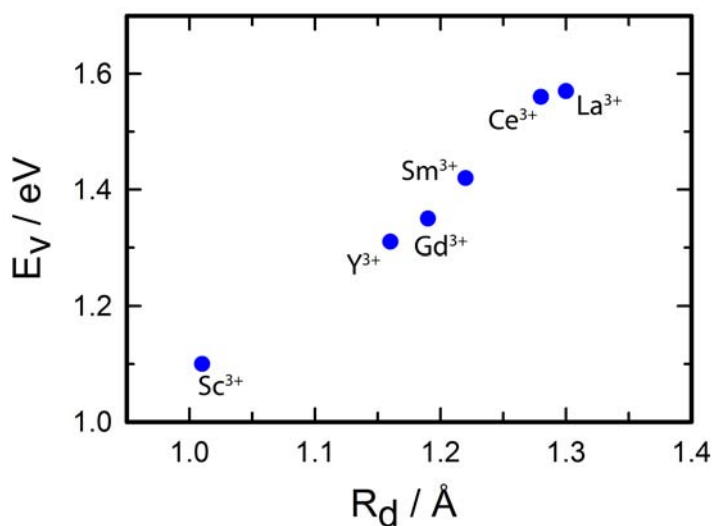


Figure 5.5: Activation energy for oxygen migration at the interface of YSZ/M-CeO<sub>2</sub> heterostructures.

In order to understand this phenomenon, we have computed the vacancy formation energy in the YSZ/SDC heterostructure. To generate a model for the Sm-doped system two Ce atoms were substituted by two Sm atoms at the interface. This way the formation of Ce<sup>3+</sup> cations is avoided when the oxygen vacancy is generated. While the lower vacancy formation energy for undoped system was 1.72 eV, this value decreases to -0.86 eV

in the Sm-doped heterostructure. This figure agrees pretty well with previous results for bulk doped ceria.<sup>29</sup> Thus vacancy formation energy is drastically reduced at the interface in doped systems and the concentration of vacancies and dopant ions should be considerably higher at the interface. However, ionic conductivity not only depends on the vacancy concentration but also on the oxygen migration barrier. To rationalize the possible effects in the oxygen hopping process we have computed this barrier at the interface for different doped systems. For doped-ceria systems, the least favorable situation (that can be associated to the rate limiting step in the anionic conduction mechanism) can be associated to the combination of the dopant cation ( $M^{3+}$ ) and yttrium cation ( $Y^{3+}$ ) at the tetrahedra shared edge. The data in Figure 5.5 show the same trend that was observed in undoped ceria systems: the barrier height decreases with decreasing cation size: i.e. while for the  $Ce^{3+}-Y^{3+}$  the barrier is 1.57 eV for the  $Sc^{3+}-Y^{3+}$  combination the barrier is 1.10 eV. This is a decrease of 0.47 eV while the decrease in the radius is just 0.29 Å. Therefore, it could be concluded that trivalent dopants which present a radius lower than that of the  $Ce^{3+}$  cation, will decrease the oxygen migration barrier and increase the interfacial ionic conductivity. However, the presence of trivalent atoms with short ionic radius have been reported to result in the formation of vacancy–dopant atoms pairs.<sup>67</sup> The presence of these associations derive in an increased probability of finding arrangements where these trivalent cations are in one of the sites of the shared edge that define the vacancy migration path. This situation should be avoided as the radius of those trivalent cations are higher than the  $Ce^{4+}$  cation radius. Thus, dopants that prefer a next nearest neighbor configuration are more convenient (e.g.  $Sm^{3+}$ ,  $Nd^{3+}$ ,  $La^{3+}$ )<sup>67</sup> and a balance between both effects should be established when selecting the most appropriate dopant.

To summarize, the ideas exposed in the preceding paragraphs allow us to rationalize the huge ionic conductivity of these epitaxial heterostructures in terms of a combination of different phenomena.

1. Strain effects have been shown to decrease the migration barrier for the intrinsic vacancies of YSZ. However, this factor is not determinant as it has been reported that YSZ/ $CeO_2$  heterostructure exhibits a negligible effect on the ionic transport properties compared to YSZ bulk phase.<sup>46</sup>
2. Vacancy formation energy has been shown to be lower at the interface, thus a higher vacancy concentration and ionic conductivity should be expected but the simultaneous presence of  $Ce^{3+}$  cations increase the oxygen hopping barrier.
3. This shortcoming can be solved by introducing dopant elements in the ceria phase. The presence of trivalent dopant cations reduces the vacancy formation energy and the vacancy concentration should increase at the interface. Simultaneously, it is possible to reduce the activation energy of the oxygen migration process by



selecting  $M^{3+}$  dopants whose radius is smaller than that of the  $Ce^{3+}$  cation and prefer a next nearest neighbor configuration with respect to the oxygen vacant.

## Conclusions

In this paper, a systematic study of the microscopic factors affecting the ionic conductivity in YSZ/doped  $CeO_2$  epitaxial heterostructures has been carried out by means of plane-wave pseudopotential DFT+U calculations. It has been found that the most important factors that influence the ionic conductivity are the interface structure and the doping of the ceria phase.

In undoped YSZ/ $CeO_2$  systems, computed oxygen migration barriers at the interface are found to follow a similar trend that in the YSZ phase: the barrier decreases with decreasing cation size. At the same time, oxygen vacancy formation energy is found to be lower at the very same interface layer. As result, the vacancy concentration is expected to increase at the interface. Thus, the enhancement of the conductivity in these heterostructures can be attributed to the interface structure. At the same time, the presence of  $Ce^{3+}$  cations at the interface is found to considerably increase the oxygen barrier hopping. This could explain recent experimental results that assigned a negligible effect to the interfacial conductivity in these heterostructures.

Doping the ceria phase with  $Sm^{3+}$  cations is found to result in a significant decrease of the oxygen vacancy formation energy. Simultaneously, trivalent dopants with lower radius than that of the  $Ce^{3+}$  cation are found to significantly decrease the oxygen migration barrier. Thus, doping the ceria phase with trivalent cations should increase the vacancy concentration at the interface and, at the same time, reduce the oxygen migration barrier. However, the presence of trivalent cation of small ionic radius has been reported to result in the formation of vacancy-dopant atoms associations. These associations derive in an increased probability of finding arrangements where one of these trivalent cations are in one of the cationic sites that define the oxygen migration path. This situation should be avoided by selecting cations that prefer a next nearest neighbor configuration and a balance between both effects should be established when selecting the most appropriate dopant.

## References

1. Hsiao, W.-I.; Lin, Y.-S.; Chen, Y.-C.; Lee, C.-S., *Chem. Phys. Lett.* **2007**, *441*, 294.
2. Niederberger, M., *Acc. Chem. Res.* **2007**, *40*, 793.
3. Kuiry, S.; Patil, S.; Deshpande, S.; Seal, S., *J. Chem. Phys. B* **2005**, *109*, 6936.
4. Vantomme, A.; Yuan, Z.-Y.; Du, G.; Su, B.-L., *Langmuir* **2005**, *21*, 1132.

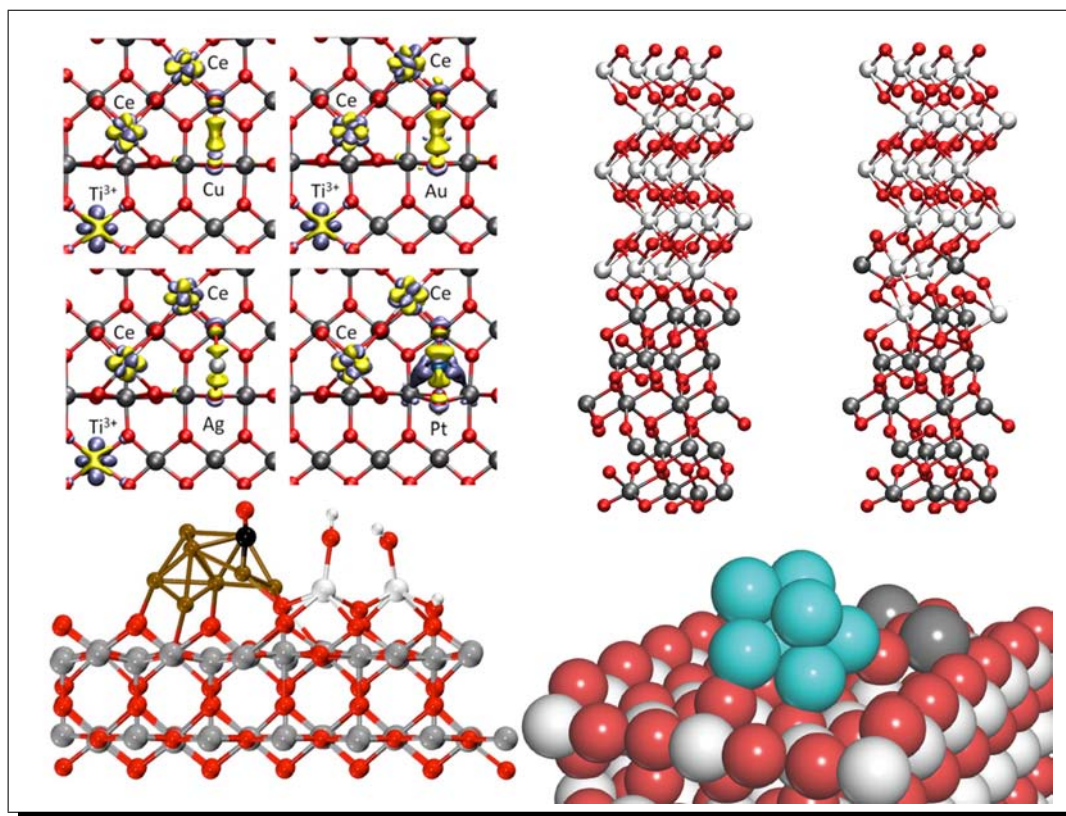
5. Sun, C.; Li, H.; Wang, Z.; Chen, L.; Huang, X., *Chem. Lett.* **2004**, 33, 662.
6. Sun, C.; Li, H.; Zhang, H.; Wang, Z.; Chen, L., *Nanotechnology* **2005**, 16, 1454.
7. Ho, C.; Yu, J.; Kwong, T.; Mak, A.; Lai, S., *Chem. Mater.* **2005**, 17, 4514.
8. Liang, X.; Wang, X.; Zhuang, Y.; Xu, B.; Kuang, S.; Li, Y., *J. Am. Chem. Soc.* **2008**, 130, 2736.
9. Yada, M.; Sakai, S.; Torikai, T.; Watari, T.; Furuta, S.; Katsuki, H., *Adv. Mater.* **2004**, 16, 1222.
10. Sun, C.; Sun, J.; Xiao, G.; Zhang, H.; Qiu, X.; Li, H.; Chen, L., *J. Chem. Phys. B* **2006**, 110, 13445.
11. Sun, C.; Li, H.; Chen, L., *J. Phys. Chem. Solids* **2007**, 68, 1785.
12. Tang, C.; Bando, Y.; Liu, B.; Golberg, D., *Adv. Mater.* **2005**, 17, 3005.
13. Han, W.-Q.; Wu, L.; Zhu, Y., *J. Am. Chem. Soc.* **2005**, 127, 12814.
14. Chen, G.; Xu, C.; Song, X.; Zhao, W.; Ding, Y.; Sun, S., *Inorg. Chem.* **2008**, 47, 723.
15. Huang, X.-S.; Sun, H.; Wang, L.-C.; Liu, Y.-M.; Fan, K.-N.; Cao, Y., *Appl. Catal. B* **2009**, 90, 224.
16. Tibiletti, D.; Amieiro-Fonseca, A.; Burch, R.; Chen, Y.; Fisher, J.; Goguet, A.; Hardacre, C.; Hu, P.; Thompsett, D., *J. Phys. Chem. B* **2005**, 109, 22553.
17. Chen, Y.; Hu, P.; Lee, M.-H.; Wang, H., *Surf. Sci.* **2008**, 602, 1736.
18. Castellani, N.; Branda, M.; Neyman, K.; Illas, F., *J. Phys. Chem. C* **2009**, 113, 4948.
19. Si, R.; Flytzani-Stephanopoulos, M., *Angew. Chem. Int. Ed.* **2008**, 47, 2884.
20. Yuan, Z.-Y.; Idakiev, V.; Vantomme, A.; Tabakova, T.; Ren, T.-Z.; Su, B.-L., *Catal. Today* **2008**, 131, 203.
21. Ilieva, L.; Pantaleo, G.; Ivanov, I.; Maximova, A.; Zanella, R.; Kaszukur, Z.; Venezia, A.; Andreeva, D., *Catal. Today* **2010**, 158, 44.
22. Zhou, K. B.; Wang, X.; Sun, X. M.; Peng, Q.; Li, Y. D., *J. Catal.* **2005**, 229, 206.
23. Mai, H. X.; Sun, L. D.; Zhang, Y. W.; Si, R.; Feng, W.; Zhang, H. P.; Liu, H. C.; Yan, C. H., *J. Phys. Chem. B* **2005**, 109, 24380.
24. Zhou, K.; Yang, Z.; Yang, S., *Chem. Mater.* **2007**, 19, 1215.
25. Acosta, B.; Smolentseva, E.; Beloshapkin, S.; Rangel, R.; Estrada, M.; Fuentes, S.; Simakov, A., *Appl. Catal. A* **2012**, 449, 96.
26. Han, W.-Q.; Wen, W.; Hanson, J.; Teng, X.; Marinkovic, N.; Rodriguez, J., *J. Phys. Chem. C* **2009**, 113, 21949.
27. Torrente-Murciano, L.; Gilbank, A.; Puertolas, B.; Garcia, T.; Solsona, B.; Chadwick, D., *Appl. Catal. B* **2013**, 132-133, 116.
28. Zhang, J.; Chen, G.; Chaker, M.; Rosei, F.; Ma, D., *Appl. Catal. B* **2013**, 132-133, 107.
29. Andersson, D. A.; Simak, S. I.; Skorodumova, N. V.; Abrikosov, I. A.; Johansson, B., *P. Natl.*

- Acad. Sci. USA* **2006**, *103*, 3518.
30. Maier, J., *Nat. Mater.* **2005**, *4*, 805.
  31. Sata, N.; Eberman, K.; Eberl, K.; Maier, J., *Nature* **2000**, *408*, 946.
  32. Barriocanal, J. G.; Calzada, A. R.; Varela, M.; Sefrioui, Z.; Iborra, E.; Leon, C.; Pennycook, S. J.; Santamaria, J., *Science* **2008**, *321*, 676.
  33. Sanna, S.; Esposito, V.; Tebano, A.; Licoccia, S.; Traversa, E.; Balestrino, G., *Small* **2010**, *6*, 1863.
  34. Boivin, J. C.; Mairesse, G., *Chem. Mater.* **1998**, *10*, 2870.
  35. Sillassen, M.; Eklund, P.; Pryds, N.; Johnson, E.; Helmersson, U.; Bottiger, J., *Adv. Funct. Mater.* **2010**, *20*, 2071.
  36. Li, B.; Zhang, J.; Kaspar, T.; Shutthanandan, V.; Ewing, R. C.; Lian, J., *Phys. Chem. Chem. Phys.* **2013**, *15*, 1296.
  37. Dyer, M. S.; Darling, G. R.; Claridge, J. B.; Rosseinsky, M. J., *Angew. Chem. Int. Edit.* **2012**, *51*, 3418.
  38. Fabbri, E.; Pergolesi, D.; Traversa, E., *Sci. Tech. Adv. Mater.* **2010**, *11*, 054503.
  39. Sayle, D. C.; Maicaneanu, S. A.; Watson, G. W., *J. Am. Chem. Soc.* **2002**, *124*, 11429.
  40. Ahn, K.; Yoo, D. S.; Prasad, D. H.; Lee, H.-W.; Chung, Y.-C.; Lee, J.-H., *Chem. Mater.* **2012**, *24*, 4261.
  41. Liang, C. C., *J. Electrochem. Soc.* **1973**, *120*, 1289.
  42. Gupta, R. K.; Agrawal, R. C., *Solid State Ionics* **1994**, *72*, 314.
  43. Lee, J. S.; Adams, S.; Maier, J., *Solid State Ionics* **2000**, *136*, 1261.
  44. Rizea, A.; Chirlesan, D.; Petot, C.; Petot-Ervas, G., *Solid State Ionics* **2002**, *146*, 341.
  45. Azad, S.; Marina, O. A.; Wang, C. M.; Saraf, L.; Shutthanandan, V.; McCready, D. E.; El-Azab, A.; Jaffe, J. E.; Engelhard, M. H.; Peden, C. H. F.; Thevuthasan, S., *Appl. Phys. Lett.* **2005**, *86*, 131906.
  46. Pergolesi, D.; Fabbri, E.; Cook, S. N.; Roddatis, V.; Traversa, E.; Kilner, J. A., *ACS Nano* **2012**, *6*, 10524.
  47. Gerstl, M.; Friedbacher, G.; Kubel, F.; Hutter, H.; Fleig, J., *Phys. Chem. Chem. Phys.* **2013**, *15*, 1097.
  48. Guo, X., *Science* **2009**, *324*.
  49. Sheldon, B. W.; Shenoy, V. B., *Phys. Rev. Lett.* **2011**, *106*, 216104.
  50. Korte, C.; Peters, A.; Janek, J.; Hesse, D.; Zakharov, N., *Phys. Chem. Chem. Phys.* **2008**, *10*, 4623.
  51. Korte, C.; Schichtel, N.; Hesse, D.; Janek, J., *Monatsh. Chem.* **2009**, *140*, 1069.
  52. Schichtel, N.; Korte, C.; Hesse, D.; Janek, J., *Phys. Chem. Chem. Phys.* **2009**, *11*, 3043.
  53. Peters, A.; Korte, C.; Hesse, D.; Zakharov, N.; Janek, J., *Solid State Ionics* **2007**, *178*, 67.

54. Kushima, A.; Yildiz, B., *J. Mater. Chem.* **2010**, *20*, 4809.
55. Fronzi, M.; Cereda, S.; Tateyama, Y.; Vita, A. D.; Traversa, E., *Phys. Rev. B* **2012**, *86*, 085407.
56. Kresse, G.; Hafner, J., *Phys. Rev. B* **1993**, *47*, 558.
57. Kresse, G.; Hafner, J., *Phys. Rev. B* **1993**, *48*, 13115.
58. Kresse, G.; Hafner, J., *Phys. Rev. B* **1994**, *49*, 14251.
59. Blochl, P. E., *Phys. Rev. B* **1994**, *50*, 17953.
60. Kresse, G.; Joubert, D., *Phys. Rev. B* **1999**, *59*, 1758.
61. Perdew, J. P.; Chevary, J. A.; Vosko, S. H.; Jackson, K. A.; Pederson, M. R.; Singh, D. J.; Fiolhais, C., *Phys. Rev. B* **1992**, *46*, 6671.
62. Perdew, J. P.; Chevary, J. A.; Vosko, S. H.; Jackson, K. A.; Pederson, M. R.; Singh, D. J.; Fiolhais, C., *Phys. Rev. B* **1993**, *48*, 4978.
63. Dudarev, S. L.; Botton, G. A.; Savrasov, S. Y.; Humphreys, C. J.; Sutton, A. P., *Phys. Rev. B* **1998**, *57*, 1505.
64. Plata, J. J.; Marquez, A. M.; Sanz, J. F., *J. Chem. Phys.* **2012**, *136*, 041101.
65. Harris, J., *Phys. Rev. B* **1985**, *31*, 1770.
66. Sheppard, D.; Terrell, R.; Henkelman, G., *J. Chem. Phys.* **2008**, *128*, 134106.
67. Nakayama, M.; Martin, M., *Phys. Chem. Chem. Phys.* **2009**, *11*, 3241.

CHAPTER  
**SIX**

Ceria as catalyst and photocatalyst



## 6.1 Introduction

Catalytic and photocatalytic activity of ceria is one of its most appreciated properties for the industry. The applicability of ceria cover a wide range o chemical processes, such as hydrogenation reactions, steam reforming, CO oxidation, hydrocarbon oxidation, nitrogen oxide reduction with ammonia and hydrogen generation by ethanol reforming.<sup>1</sup> In this section we will focus on catalytic processes related to the so-called hydrogen economy, in particular the water gas shift (WGS) reaction and the photocatalytic water splitting.

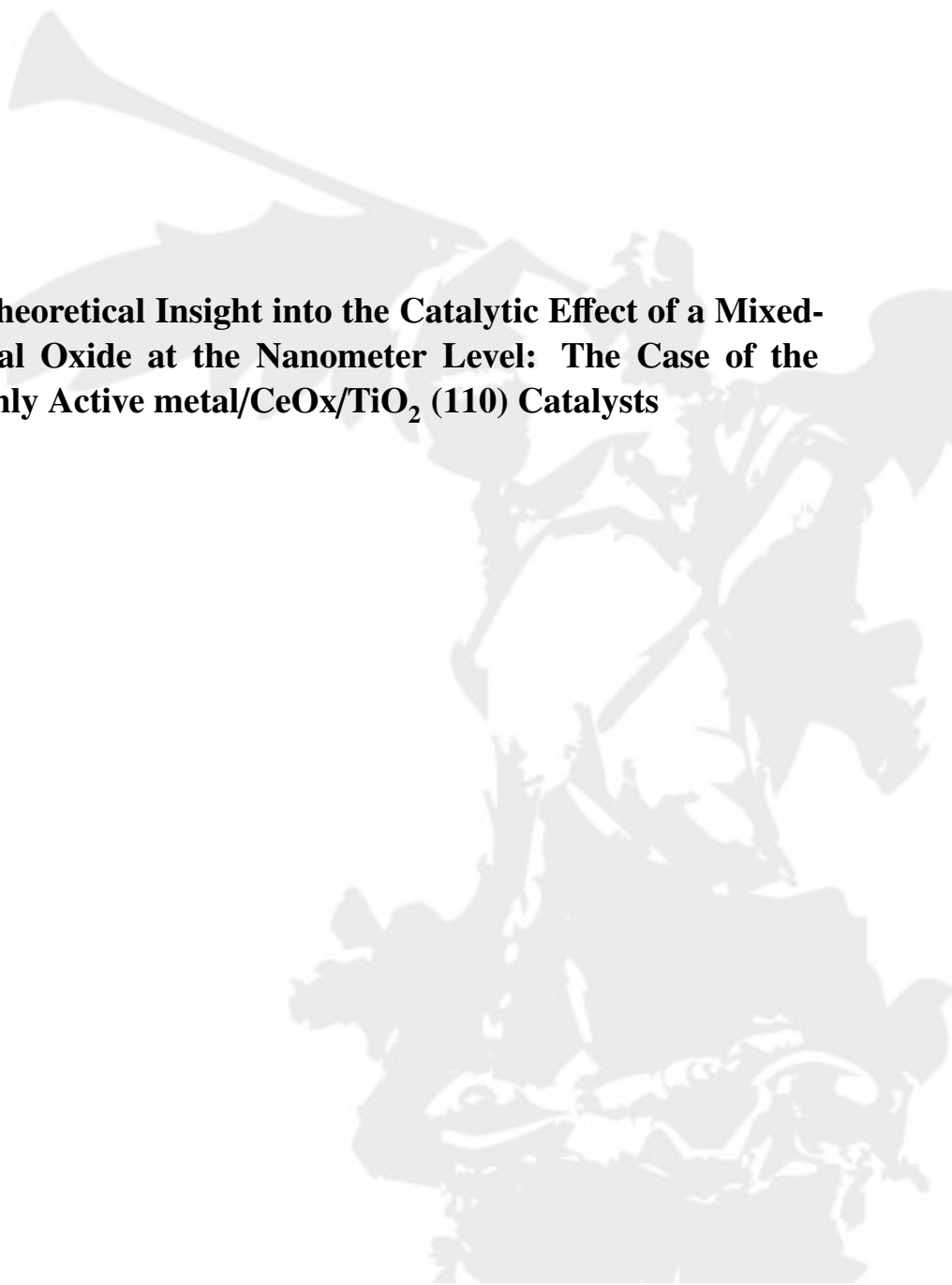
The WGS reaction ( $\text{H}_2\text{O}(\text{g}) + \text{CO}(\text{g}) \longleftrightarrow \text{H}_2(\text{g}) + \text{CO}_2(\text{g})$ ) plays a key role in several industrial processes. For instance, it is used to produce high-purity hydrogen for ammonia synthesis or it is also also a part of methanol synthesis. During the last decade, there has been renewed interest in the WGS reaction in connection with fuel cell-powered vehicles, where hydrogen is obtained via partial oxidation and steam reforming of hydrocarbons. Pt anodes in fuel cell are poisoned by CO so the reformed fuel, which contains 1-10% CO, have to be treated.<sup>2,3</sup> The WGS reaction is an exothermic process, so low reaction temperature favors high conversion rates. Because of that, the development of a more active catalyst is crucial to lower the temperature and reduce the volume of the reformer system. Current industrial catalysts for the WGS reaction are commonly mixtures of Fe-Cr and Zn-Al-Cu oxides, used at temperatures between 350-500 °C and 180-250 °C, respectively.<sup>4</sup> These catalysts have some drawbacks: the low activity of the former catalyst at high temperature, the pyrophoric nature of the latter, the lengthy preconditioning of both types and the large reactor volume dictated by the slow kinetics of the Cu-ZnO-Al<sub>2</sub>O<sub>3</sub> catalyst. These limitations therefore make classical WGS catalysts unsuitable for use in small-scale reformers for fuel cells, where fast response and low catalyst volume are mandatory. Improved catalysts are being sought, particularly for low temperatures. A second generation of improved catalysts able to work at lower temperature (e.g., at T<sub>i</sub>150) are based on coinage metals (Au, Cu or Pt) supported on ceria and titania. These nanostructured catalysts are very promising candidates for high activity, low temperature operation in WGS systems. In this chapter we will analyze several systems belonging to a new family of highly active catalysts, in particular mixed heterostructures that put together the ceria/titania interface and noble metal.<sup>5</sup>

From an environmental point of view, the main disadvantage of the reforming and WGS processes is that massive production of carbon dioxide.<sup>6</sup> That is why it is important to find alternatives to produce H<sub>2</sub> by employing carbon-free energy precursors.<sup>7,8</sup> Among the methods for H<sub>2</sub> generation outside of the carbon cycle, that based on solar irradiation attracts the greatest attention in view of its potential to use the abundance of solar energy. Solar energy can be used to produce hydrogen from water using inorganic photo-semiconductors that catalyze the water-splitting reaction ( $\text{H}_2\text{O} \longrightarrow \frac{1}{2}\text{O}_2 + \text{H}_2(\text{g})$ ). Two types of experimental configurations are used to design photocatalysts for photochem-

ical water splitting, photoelectrochemical cells and particulate photocatalytic systems. Photoelectrochemical cells are more efficient so far but photocatalytic systems are simpler and less expensive. Taking into account the processes involved in the dissociation of water on particulate photocatalysts under visible light irradiation, the materials used as photocatalysts must satisfy several functional requirements with respect to band gap energy and electrochemical properties:<sup>9</sup>

1. The material should present suitable solar visible-light absorption capacity, and band edge potentials appropriate for overall water splitting
2. It should be able to separate photoexcited electrons from reactive holes.
3. It is necessary to minimize energy losses related to charge transport and recombination of photoexcited charges
4. The photocatalyst should be chemical stable to corrosion and photocorrosion in aqueous environments
5. It should exhibit kinetically suitable electron transfer properties from photocatalyst surface to water interface.

Because of most of these properties are going to be associated to the electronic structure of the semiconductor, to modify or tune the band gap of the material of paramount interest. For instance, anion-cation codoping is one of the most used techniques, and its scope has been theoretically examined in previous work carried out in our group. In this chapter, we will look into a different direction, related with the properties of semiconductor heterostructures which have exhibited excellent performance as photocatalyst.



## **6.2 A Theoretical Insight into the Catalytic Effect of a Mixed-Metal Oxide at the Nanometer Level: The Case of the Highly Active metal/CeO<sub>x</sub>/TiO<sub>2</sub> (110) Catalysts**



THE JOURNAL OF CHEMICAL PHYSICS **132**, 104703 (2010)

## A theoretical insight into the catalytic effect of a mixed-metal oxide at the nanometer level: The case of the highly active metal/CeO<sub>x</sub>/TiO<sub>2</sub>(110) catalysts

Jesús Graciani,<sup>1,2,a)</sup> José J. Plata,<sup>2</sup> Javier Fdez. Sanz,<sup>2</sup> Ping Liu,<sup>1</sup> and José A. Rodríguez<sup>1</sup>

<sup>1</sup>Department of Chemistry, Brookhaven National Laboratory, Upton, New York 11973, USA

<sup>2</sup>Departamento de Química Física, Facultad de Química, Universidad de Sevilla, Sevilla E-41012, Spain

(Received 17 December 2009; accepted 5 February 2010; published online 9 March 2010)

The structural and electronic properties of CeO<sub>x</sub> species supported on the rutile TiO<sub>2</sub>(110) surface have been examined by means of periodic density-functional calculations that use a generalized gradient approximation functional including a Hubbard-like type correction. Deposition of Ce atoms leads in a first step to Ce<sup>3+</sup> ions bound to the surface through bridge and in-plane oxygen atoms, the released electrons occupying the Ti 3*d* empty orbitals. Further addition of Ce and molecular oxygen gives place to Ce<sub>2</sub>O<sub>3</sub> dimers diagonally arranged on the surface, in agreement with the spots observed in the scanning tunnel microscope images. The formation process of CeO<sub>x</sub> nanoparticles (NPs) on the TiO<sub>2</sub> surface is highly exothermic and our calculations show that the redox properties of the Ce(III)-Ce(IV) couple are significantly altered when it is supported on TiO<sub>2</sub>. In particular the reactivity against CO/O<sub>2</sub> indicates that on the surface the presence of Ce(III) is favored over Ce(IV) species. Our results also indicate that the CeO<sub>x</sub>/TiO<sub>2</sub> interface should be seen like a real mixed-metal oxide rather than a supported NP of ceria. Finally, in the context of the high catalytic activity of the *M*/CeO<sub>x</sub>/TiO<sub>2</sub> (*M*=Au,Cu,Pt) systems in the water-gas shift reaction, we have examined the dissociation of water on the CeO<sub>x</sub>/TiO<sub>2</sub> surface and estimated a barrier as small as 0.04 eV, i.e. ~8 times smaller than that computed for a TiO<sub>2</sub> oxygen vacancy. This result agrees with the experimental superior catalytic activity of the *M*/CeO<sub>x</sub>/TiO<sub>2</sub> systems over *M*/TiO<sub>2</sub>. © 2010 American Institute of Physics. [doi:10.1063/1.3337918]

### I. INTRODUCTION

Catalytic processes able to reduce the environmental pollution or generate new clean renewable sources of energy have received an increasing attention and become one of the hot spots in chemistry.<sup>1–5</sup> In this regard, a number of works have been devoted to design new better catalyst intended to eliminate CO, either by plane oxidation ( $\text{CO} + \frac{1}{2}\text{O}_2 \rightarrow \text{CO}_2$ ) or further transformation through, for instance, the water gas shift (WGS) reaction, ( $\text{CO} + \text{H}_2\text{O} \rightarrow \text{CO}_2 + \text{H}_2$ ), widely used to produce H<sub>2</sub> clean enough to be used in fuel cells.<sup>3–7</sup> Many metal/metal-oxide systems have been found to catalyze these important reactions under different conditions, and among them, two of the most efficient systems are based on gold nanoparticles (NPs), supported on a reducible metal oxide such as titania or ceria (Au/TiO<sub>2</sub> and Au/CeO<sub>2</sub>).<sup>3–15</sup> The ability of both systems to easily generate reduced species of Ti and Ce (Ti<sup>3+</sup>/Ce<sup>3+</sup>) has been found to play a crucial role on their catalytic activities.<sup>16–19</sup>

In the WGS reaction, previous work performed on a variety of systems such as Au/CeO<sub>2</sub>, Au/TiO<sub>2</sub>, Au/TiO<sub>2-x</sub>N<sub>y</sub>, Cu/TiO<sub>2</sub>, CeO<sub>x</sub>/Au(111), CeO<sub>x</sub>/Cu(111), and Au/CeO<sub>x</sub>/TiO<sub>2</sub>, has shown that the main role of the metal is to adsorb CO while the role of the oxide is to dissociate water.<sup>12,20–23</sup> Although all the steps involved in the WGS

reaction might occur on the surface of the metal, or metal NP, the high activation barriers estimated for the dissociation of H<sub>2</sub>O makes the bare metal a quite inefficient catalyst.<sup>24,25</sup> That is why it is critical that the properties of the oxide facilitate H<sub>2</sub>O dissociation.<sup>20,12</sup> On its turn, metal-oxide surfaces readily adsorb water, and are able to dissociate H<sub>2</sub>O easily, mainly at the O vacancy sites, to produce hydroxyls that cover the surface. However, in a WGS environment, these hydroxyls usually react with CO to give rise to very stable intermediates (HCOO, CO<sub>x</sub>) that stop the reaction.<sup>20</sup> Therefore, an adequate combination of the metal oxide and metal properties leads to a high active catalyst: H<sub>2</sub>O is easily dissociated on the oxide and less stable intermediates which evolve to products with low activation barriers are formed on the metal particle or at the interface.

Oxygen vacancies, which involve the presence of Ti<sup>3+</sup> or Ce<sup>3+</sup> species, are the main active sites for dissociative chemisorption of water on TiO<sub>2</sub> and CeO<sub>2</sub>.<sup>20,12,22,26–31</sup> Therefore the presence of reduced species Ti<sup>3+</sup> or Ce<sup>3+</sup> is essential to achieve high catalytic activity in the WGS. For instance, a catalyst consisting of CeO<sub>x</sub> NPs supported on Au(111) has activities higher than those of standard WGS catalysts such as Cu(111) or Cu(100).<sup>20</sup> The activity was found to be directly related to the presence of some Ce<sup>3+</sup> species. Another way to enlarge the concentration of active Ce<sup>3+</sup> sites is to modify the pure oxide by mixing it with a different metal oxide. The properties of these mixed-metal oxides can be very different from those of the pure oxides. Higher effects

<sup>a)</sup>Author to whom correspondence should be addressed. Electronic mail: graciani@us.es.

can be expected by mixing the oxides at the nanometer level. In fact, in our previous work<sup>21</sup> we have shown that the growing of CeO<sub>x</sub> NPs on TiO<sub>2</sub> leads to the formation of some structures of cerium oxide imposed by the interaction with the host oxide in which the relative stability of Ce<sup>4+</sup>/Ce<sup>3+</sup> is strongly affected to the point that all Ce atoms are in a +3 oxidation state. Deposition of Au nanoclusters on these mixed metal-oxide CeO<sub>x</sub>/TiO<sub>2</sub> surfaces leads to catalysts that show a dramatic improvement in the activity, even larger than that observed for the WGS on CeO<sub>x</sub>/Au(111) or Au/CeO<sub>2</sub>.<sup>20,21</sup> Extremely high WGS activity is also found for the Cu/CeO<sub>x</sub>/TiO<sub>2</sub>(110) and Pt/CeO<sub>x</sub>/TiO<sub>2</sub>(110) systems.<sup>32</sup>

Although a direct influence of the mixed-metal oxide properties on the catalytic activity has been suggested, a detailed analysis of the CeO<sub>x</sub>/TiO<sub>2</sub> interface at the electronic level has not yet been reported. For instance, the origin of the predominance of Ce<sup>3+</sup> over Ce<sup>4+</sup> species at the surface, or the ability of such a system to dissociate water molecules, still remain open questions. In the present paper we report a theoretical work based on periodic density-functional calculations of the formation process of CeO<sub>x</sub> NPs on the TiO<sub>2</sub> surface from the interaction of Ce/TiO<sub>2</sub> with O<sub>2</sub>, as well as their redox properties, e.g., their reactions with CO/O<sub>2</sub>. We study the relation between the geometrical and electronic structures and their impact on the reactivity. Finally we examine the interaction and dissociation of water on the CeO<sub>x</sub>/TiO<sub>2</sub> surface. Since the TiO<sub>2-x</sub> system has also been found to be a good system for the dissociative chemisorption of water, and the formation of TiO<sub>x</sub> species on the surface of TiO<sub>2</sub> from interstitial Ti has been recently shown,<sup>33</sup> we have also performed some calculations for the TiO<sub>x</sub>/TiO<sub>2</sub> system in order to compare it with CeO<sub>x</sub>/TiO<sub>2</sub>.

## II. DENSITY-FUNCTIONAL CALCULATIONS

The density functional theory (DFT) calculations were performed using the plane-wave-pseudopotential approach within the projector augmented wave method<sup>34</sup> together with the GGA exchange correlation functional proposed by Perdew *et al.*<sup>35</sup> as implemented in the VASP 4.6 code.<sup>36,37</sup> A plane-wave cutoff energy of 400 eV was used. We treated the Ti (3s, 3p, 3d, 4s), Ce (4f, 5s, 5p, 5d, 6s), and O (2s, 2p) electrons as valence states, while the remaining electrons were kept frozen as core states. To obtain faster convergence, thermal smearing of one-electron states ( $k_B T = 0.05$  eV) was allowed using the Gaussian smearing method to define the partial occupancies. We chose a (4 × 2) surface model with the aim to have isolated CeO<sub>x</sub> monomers and dimers on the TiO<sub>2</sub>(110) surface. The distance between two nearest Ce<sub>2</sub>O<sub>3</sub> dimers was ~6 Å, which is a reasonable distance with a computationally affordable model. In order to avoid spurious effects due to the finite thickness of the slab representing the surface, we used a recently published model of six layers.<sup>38,39</sup> In this model the two lowest layers were fixed at the optimized atomic bulk positions while atoms in the upper four layers were allowed to relax. This surface model has been shown to minimize the well-known energy oscillations as a function of the number of layers (even-odd) and reaches

convergence for both the geometric and electronic surface structures.<sup>38,39</sup> This surface model, that amounts to 288 atoms, has been successfully used in previous works.<sup>21,22,40,41</sup> The energy was estimated at the gamma point. In order to represent adequately the electronic structure of Ce (in particular the 4f level of the Ce<sup>3+</sup> species) we used the GGA + *U* formalism. The Hubbard *U* term was added to the plain GGA functional employing the rotationally invariant approach proposed by Dudarev *et al.*,<sup>42</sup> in which the Coulomb *U* and exchange *J* parameters are combined into a single parameter  $U_{\text{eff}} = U - J$ . For Ce we have used the  $U_{\text{eff}}$  of 4.5 eV which was self-consistently calculated by Fabris *et al.*<sup>43</sup> using the linear-response approach of Cococcioni and de Gironcoli<sup>44</sup> and which is in the range of values usually proposed in the literature (4.5–5.5 eV) for GGA + *U* calculations.<sup>45–53</sup> For the 3d states of Ti we also chose a  $U_{\text{eff}}$  parameter of 4.5 eV as it reproduces the experimental values of the gap between the Ce<sup>3+</sup> 4f and Ti<sup>3+</sup> 3d levels observed in the valence photoemission spectra of Ce/TiO<sub>2</sub>(110) system.<sup>21</sup> Although lower values for  $U_{\text{eff}}$  have also been proposed for a balanced description of bulk CeO<sub>2</sub> and Ce<sub>2</sub>O<sub>3</sub> oxides,<sup>54,55</sup> the set of parameters we have selected allows for a correct description of the gaps observed in the experimental photoemission spectra of our systems consisting of CeO<sub>x</sub> clusters supported on the TiO<sub>2</sub>(110) surface.<sup>21</sup> Furthermore, the presence of Ce<sup>3+</sup> species was indicated by a characteristic 4f peak in the band gap and later confirmed by the magnetization of the Ce atoms (higher than 0.9 electrons) found in the calculations.

The adsorption energy for a given species *X* (where *X* stands for Ce atom, H<sub>2</sub>O, CO, etc.) has been calculated as

$$E_{\text{ads}}(X) = E(X/\text{TiO}_2) - E(X) - E(\text{TiO}_2),$$

where  $E_{\text{ads}}(X)$  is the adsorption energy of *X* on TiO<sub>2</sub>(110),  $E(X/\text{TiO}_2)$  is the total energy of the system in which *X* is adsorbed on the TiO<sub>2</sub>(110) surface,  $E(X)$  is the energy of the isolated *X* and  $E(\text{TiO}_2)$  is the energy of the slab model of the surface.

Transitions states have been calculated by using the climbing image (CI) version of the nudged elastic band (NEB) algorithm<sup>56</sup> and in all cases, after a vibrational analysis, a single imaginary frequency has been obtained for these structures. Since these calculations have a huge computational cost in the transitions state searches, the model was reduced to four layers. The reliability of this reduced model was verified by comparing the reaction energy for the water dissociation at the surface from both models: -0.70 eV (six-layer thick model) versus -0.64 eV (four-layer thick model).

## III. RESULTS AND DISCUSSION

### A. Growth of the CeO<sub>x</sub> particles on TiO<sub>2</sub>(110)

Previous scanning tunneling microscopy (STM) results have shown the formation of CeO<sub>x</sub> NPs when depositing Ce on TiO<sub>2</sub>(110) in oxygen atmosphere.<sup>21</sup> At low Ce coverage, two kinds of CeO<sub>x</sub> spots were identified and assigned to single Ce atoms and Ce–Ce dimers, which were bonded to bridge O atoms. To determine the structure, stability and oxidation state of these species, we have simulated a process of

104703-3 Nanomixed-metal oxide: The catalytic effect

J. Chem. Phys. **132**, 104703 (2010)

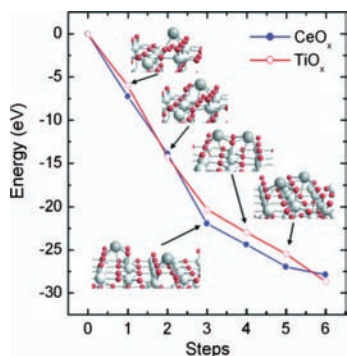


FIG. 1. Energy pathway for the formation of CeO<sub>x</sub> and TiO<sub>x</sub> species on TiO<sub>2</sub>(110) starting from the adsorption of Ce/Ti atoms and subsequent progressive interaction with O<sub>2</sub>. *M* indicates Ce or Ti metal adatoms in each case. Colors: Ce/Ti adatoms (dark gray), Ti atoms of the TiO<sub>2</sub> support (soft gray) and O (soft red). Steps: (1) *M* atom adsorption, (2) O<sub>2</sub> adsorption-dissociation: formation of the 1st monomer (MO<sub>2</sub>), (3) 2nd *M* atom adsorption, (4) 1st dimer formation (M<sub>2</sub>O<sub>2</sub>), (5) (1/2)O<sub>2</sub> adsorption and 2nd dimer formation (M<sub>2</sub>O<sub>3</sub>), and (6) (1/2)O<sub>2</sub> adsorption and degradation in monomers (2MO<sub>2</sub>).

sequential adsorption-oxidation for Ce deposited on TiO<sub>2</sub>. Figure 1 shows the energy pathway for such a process. The adsorption energy of the first Ce atom is very high (−7.01 eV). On the most stable adsorption site the Ce atom is three-fold coordinated and interacts with one O from the plane and two bridge O (see Fig. 1, step 1). The formal oxidation state is +3, which gives rise to the characteristic 4*f* peak above the O 2*p* band on the projected density of states (DOS) (bottom panel in Fig. 2). Upon adsorption, the Ce atom (6*s*<sup>2</sup>5*d*4*f*) formally releases three electrons to the oxide, that are transferred from the Ce 6*s* and 5*d* levels to the lower energy Ti 3*d* states, reducing three Ti atoms to Ti<sup>3+</sup>. Two of them are

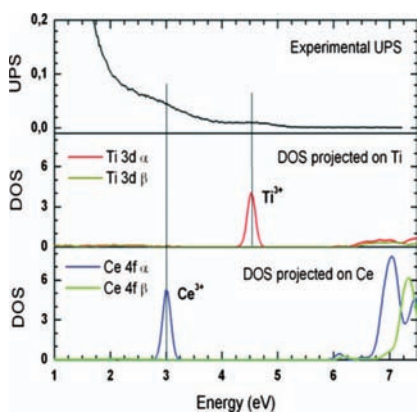
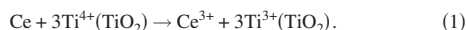
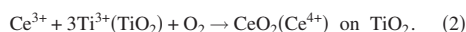


FIG. 2. Experimental photoemission spectrum (top) (Ref. 21), and calculated DOS projected on the reduced Ti atom (middle) and the adsorbed Ce atom (bottom) for the deposition of Ce on TiO<sub>2</sub>(110). In the calculation the *U*<sub>eff</sub> parameter used for both Ce 4*f* and Ti 3*d* is 4.5 eV. (Reproduced from our previous work in Proc. Natl. Acad. Sci. U.S.A., Ref. 21).

located in the surface layer and the third one is located in the subsurface layer. The fourth valence electron of Ce remains in a 4*f* orbital, whose energy is lower than the empty Ti 3*d* levels (Fig. 2), and therefore is not transferred, leaving the oxidation state of Ce as +3. To make a Ce<sup>4+</sup> ion it would be necessary to have empty states in the O 2*p* band that is lower in energy than the Ce 4*f* level. The high chemisorption energy that we calculated can be understood bearing in mind that there are two complementing contributions to the bond: the large stabilization of the three electrons that shift from high to low energy levels, Ce(5*d*6*s*<sup>2</sup>)→Ti(3*d*), and the strong electrostatic energy gain that arises from the interaction of the Ce<sup>3+</sup> cation with three surface O<sup>2−</sup> anions. Thus, the adsorption process of atomic Ce involves direct bonding with O atoms of the titania and an electron transfer that could be described as



On the other hand, to get Ce<sup>4+</sup> ions on the stoichiometric oxide would need the presence of extra oxygen. Given that CeO<sub>x</sub> species are formed in the presence of O<sub>2</sub>,<sup>21</sup> it is appropriate to study the interaction of adsorbed Ce with oxygen. The adsorption-dissociation of O<sub>2</sub> over adsorbed atomic Ce is a highly exothermic process (−6.88 eV). The final structure is a unit of CeO<sub>2</sub> over TiO<sub>2</sub>, where the O atoms are adsorbed on the in-plane Ti atoms and strongly interact with the Ce atom that remains in the initial position (see Fig. 1, step 2). This structure is similar to that observed by Wendt *et al.*<sup>43</sup> for interstitial Ti interacting with O<sub>2</sub> on the TiO<sub>2</sub>(110) surface. The formal oxidation state of the Ce in this configuration is +4. This was neatly observed on the projected DOS on Ce (not shown) where the characteristic 4*f* peak of Ce<sup>3+</sup> completely disappeared. A further electron rearrangement comes from the fact that to fill the O 2*p* orbitals, in addition to the Ce 4*f*, three more electrons are needed, and therefore 3Ti<sup>3+</sup>, previously reduced, are reoxidized to Ti<sup>4+</sup>. This new multielectron transfer, together with the strong electrostatic Ce<sup>4+</sup>–O<sup>2−</sup> interaction explain the high energy released in the process, which could be described as



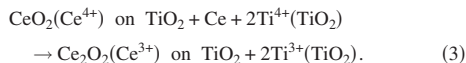
We will call this CeO<sub>2</sub> particle a monomer, which is identified as the small spots observed in STM images for CeO<sub>x</sub>/TiO<sub>2</sub>(110).<sup>21</sup>

Deposition of the second Ce atom at a surface position far from the monomer (see Fig. 1, step 3) releases an energy of −8.03 eV. As in the case of the first Ce atom, the incoming second Ce atom releases three electrons, one of them does not go to the relatively high energy Ti 3*d* levels, but rather to the lower energy Ce 4*f* of the CeO<sub>2</sub> monomer. Therefore, the Ce<sup>4+</sup> of the monomer is reduced to Ce<sup>3+</sup>. If we now move this second Ce atom close to the neighbors of the first Ce atom, there is a release of energy that becomes larger when it is placed in between the two extra O atoms from the CeO<sub>2</sub> monomer and a row of bridge O of the TiO<sub>2</sub>(110) surface (Fig. 1, step 4), the stabilization being in this case of −2.45 eV. Formally it corresponds to a Ce<sub>2</sub>O<sub>2</sub> dimer adsorbed on the surface. The energy exchange for the whole process, i.e. direct transformation from steps 2 to 4, would be

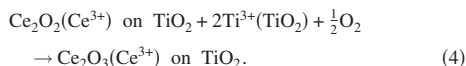
104703-4 Graciani *et al.*

J. Chem. Phys. **132**, 104703 (2010)

as large as  $-10.48$  eV. This highly exothermic process clearly implies that as long as “free” Ce atoms and monomers coexist on the surface, dimers will be formed from their interaction. The oxidation state for both Ce atoms in the dimer was  $\text{Ce}^{3+}$ . The process could be described as

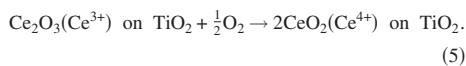


We will now consider the interaction of a  $\text{Ce}_2\text{O}_2$  dimer with oxygen to form a dimer with a composition of  $\text{Ce}_2\text{O}_3$  (Fig. 1, steps 4 and 5). It is well known that the presence of oxygen vacancies on  $\text{TiO}_2(110)$  (which formally involves two  $\text{Ti}^{3+}$  cations/vacancy) generates adsorbed O atoms under oxygen pressure. After deposition of Ce atoms and formation of the first dimers we have generated  $\text{Ti}^{3+}$  species [see Eqs. (1) and (3)] which are able to dissociate oxygen. The presence of such adsorbed O atoms after Ce deposition under oxygen pressure were observed in STM images,<sup>21</sup> and prompted us to consider models with a extra atomic oxygen adsorbed on the surface. Indeed, the O atoms readily react with the surface reoxidizing  $\text{Ti}^{3+}$  centers and forming  $\text{Ce}_2\text{O}_3$  dimer. The process could be described as



The energy that is released in this process is  $-2.59$  eV and the structure obtained is reported in Fig. 1, step 5.

Let us now complete the oxidation of the system by adding an extra oxygen atom, i.e., the transformation from the  $\text{Ce}_2\text{O}_3$  dimer to two  $\text{CeO}_2$  monomers (Fig. 1, steps 5 and 6). As can be seen the process is exothermic but, in contrast to the previous oxidation step, (steps 4  $\rightarrow$  5), the released energy amounts for only  $-0.92$  eV (roughly one third). The reason for this is that now there are no longer high energy Ti 3d electrons but two electrons in relatively low energy Ce 4f states. Since the incoming O 2p states are lower in energy than the 4f, the electronic transfer process from 4f to 2p states is still favorable, but the released energy is much lower. This means that as long as  $\text{Ti}^{3+}$  species exist,  $\text{O}_2$  will prefer to adsorb and dissociate on them because the stabilization energy for the system is much higher. Therefore, even though the oxidation process of dimers is favorable, it is not the preferred site for the adsorption and dissociation of  $\text{O}_2$ . In consequence, the oxidation of  $\text{Ce}_2\text{O}_3$  will not happen until all the  $\text{Ti}^{3+}$  species completely disappear from the system. The process could be described as



### B. Formation energy and redox properties

The structures seen in Fig. 1 and in STM images<sup>21</sup> for the ceria clusters in contact with  $\text{TiO}_2(110)$  are quite different from the fluorite structure characteristic of bulk  $\text{CeO}_2$ . Furthermore, the energetic analysis that we have discussed so far might appear surprising if we compare it with the same process in bulk. The energy involved in the oxidation process

TABLE I. Formation energies (eV) per Ce atom (see the text for details) of bulk and adsorbed-particle phases of  $\text{CeO}_2$  and  $\text{Ce}_2\text{O}_3$  species. The differences between the phases for each species and between the species for each phase are shown for easy measuring of the supported-particle effect on the formation energy (0.87 eV/Ce atom).

	Bulk	Particle on surface	$\Delta E$ (particle-bulk)
$\text{CeO}_2$	-14.50	-13.88	0.62
$\text{Ce}_2\text{O}_3$	-13.22	-13.47	-0.25
$\Delta E(\text{Ce}_2\text{O}_3 - \text{CeO}_2)$	1.28	0.41	0.87

from  $\text{Ce}_2\text{O}_3$  (bulk) to  $2\text{CeO}_2$  (bulk) in the presence of  $\frac{1}{2}\text{O}_2$  (g) is  $-2.56$  eV (theory) and  $-3.95$  eV (exp), respectively.<sup>57</sup> The fact that the oxidation is less favored when  $\text{CeO}_x$  NPs are supported on the  $\text{TiO}_2(110)$  surface might arise from two possibilities: either  $\text{Ce}_2\text{O}_3$  NPs are stabilized, or  $\text{CeO}_2$  NPs are destabilized when they are deposited on the titania surface, and of course it may also due to a combination of both contributions. In order to try to quantify these effects we have estimated the formation energy for such mixed-metal oxide phases, and compared with the formation of the bulk phases. The formation energy (per Ce atom) for the bulk phase may be written as

$$\Delta E_f(\text{CeO}_x) = E(\text{CeO}_x) - E(\text{Ce, atom}) - \frac{x}{2}E(\text{O}_2, g)$$

and for the particles on the surface as

$$\begin{aligned} \Delta E_f(\text{CeO}_x) &= E(\text{CeO}_x/\text{TiO}_2) - E(\text{TiO}_2, \text{slab}) \\ &\quad - E(\text{Ce, atom}) - \frac{x}{2}E(\text{O}_2, g), \end{aligned}$$

where  $E(\text{CeO}_x)$  is the bulk energy per Ce atom,  $E(\text{CeO}_x/\text{TiO}_2)$  is the energy of the  $\text{TiO}_2$  slab with a  $\text{CeO}_x$  particle adsorbed,  $E(\text{Ce, atom})$  is the energy of one Ce atom,  $E(\text{O}_2, g)$  is the energy of the  $\text{O}_2$  molecule, and  $E(\text{TiO}_2, \text{slab})$  is the energy of the  $\text{TiO}_2$  slab. It is known that the formation energy is calculated with respect to the most stable phase (in this case we should use for Ce the energy from metallic bulk Ce per Ce atom). However, we are not interested in the exact values for the formation energy but in the difference among them, which is the same and not dependent on the reference energy for Ce. The results are shown in Table I.

The formation energy for a  $\text{CeO}_2$  particle on the surface is lower (in absolute value) than for bulk  $\text{CeO}_2$ . It means that the particle would prefer to be as  $\text{CeO}_2$  bulk rather than an isolated particle on  $\text{TiO}_2(110)$ . This is rather easy to understand, considering the reduction on coordination with the O atoms and the loss of Madelung energy. The instability introduced by the change in environment is 0.62 eV/Ce atom (see Table I). Instead, the  $\text{Ce}_2\text{O}_3$  particle is stabilized on the surface with respect to the bulk by  $-0.25$  eV/Ce atom (see Table I). Therefore, the combined effect of the  $\text{Ce}_2\text{O}_3$  stabilization and the  $\text{CeO}_2$  destabilization on the surface is the responsible for reducing the relative stability of  $\text{CeO}_2$  and  $\text{Ce}_2\text{O}_3$  from 1.28 eV/Ce atom in the bulk to 0.41 eV/Ce atom when in the form of a mixed-metal oxide on  $\text{TiO}_2(110)$ . Our calculations show that the destabilization of  $\text{CeO}_2$  is significantly higher than the stabilization of  $\text{Ce}_2\text{O}_3$  (see Table I).

104703-5 Nanomixed-metal oxide: The catalytic effect

J. Chem. Phys. **132**, 104703 (2010)

TABLE II. Redox properties of the couple Ce<sub>2</sub>O<sub>3</sub>/CeO<sub>2</sub> measured through their reaction energies with CO/O<sub>2</sub> for supported particle and bulk phases. The difference in the reaction energy between both phases for each reaction is shown for easy measuring of the supported-particle effect.

		Particles (P)	Bulk (B)	Δ (P-B)
Oxidation	Ce <sub>2</sub> O <sub>3</sub> + $\frac{1}{2}$ O <sub>2</sub> → 2CeO <sub>2</sub>	-0.92	-2.56	1.64
Reduction	2CeO <sub>2</sub> + CO → Ce <sub>2</sub> O <sub>3</sub> + CO <sub>2</sub>	-2.35	-0.71	-1.64

The fact that the formation energies of CeO<sub>2</sub> and Ce<sub>2</sub>O<sub>3</sub> are similar in the case of a mixed-metal oxide (the difference is only 0.41 eV in 13.88 eV, i.e. 3%) means that the system is almost equally stabilized, on a per Ce atom basis, by the formation of CeO<sub>2</sub> monomers or Ce<sub>2</sub>O<sub>3</sub> dimers. This result appears to be of great importance for catalysis on cerium oxides, as the CeO<sub>2</sub> ↔ Ce<sub>2</sub>O<sub>3</sub> conversion has been found to play an essential role in many catalytic processes as the three-way car exhaust catalysis, SO<sub>x</sub> destruction, alcohol synthesis from hydrogenation of CO or CO<sub>2</sub>, and the water gas shift reaction.<sup>58–60</sup> There is evidence that in these cases CeO<sub>2</sub> does not only work as a support for different precious metals, but rather, due to its facile reducibility, ceria can also directly participate in different steps of the catalytic process. Its activity is precisely ascribed to its oxygen storage capacity,<sup>58,60</sup> i.e., easily taking up and releasing oxygen under oxidizing and reducing conditions, respectively, which takes place according to the formal reaction scheme: 2CeO<sub>2</sub> → Ce<sub>2</sub>O<sub>3</sub> + 0.5O<sub>2</sub>. Our calculations bring theoretical evidence that the energetic preference for this reaction can be related to the similarity of the formation energy of Ce<sup>3+</sup> and Ce<sup>4+</sup> species on the TiO<sub>2</sub>(110) substrate. It also suggests that we could easily tune the system to favor a given oxidation state, as the main final oxidation state will be determined by the specific conditions under which the reaction takes place, but not by the intrinsic nature of the Ce species. If the system reacts with reducing species the main final oxidation states will be Ce<sup>3+</sup> while an oxidizing environment will lead the system to Ce<sup>4+</sup>. So, if the oxygen storage capacity is high in the bulk phase, it will be even higher in the mixed-metal oxide phase at the nanometer level in the system CeO<sub>x</sub>/TiO<sub>2</sub>, what allows us to expect a higher catalytic activity than that of bare CeO<sub>2</sub>. This has been shown for the WGS reaction case where the catalytic activity of *M*/CeO<sub>x</sub>/TiO<sub>2</sub> (*M*=Au, Cu or Pt) was found to be more than two times higher than that of *M*/CeO<sub>2</sub> or *M*/TiO<sub>2</sub>.<sup>21,32</sup>

To check the effect of environment on the CeO<sub>2</sub> ↔ Ce<sub>2</sub>O<sub>3</sub> exchange, we have calculated the energies involved in the processes of oxidation of Ce<sub>2</sub>O<sub>3</sub> with O<sub>2</sub> to give CeO<sub>2</sub>, and reduction in CeO<sub>2</sub> with CO to give CO<sub>2</sub> and Ce<sub>2</sub>O<sub>3</sub>. Table II shows the energetics for both bulk ceria and CeO<sub>x</sub> NPs supported on TiO<sub>2</sub>(110). In the bulk phase, it has been experimentally found that the oxidation process is strongly favored (−3.95 eV) while the reduction process by CO is not (the energy cost is 1.02 eV).<sup>57</sup> Our DFT calculations show a similar trend: the oxidation is more favored than the reduction (−2.56 eV versus −0.71 eV). We can see in Table II that the tendency in the mixed-metal oxide phase at the nanometer level is just the opposite than in bulk phase.

The reduction by CO is now clearly more favored (−2.35 eV) than the oxidation (−0.92 eV). Therefore, an inversion of the oxidation-reduction tendency of the system takes place when we move from bulk to CeO<sub>x</sub> particles supported on TiO<sub>2</sub>. At the nanometer level the mixed-metal oxide effect on the redox properties of the couple Ce<sub>2</sub>O<sub>3</sub>/2CeO<sub>2</sub> could be estimated to be 1.64 eV, as the reduction process is favored by −1.64 eV and the oxidation hampered by 1.64 eV with respect to the bulk (see Table II). Our conclusion that to reduce Ce<sup>4+</sup> to Ce<sup>3+</sup> is easier for the mixed-metal oxide, was confirmed by comparing the behavior of CeO<sub>2</sub>(111) and CeO<sub>x</sub>/TiO<sub>2</sub>(110). For example, a CeO<sub>2</sub>(111) surface did not undergo reduction under an atmosphere of 20 Torr of CO at 400 K, while a CeO<sub>2</sub>/TiO<sub>2</sub>(110) surface under the same conditions was completely transformed into Ce<sub>2</sub>O<sub>3</sub>/TiO<sub>2</sub>(110).<sup>21</sup>

### C. TiO<sub>x</sub> versus CeO<sub>x</sub> particles on TiO<sub>2</sub>(110)

In a recent article the formation of TiO<sub>x</sub> clusters on the TiO<sub>2</sub> surface, formed by direct interaction of O<sub>2</sub> with interstitial Ti atoms which move from the bulk to the surface, has been reported.<sup>33</sup> To compare the behavior of CeO<sub>x</sub> and TiO<sub>x</sub> species on TiO<sub>2</sub> we report in Fig. 1 the adsorption-oxidation path for Ti. As can be seen the *M*<sup>4+</sup> states (where *M* is the metal) are more stable for Ti than for Ce (Fig. 1, steps 2 and 6). In contrast, the *M*<sup>3+</sup> states are always more stable with Ce than with Ti (Fig. 1, steps 1, 3–5). The difference is due to the higher energy of the 3*d* Ti<sup>3+</sup> valence electron (see Fig. 2), while for Ce<sup>3+</sup> the 4*f* electron is in a significantly lower level. In this case, the Ce center is neither greatly destabilized by forming Ce<sup>3+</sup> nor greatly stabilized when moves to Ce<sup>4+</sup>. This is in contrast to Ti, which is relatively more destabilized when reduced to Ti<sup>3+</sup> and, consequently, the stabilization is much higher when it is reoxidized to Ti<sup>4+</sup>. This makes the oxidation step from supported Ti<sub>2</sub>O<sub>3</sub> to TiO<sub>2</sub> in O<sub>2</sub> presence much more favored −3.23 eV than the same step in the case of Ce (−0.92 eV) (see Fig. 1, steps 5–6). It also explains that the reduction from supported TiO<sub>2</sub> to Ti<sub>2</sub>O<sub>3</sub> in the presence of CO is almost thermoneutral (−0.04 eV), while the same step in the case of supported ceria is neatly exothermic −2.35 eV.

### D. Electronic structure and the relative stability

Overall, our calculations show that Ce<sub>2</sub>O<sub>3</sub> is stabilized as mixed-metal oxide on the surface of TiO<sub>2</sub> compared to the bulk phase, while CeO<sub>2</sub> is destabilized. As a result, the TiO<sub>2</sub>-supported ceria cluster can be oxidized or reduced in a much easier way than the bulk materials. To better understand the different stability between these phases, we have calculated the DOS projected on Ce and O atoms in both bulk and supported-particle phases for Ce<sub>2</sub>O<sub>3</sub> and CeO<sub>2</sub>. Here, the DOS for the isolated free particle with the same geometry that the supported particle has also been included for comparison, in order to determine the effect of the structure of the NP and the effect of the interaction with the support. As shown in Fig. 3, the formation of the mixed-metal oxide involves significant changes in the electronic structure. For the free particle, molecular bands with strongly mixed Ce 4*f* and O 2*p* were observed, indicating a high degree of

104703-6 Graciani *et al.*

J. Chem. Phys. **132**, 104703 (2010)

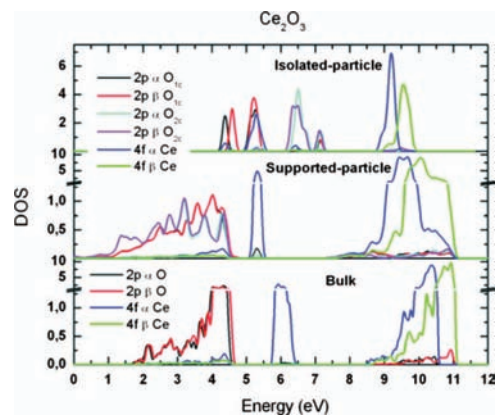


FIG. 3. DOS projected on Ce and O atoms of the  $\text{Ce}_2\text{O}_3$  unit for the systems: perfect bulk (bottom), supported particle on  $\text{TiO}_2(110)$  (middle), and isolated particle with the same geometry than that of the supported one (top).  $\text{O}_{1c}$  and  $\text{O}_{2c}$  stand for oxygen atoms mono- and bi-coordinated to Ce atoms respectively.

covalency. That is, the isolated  $\text{Ce}_2\text{O}_3$  unit is electronically transformed into a molecule. However, when this particle is deposited on  $\text{TiO}_2$ , the electronic structure of the particle returns to a solidlike DOS with wide O 2p and Ce 4f bands (see Fig. 3). The effect of the interaction with the support is very important since it “crystallizes” the electronic structure of the cerium oxide particle from an initial “molecular” distribution, leading to a true mixed-metal oxide rather than a supported particle.

Compared to bulk  $\text{Ce}_2\text{O}_3$ , the 2p and 4f main bands are wider in the nanomixed-metal oxide. As a consequence, after deposition, the band-gap between the top of the O 2p band and the bottom of the main Ce 4f band is reduced by 1.44 eV. In addition, the Ce 4f band, that corresponds to the valence electron of the reduced specie  $\text{Ce}^{3+}$  and locates in the midband gap between the main O 2p and the conduction bands, is shifted by 0.8 eV to the lower energies in the mixed-metal oxide. In other words, the 4f valence electron of  $\text{Ce}^{3+}$  is stabilized with respect to bulk phase. As shown in Fig. 3, there is almost no gap between the O 2p band and 4f  $\text{Ce}^{3+}$  little band in the mixed-metal oxide. This close distribution allows a higher mixing between the two bands, and therefore increases the covalent character of the bond. In fact, we can see in Fig. 3 that O 2p band appears at the same energy as  $\text{Ce}^{3+}$  4f band, indicating a certain covalent character of the Ce–O bond in the particle. In contrast, the Ce–O overlapping is, however, much lower in the bulk phase. Furthermore, the width of the little 4f peak of  $\text{Ce}^{3+}$  is also reduced by 0.25 eV when going from bulk to surface nanomixed-metal oxide, indicating a more localized molecular feature (approaching a single level energy like in the molecules) with respect to the bulk. That is, the  $\text{Ce}_2\text{O}_3$  unit seems to be crystallized by the interaction with the support, but some covalent character coming from the molecular electronic structure of the isolated particle remains in the sup-

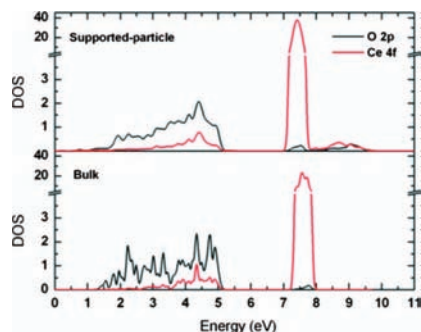


FIG. 4. DOS projected on Ce and O atoms of the  $\text{CeO}_2$  unit for the systems: perfect bulk (bottom) and supported particle on  $\text{TiO}_2(110)$  (top).

ported particle. This remaining covalency helps stabilizing the supported  $\text{Ce}_2\text{O}_3$  unit by lowering the energy of the  $\text{Ce}^{3+}$  4f band.

As the 4f band of fully oxidized  $\text{Ce}^{4+}$  is completely empty no electronic-induced change in the energy is expected by the interaction with the support. Indeed, no significant differences are observed when the DOS of the supported  $\text{CeO}_2$  unit and that of the bulk are compared (Fig. 4). Therefore, there is no electronic stabilization in the  $\text{CeO}_2$  unit when going from bulk to surface nanomixed-metal oxide. Accordingly, the loss of the Madelung potential and coordination with O atoms is not electronically compensated, and  $\text{CeO}_2$  is more stable as bulk phase than as nanomixed-metal oxide on the  $\text{TiO}_2$  surface.

#### E. Adsorption and dissociation of $\text{H}_2\text{O}$ on $\text{CeO}_x/\text{TiO}_2(110)$

As stated in Sec. I, all the steps involved in the WGS reaction can take place on the surfaces of the plain metals or metal NPs, but for the dissociation of  $\text{H}_2\text{O}$  a high activation barrier has been predicted.<sup>24,25</sup> In contrast, water easily dissociates on the metal oxide, therefore, an adequate coupling of the oxide and metal properties leads to a high active catalyst. That is why  $\text{Au}/\text{TiO}_2$  or  $\text{Cu}/\text{TiO}_2$  are efficient WGS catalysts.<sup>22</sup> The activation energy for the dissociation of  $\text{H}_2\text{O}$  on  $\text{TiO}_2$  oxygen vacancies has been calculated to be 0.35 eV (Ref. 27) while on the (111) surface of Au and Cu the barrier increases to 1.95 eV (Ref. 61) and 1.36 eV,<sup>62</sup> respectively. Although, the presence of steps in the metal surfaces can decrease the activation energy for the dissociation of  $\text{H}_2\text{O}$  on Cu from 1.36 eV in  $\text{Cu}(111)$  to 0.9 eV (or 0.71 eV with the zero-point correction) in  $\text{Cu}(321)$ ,<sup>63</sup> the activation energy is still twice the activation barrier in the  $\text{TiO}_2(110)$  oxygen vacancy. Therefore, any oxide, which decreases the barrier for the dissociation of  $\text{H}_2\text{O}$ , is expected to improve the catalytic activity of the system  $M/\text{MO}_x$  (where  $M$  is a metal). Since we have shown that the  $\text{Au}/\text{CeO}_x/\text{TiO}_2$  system is three times more active than  $\text{Au}/\text{TiO}_2$  for the WGS reaction and four times more active than  $\text{Cu}/\text{ZnO}$ , the most common WGS catalyst used in the industry,<sup>21</sup> it has been postulated that the barrier for the water dissociation on the  $\text{CeO}_x$  par-

104703-7 Nanomixed-metal oxide: The catalytic effect

J. Chem. Phys. **132**, 104703 (2010)

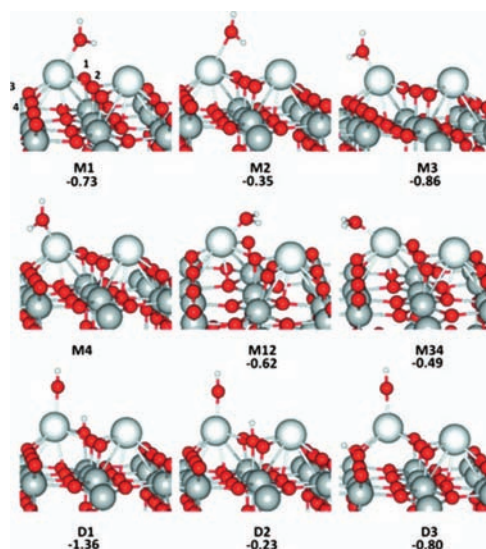


FIG. 5. Adsorption sites, geometries, and adsorption energies (eV) for the dissociation of water on Ce<sub>2</sub>O<sub>3</sub>/TiO<sub>2</sub>(110). In order to simplify the view only the Ce<sub>2</sub>O<sub>3</sub> particle and water are shown in the figure. The nonequivalent oxygen atoms have been labeled as: 1, 2, 3, and 4. Atom colors: red (O), dark gray (Ti), white (big spheres, Ce) and white (small spheres, H).

ticles will be smaller than on TiO<sub>2-x</sub>. With the aim to confirm this aspect we report here an energetic analysis for the dissociation of water on CeO<sub>x</sub>/TiO<sub>2</sub>(110).

To begin our analysis we examined the adsorption of a water molecule in the molecular and dissociated forms. Two different orientations were taken into account in which water can establish one or two hydrogen bonds (Fig. 5). Labels M and D refer to molecularly and dissociatively adsorbed water molecules, while the numbers indicate the oxygen atom to which is bound through hydrogen bond. Results for adsorption energies are reported in Fig. 5. For the molecular case, the larger interaction energy is  $-0.86$  eV (site M3), although there is another site, (M1) slightly less favored ( $-0.73$  eV). However, in the case of dissociated water there is a clear preference for site D1, where the transferred hydrogen binds oxygen O1 (see Fig. 5) that is the one with lower coordination, and therefore, the one with larger basicity. Given that the D1 site is by far the most stable, we considered a path for the water dissociation process, that may be easily visualized as the cleavage of an O–H bond starting from the configuration corresponding to M1 (Fig. 6). The transition state search using the CI-NEB algorithm showed an activation barrier of only  $0.04$  eV, i.e., eight times smaller than that found in the TiO<sub>2</sub> oxygen vacancy (see Fig. 6).<sup>27</sup> Moreover, the reaction energy for the dissociation of water on CeO<sub>x</sub>/TiO<sub>2</sub> was found to be  $-0.70$  eV, while on the oxygen vacancies of TiO<sub>2</sub> the estimated value was  $\sim -0.4$  eV. These results unambiguously indicate the larger ability of CeO<sub>x</sub>/TiO<sub>2</sub> to dissociate water and, therefore, can help to explain the superior WGS catalytic activity of the M/CeO<sub>x</sub>/TiO<sub>2</sub> (M = Au, Cu, Pt) systems over M/TiO<sub>2</sub>.<sup>21,32</sup>

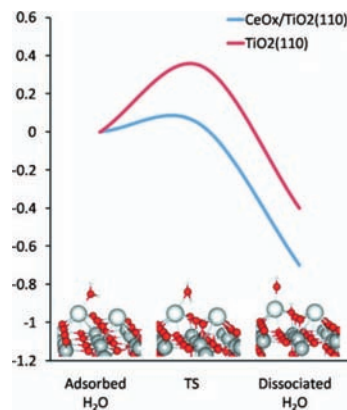


FIG. 6. Energy pathway for the dissociation of a H<sub>2</sub>O molecule on Ce<sub>2</sub>O<sub>3</sub>/TiO<sub>2</sub>(110) (our calculations) and on an oxygen vacancy of TiO<sub>2</sub>(110) (Ref. 27). Initial and final geometries for the dissociation on Ce<sub>2</sub>O<sub>3</sub>/TiO<sub>2</sub>(110) are shown. While for reduced TiO<sub>2</sub>(110) surface the reaction energy is  $\sim -0.4$  eV with an activation barrier of  $0.35$  eV, for Ce<sub>2</sub>O<sub>3</sub>/TiO<sub>2</sub>(110) the reaction energy is more exothermic ( $-0.7$  eV) with an activation barrier of only  $0.04$  eV. For atom colors see Fig. 5.

#### IV. SUMMARY AND CONCLUSIONS

In this paper we report a theoretical study of the structural and electronic properties of CeO<sub>x</sub> species supported on the rutile TiO<sub>2</sub>(110) surface by means of periodic GGA density-functional calculations that include a Hubbard-like correction  $U_{\text{eff}}$ . Deposition of Ce followed by reaction with O<sub>2</sub> gives rise to the formation of Ce<sub>2</sub>O<sub>3</sub> dimers diagonally arranged on the TiO<sub>2</sub>(110) surface, in agreement with the experimental observations. The redox properties of these CeO<sub>x</sub> NPs have been analyzed and found to be quite different from those of bulk ceria. Thus, the reduction process:  $2\text{CeO}_2 + \text{CO} \rightarrow \text{Ce}_2\text{O}_3 + \text{CO}_2$  is favored over the oxidation reaction:  $\text{Ce}_2\text{O}_3 + (1/2)\text{O}_2 \rightarrow 2\text{CeO}_2$ . Moreover, while, as expected, the CeO<sub>2</sub> species are less stable as supported NPs on TiO<sub>2</sub>(110) than as bulk, the Ce<sub>2</sub>O<sub>3</sub> species are stabilized when they are supported. These results suggest that the CeO<sub>x</sub>/TiO<sub>2</sub> interface behaves like a mixed-metal oxide rather than a supported NP of CeO<sub>x</sub>, and that this mixed-metal oxide favors the +3 oxidation state over the +4 under WGS reaction conditions. This is in contrast to the behavior of the TiO<sub>x</sub>/TiO<sub>2</sub>(110) system, for which our calculations show that the reduced state Ti<sup>3+</sup> is not favored over the Ti<sup>4+</sup>. This difference is obviously due to the fact that the  $3d$  occupied states in Ti<sup>3+</sup> are significantly higher in energy than the  $4f$  states of Ce<sup>3+</sup>, and as a result, under WGS reaction conditions, a full oxidation of Ti is expected, with loss of the potential activity of Ti<sup>3+</sup> centers.

The effect of a mixed-metal oxide at the nanometer level on the WGS catalytic activity has been analyzed by studying the interaction of the CeO<sub>x</sub>/TiO<sub>2</sub>(110) system with water. The dissociation process is quite exothermic,  $-0.70$  eV, while the activation energy for the dissociation is estimated to be as small as  $0.04$  eV. This is in contrast to a common support widely used in these reactions, namely TiO<sub>2</sub>, for

104703-8 Graciani *et al.*

J. Chem. Phys. **132**, 104703 (2010)

which the barrier for the dissociation in an oxygen vacancy has been calculated to be 0.35 eV.<sup>27</sup> This larger ability of CeO<sub>x</sub>/TiO<sub>2</sub> to dissociate water may help to explain the superior WGS catalytic activity of the M/CeO<sub>x</sub>/TiO<sub>2</sub> (M = Au, Cu, Pt) systems over M/TiO<sub>2</sub>.<sup>21,32</sup>

#### ACKNOWLEDGMENTS

This work was supported by the Spanish Ministerio de Ciencia e Innovación, MICINN, (Grant Nos. MAT2005-01872 and CSD2008-0023), and Junta de Andalucía (Grant No. FQM-132). The work done at the Brookhaven Nat. Lab was funded by the U.S. Department of Energy, Division of Chemical Sciences (Grant No. DE-AC02-98CH10886). We also thank the computational resources provided by the Barcelona Supercomputing Center-Centro Nacional de Supercomputación (Spain).

<sup>1</sup>N. Kruse, A. Frennet, and J. -M. Bastin, *Top. Catal.* **16/17**, 1 (2001).  
<sup>2</sup>D. E. Webster, *Top. Catal.* **16/17**, 33 (2001).  
<sup>3</sup>*Recent Advances in Catalysis for Hydrogen Production and Fuel Processing for Fuel Cells*, edited by C. Song (Springer Science + Business Media, Luxembourg), Top Catal. 49, 1–24 (2008).  
<sup>4</sup>*Catalysis by Gold*, edited by G. J. Hutchings and D. W. Goodman (Springer Science + Business Media, Luxembourg), 44, 1–343 (2007).  
<sup>5</sup>*Catalysis by Gold*, edited by G. J. Hutchings and M. Haruta (Elsevier, Amsterdam), Appl. Catal. A: Gen. 291, 1–262 (2005).  
<sup>6</sup>R. Burch, *Phys. Chem. Chem. Phys.* **8**, 5483 (2006).  
<sup>7</sup>O. Thinin, F. Diehl, P. Avenier, and Y. Schuurman, *Catal. Today* **137**, 29 (2008).  
<sup>8</sup>M. Haruta, N. Yamada, T. Kobayashi, and S. Ijima, *J. Catal.* **115**, 301 (1989).  
<sup>9</sup>M. Valden, X. Lai, and D. W. Goodman, *Science* **281**, 1647 (1998).  
<sup>10</sup>M. S. Chen and D. W. Goodman, *Science* **306**, 252 (2004).  
<sup>11</sup>Q. Fu, H. Saltsburg, and M. Flytzani-Stephanopoulos, *Science* **301**, 935 (2003).  
<sup>12</sup>J. A. Rodriguez, P. Liu, J. Hrbek, J. Evans, and M. Perez, *Angew. Chem., Int. Ed.* **46**, 1329 (2007).  
<sup>13</sup>J. Guzman, S. Carrettin, J. C. Fierro-Gonzalez, B. C. Gates, and A. Corma, *Angew. Chem., Int. Ed.* **44**, 4778 (2005).  
<sup>14</sup>W. Deng and M. Flytzani-Stephanopoulos, *Angew. Chem., Int. Ed.* **45**, 2285 (2006).  
<sup>15</sup>R. Si and M. Flytzani-Stephanopoulos, *Angew. Chem., Int. Ed.* **47**, 2884 (2008).  
<sup>16</sup>M. S. Chen and D. W. Goodman, *Top. Catal.* **44**, 41 (2007).  
<sup>17</sup>C. T. Campbell and C. H. F. Peden, *Science* **309**, 713 (2005).  
<sup>18</sup>F. Esch, S. Fabris, L. Zhou, T. Montini, C. Africh, P. Fornasiero, G. Comelli, and R. Rosei, *Science* **309**, 752 (2005).  
<sup>19</sup>S. Torbrügge, M. Reichling, A. Ishiyama, S. Morita, and O. Custance, *Phys. Rev. Lett.* **99**, 056101 (2007).  
<sup>20</sup>J. A. Rodriguez, S. Ma, P. Liu, J. Hrbek, J. Evans, and M. Perez, *Science* **318**, 1757 (2007).  
<sup>21</sup>J. B. Park, J. Graciani, J. Evans, D. Stacchiola, S. Ma, P. Liu, A. Nambu, J. F. Sanz, J. Hrbek, and J. A. Rodriguez, *Proc. Natl. Acad. Sci. U.S.A.* **106**, 4975 (2009).  
<sup>22</sup>J. A. Rodriguez, J. Evans, J. Graciani, J. B. Park, and J. F. Sanz, *J. Phys. Chem. C* **113**, 7364 (2009).  
<sup>23</sup>J. A. Rodriguez, J. Graciani, J. Evans, J. B. Park, F. Yang, D. Stacchiola, S. D. Senanayake, S. Ma, M. Pérez, P. Liu, J. F. Sanz, and J. Hrbek, *Angew. Chem., Int. Ed.* **48**, 8047 (2009).  
<sup>24</sup>A. A. Phatak, W. N. Delgass, F. H. Ribeiro, and W. F. Schneider, *J. Phys. Chem. C* **113**, 7269 (2009).  
<sup>25</sup>P. Liu and J. A. Rodriguez, *J. Chem. Phys.* **126**, 164705 (2007).  
<sup>26</sup>M. A. Henderson, *Surf. Sci. Rep.* **46**, 1 (2002).  
<sup>27</sup>J. Oviedo, R. Sanchez-de-Armas, M. A. San Miguel, and J. F. Sanz, *J.*

*Phys. Chem. C* **112**, 17737 (2008).  
<sup>28</sup>T. Wu, W. E. Kaden, and S. L. Anderson, *J. Phys. Chem. C* **112**, 9006 (2008).  
<sup>29</sup>G. Ketteler, S. Yamamoto, H. Bluhm, K. Andersson, D. E. Starr, D. F. Ogletree, H. Ogasawara, A. Nilsson, and M. Salmeron, *J. Phys. Chem. C* **111**, 8278 (2007).  
<sup>30</sup>S.-C. Li, Z. Zhang, D. Sheppard, B. D. Kay, J. M. White, Y. Du, I. Lyubinetsky, G. Henkelman, and Z. Dohnalek, *J. Am. Chem. Soc.* **130**, 9080 (2008).  
<sup>31</sup>S. Kajita, T. Minato, H. S. Kato, M. Kawai, and T. Nakayama, *J. Chem. Phys.* **127**, 104709 (2007).  
<sup>32</sup>J. B. Park, J. Graciani, J. Evans, D. Stacchiola, S. D. Senanayake, L. Barrio, P. Liu, J. F. Sanz, J. Hrbek, and J. A. Rodriguez, *J. Am. Chem. Soc.* **132**, 356 (2010).  
<sup>33</sup>S. Wendt, P. T. Sprunger, E. Lira, G. K. H. Madsen, Z. Li, J. Ø. Hansen, J. Mathiesen, A. Blekinge-Rasmussen, E. Lægsgaard, B. Hammer, and F. Besenbacher, *Science* **320**, 1755 (2008).  
<sup>34</sup>G. Kresse and J. Joubert, *Phys. Rev. B* **59**, 1758 (1999).  
<sup>35</sup>J. Perdew, J. Chevary, S. Vosko, K. Jackson, M. Pederson, D. Singh, and C. Fiolhais, *Phys. Rev. B* **46**, 6671 (1992).  
<sup>36</sup>G. Kresse and J. Hafner, *Phys. Rev. B* **47**, 558 (1993).  
<sup>37</sup>G. Kresse and J. Furthmüller, *Comput. Mater. Sci.* **6**, 15 (1996); *Phys. Rev. B* **54**, 11169 (1996).  
<sup>38</sup>K. J. Hameeuw, G. Cantele, D. Ninno, F. Trani, and G. Iadonisi, *J. Chem. Phys.* **124**, 024708 (2006).  
<sup>39</sup>S. J. Thompson and S. P. Lewis, *Phys. Rev. B* **73**, 073403 (2006).  
<sup>40</sup>J. Graciani, A. Nambu, J. Evans, J. A. Rodriguez, and J. F. Sanz, *J. Am. Chem. Soc.* **130**, 12056 (2008).  
<sup>41</sup>J. Graciani, L. J. Álvarez, J. A. Rodriguez, and J. F. Sanz, *J. Phys. Chem. C* **112**, 2624 (2008).  
<sup>42</sup>S. L. Dudarev, G. A. Botton, S. Y. Savrasov, C. J. Humphreys, and A. P. Sutton, *Phys. Rev. B* **57**, 1505 (1998).  
<sup>43</sup>S. Fabris, S. de Gironcoli, S. Baroni, G. Vicario, and G. Balducci, *Phys. Rev. B* **72**, 237102 (2005).  
<sup>44</sup>M. Cococcioni and S. de Gironcoli, *Phys. Rev. B* **71**, 035105 (2005).  
<sup>45</sup>C. W. M. Castleton, J. Kullgren, and K. Hermansson, *J. Chem. Phys.* **127**, 244704 (2007).  
<sup>46</sup>D. A. Andersson, S. I. Simak, B. Johansson, I. A. Abrikosov, and N. V. Skorodumova, *Phys. Rev. B* **75**, 035109 (2007).  
<sup>47</sup>M. Nolan, S. Grigoleit, D. C. Sayle, S. C. Parker, and G. W. Watson, *Surf. Sci.* **576**, 217 (2005).  
<sup>48</sup>M. Nolan, S. C. Parker, and G. W. Watson, *Surf. Sci.* **595**, 223 (2005).  
<sup>49</sup>M. Nolan, S. C. Parker, and G. W. Watson, *J. Phys. Chem. B* **110**, 2256 (2006).  
<sup>50</sup>M. B. Watkins, A. S. Foster, and A. L. Shluger, *J. Phys. Chem. C* **111**, 15337 (2007).  
<sup>51</sup>Z. Yang, Z. Lu, and G. Luo, *Phys. Rev. B* **76**, 075421 (2007).  
<sup>52</sup>J. L. F. Da Silva, *Phys. Rev. B* **76**, 193108 (2007).  
<sup>53</sup>J. L. F. Da Silva, M. V. Ganduglia-Pirovano, J. Sauer, V. Bayer, and G. Kresse, *Phys. Rev. B* **75**, 045121 (2007).  
<sup>54</sup>C. Loschen, J. Carrasco, K. M. Neyman, and F. Illas, *Phys. Rev. B* **75**, 035115 (2007).  
<sup>55</sup>C. Loschen, A. Migani, S. T. Bromley, F. Illas, and K. M. Neyman, *Phys. Chem. Chem. Phys.* **10**, 5730 (2008).  
<sup>56</sup>G. Henkelman, B. Uberuaga, and H. Jonsson, *J. Chem. Phys.* **113**, 9901 (2000).  
<sup>57</sup>D. R. Lide, *CRC Handbook of Chemistry and Physics*, 87th ed. (CRC, Cleveland, 2006).  
<sup>58</sup>A. Trovarelli, *Catal. Rev. - Sci. Eng.* **38**, 439 (1996).  
<sup>59</sup>M. Shelef and R. W. McCabe, *Catal. Today* **62**, 35 (2000).  
<sup>60</sup>A. Trovarelli, *Catalysis by Ceria and Related Materials*, 1st ed. (World Scientific, Singapore, 2002).  
<sup>61</sup>S. Kandoi, A. A. Gokhale, L. C. Grabow, J. A. Dumesic, and M. Mavrikakis, *Catal. Lett.* **93**, 93 (2004).  
<sup>62</sup>A. A. Gokhale, J. A. Dumesic, and M. Mavrikakis, *J. Am. Chem. Soc.* **130**, 1402 (2008).  
<sup>63</sup>J. L. C. Fajín, M. N. D. S. Cordeiro, F. Illas, and J. R. B. Gomes, *J. Catal.* **268**, 131 (2009).



### 6.3 Cu deposited on CeO<sub>x</sub>-modified TiO<sub>2</sub>(110): nature of the metal-support interaction and mechanism of the WGS reaction

José J. Plata, Jesús Graciani, José A. Rodríguez and Javier Fdez. Sanz

**Abstract:** To understand the behavior of the highly active Metal/CeO<sub>x</sub>/TiO<sub>2</sub> system, the bonding mechanism for the adsorption of Cu, Ag Au and Pt atoms on pure and CeO<sub>x</sub>-modified TiO<sub>2</sub>(110) surface has been analyzed by means of density functional calculations including a Hubbard-like term (DFT+U) to account for self-interactions effects. While Cu and Ag bind the surface mainly through charge transfer reducing one Ti<sup>4+</sup> atom of the surface to Ti<sup>3+</sup>, Au and Pt do it by electrostatic polarization. Favorable contributions to the bond appear when the metal is in contact with the CeO<sub>x</sub> particle increasing the adsorption energy, and, in the case of Au, a large contribution of the charge transfer to the bonding mechanism is then observed. The minimum energy path for the WGS reaction on the new highly active catalytic system Cu/CeO<sub>x</sub>/TiO<sub>2</sub>(110) has been obtained from state-of-the-art theoretical calculations. Main steps as adsorption-dissociation of water, and \*OCOH carboxyl intermediate formation-deprotonation have been studied. In this very particular system water dissociation is no longer the rate-limiting step since the energy barrier for this process is only 0.04 eV. One important insight of the present work is to show that easy full-hydration of the ceria particles strongly lowers the reaction barrier for the deprotonation of the \*OCOH intermediate and facilitates the evolution of the WGS reaction. For the first time it has been found a system on which the WGS reaction is able to work with all the involved energy barriers below 0.5 eV. This extraordinary behavior makes the Metal/CeO<sub>x</sub>/TiO<sub>2</sub> family outstanding candidate for industrial application as catalysts in the WGS reaction.

#### Introduction

In the past years there has been an increasing global concern about the environmental pollution. A huge research effort has been carried out by the scientific community and by the whole society in the searching for new, clean and renewable sources of energy.<sup>10</sup> One of the strategies to reach this goal is to use hydrogen as source of energy. The reaction of H<sub>2</sub> with O<sub>2</sub> in the proper way may produce electricity and just H<sub>2</sub>O as byproduct. However, the regular and massive sources of H<sub>2</sub> (usually as a subproduct from the refineries) very often contain CO, which poisons and collapses the fuel cell. The usual way to remove all CO from the H<sub>2</sub> source is by coupling a reactor containing H<sub>2</sub>O steam and a convenient catalyst to produce the so-called water-gas shift reaction (WGS): H<sub>2</sub>O + CO → H<sub>2</sub> + CO<sub>2</sub>,

in which CO is removed and more H<sub>2</sub> is produced.<sup>11,12</sup> This purified source of H<sub>2</sub> is then introduced in the fuel cell.

The WGS reaction has received much attention due to its important technological applications. Many catalytic systems, usually based on metal particles supported on an oxide, have been studied from theory and experiment, to improve the performance of the WGS reaction.<sup>11-20</sup> The main conclusion from those studies is that the WGS catalyst is bi-functional: a metal phase (usually supported nanoparticles) is needed for CO adsorption, while a reducible<sup>21-24</sup> oxide phase (usually TiO<sub>2</sub> or CeO<sub>2</sub>) is necessary for the adsorption and dissociation of water.<sup>5,17,25-27</sup> Low stable intermediates, which easily evolve to products, would be formed at the interface, avoiding the formation of the high stable intermediates, which stop the reaction (observed usually on the pure oxide).<sup>25</sup> It is interesting to note that neither pure metal,<sup>28,29</sup> nor pure oxide can carry out by itself the WGS reaction,<sup>25</sup> but together they achieve great activity, being present therefore a remarkable synergy between them.

In the case of CeO<sub>2</sub>, a direct correlation between the amount of reduced species Ce<sup>3+</sup> and the WGS catalytic activity has been found,<sup>25</sup> showing the importance of the reducibility of the oxide for the dissociation of water<sup>17,25,26,30-35</sup> and, in general, for the reactivity of CeO<sub>2</sub> surfaces.<sup>1</sup> Recently, some papers by Rodriguez *et al.* have shown, from experiment<sup>5,36,37</sup> and theory<sup>38</sup>, a new generation of highly active WGS catalysts, in which the amount of the active reduced species Ce<sup>3+</sup> on the surface of the support is highly increased with respect to the conventional oxide supports. This new oxide phase consists of a mixed-metal oxide at the nanometer level: really small CeO<sub>x</sub> particles (in fact dimers) are formed on the TiO<sub>2</sub> surface, being the interaction between them so high that the geometric and electronic properties of the CeO<sub>x</sub> particles are strongly modified, increasing the reducibility of Ce, and consequently improving the catalytic activity. Moreover, it has been experimentally shown that the presence of the CeO<sub>x</sub> particles on the TiO<sub>2</sub> surface increases the dispersion and the resistance to the thermal agglomeration of the metal particles on the TiO<sub>2</sub> surface pointing to a CeO<sub>x</sub> induced higher metal-support interaction.<sup>36</sup> This strong metal-support interaction decreases the size of the metal particles, increasing thus the catalytic activity. The performance of different metal particles on these new catalytic systems, show the sequence Pt≈Cu>>Au.<sup>36</sup> Platinum is only slightly more active than copper, being copper much cheaper. Therefore, Cu is a very good candidate as metal phase for these catalytic systems in order to an industrial-massive production. Though Pt, Cu and Au have been experimentally studied, no experimental or theoretical studies on the Ag/CeO<sub>x</sub>/TiO<sub>2</sub> systems. However, it has been shown that Ag is indeed a good catalyst for some reactions in different systems based on Ag and CeO<sub>2</sub>. On the other hand, though there are many experimental results for Cu, Au and Pt,<sup>5,36,39</sup> there is a lack of theoretical studies on the interaction of the metal particles with these highly modified oxide supports. Questions about the nature of the metal-support

interaction, the influence of that interaction in the geometry and electronic structures of the metal particles and, more interestingly, the reaction pathway on these new systems (including the nature and stability of the intermediates), have not been solved yet. The purpose of the present work is to study by means of state-of-the-art DFT calculations the nature of the interaction of Cu, Ag, Au and Pt with the nano-mixed-metal oxide support CeO<sub>x</sub>/TiO<sub>2</sub>, and more importantly the influence of that interaction on the WGS reactivity of the system Cu/CeO<sub>x</sub>/TiO<sub>2</sub>.

The paper is organized as follows: first we describe the theoretical methods we have used; second we study the adsorption of the metal atoms on the pure and CeO<sub>x</sub>modified TiO<sub>2</sub> support; then we focus on the adsorption of a Cu<sub>8</sub> cluster on the studied surface and finally we show our results for the WGS-reaction on the Cu/CeO<sub>x</sub>/TiO<sub>2</sub> system.

## Methods

The DFT calculations were performed using the plane-wave-pseudopotential approach within the projector augmented wave method (PAW)<sup>40</sup> together with the GGA exchange correlation functional proposed by Perdew *et al.*<sup>41</sup> as implemented in the VASP 4.6 code.<sup>42,43</sup> A plane-wave cutoff energy of 400 eV was used. We treated the Ti (3*s*, 3*p*, 3*d*, 4*s*), Ce (4*f*, 5*s*, 5*p*, 5*d*, 6*s*), Cu (3*d*, 4*s*), Ag (4*d*, 5*s*), Au (5*d*, 6*s*), Pt (5*d*, 6*s*) and O (2*s*, 2*p*) electrons as valence states, while the remaining electrons were kept frozen as core states. To obtain faster convergence, thermal smearing of one-electron states ( $k_B T = 0.05$  eV) was allowed using the Gaussian smearing method to define the partial occupancies. The energy was estimated at the gamma point.

We chose a (6x2) surface model with the aim to have isolated CeO<sub>x</sub> dimers and metal clusters on the TiO<sub>2</sub> (110) surface (see figure 1). The slab was 12 atomic layers thick or four TiO<sub>2</sub>-trilayers, as it is known that thicker supercell models gave comparable results in a similar study.<sup>44</sup> In all cases, the two lower TiO<sub>2</sub> trilayers were kept frozen while the rest of the atoms were allowed to fully relax their atomic positions (see figure 6.1). The supercell slab model is separated from their images by a vacuum of 15 Å, considered enough to avoid interaction between the slabs. For building the supercell model we used the optimized lattice parameters for the bulk  $a = 4.1616$ ,  $c = 2.974$  Å, and  $u = 0.304$  Å. On the nomenclature used to call the surface atoms see figure 6.1c.

In order to represent adequately the electronic structure of Ce (in particular the 4*f* level of the Ce<sup>3+</sup> species) we used the GGA+U formalism. The Hubbard U term was added to the plain GGA functional employing the rotationally invariant approach proposed by Dudarev *et al.*,<sup>45</sup> in which the Coulomb U and exchange J parameters are combined into a single parameter  $U_{eff} = U - J$ . For Ce we have used the  $U_{eff}$  of 4.5 eV which was self-consistently calculated by Fabris *et al.*<sup>46</sup> using the linear-response approach of Cococcioni and de Gironcoli<sup>47</sup> and which is in the range of values usually proposed in

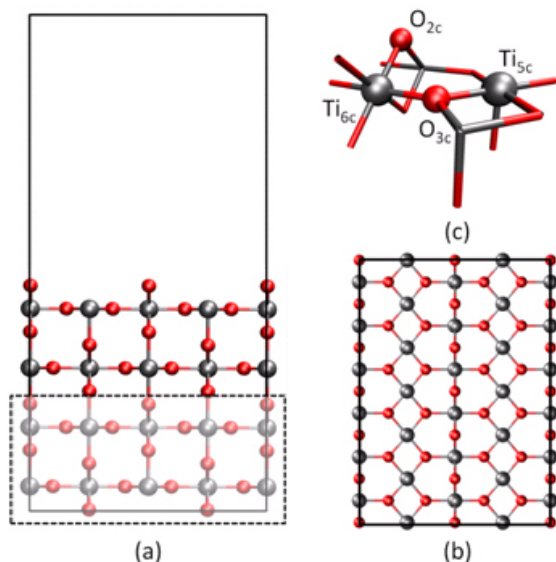


Figure 6.1: Supercell slab model used for representing the TiO<sub>2</sub>(110) surface. (a) Side view. The solid line indicates the supercell and the dashed line shows the atoms kept fixed at their bulk positions. (b) Top view of the supercell, showing the 6x2 surface cell. (c) Different atoms present in the TiO<sub>2</sub>(110) surface.

the literature (4.5-5.5 eV) for GGA+U calculations.<sup>48-56</sup> For the 3*d* states of Ti we also chose a  $U_{eff}$  parameter of 4.5 eV as it reproduces the experimental values of the gap between the Ce<sup>3+</sup> 4*f* and Ti<sup>3+</sup> 3*d* levels observed in the valence photoemission spectra of Ce/TiO<sub>2</sub>(110) system.<sup>5</sup> Although lower values for  $U_{eff}$  have also been proposed for a balanced description of bulk CeO<sub>2</sub> and Ce<sub>2</sub>O<sub>3</sub> oxides,<sup>57,58</sup> the set of parameters we have selected allows for a correct description of the gaps observed in the experimental photoemission spectra of our systems consisting of CeO<sub>*x*</sub> clusters supported on the TiO<sub>2</sub>(110) surface.<sup>5</sup> The presence of Ce<sup>3+</sup> species was indicated by a characteristic 4*f* peak in the band gap and later confirmed by the magnetization of the Ce atoms (higher than 0.9 electrons) found in the calculations. In the same way the presence of Ti<sup>3+</sup> species was indicated by a characteristic 3*d* peak in the band gap and later confirmed by the magnetization of the Ti atoms (higher than 0.8 electrons) found in the calculations. These  $U_{eff}$  parameters for Ce and Ti have been used successfully for the CeO<sub>*x*</sub>/TiO<sub>2</sub>(110) systems in previous papers.<sup>5,36,38</sup>

The adsorption energy for a given species X, (where X stands for metal cluster, H<sub>2</sub>O,

CO, etc.) has been calculated as:

$$E_{ads}(X) = E(X/CeO_2/TiO_2) - E(X) - E(CeO_2/TiO_2) \quad (6.1)$$

Where  $E_{ads}(X)$  is the adsorption energy of X on CeO<sub>x</sub>/TiO<sub>2</sub>(110),  $E(X/CeO_x/TiO_2)$  is the total energy of the system in which X is adsorbed on the CeO<sub>x</sub>/TiO<sub>2</sub>(110) surface,  $E(X)$  is the energy of the isolated X and  $E(CeO_x/TiO_2)$  is the energy of the slab model of the surface consisting on a Ce<sub>2</sub>O<sub>3</sub> dimer on TiO<sub>2</sub>(110). For more details of the structure of the CeO<sub>x</sub>/TiO<sub>2</sub>(110).<sup>5,36,38</sup> Obviously, when the molecules H<sub>2</sub>O or CO are adsorbed on the Metal/CeO<sub>x</sub>/TiO<sub>2</sub> system, the calculation of the adsorption energy is modified accordingly:

$$E_{ads}(X) = E(X/M/CeO_2/TiO_2) - E(X) - E(M/CeO_2/TiO_2) \quad (6.2)$$

Where  $E_{ads}(X)$  is the adsorption energy of X on M/CeO<sub>x</sub>/TiO<sub>2</sub>(110),  $E(X/M/CeO_x/TiO_2)$  is the total energy of the system in which X is adsorbed on the M/CeO<sub>x</sub>/TiO<sub>2</sub>(110) surface,  $E(X)$  is the energy of the isolated X and  $E(M/CeO_x/TiO_2)$  is the energy of the slab model of the surface consisting on a metal cluster and a Ce<sub>2</sub>O<sub>3</sub> dimer on TiO<sub>2</sub>(110).

Charge density differences (CDD) were calculated by subtracting to the total charge density of the system the charge density calculated for the isolated parts of the system. For instance, for Cu adsorption on TiO<sub>2</sub>(110), we subtract to the charge density of the system Cu/TiO<sub>2</sub> the charge density of an isolated Cu atom and the charge density of the isolated TiO<sub>2</sub>(110) surface, keeping the involved atoms in the same position of the same supercell than in the complete system. In that way it is possible to see directly in the real space where charge density is gained and where is lost, and see in that way the formation of bonds or charge transfer processes.

Transitions states have been calculated by using the climbing image version of the nudged elastic band (NEB) algorithm<sup>59</sup> and in all cases, after a vibrational analysis, a single imaginary frequency has been obtained for these structures.

## Results and discussion

### Cu, Ag, Au and Pt adsorption on pure and CeO<sub>x</sub>-modified TiO<sub>2</sub>(110)

We start this section by reviewing the interaction between a single noble atom and the TiO<sub>2</sub>(110) surface. The most stable adsorption sites on the TiO<sub>2</sub>(110) for Cu, Ag, Au and Pt atoms are well known and have been studied previously (see figure 6.2).<sup>60–65</sup> However, for the sake of comparison a quick analysis of the nature of interaction metal-surface is needed. These preliminary considerations will help us to analyze the differential effects arising when the metal is absorbed on the same surface in the presence of the CeO<sub>x</sub> nanoparticles. The starting point is the calculation of adsorption energies, Bader charges

and density of states DOS for the four metal atoms on the bare  $\text{TiO}_2(110)$  surface. The main results are shown in Table 6.1.

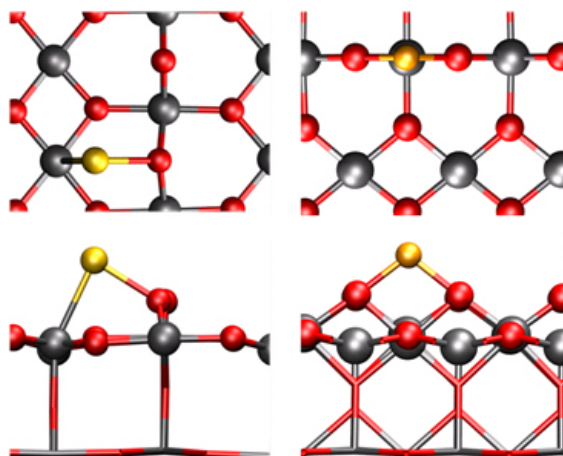


Figure 6.2: Most stable adsorption sites for Cu and Ag (right side) and Au and Pt (left side). Top view (top) and side view (bottom). Ti (gray), O (red).

Table 6.1: Adsorption energy (eV), metal Bader charges (Q) and qualitative bond contributions for single metal deposition on  $\text{TiO}_2(110)$  and  $\text{CeO}_x/\text{TiO}_2(110)$  surfaces.

Metal	$E_{ads}$ / eV	$\text{TiO}_2(110)$		$\text{CeO}_x/\text{TiO}_2(110)$		
		Charge	Bond contribution	$E_{ads}$	Charge	Bond contribution
Cu	-1.91	0.76	I+C	-2.65	0.68	I+C
Au	-1.01	0.71	I	-1.34	0.63	I
Ag	-0.71	0.04	P	-0.79	0.42	I
Pt	-2.53	0.10	P+C	-3.19	0.17	P+C

The strongest interaction is found for Pt, 2.53 eV, followed by Cu (1.91 eV), Ag (1.01 eV) and Au (0.72 eV). These results roughly agree with previous calculations,<sup>60,63–65</sup> and the deviations are due to the differences in models and computational details: cluster vs. periodic approaches, thickness of the slabs,<sup>66</sup> Hubbard on-site corrections, etc. In any case, within the Group 11, we see that the interaction of Cu is  $\sim 0.9$  eV higher than that of

Ag, which is of the same order of that of Au. The same behavior has been observed for ceria surfaces,<sup>67</sup> and is also close to that reported for a less reducible surface as alumina.<sup>68</sup> If we consider the Bader charges,  $Q$ , we can distinguish clearly two behaviors: for Cu and Ag ( $Q \sim 0.7 e$ ) there is a clear charge transfer to the surface, while Au and Pt remain practically uncharged. Upon deposition Cu and Ag reduce the surface, in particular one of the Ti<sub>5c</sub> atoms lying at the channels, passing from Ti<sup>4+</sup> to Ti<sup>3+</sup>, as might be easily seen in the charge density difference (CDD) isosurfaces (Figure 6.3), where reduced Ti atom clearly appears in the surface.

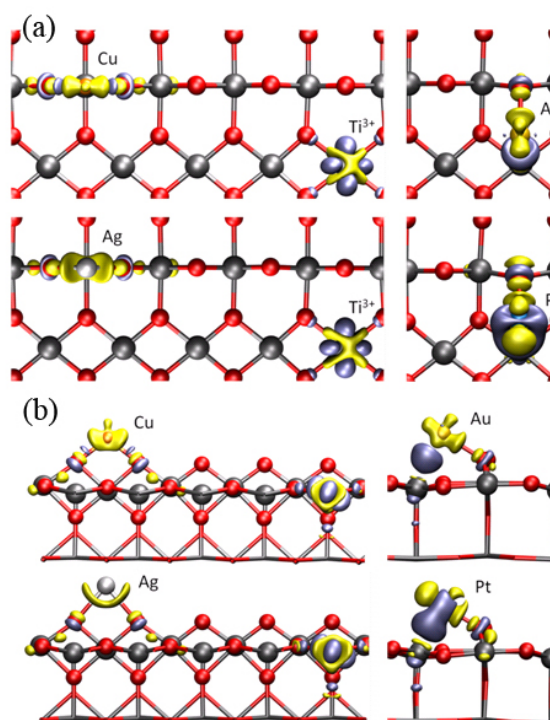


Figure 6.3: Charge density difference isodensities for Cu, Ag, Au and Pt adsorbed at their most stable position on TiO<sub>2</sub>(110). Top view (a) and side view (b). The gaining of charge is represented by an isosurface of 0.05 in iceblue and losing of charge by an isosurface of -0.05 in yellow. Ti (gray), O (red), Cu (orange), Ag (white), Au (golden) and Pt (metallic blue). Ti<sup>3+</sup> ions are labelled when they appear.

Moreover, the DOS projected on the reduced Ti atom consistently exhibits the characteristic 3d little peak in the band gap (not shown). And finally, we found a magnetization

for that Ti atom of 0.88. The CCD maps also show for Cu a larger covalent contribution than in the case of Ag, in agreement with the higher interaction energy. In the case of Au and Pt, since the oxidation resulting from the deposition is low,  $Q=0.04$  and  $0.10$ , the ionic component is practically absent. The metal-surface bond arises from metal polarization and, in the case of Pt, covalent contributions. The  $d^9 s^1$  orbitals of Pt give place to better overlap with surface orbitals than the  $sp$  Au hybridized orbitals as shown in Figure 6.3b, which is consistent with the larger interaction obtained for Pt.

The results for the adsorption of the metals on the  $\text{CeO}_x$ -modified  $\text{TiO}_2(110)$  surface are also shown in Table 6.1. For all the metal atoms considered the most stable adsorption site on this surface was at the position depicted in Figure 6.4, i.e., the adsorbed atom interacting directly with the adsorbed  $\text{CeO}_x$  particles. More interesting, whatever the noble metal is, the interaction energy is found larger than that obtained for the unmodified surface, however the change has not the same extent in all the cases. The adsorption energies were  $-2.65$  eV,  $-1.34$  eV,  $-0.94$  eV and  $-3.19$  eV for Cu, Ag, Au and Pt respectively. Thus, while Cu and Pt reinforce the interaction with the surface by roughly  $0.7$  eV, for Ag and Au only a small change is observed ( $E_{ads}$  increases by  $-0.33$  eV and  $-0.22$  eV respectively).

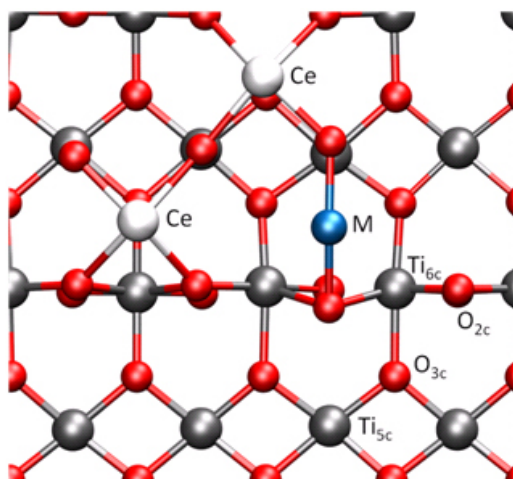


Figure 6.4: Top view of the most stable adsorption position for Cu, Ag, Au and Pt on  $\text{CeO}_x/\text{TiO}_2(110)$ . Ti (gray), O (red), Metal M (blue).

Concerning the surface reduction one can observe that small changes in the charges are found for Cu, Ag and Pt, however, for Au, the Bader charge calculation shows a charge transfer of  $0.42 |e^-|$  to the surface. This is in contrast with the almost negligible Au oxidation predicted for the  $\text{CeO}_2(111)$  surface, although whether the oxidation happens or not has been a controversial issue.<sup>67,69</sup> In the present case, gold oxidation is also



confirmed by CDD isosurfaces (Figure 6.5), DOS projected on the reduced Ti<sub>5c</sub> atom and its magnetization. We relay this behavior of Au with the very special place of the surface where it is adsorbed. It has been shown in previous studies that when Au is adsorbed in a geometry in which a linear O-Au-O bond can be reached, the oxidation process of Au is strongly facilitated.<sup>70</sup> In the present analysis it appears that there is just charge transfer from Au atom to one Ti<sub>5c</sub> of the surface and the following favorable electrostatic interaction between the Au cation and the neighbor O anions. No evidence of significant covalent contribution to the Au-O bond is found in the CDD isosurfaces. Other positions of the surface tested indicate that the Au-surface interaction is essentially analogous to the pure TiO<sub>2</sub>(110) surface. In other words, at this particular adsorption site, the bond mechanism of Au and Ag are quite similar.

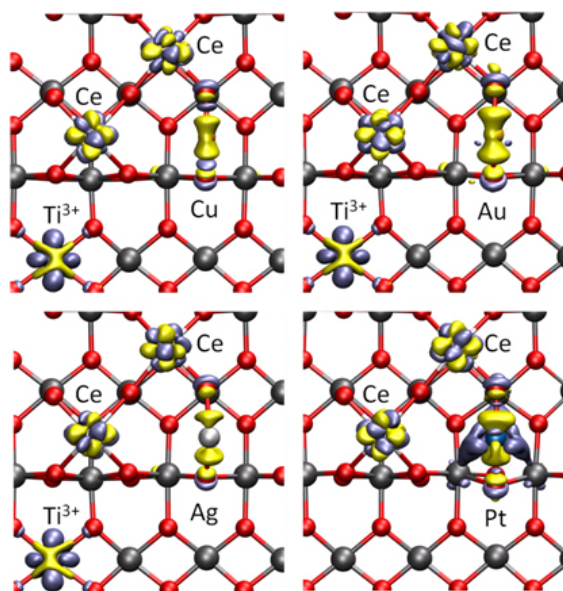


Figure 6.5: Charge density difference isodensities for Cu, Ag, Au and Pt adsorbed at their most stable position on CeO<sub>x</sub>/TiO<sub>2</sub>(110). The gaining of charge is represented by an isosurface of 0.05 in iceblue and losing of charge by an isosurface of -0.05 in yellow. Ti (gray), O (red), Cu (orange), Ag (white), Au (golden) and Pt (metallic blue). Ti<sup>3+</sup> and Ce<sup>3+</sup> ions are labelled when they appear.

For Cu and Ag the bonding mechanism remains practically identical as in the pure surface, i.e., ionic-covalent for Cu and mainly ionic for Ag as can be seen in the CDD isosurfaces shown in figure 6.5. For Pt, additional favorable covalent contributions due to the Pt-O bond are also incorporated. In summary, we can conclude that the effect of the

presence of the  $\text{CeO}_x$  particles in the  $\text{TiO}_2(110)$  surface on the metalsupport interaction is a local effect. The adsorption energy (and even the bonding mechanism for Au) is strongly modified only when the metal atoms interact directly with the  $\text{CeO}_x$  particle.

### Adsorption of Cu nanoclusters on $\text{CeO}_x$ -modified $\text{TiO}_2(110)$

The model we selected to describe a Cu nanoparticle on the  $\text{CeO}_x$ - $\text{TiO}_2(110)$  surface was derived from that used in a previous paper where we analyzed the electronic and catalytic properties of the  $\text{Cu}/\text{TiO}_2(110)$  catalyst. It consisted of 3D  $\text{Cu}_8$  nanocluster, with a truncated pyramid shape formed by 5 atoms in the layer in contact with the surface. It was found that the  $\text{Cu}_8$  cluster mainly binds to the O atoms of the  $\text{TiO}_2$  surface.

The  $\text{Cu}_8$  nanocluster was added to the  $\text{CeO}_x$ - $\text{TiO}_2(110)$  model surface exploring several possible sites, and we found that, as isolated atoms do, Cu clusters adsorb stronger near the  $\text{CeO}_x$  particles. The adsorption energy at this site is -3.50 eV, while on the perfect surface is of -3.02 eV. Moreover, as could be expected since 5 Cu atoms from the 8 of the cluster are in contact with the surface, there is a larger electron transfer ( 1.4 e). However, the averaged oxidation state of these 5 Cu atoms is  $Q_{Cu} \sim 0.3$ , the 3 Cu atoms at the top of the metal particle remaining almost neutral. A view of the model is reported in Figure 6.6.

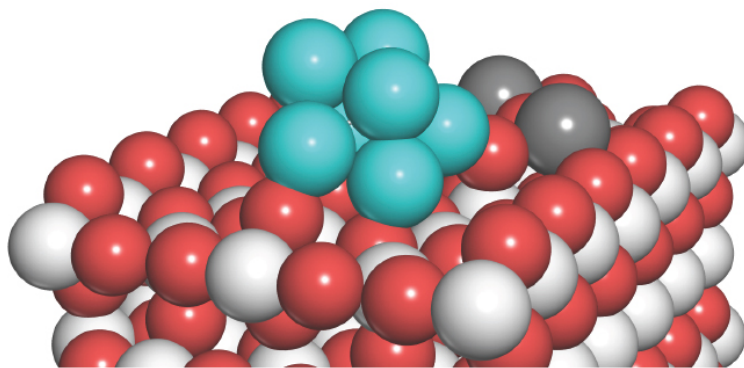


Figure 6.6:  $\text{Cu}_8/\text{CeO}_x/\text{TiO}_2$  slab model.

### Reaction mechanism for WGS reaction on $\text{Cu}/\text{CeO}_x/\text{TiO}_2$

Let us now analyse the mechanism for the WGS reaction on the  $\text{CeO}_x/\text{TiO}_2$  surface. In previous studies Rodriguez *et al.* have shown that the reaction for a metal/metal-oxide catalyst happens at the metal-titania interface.<sup>26</sup> It has been suggested that it takes place via a carboxyl  $\text{COOH}$  intermediate, and involves the following steps.<sup>26</sup>



Adsorption is the first step of the mechanism and preconfigures the profile of the catalytic cycle. In principle, because of the high strength of the OH bond, it is assumed that the dissociation of water is the rate limiting step and the most important barrier to overcome. How WGS catalysts could be modified in order to improve adsorption and dissociation of H<sub>2</sub>O has long deserved much attention, and some previous results are reported in Table 6.2 for the sake of comparison.

Table 6.2: Adsorption energy ( $E_{ads}$ ), activation energy ( $E_a$ ) and reaction energy ( $\Delta E$ ) for water dissociation.

System	$E_{ads}$ / eV	$E_a$ / eV	$\Delta E$ / eV
Cu(111) <sup>71</sup>	-0.18	1.36	0.37
Cu/TiO <sub>2</sub> (interface) <sup>72</sup>	-1.09	0.52	-0.04
Cu/TiO <sub>2</sub> (vac) <sup>72</sup>	-0.72	0.35	-0.14
Au/TiO <sub>2</sub> (oxide) <sup>26</sup>	-	0.60	0.60
Au/TiO <sub>2</sub> (metal) <sup>26</sup>	-	1.30	0.09
Au/TiO <sub>2</sub> (interface) <sup>26</sup>	-	0.56	0.09
CeO <sub>x</sub> /TiO <sub>2</sub> (interface) <sup>38</sup>	-0.73	0.04	-0.63
Cu/CeO <sub>x</sub> /TiO <sub>2</sub> (interface)	-0.65	0.04(0.40)	-0.81(0.02)

Compared to the Cu (111) surface,<sup>71</sup> there is an increase of adsorption energy and a decrease of the activation barrier in metal/TiO<sub>2</sub><sup>72,73</sup> catalysts due to the easier adsorption

of water molecules on oxide vacancies or in areas close to the metal cluster. We have recently characterised CeO<sub>x</sub> NPs on TiO<sub>2</sub> (110) surface, which exhibited low coordinated Ce<sup>3+</sup> ions.<sup>5,36</sup> We found that these ions act as active sites where water molecules are adsorbed and then dissociated with almost no apparent barrier ( $E_a = 0.04$  eV) in a strong exothermic process ( $DE = -0.73$  eV).<sup>38</sup>

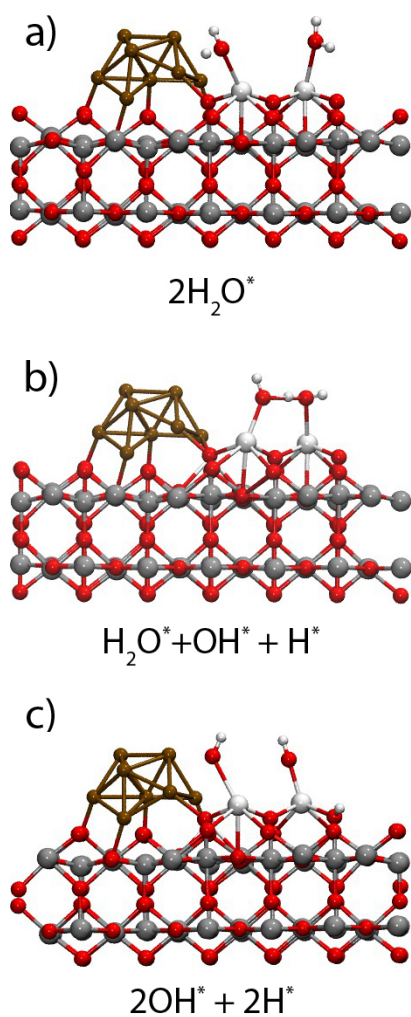


Figure 6.7: Calculated structures for the reactants and intermediates of the water adsorption and dissociation on Cu/CeO<sub>x</sub>/TiO<sub>2</sub> catalyst. Only the 2 first layers of the four-layer titania slab used in DF calculations are shown.

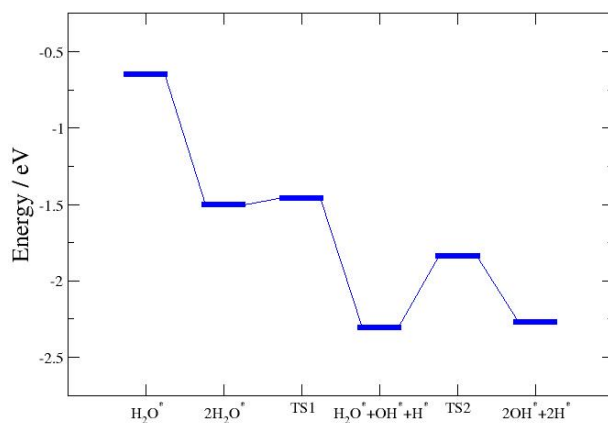


Figure 6.8: Reaction profile for water adsorption and dissociation on Cu/CeO<sub>x</sub>/TiO<sub>2</sub> system. The zero energy is taken as the sum of the energies of the bare Cu/CeO<sub>x</sub>/TiO<sub>2</sub>, gas phase water and carbon monoxide.

The presence of the Cu<sub>8</sub> nanocluster does not significantly alter these values, the process being practically barrierless with a reaction energy of -065 eV. As can be seen in Figure 6.7, water molecule adsorbs on top of a Ce<sup>3+</sup> ion, and since still there is one more Ce<sup>3+</sup> ion available we checked adsorption of a second water molecule. This process was also found favorable, the reaction energy being almost the same than for the first molecule. This is not the case for dissociation energies since while the first dissociation barrier is of only 0.04 eV and strongly exothermic, for the second dissociation the activation energy is of 0.43 eV, and the process is practically thermoneutral. The energy profiles for these steps are gathered in Figure 6.8. The model indicate therefore, that for a Ce2 surface dimer we would find 2 adsorbed water molecule, one of them always dissociated and the other either dissociated or not, with the same likelihood, Figures 6.7b and 6.7c.

Next steps in the mechanism are the CO adsorption and the formation of the carboxyl intermediate. For M/TiO<sub>2</sub> based catalyst in which water dissociation barrier is lowered, the formation of OCOH species should become the rate-limiting step, as shown in Table 6.3.

Table 6.3: Adsorption energy,  $E_{ads}$ , activation energy ( $E_a$ ) and reaction energy ( $\Delta E$ ) for water carboxyl intermediate formation.

System	$E_{ads}$ / eV	$E_a$ / eV	$\Delta E$ / eV
Cu(111) <sup>71</sup>	-0.09	0.61	0.01
Cu(cluster) <sup>73</sup>	-0.60	1.15	1.0
Au/TiO <sub>2</sub> (interface) <sup>26</sup>	-	0.86	0.38
Cu/TiO <sub>2</sub> (vac) <sup>26</sup>	-	0.90	0.70
Cu/TiO <sub>2</sub> (vac) <sup>72</sup>	-0.91	0.88	0.60
Cu/CeO <sub>x</sub> /TiO <sub>2</sub> (interface)	-0.50	0.51	0.08

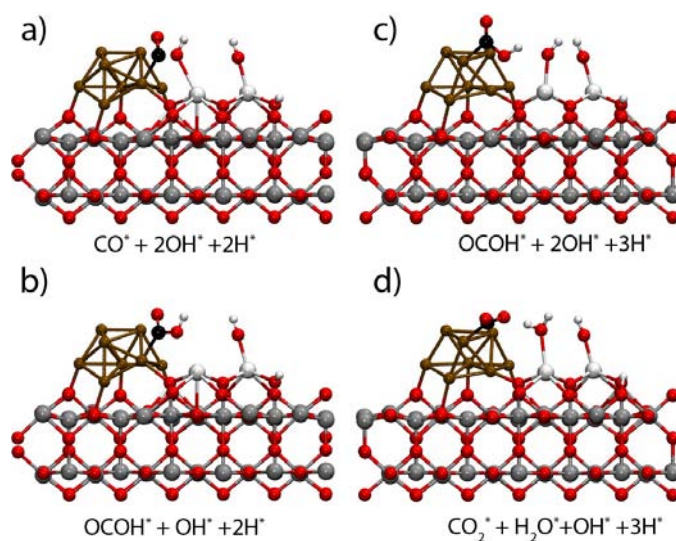


Figure 6.9: Calculated structures for the reactants and intermediates of the CO oxidation on Cu/CeO<sub>x</sub>/TiO<sub>2</sub> catalyst. Only the 2 first layers of the four-layer titania slab used in DF calculations are shown.

Starting from the structure where both water molecules are dissociated, we first adsorb a CO molecule on the catalyst model. One can expect that CO will preferentially adsorb on low coordinated metal atoms of the cluster, especially in the second layer, edges and corners, so we have combined this fact with positions in which CO and OH are close enough to produce carboxyl species (see Figure 6.9a). The carboxyl species is reached by a shift of an OH group initially bound to a Ce<sup>3+</sup> ion as indicated in

Figure 6.9b. The activation energy obtained is 0.50 eV, smaller than that reported for the Cu/TiO<sub>2</sub> catalyst,<sup>73</sup> and comparable to that estimated by Peng et al.<sup>72</sup> for a system with similar characteristics. Moreover this step is thermoneutral, which significantly favors the formation of the carboxyl intermediate compared to other catalysts where the reaction is a highly endothermic process (see Table 6.3).

The energy profile describing these steps are depicted in Figure 6.10. On the other hand, after the formation of the carboxyl intermediate, a Ce<sup>3+</sup> ion is accessible for the adsorption of a new water molecule that could again easily dissociate. This will be the starting point for the next step in which a deprotonation of the carboxyl intermediate takes place. This step is one the easier steps in the mechanism, and has been analyzed several times. For Cu(111) Mavrikakis et al. have reported an activation energy of 0.42 eV, and the deprotonation was found to be assisted by an hydroxyl group to generate a water molecule.<sup>71</sup> In M/TiO<sub>2</sub> type catalyst the values fluctuated between 0.05 to 0.5 eV, and an oxygen atom of the oxide surface also assists the process. In all these cases this is not the rate limiting of the reaction.

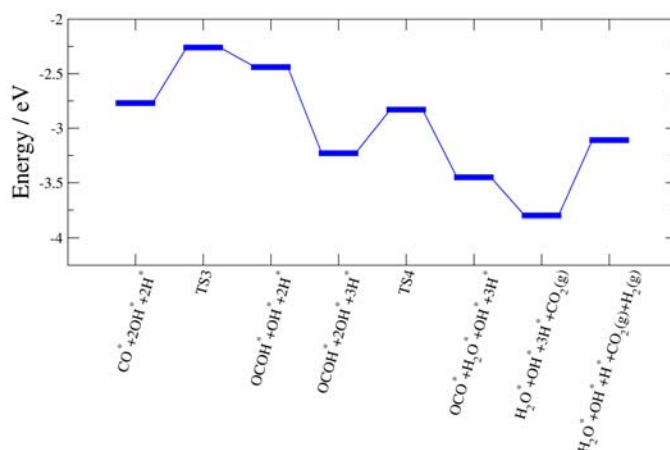


Figure 6.10: Reaction profile for Co oxidation on Cu/CeO<sub>x</sub>/TiO<sub>2</sub> system. The zero energy is taken as the sum of the energies of the bare Cu/CeO<sub>x</sub>/TiO<sub>2</sub>, gas phase water and carbon monoxide.

In the present study, for the Cu/CeO<sub>x</sub>/TiO<sub>2</sub> catalyst, we have obtained an activation energy of 0.39 eV, which is smaller than previous barriers exposed below. Also, and more interesting, this step is exothermic, by 0.22 eV, while in previous reported studies this

process is exo or endo about 0.5 eV. Finally, H<sub>2</sub> formation and products desorption take place. The gross energetic changes associated to these steps are also schematized in Figure 6.10.

The energy profile obtained confirms previous experimental results, which demonstrate the high performance of this catalyst.<sup>36</sup> CeO<sub>x</sub> NP improves energy adsorption, decrease the activation energy for water dissociation and increase the exothermicity of the process. The released energy can be used to overcome the energy barriers for the following steps. The CeO<sub>x</sub> dimer also facilitates the formation of carboxyl species, because hydroxyls are more accessible to CO molecules adsorbed on metal cluster. Although the redox mechanism has been identified as preferential in Pt/CeO<sub>2</sub> systems, the characterized microstructure of Cu/CeO<sub>x</sub>/TiO<sub>2</sub> reduces the activation energy for carboxyl formation. All these improvements get a reaction pathway in which all barriers are below 0.5 eV, the lowest value reported as far as we know. This profile ensures that the reaction can be carried out under mild conditions and low temperatures using one of the most inexpensive noble metals as copper.

### Summary and conclusions

In this work we have analyzed the nature of the metal-support interaction of Cu, Ag, Au and Pt on CeO<sub>x</sub>-modified TiO<sub>2</sub>(110) surfaces, and the WGS reaction pathway on the Cu/CeO<sub>x</sub>/TiO<sub>2</sub>(110) three-component catalyst. We first revised the interaction energies and bond mechanism between single noble atoms and the perfect TiO<sub>2</sub>(110) surface. The obtained adsorption energies are: 1.91, 1.01, 0.72 and 2.53 eV For Cu, Ag, Au and Pt, respectively. For Cu and Ag there is a large charge transfer (0.7 |e<sup>-</sup>|) from the metal to the surface, reducing a Ti<sup>4+</sup> ion to Ti<sup>3+</sup>. In the case of Cu, beyond this ionic ingredient to the bond, significant covalent contributions are observed. For Au and Pt, the mechanism is governed by the metal polarization, with negligible charge transfer to the metal oxide surface. In CeO<sub>x</sub>/TiO<sub>2</sub>(110) the bonding mechanism for Cu, Ag and Pt remain essentially the same than when deposited on the pure TiO<sub>2</sub>(110) surface but geometrical characteristics of the adsorption site makes favorable contributions to the bond appear, increasing the adsorption energy. In the case of Au not only these favorable contributions appear, but also a significant charge transfer toward the surface can be observed. The adsorption energies obtained for deposition onto the ceria-modified titania surface are -2.65 eV, -1.34 eV, -0.94 eV and -3.19 eV for Cu, Ag, Au and Pt respectively. Compared with the experimental activity, it is worth noting the correlation between these energies and the catalytic activity: Pt>=Cu>Au>Ag.

For the Cu<sub>8</sub> cluster the nature of the metal-support interaction is similar than that for Cu atom in Cu/CeO<sub>x</sub>/TiO<sub>2</sub>(110) and Cu/TiO<sub>2</sub>(110). Obviously the charge transfer from the metal to the surface (1.4 |e<sup>-</sup>|) and the adsorption energy (-3.50 eV) are higher in the



cluster as it has 5 atoms in contact with the surface.

To elucidate the mechanism of the WGS reaction, we have studied the main steps involved in the whole process: adsorption-dissociation of water and formation-deprotonation of the \*OCOH intermediate. We have found that water dissociation is no longer the rate-limiting step in this system, since it has a energy barrier of only 0.04 eV. On the other hand, we have proposed a reaction path in which all the involved energy barriers are below 0.5 eV. To the best of our knowledge it is the first time that such a low-barrier path has been found. The key to get the system working under so low barriers is the hydration/hydroxylation of the cerium oxide particle. This hydration is an exothermic and low barrier process which, furthermore, allows an easy deprotonation of the \*OCOH carboxyl intermediate that finally may lead the reaction to the final products CO<sub>2</sub> and H<sub>2</sub>. All these findings may contribute to a deep understanding of the extraordinary catalytic activity of the new family of catalysts Metal/CeO<sub>x</sub>/TiO<sub>2</sub>, and may foster further research in order to find new and better WGS reaction catalysts.

## 6.4 Nature of the mixed-oxide interface in ceria-titania system for photocatalytic water splitting

This section partially correspond to the theoretical work published in: "Nature of the Mixed-Oxide Interface in Ceria-Titania Catalysts: Clusters, Chains and Nanoparticles"

*J. Phys. Chem. C*, **2013**

DOI:10.1021/jp3125268

### Introduction

The mixing of two different metal oxides could improve the performance of the involved oxides by producing different physical and chemical properties with respect to the individual components.<sup>16,74,75</sup> For instance, TiO<sub>2</sub> doping with other metal oxides has been intensively studied during last years in order to modify the gap of the system and be able to split water efficient in visible light. Ceria is a good candidate to mix with TiO<sub>2</sub> because of its catalytic properties associated to the redox pair Ce<sup>3+</sup>/Ce<sup>4+</sup>. Moreover, the substitution of Ti<sup>4+</sup> by cerium ions improves the thermal resistance to sintering and the redox properties of TiO<sub>2</sub>.<sup>36,76</sup>

Some studies which were focused on the properties of CeO<sub>2</sub>-TiO<sub>2</sub> powders has been published in last years in order to use it as catalyst and photocatalyst.<sup>77-80</sup> For instance, some authors have demonstrated that a 10 wt% of CeO<sub>2</sub> in ceria-titania catalyst increases thermal stability of this material against particle sintering and pore collapse.<sup>77</sup> Moreover, it has been reported that ceria doped TiO<sub>2</sub> shows activity for the photochemical degradation of methylene blue under visible-light irradiation.<sup>78,79</sup> Despite some theoretical calculations have suggested that the presence of reduced cerium cations is necessary in order to enhance the photo-catalytic activity of TiO<sub>2</sub>,<sup>80</sup> there were not strong experimental evidences of this correlation until now. However, last year, it has been demonstrated that it is possible to synthesize ceria/titania heterostructures in which Ce<sup>3+</sup> ions are stabilized. Furthermore, Pt/CeO<sub>x</sub>/TiO<sub>2</sub> has been found to be an excellent candidate as photocatalyst for water splitting.<sup>81</sup> Despite of the good performance of this system, the mechanism which stabilizes the Ce<sup>3+</sup> ions are still unknown. Our objective here is to explore the nature of the mixed-oxide interface and characterized its structural and electronic properties which determine its performance as photocatalyst.

## Density Functional Theory Calculations

The density functional theory (DFT) calculations were made using the generalized gradient approximation (GGA) exchange correlation functional proposed by Perdew et al.<sup>41</sup> and the projector augmented wave method (PAW)<sup>40</sup> as implemented in the Vienna Ab-initio simulation package (VASP) 5.2 code.<sup>40,43</sup> A plane-wave cutoff energy of 400 eV was used. The Ti ( $3s, 3p, 3d, 4s$ ), Ce ( $4f, 5s, 5p, 5d, 6s$ ) and O ( $2s, 2p$ ) electrons were treated as valence states, while the remaining electrons were kept frozen as core states. To obtain faster convergence, thermal smearing of one-electron states ( $k_B T = 0.05$  eV) was allowed using the gaussian smearing method to define the partial occupancies. To adequately represent the electronic structure of Ce (in particular the  $4f$  level of the  $Ce^{3+}$  species) we used the GGA+U formalism. The Hubbard U term (on-site repulsion) was added to the plain GGA functional using the rotationally invariant approach proposed by Dudarev et al.,<sup>45</sup> in which the Coulomb U and exchange J parameters are combined into a single parameter  $U_{eff} = U - J$ . For Ce we have used a  $U_{eff}$  of 4.5 eV which was self-consistently estimated by Fabris et al.<sup>46</sup> using the linear-response approach of Cococcioni and de Gironcoli<sup>47</sup> and which is in the range of values usually proposed in the literature (4.5-5.5 eV) for GGA+U calculations.<sup>48-56</sup> To represent the  $3d$  states of Ti a  $U_{eff}$  parameter of 4.5 eV was used, as it reproduces the experimental values of the gap between the  $Ce^{3+}$   $4f$  and  $Ti^{3+}$   $3d$  levels observed in the valence photoemission spectra of  $Ce/TiO_2(110)$  system.<sup>5</sup> The presence of  $Ce^{3+}$  species was indicated by a characteristic  $4f$  peak in the band gap and later confirmed by the magnetization of the Ce atoms (higher than 0.9 electrons) found in the calculations. These  $U_{eff}$  parameters for Ce and Ti have been used successfully for the  $CeO_x/TiO_2(110)$  systems in previous papers.<sup>5,36,38</sup> Microscopy data indicates the growth of  $CeO_2(001)$  particles on  $TiO_2(112)$  surface facets.

Consequently, the ceria-titania models were built to mimic this relationship. Because the  $CeO_2(001)$  and  $TiO_2(112)$  are polar surfaces the charge of the bottom and top layers of the slab are opposite, and as a result a dipole moment appears. These surfaces, called type 3 according to Tasker classification,<sup>82</sup> are not stable and reconstruct. The usual way to model these surfaces is to move half of the charge from the top layer to the bottom layer quenching the dipole moment of the slab.<sup>82</sup> Accordingly, in our models, half of the O atoms of the top O-layer (belonging to  $CeO_2$ ) were moved to the Ti-layer at the bottom of the slab ( $TiO_2$ ). However, because at the ceria-titania interface a net dipole moment still remains, in the present study we have used a dipole correction based on implementations in the VASP program.<sup>83,84</sup> To describe phenomena at the interface between a ceria particle and the titania support, a slab was built with 5  $CeO_2$  layers on top of 5  $TiO_2$  layers to model the  $CeO_2(001)/TiO_2(112)$  system. In order to have converged properties with the number of k-points in the supercell we used a grid of  $3 \times 3 \times 1$  k-points in the reciprocal space for the slab model. To avoid the misfit of both surfaces, we did not use the conventional lattice

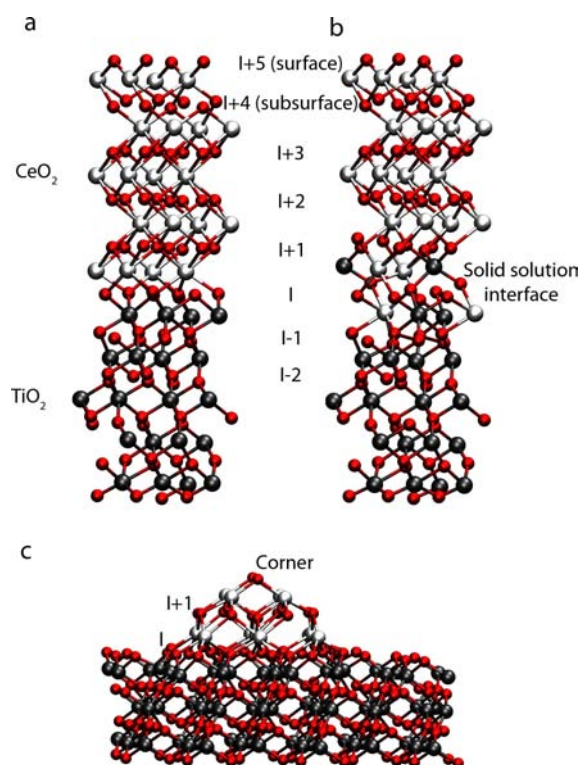


Figure 6.11: CeO<sub>x</sub>(001)/TiO<sub>2</sub>(112) system as (a) 5 CeO<sub>2</sub> layers on top of 5 TiO<sub>2</sub> layers model, (b) 5 CeO<sub>2</sub> layers on top of 5 TiO<sub>2</sub> layers with solid solution interface model and (c) CeO<sub>2</sub> nanocluster model. I+x label indicate the different oxygen layer in which the vacancy has been created. Atom color: O= red, Ti= grey, Ce= white.

vectors for the TiO<sub>2</sub>(-112) *a* and *b* but (*a*+*b*) and (*a*-*b*), directions [110] and [1-10]; it could be denoted as ( $\sqrt{2}x\sqrt{2}$ )R45 TiO<sub>2</sub>(-112) in Woods notation. For the same reason, we used a (2x2) unit cell for the CeO<sub>2</sub>(001) surface, as a result, the misfit in the cell parameters is only -1.7 %. The cell is not completely orthorhombic; *a* and *b* are 90.00 but *γ* is 91.09 because the lattice vector *a* (5.443 Å) is slightly longer than the *b* vector (5.340 Å) in the TiO<sub>2</sub>(112) conventional surface unit cell. Therefore, *a* and *b* are orthogonal, while the diagonal vectors (*a* + *b*) and (*a* - *b*) are not. Thus, the misfit in the *γ* angle between CeO<sub>2</sub>(001) (orthogonal) and TiO<sub>2</sub>(112) (not orthogonal) in this orientation is 1.2 %. All of the atoms of the supercell were allowed to fully relax their atomic positions. The slab model is separated from their images by a vacuum of ~ 15 Å, considered enough to avoid interaction between them. For building the supercell model we used the optimized lattice

parameters for bulk anatase:  $a = 3.786 \text{ \AA}$  and  $c = 9.541 \text{ \AA}$

## Results and discussion

DFT calculations were performed to analyze the interaction between both oxides. The energy of oxygen vacancy formation,  $E_v$ , was calculated as a function of layer position, at the interface (labeled as I in Figure 6.11) as well as in the ceria (labeled as I+1, I+2...) and titania layers (labeled as I-1 and I-2). The values of  $E_v$  range between 2.45 and 4.24 eV, corresponding to the I+5 and I-2 planes respectively. However, these values depend on the thickness of the ceria slab used in the model.

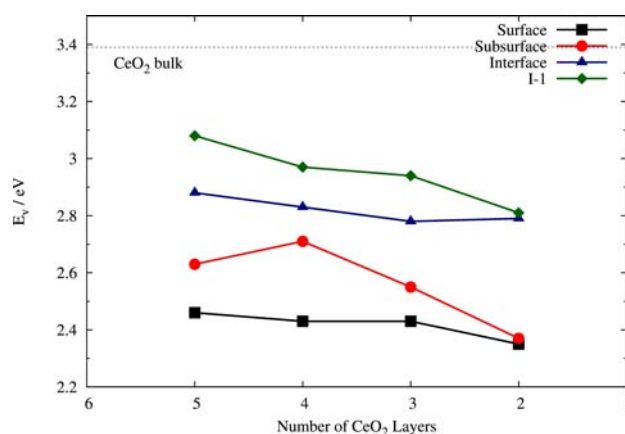


Figure 6.12: Computed  $E_v$  for  $\text{CeO}_x(001)/\text{TiO}_2(112)$  system with different number of  $\text{CeO}_2$  layers.

In Figure 6.12,  $E_v$  for specific positions is reported as a function of model size. While there is a dependence on the ceria thickness, the most favorable position to create a vacancy is the ceria surface, regardless of model size. The values of  $E_v$  at the surface, 2.35 and 2.45 eV, are remarkably close to previous calculations computed for bare (100)  $\text{CeO}_2$  surface using a similar setup, 2.27 eV.<sup>49</sup> Interestingly,  $E_v$  in the  $\text{TiO}_2$  (I-1) falls between 2.81 and 3.08 eV, significantly lower than the value of 5.14 eV that we have estimated for bulk anatase. While the vacancy energy formation for the ceria-titania interface is computed to be between 2.83 and 2.88 eV, also noticeably lower than the value reported by Nolan *et al.* for bulk  $\text{CeO}_2$  of 3.39 eV.<sup>85</sup> This behavior can be understood if we analyze the localization of the two cerium ions bearing the 4f electrons that appear when a vacancy is generated. The relaxation of the coordination sphere around the  $\text{Ce}^{3+}$  ions creates a small polaron whose stability could be responsible for the stability of the vacancy. In fact, it

has been reported that charge distribution around the vacancy can modify the  $E_v$  values for the same site by more than 0.5 eV.<sup>86</sup> The largest reduction in  $E_v$  is found when  $Ce^{3+}$  are arranged as next neighbors to the vacancy on one side, and at sites that facilitate their characteristic breathing polaronic expansion, on the other side. Because of the smaller ionic radius of Ti, the polaronic relaxation of  $Ce^{3+}$  in the interface is facilitated. This idea is actually supported by the fact that an electron charge analysis shows that the 4*f* electrons are located on Ce atoms belonging to the interface even when the vacancy is created in the I+1 and I+2 oxygen planes. Additionally, when the O vacancy is created in the titania-oxygen planes, the electrons are found occupying 4*f* orbitals of cerium atoms located at the interface. As a result the large stabilization of the vacancies around the interface with respect to bulk titania would lead to a diffusion of the vacancies towards the interface, and their subsequent accumulation.

Table 6.4:  $E_v$  values for nanocluster model and solid solution interface. In and surf labels indicate if the vacancy is inside of the  $CeO_2$  nanocluster or in one of its faces.

Metal	Site/Layers	$E_v / eV$
Cluster	Tip	2.38
	I+1(in)	2.93
	I+1(surf)	2.29
	I(in)	2.82
	I(border)	1.29
	TiO <sub>2</sub>	2.48
Solid solution	5 layers	1.98
	2 layers	1.37

Comparison of the bulk sensitive partial fluorescence yield (PFY) and surface sensitive partial electron yield (PEY) previous measurements suggests that the amount of  $Ce^{3+}$  in the inner region, i.e. the interface region, is higher. This finding suggests  $Ce^{3+}$  centers, and therefore oxygen vacancies, appear to be particularly stabilized in the interface with respect to the surface, which is not consistent with the DFT results reported in Figure 6.12. However, STEM EELS measurements indicate intermixing of metal cations at the oxide-oxide interface. The result is consistent with the fact that ceria and titania can form solid solutions.<sup>81</sup> Moreover, in STM studies of ceria on a TiO<sub>2</sub>(110) surface, there was evidence for intermixing of metal cations at the oxide-oxide interface.<sup>81</sup> This cation intermixing could be associated with the facile formation of  $Ce^{3+}$  sites detected by NEXAFS and was not taken into account in those previous calculations. To reproduce this intermixing in our model we have interchange two Ce cations with two Ti cations

to generate a solid solution interface two-layer thick (see Figure 6.11b). Additionally, in order to take into account the effects of border and step sites, a new model was developed in which a ceria nanoparticle rather than a slab is adsorbed on a titania surface (Figure 6.11c). The vacancy formation energies,  $E_v$ , for these two new models are included in Table 6.4. The  $E_v$  values obtained are similar to those reported above for the 2 slab model (Figure 6.11a) in the tip, inside the nanoparticle and at the interface; however, it decreases drastically at the border of the nanoparticle and at the solid solution interface. This result gives further support to the higher  $Ce^{3+}/Ce^{4+}$  ratio found with PFY mode. Notice that this solid solution interface further favors the polaronic expansion of  $Ce^{3+}$  without modifying significantly the coordination properties of metal centers.

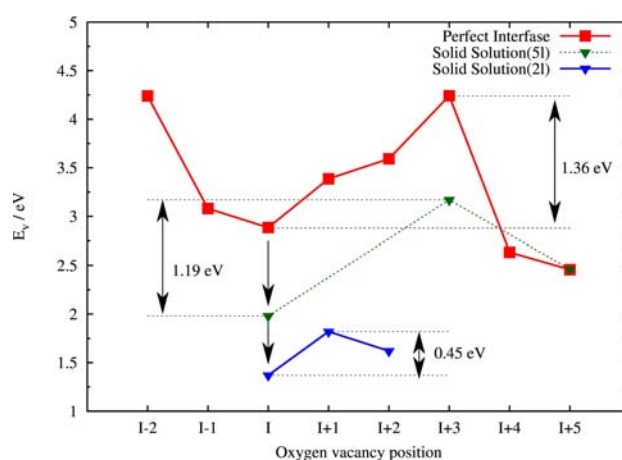


Figure 6.13: Thermodynamic barrier for polaron-vacancy migration in  $CeO_x(001)/TiO_2(112)$  with 5 and 2  $CeO_2$  layers system with well separated phases or producing a solid solutions in the interface.

The theoretical and experimental results indicate that there is a strong stabilization of  $Ce^{3+}$  located at the interface region. To illustrate this point, in Figure 6.13, the calculated oxygen vacancy formation energies ( $E_v$ ) are plotted as a function of the different oxygen planes for several models. For a perfect interface (without intermixing), the calculations indicate the interface is a local minimum while the surface layer is the global minimum of the system. Thus, the interface can still trap O vacancies because there is a significant barrier to diffusion from the ceria-titania interface to the surface. By comparison, when the solid solution model is considered, which we believe to be a more accurate physical representation of the system, the surface is no longer the global minima but now the interface layer is now the most preferential site for oxygen vacancies. Oxygen vacancy migration from the surface to the interface would be favorable, leading to a higher amount

of  $\text{Ce}^{3+}$  at the mixed interface than at the surface. This is in very good agreement with the experimental results. The calculated values strongly depend on the thickness of the  $\text{CeO}_2$  film but regardless of the model used the intermixed interface remains the global energy minimum. Therefore, vacancies may more easily migrate depending on the size of the ceria but the interface remains the most preferred site. The migration of  $\text{Ti}^{4+}$  into the ceria lattice at the oxide-oxide interface of ceria-titania facilitates the formation of  $\text{Ce}^{3+}$  sites, which can be very useful in catalytic processes. For example, the existence of  $\text{Ce}^{3+}$  in  $\text{M/CeO}_x/\text{TiO}_2$  ( $\text{M} = \text{Cu}, \text{Au}, \text{Pt}$ ) facilitates the dissociation of water making these systems excellent catalysts for the production of hydrogen through the water-gas shift reaction ( $\text{H}_2\text{O} + \text{CO} \rightarrow \text{H}_2 + \text{CO}_2$ ).<sup>36,87</sup> Furthermore, in ceria-titania, the  $\text{Ce}^{3+}$  ions introduce additional states in the band gap, corresponding to the partially occupied  $4f$  levels, and thereby reduce the band gap to about 2.2 eV.<sup>36,81</sup> This value is significantly lowered with respect to the clean surfaces of both ceria and titania. UV-Vis spectra have shown that ceria-titania can absorb photons in the visible region and when combined with Pt it can be used in the photocatalytic splitting of water.<sup>81</sup>

## Conclusions

In summary, we have studied the nature of the mixed-oxide interface in ceria-titania photocatalyst. Different interface models were proposed in order to take into account the different ceria nanostructures that have been characterized on the titania surface. Vacancy formation energies were evaluated in both phases in different planes at also in the interface. It was found that  $\text{Ce}^{3+}$  ions were stabilized at the grain boundaries or border and at the solid-solution interface between both oxides. DFT calculations can explain previous PFY and PEY measurement which found higher concentration at the interface than in the surface. Moreover, the migration for vacancy- $\text{Ce}^{3+}$  presented a high barrier which decreased when the number of  $\text{CeO}_2$  layer are diminished. However, the global minima is always obtained when the vacancy and the  $\text{Ce}^{3+}$  are placed at the interface. This fact could explain the presence of  $\text{Ce}^{3+}$  even at high oxidative conditions.

## References

1. Trovarelli, A., *Catalysis by Ceria and related Materials*, World Scientific **2002**.
2. Oetjen, H.; Schmidt, V.; Stimming, U.; Trila, F., *J. Electrochem. Soc.* **1996**, *143*, 3838.
3. Tanaka, Y.; Utaka, T.; Kikuchi, R.; Sasaki, K.; Eguchi, K., *Appl. Catal.* **2003**, *242*, 287.
4. Spencer, M. S., *Top. Catal.* **1999**, *8*, 259.
5. Park, J. B.; Graciani, J.; Evans, J.; Stacchiola, D.; Ma, S.; Liu, P.; Nambu, A.; Sanz, J. F.; Hrbek, J.; Rodriguez, J. A., *Proc. Natl. Acad. Sci.* **2009**, *106*, 4975.



6. Navarro, R. M.; na, M. A. P.; Fierro, J. L. G., *Chem. Rev.* **2007**, *107*, 3952.
7. Lewis, N. S.; Nocera, D. G., *Proc. Nat. Acad. Sci. USA* **2006**, *103*, 15729.
8. Kudo, A.; Miseki, Y., *Chem. Soc. Rev.* **2009**, *38*, 253.
9. Navarro, R. M.; Alvarez, M. C.; Valle, F.; Villoria, J. A.; Fierro, J. L. G., *ChemSusChem* **2009**, *2*, 471.
10. Webster, D. E., *Top. Catal.* **2001**, *16*, 33.
11. Burch, R., *Phys. Chem. Chem. Phys.* **2006**, *8*, 5483.
12. Thinon, O.; Diehl, F.; Avenier, P.; Schuurman, Y., *Catal. Today* **2008**, *137*, 29.
13. Haruta, M.; Yamada, N.; Kobayashi, T.; Iijima, S., *J. Catal.* **1989**, *115*, 301.
14. Valden, M.; Lai, X.; Goodman, D. W., *Science* **1998**, *281*, 1647.
15. Chen, M. S.; Goodman, D. W., *Science* **2004**, *306*, 252.
16. Fu, Q.; Saltsburg, H.; Flytzani-Stephanopoulos, M., *Science* **2003**, *301*, 935.
17. Rodriguez, J. A.; Liu, P.; Hrbek, J.; Evans, J.; Perez, M., *Angew. Chem-Int. Edit.* **2007**, *46*, 1329.
18. Guzman, J.; Carrettin, S.; Fierro-Gonzalez, J. C.; Hao, Y. L.; Gates, B. C.; Corma, A., *Angew. Chem-Int. Edit.* **2005**, *44*, 4778.
19. Deng, W. L.; Flytzani-Stephanopoulos, M., *Angew. Chem-Int. Edit.* **2006**, *45*, 2285.
20. Si, R.; Flytzani-Stephanopoulos, M., *Angew. Chem. Int. Edit.* **2008**, *47*, 2884.
21. Chen, M. S.; Goodman, D. W., *Top. Catal.* **2007**, *44*, 41.
22. Campbell, C. T.; Peden, C. H. F., *Science* **2005**, *309*, 713.
23. Esch, F.; Fabris, S.; Zhou, L.; Montini, T.; Africh, C.; Fornasiero, P.; Comelli, G.; Rosei, R., *Science* **2005**, *309*, 752.
24. Torbruegge, S.; Reichling, M.; Ishiyama, A.; Morita, S.; Custance, O., *Phys. Rev. Lett.* **2007**, *99*, 056101.
25. Rodriguez, J. A.; Ma, S.; Liu, P.; Hrbek, J.; Evans, J.; Perez, M., *Science* **2007**, *318*, 1757.
26. Rodriguez, J. A.; Evans, J.; Graciani, J.; Park, J.-B.; Liu, P.; Hrbek, J.; Sanz, J. F., *J. Phys. Chem. C* **2009**, *113*, 7364.
27. Rodriguez, J. A.; Graciani, J.; Evans, J.; Park, J. B.; Yang, F.; Stacchiola, D.; Senanayake, S. D.; Ma, S.; Perez, M.; Liu, P.; Sanz, J. F.; Hrbek, J., *Angew. Chem-Int. Edit.* **2009**, *48*, 8047.
28. Phatak, A. A.; Delgass, W. N.; Ribeiro, F. H.; Schneider, W. F., *J. Phys. Chem. C* **2009**, *113*, 7269.
29. Liu, P.; Rodriguez, J. A., *J. Chem. Phys.* **2007**, *126*, 164705.
30. Henderson, M. A., *Surf. Sci. Rep.* **2002**, *46*, 1.
31. Oviedo, J.; de Armas, R. S.; Miguel, M. A. S.; Sanz, J. F., *J. Phys. Chem. C* **2008**, *112*, 17737.
32. Ketteler, G.; Yamamoto, S.; Bluhm, H.; Andersson, K.; Starr, D. E.; Ogletree, D. F.; Oga-

- sawara, H.; Nilsson, A.; Salmeron, M., *J. Phys. Chem. C* **2007**, *111*, 8278.
33. Li, S.-C.; Zhang, Z.; Sheppard, D.; Kay, B. D.; White, J. M.; Du, Y.; Lyubinetsky, I.; Henkelman, G.; Dohnalek, Z., *J. Am. Chem. Soc.* **2008**, *130*, 9080.
  34. Kajita, S.; Minato, T.; Kato, H. S.; Kawai, M.; Nakayama, T., *J. Chem. Phys.* **2007**, *127*, 104709.
  35. Wu, T.; Kaden, W. E.; Anderson, S. L., *J. Phys. Chem. C* **2008**, *112*, 9006.
  36. Park, J. B.; Graciani, J.; Evans, J.; Stacchiola, D.; Senanayake, S. D.; Barrio, L.; Liu, P.; Sanz, J. F.; Hrbek, J.; Rodriguez, J. A., *J. Am. Chem. Soc.* **2010**, *132*, 356.
  37. Gonzalez, I. D.; Navarro, R. M.; Alvarez-Galvan, M. C.; Rosa, F.; Fierro, J. L. G., *Catal. Commun.* **2008**, *9*, 1759.
  38. Graciani, J.; Plata, J. J.; Sanz, J. F.; Liu, P.; Rodriguez, J. A., *J. Chem. Phys.* **2010**, *132*, 104703.
  39. Gonzalez, I. D.; Navarro, R. M.; Wen, W.; Marinovic, N.; Rodriguez, J. A.; Rosa, F.; Fierro, J. L. G., *Catal. Today* **2009**, *49*, 372.
  40. Kresse, G.; Joubert, D., *Phys. Rev. B* **1999**, *59*, 1758.
  41. Perdew, J. P.; Chevary, J. A.; Vosko, S. H.; Jackson, K. A.; Pederson, M. R.; Singh, D. J.; Fiolhais, C., *Phys. Rev. B* **1992**, *46*, 6671.
  42. Kresse, G.; Hafner, J., *Phys. Rev. B* **1993**, *47*, 558.
  43. Kresse, G.; Furthmuller, J., *Phys. Rev. B* **1996**, *54*, 11169.
  44. Marquez, A. M.; Plata, J. J.; Sanz, J. F., *J. Phys. Chem. C* **2009**, *113*, 19973.
  45. Dudarev, S. L.; Botton, G. A.; Savrasov, S. Y.; Humphreys, C. J.; Sutton, A. P., *Phys. Rev. B* **1998**, *57*, 1505.
  46. Fabris, S.; de Gironcoli, S.; Baroni, S.; Vicario, G.; Balducci, G., *Phys. Rev. B* **2005**, *72*, 237102.
  47. Cococcioni, M.; de Gironcoli, S., *Phys. Rev. B* **2005**, *71*, 035105.
  48. Castleton, C. W. M.; Kullgren, J.; Hermansson, K., *J. Chem. Phys.* **2007**, *127*, 244704.
  49. Nolan, M.; Grigoleit, S.; Sayle, D. C.; Parker, S. C.; Watson, G. W., *Surf. Sci.* **2005**, *576*, 217.
  50. Nolan, M.; Parker, S. C.; Watson, G. W., *Surf. Sci.* **2005**, *595*, 223.
  51. Nolan, M.; Parker, S. C.; Watson, G. W., *J. Phys. Chem. B* **2006**, *110*, 2256.
  52. Watkins, M. B.; Foster, A. S.; Shluger, A. L., *J. Phys. Chem. C* **2007**, *111*, 15337.
  53. Yang, Z.; Lu, Z.; Luo, G., *Phys. Rev. B* **2007**, *76*, 075421.
  54. Silva, J. L. F. D., *Phys. Rev. B* **2007**, *76*, 193108.
  55. Silva, J. L. F. D.; Ganduglia-Pirovano, M. V.; Sauer, J.; Bayer, V.; Kresse, G., *Phys. Rev. B* **2007**, *75*, 045121.
  56. Andersson, D. A.; Simak, S. I.; Johansson, B.; Abrikosov, I. A.; Skorodumova, N. V., *Phys. Rev. B* **2007**, *75*, 035109.

57. Loschen, C.; Carrasco, J.; Neyman, K. M.; Illas, F., *Phys. Rev. B* **2007**, *75*, 035115.
58. Loschen, C.; Migani, A.; Bromley, S. T.; Illas, F.; Neyman, K. M., *Phys. Chem. Chem. Phys.* **2008**, *10*, 5730.
59. Henkelman, G.; Uberuaga, B. P.; Jonsson, H., *J. Chem. Phys.* **2000**, *113*, 9901.
60. Giordano, L.; Pacchioni, G.; Bredow, T.; Sanz, J. F., *Surf. Sci.* **2001**, *471*, 21.
61. Pillay, D.; Wang, Y.; Hwang, G. S., *Catal. Today* **2005**, *105*, 78.
62. Pillay, D.; Wang, Y.; Hwang, G. S., *Korean J. Chem. Eng.* **2004**, *21*, 537.
63. Iddir, H.; Ogut, S.; Browning, N. D.; Disko, M. M., *Phys. Rev. B* **2006**, *73*, 039902.
64. Iddir, H.; Ogut, S.; Browning, N. D.; Disko, M. M., *Phys. Rev. B* **2005**, *72*, 081407.
65. Marquez, A. M.; Graciani, J.; Sanz, J. F., *Theor. Chem. Acc.* **2010**, *126*, 265.
66. Sanz, J. F.; Marquez, A. M., *J. Phys. Chem. C* **2007**, *111*, 3949.
67. Branda, M. M.; Castellani, N. J.; Grau-Crespo, R.; de Leeuw, N. H.; Hernandez, N. C.; Sanz, J. F.; Neyman, K. M.; Illas, F., *J. Chem. Phys.* **2009**, *131*, 094702.
68. Hernandez, N. C.; Marquez, A. M.; Sanz, J. F., *Surf. Sci.* **2005**, *575*, 189.
69. Hernandez, N. C.; Grau-Crespo, R.; de Leeuw, N. H.; Sanz, J. F., *PCCP* **2009**, *11*, 5246.
70. Plata, J. J.; Ruiz-Tagle, I.; Marquez, A. M.; Sanz, J. F., *J. Phys. Chem. Lett.* **2012**, *3*, 2092.
71. Gokhale, A. A.; Dumesic, J. A.; Mavrikakis, M., *J. Am. Chem. Soc.* **2008**, *130*, 1402.
72. Peng, S.-F.; Ho, J.-J., *Phys. Chem. Chem. Phys.* **2011**, *13*, 20393.
73. Rodriguez, J. A.; Liu, P.; Wang, X.; Wen, W.; Hanson, J.; Hrbek, J.; Perez, M.; Evans, J., *Catal. Today* **2009**, *143*, 45.
74. Fernandez-Garcia, M.; Martinez-Arias, A.; Hanson, J. C.; Rodriguez, J. A., *Chem. Rev.* **2004**, *104*, 4063.
75. Rodriguez, J. A.; Hrbek, J., *Surf.Sci.* **2010**, *604*, 241.
76. Trovarelli, A., *Catal. Rev. Sci. Eng.* **1996**, *38*, 439.
77. Lopez, T.; Rojas, F.; R. Alexander-Katz, F. G.; Balankin, F.; Buljan, A., *J. Solid State Chem.* **2004**, *38*, 1873.
78. Li, G.; Zhang, D.; Yu, J. C., *Phys. Chem. Chem. Phys.* **2009**, *11*, 3775.
79. Xiea, J.; Jianga, D.; Chena, M.; Lia, D.; Zhua, J.; Lua, X.; Yan, X., *Colloids Surf. A* **2010**, *372*, 107.
80. Catlow, C. R. A.; Guo, Z. X.; Miskufova, M.; Shevlin, S. A.; Smith, A. G. H.; Sokol, A. A.; Walsh, A.; Wilson, D. J.; Woodley, S. M., *Phil. Trans. R. Soc. A* **2010**, *368*, 3379.
81. Kundu, S.; Ciston, J.; Senanayake, S. D.; Arena, D. A.; Fujita, E.; Stacchiola, D.; Barrio, L.; Navarro, R. M.; Fierro, J. L. G.; Rodriguez, J. A., *J. Phys. Chem. C* **2012**, *116*, 14062.
82. Tasker, P. W., *J. Phys. C Solid State* **1979**, *12*, 4977.
83. Makov, G.; Payne, M. C., *Phys. Rev. B* **1995**, *51*, 4014.

84. Neugebauer, J.; Scheffler, M., *Phys. Rev. B* **1992**, *46*, 16067.
85. Nolan, M.; Fearon, J. E.; Watson, G. W., *Solid State Ionics* **2006**, *177*, 3069.
86. Ganduglia-Pirovano, M. V.; Silva, J. L. F. D.; Sauer, J., *Phys. Rev. Lett.* **2009**, *102*, 026101.
87. Barrio, L.; Zhou, G.; Gonzalez, I. D.; Estrella, M.; Hanson, J.; Rodriguez, J. A.; Navarro, R. M.; Fierro, J. L. G., *Phys. Chem. Chem. Phys.* **2012**, *14*, 2192.

---

**CHAPTER  
SEVEN**

---

**Conclusions**

Different methods have been used to analyze the structural and electronic properties of ceria and related materials. Pure GGA exchange-correlation functionals fail to describe the strongly correlated nature of reduced ceria, while hybrid functionals adequately tackle with the problem of the self-interaction error, though the amount of exact exchange and the functional have to be chosen carefully. While all hybrid functionals appropriately describe the crystal structure of  $\text{CeO}_2$  and  $\text{Ce}_2\text{O}_3$  oxides, high deviations were found for the band gaps. Within the original formulation, the HSE, PBE0 and B1-WC functionals appear to be the best suited for this kind of materials.

Because of the high computational cost of hybrid functionals in a plane-waves framework, alternative approaches using the Hubbard on-site correction DFT+U have been investigated. In particular a DFT+U scheme that incorporate the U parameter on both Ce  $4f$  and O  $2p$  orbitals has been optimized and shown to be a relatively reliable and efficient alternative. The combination of  $U^f$  and  $U_p$  leads to a moderately improved description of the lattice parameters, band gap and reaction energies and partially corrects the self-interaction error. In a further step, G0W0@PBE+U type approach has also been explored.

Ab initio quantum theory has been employed to determine and characterize the nature of the electron transfer process between adjacent  $\text{Ce}^{3+}$  and  $\text{Ce}^{4+}$  centers in bulk ceria. First we have identified the small polaron nature of the reduced Ce ions. Within the two-state Marcus model, we have estimated the electronic coupling matrix element or electron transfer integral,  $V_{AB}$ . Using diabatic wave functions determined at the Hartree-Fock level of theory we estimated for this quantity a value of 65 meV. Using an adiabatic approach enabled us to compute  $V_{AB}$  from DFT calculations employing several exchange-correlation functionals. The obtained values fall in the 68-88 meV range (mean value  $V_{AB} = 81$  meV). From the energy profiles determined at the UHF level of theory for the electron

transfer process along an idealized reaction path we obtained a reorganization energy  $\lambda$  of 1.96 eV, and an adiabatic barrier for the polaron hopping of 0.40 eV, in very good agreement with activation energy estimated from conductivity experiments performed on reduced ceria. Finally, the transmission coefficient  $\kappa$  was estimated to be 0.81, indicating that the electron transfer process is mainly adiabatic.

The activation barrier for the polaron hopping or electron transfer between  $\text{Ce}^{3+}$  and  $\text{Ce}^{4+}$  ions, responsible for the electron mobility, depends on the proximity to oxygen vacancies. When the  $\text{Ce}^{3+}$ - $\text{Ce}^{4+}$  pair is located well apart from the defect, the estimated barriers are 0.45-0.50 eV, closed to that found for non-defective bulk ceria. However, when the polaron is located at the neighborhood of the vacancy, a significant lowering of the activation energy can be observed for both surface and bulk models, with barriers in the 0.28-0.37 eV range. With respect to the oxygen migration, the energy profiles indicate that the lowest pathway involves oxygen atom making its way through a ( $\text{Ce}^{4+}$ - $\text{Ce}^{4+}$ ) pair toward the adjacent vacancy. Under these conditions the estimated barrier may be as low as 0.12 eV. However, the activation energy significantly increases when the oxygen moves to a vacancy traversing between ( $\text{Ce}^{3+}$ - $\text{Ce}^{4+}$ ) or ( $\text{Ce}^{3+}$ - $\text{Ce}^{3+}$ ) pairs. In such a case it would be preferable to transfer an electron to a nearby  $\text{Ce}^{4+}$  to facilitate the oxygen migration. In summary, charge transport in ceria might be viewed as a collaborative movement of electron transfer and ionic migration. Electron transfer is facilitated by the presence of oxygen vacancies, while oxygen (vacancy) migration is much easier when the atomic displacement occurs through non-reduced  $\text{Ce}^{4+}$  ions. This approach has been the first attempt to provide a quantitative description at the microscopic level of the charge and mass transport across the ceria surface.

The charge transport was also analyzed by means of DFT+U calculations in YSZ/doped  $\text{CeO}_2$  epitaxial heterostructures, where a huge ionic conductivity has been observed. The effect of the strain on the YSZ layers was evaluated and compared with previous results. The most important factor to increase the conductivity is the effect produced in the interface and ceria doping, which decreases the vacancy formation energy and facilitates the localization of vacancies and  $\text{Ce}^{3+}$  at the interface. Doping also diminishes the activation energy for vacancy migration.

As paradigm of 1D ceria nanostructures the structural and electronic properties of ceria nanotubes have been investigated. Negative strain energies have been predicted using DFT calculations with a hybrid functional for single walled monolayer ceria NTs. The NT stability was interpreted on the basis of interactions between terminating surface oxygen atoms. The reduction of NT strain and the reinforcement of covalency have been identified as the main factors determining the NT stability. Gold atoms show different behavior depending on the adsorption site (inside or outside the NT). Compared to  $\text{CeO}_2(111)$  surface, we found that gold atoms are more easily oxidized upon deposition, and therefore high catalytic activity is expected for these systems in processes where

either the reducibility of the support or the presence of cationic gold are expected to be key factors.

Ceria-titania interfaces show outstanding catalytic activities in several reactions, in particular the WGS reaction. The activity of coinage metals supported on these interfaces has been simulated using a Cu<sub>8</sub> nanocluster deposited on the CeO<sub>x</sub>/TiO<sub>2</sub> (110) surface. Assuming the carboxyl mechanism for this reaction, stationary points, activation barriers and reaction energies have been determined. Water dissociation is found to be exothermic and almost barrierless, indicating that this process is no longer the rate-limiting step. The carboxyl formation involves a barrier of 0.5 eV, significantly lower than that estimated for Cu/TiO<sub>2</sub>. The overall energy barriers in this system are below 0.5 eV, being, to the best of our knowledge, the first time that such a low-barrier path has been found. The key to get the system working under so low barriers is the full hydration of the oxide particle. This full hydration is an exothermic and low barrier process which, furthermore, allows an easy deprotonation of the \*OCOH intermediate which finally may lead the reaction to the final products CO<sub>2</sub> and H<sub>2</sub>.

To end up with the catalytic part of the report, the nature of the mixed-oxide interface in ceria-titania photocatalyst has been studied. Different interface models were proposed in order to take into account the diverse ceria nanostructures that have been characterized on the titania surface. Vacancy formation energies were evaluated in both phases in different planes at the interface. It was found that Ce<sup>3+</sup> ions were stabilized at the grain boundaries or border and at the solid-solution interface between both oxides. DFT calculations can explain previous PFY and PEY measurement, which found higher concentration at the interface than in the surface. Moreover, the migration for vacancy-Ce<sup>3+</sup> presented a high barrier which decreased when the number of CeO<sub>2</sub> layer are diminished. However, the global minima are always obtained when the vacancy and the Ce<sup>3+</sup> are placed at the interface. This fact could explain the presence of Ce<sup>3+</sup> even at high oxidative conditions.





## Other publications

### Pd-based catalysts

- José J. Plata, Mónica Gracia-Mota, Ataulpa Braga, Nuria López, and Feliu Maseras; Vinyl Acetate Synthesis on Homogeneous and Heterogeneous Pd-Based Catalyst: A theoretical Analysis on the Reaction Mechanism, *J. Phys. Chem. A* **2009**, *113*, 1175811762

### CO oxidation in Au/Y<sub>2</sub>O<sub>3</sub>/TiO<sub>2</sub>

- José J. Plata, Antonio M. Márquez, Javier Fernández Sanz, Rafael Sánchez Avelaneda, Francisca Romero-Sarriá, María Isabel Domínguez, Miguel Ángel Centeno, and José Antonio Odriozola; Gold Nanoparticles on Yttrium Modified Titania: Support Properties and Catalytic Activity, *Top. Catal.* **2011**, *54*, 219-228
- Francisca. Romero-Sarria, José. J. Plata, O. H. Laguna, Antonio. Mrquez, Miguel. Ángel. Centeno, José. Fdez Sanz, José. A. Odriozola; Role of the surface oxygen vacancies in gold based catalysts for CO oxidation, *Submitted*

### VOCs adsorption in TiO<sub>2</sub>

- Antonio M. Márquez, José J. Plata, and Javier Fernández Sanz; Role of Coverage and Surface Oxidation Degree in the Adsorption of Acetone on TiO<sub>2</sub> (110). A Density Functional Study, *J. Phys. Chem. C* **2009**, *113*, 19973-19980

- José J. Plata, Veronica Collico, Antonio M. Márquez, and Javier Fernández Sanz; Understanding Acetaldehyde Thermal Chemistry on the  $\text{TiO}_2$  (110) Rutile Surface: From Adsorption to Reactivity, *J. Phys. Chem. C* **2011**, *115*, 2819-2825
- José J. Plata, Veronica Collico, Antonio M. Márquez, and Javier Fernández Sanz; Analysis of the Origin of Lateral Interactions in the Adsorption of Small Organic Molecules on Oxide Surfaces, *Theo. Chem. Acc.* **2013**, *132*, 1311

### W,N-TiO<sub>2</sub> doping

- Antonio M. Márquez, José J. Plata, Yanaris Ortega, and Javier Fernández Sanz; Structural Defects in W-Doped  $\text{TiO}_2$  (101) Anatase Surface: Density Functional Study *J. Phys. Chem. C* **2011**, *115*, 16970-16976
- José J. Plata, Antonio M. Márquez, Gerardo Colón, Yanaris Ortega, Marcos García-Fernández, and Javier Fernández Sanz; Making Photo-selective  $\text{TiO}_2$  Materials by CationAnion Codoping: From Structure and Electronic Properties to Photoactivity *J. Phys. Chem. C* **2012**, *116*, 18759-18767

### Excited states dynamics

- José J. Plata, Marie-Catherine Heitz, and Fernand Spiegelman; Effect of Structure and Size on the Excited States Dynamics of CaArn Clusters, *Eur. Phys. J. D* **2013**, *67*, 17